2016

Design, Fabrication and Characterization of Photonic Crystal Light-Emitting Diodes for Solid-State Lighting

Anand Kadiyala

Recommended Citation

Kadiyala, Anand, "Design, Fabrication and Characterization of Photonic Crystal Light-Emitting Diodes for Solid-State Lighting" (2016). *Graduate Theses, Dissertations, and Problem Reports*. 5917.
https://researchrepository.wvu.edu/etd/5917

Design, Fabrication and Characterization of Photonic Crystal Light-Emitting Diodes for Solid-State Lighting

Anand Kadiyala
B.E. Electronics and Communication Engineering, Osmania University, India

Dissertation
Submitted to the
Benjamin M. Statler College of Engineering and Mineral Resources
at
West Virginia University
in partial fulfillment of the requirements
for the degree of

Doctor of Philosophy

in

Electrical Engineering

Dr. Jeremy Dawson, Chair
Dr. Lawrence Hornak
Dr. Dimitris Korakakis
Dr. David Graham
Dr. Charter Stinespring

Lane Department of Computer Science and Electrical Engineering
West Virginia University

Morgantown, West Virginia
2016

Keywords: Solid-State Lighting, Light-Emitting Diodes, III-V Nitrides, Photonic Crystals, Hydrogen Silsesquioxane, Electron Beam Lithography, Nanosphere Lithography, Large-Scale Fabrication & Integration

Abstract

Design, Fabrication and Characterization of Photonic Crystal Light-Emitting Diodes for Solid-State Lighting

Anand Kadiyala

Residential, commercial, and industrial lighting applications contribute to ~19% of total energy consumption worldwide. The application of more efficient sources of lighting, such as solid-state lighting (SSL) sources, could result in potential energy savings of about 65%. Current technologies employ semiconductor-based light-emitting diodes (LEDs) as the core elements of SSL devices to provide general-purpose light in a wide range of color temperatures. However, there still exists several device level issues, such as poor material quality, low quantum efficiencies, large percentage of light being trapped, etc. These non-idealities are barriers for SSL sources replacing incandescent and compact fluorescent sources on an equivalent lumens-per-watt basis.

WVU SSL research interests involve addressing device-level issues associated with III-V nitride materials, as well as optimizing the growth of materials and performance of fabricated devices. One major goal of research efforts is to provide solutions for improvement in light extraction in III-nitride-based devices through the use of integrated, device-level optical elements such as photonic crystals. Photonic Crystals (PhCs) are periodic dielectric structures that possess unique optical properties. PhCs are known for possessing an optical band gap that enables blocking of certain range of wavelengths based on their feature sizes. Additionally, they can also be utilized as diffractive elements when placed in the path of the photons. PhC structures in LEDs are commonly utilized for light extraction improvement and the integration process into the device structure often results in sub-optimal electrical characteristics. The work presented here provides the details of novel processes to add nanophotonic structures to metal and transparent conducting contacts (like indium tin oxide (ITO)) for indium gallium nitride/gallium nitride (InGaN/GaN) based multi-quantum well blue LEDs with emission wavelength in range of λ=440-470 nm. The developed integration processes will enable improvement in the light extraction of the devices while reducing damage to the active regions of the device and maintaining optimal electrical characteristics. Novel electron beam resist like hydrogen silsesquioxane (HSQ) was utilized to achieve integration of PhCs with minimal degradation. Due to its unique chemical properties, a new classification of PhC structures were realized, that involves cured form of HSQ and named hybrid PhCs. Applying this process, hybrid PhC structures with features of 150 nm in diameter with a pitch of 500 nm in triangular and square lattice configurations fabricated in ITO contacts were integrated into the LEDs. As a result, the devices with hybrid PhC structures showed an improvement of ~5x in intensity when compared to the unpatterned device.

This work also involved the development of novel bilayer methods using HSQ and sacrificial polymer layers for successful integration of PhCs with holes in transparent conducting layer contacts like ITO. The bilayer process developed will enable in realizing the more traditional PhC structures without the aforementioned process induced sub-optimal electrical characteristics. Additionally, nanosphere lithography (NSL) techniques like spin coating and thermal evaporation were explored as alternative patterning methodologies to enable integration of PhC structures on a large-scale. Utilizing thermal evaporation method, a 98.5 % coverage of uniform single layer of polystyrene beads was achieved over a 1.5 x 1.5 cm^2 area. This approach to device fabrication will allow PhCs to be integrated into commercial devices inducing less structural damage.

To my family & friends…

Acknowledgments

I would like to take this opportunity to express my deep gratitude towards my advisor, Dr. Jeremy Dawson for his guidance towards my thesis work. Dr. Dawson's wisdom, patience and constant encouragement are some of the reasons that have made the findings in this thesis possible. I wish to thank my committee members, Dr. Lawrence Hornak, Dr. Dimitris Korakakis, Dr. David Graham and Dr. Charter Stinespring, whose support, and helpful advice have been critical to my work.

I would like to thank Dr. Dimitris Korakakis for his support and guidance while working with the III-V nitride materials and treating me as one of his own graduate students. I would also like to thank Dr. Kolin Brown, Dr. Weiqiang Ding, Mr. Harley Hart, Dr. Marcela Redigolo, Dr. Huiyuan Li, Trina Wafle and other SRF staff, for their support and guidance in the cleanroom and other research facilities.

I am also grateful to have worked with some amazing graduate and undergraduate students. Specifically, Dr. Sridhar Kuchibhatla, Dr. Lee Rodak, Dr. Rohit Goswami, Dr. Ronak Rahimi, Dr. Vishal Narang, Dr. Kyoungnae Lee, Hyma Yalamanchili, Kyle Smith, Chloe Snyder, Maurya Srungarapu, Seth Leffel, Brianna Maze, Christo Robison, Matthew Pachol, Srinitya Musunuru, Lekha Kuchipudi, Kenneth Hite, Laurell Pell, Joshua Justice, Rupa Indrani and Sujan Kasani have all contributed towards a constructive learning environment and have enjoyed working with them. I would like to take a moment to also acknowledge undergraduate students who have learned and contributed towards research findings, viz. Caroline Kilemi, Alicia Kadiri, Brad Potteiger, Kathryn Smith, Melanie Wieland, Taylor Price and Jequil Hartz. Particularly, Brad Potteiger, Melanie Wieland and Jequil Hartz who have helped in developing some of the automation codes that were used in this research. Overall, the journey with these amazing people has been nothing but rewarding. Finally, I would like to dedicate this dissertation to my family and my friends.

Table of Contents

List of Figures

List of Tables

1. Introduction

The solid-state lighting (SSL) industry uses semiconductor based light emitting diodes (LEDs) as the core elements to generate light. LED lighting is based on conversion of electron-hole recombination to photon energy instead of filaments (incandescent bulbs) or gaseous plasma (fluorescent lamps). This industry has the potential to revolutionize and replace the current lighting technologies (viz. incandescent, compact fluorescent lamps, halogen lamps etc.) due to a number of advantages including reduced loses in energy conversion, directionality, controllability, long life, color tunability, and aesthetic appeal [1].

The driving motivation behind the SSL industry is to produce energy efficient lighting methods for general illumination. It has been proven that LED lighting have higher efficiencies, life time and savings in comparison to the conventional methods as shown in the Figure 1.1. Department of Energy (DOE) predicts the energy savings by SSL technology by 2025 will be about one-half of current consumption for lighting in the US [2]. To achieve this rate of energy savings, there needs to be improvement in several areas of the lighting technology. These areas include the synthesis of ideal active materials, device structure and fabrication methods, packaging materials and techniques, efficient driving circuitry and light extraction methods.

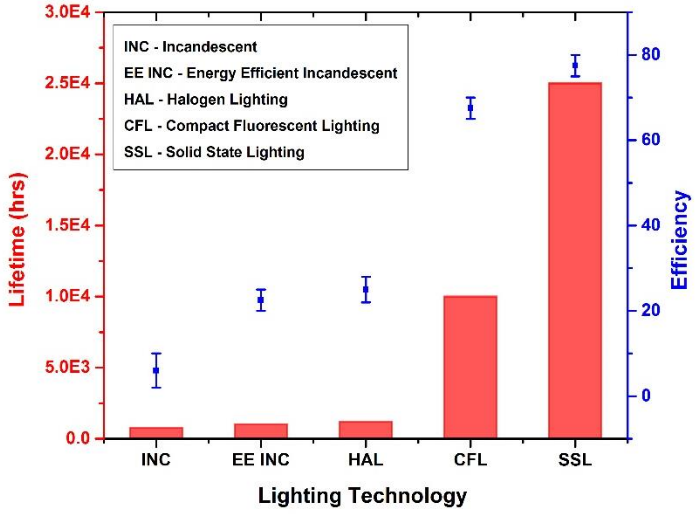

Figure 1.1 Lifetime and efficiency comparison for different lighting technologies (graph reproduced using the data from [1], [2], [3])

The major requirement of general illumination technology is to produce visible white light which comprises of all wavelengths between 400 nm and 700 nm. Using LEDs as core elements, white light can be produced by using ultraviolet (UV) or blue LEDs and color converting phosphor composites [11], by color mixing with primary colored LEDs [12] and a combination of both (hybrid method LEDs). Current methods of white light generation follow the first method that contain blue LED chips and color converting phosphors.

Group III-V nitride materials are known for their wide direct band gap energies. The band gap energies for these materials range from ~0.7 eV (Indium Nitride - InN) to ~6.4 eV (Aluminum Nitride - AlN). Gallium Nitride (GaN) is one such material that has a wide direct band gap energy of ~3.4 eV [4]. These materials can be alloyed to form tertiary and quaternary compounds that have effective band gaps that can sweep the entire visible spectrum as shown in the Figure 1.2. Various alloy combinations of these binary materials (InN, GaN, AlN) allow the tuning of the band gap continuously and monotonically, along with the band structure, electronic and optical properties of the compound [4].

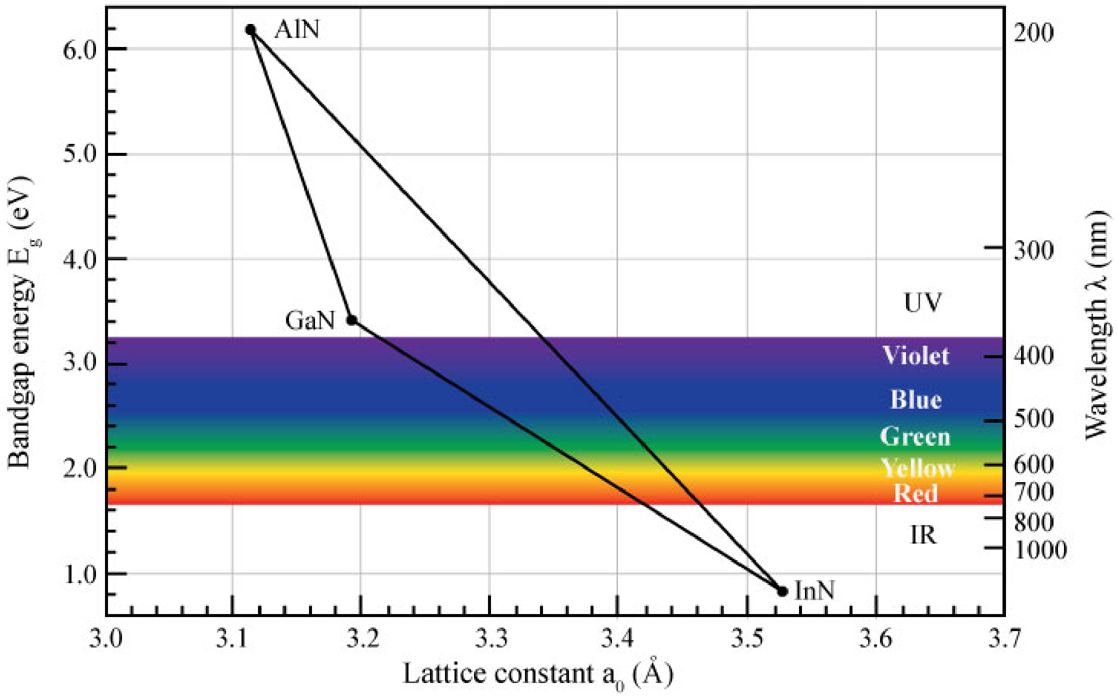

Figure 1.2 Band gap energies versus the lattice constant (reproduced from [4])

Indium gallium nitride (InGaN) is one such tertiary compound of the group-III nitrides formed by alloying InN (0.7 eV) and GaN (3.4 eV) and allows the formation of heterostructures like GaN/InGaN. The resulting material $In_xGa_{1-x}N$ will have a band gap ranging between the extremities depending on the alloy percentage (x). By tuning the percentage of indium in the compound, the effective band gap to produce a blue light can be achieved. Most of these alloyed compounds are considered to be dielectric and have unique electrical and optical properties that can be used in many electronic and photonic applications. For the entirety of this dissertation, InGaN/GaN based multiple quantum well (MQW) LEDs are studied and the various issues affecting the performance will be addressed.

1.1. Statement of Dissertation

The measure of a light source's efficiency is called luminous efficacy, which translates to number of lumens per watt. Lumen (lm) is the measure of the luminous flux, the amount of visible light emitted by a source. However, this measure of efficacy is considered the higher level efficiency of the source. In this area of SSL, to improve the luminous efficacy of the light source, the efficiency of the underlying solid state component (LEDs) has to be improved. The overall efficiency of an LED called external quantum efficiency (EQE - η_o) is denoted as the ratio of the number of photons emitted to the number of electrons injected. EQE is usually determined by the product of the other quantum efficiencies viz. injection efficiency (IE - η_{inj}), recombination efficiency (RE – η_r) and extraction efficiency (EE - η_{ext}) as shown in the equation 1.1 [5].

$$\eta_o = \eta_{inj} \times \eta_r \times \eta_{ext} \tag{1.1}$$

The three components of the above equation depict three different quantum efficiencies related to three different steps of the device operation. The injection efficiency gives the measure of the number of electrons injected into the active region of the total number of electron passing through an LED. The recombination efficiency or the internal quantum efficiency is the measure of the number of photons generated to the number of injected electrons. The extraction efficiency is the measure of the number of photons emitted into the free space to the total number of photons generated. Usually, the injection efficiency of the device is pretty high and is close to a 100 % at high currents. The recombination efficiency is close to 50 – 100 %, depending on the structure of the LED. Finally, the extraction efficiency ranges from 10 % - 73 % depending on the extraction method used in the structure [6]. From the above descriptions, the deciding factor for a high luminous efficacy LED bulb relies on the extraction efficiency of the underlying LEDs.

Within the device (LED), the light is generated by the electron-hole pair recombination and these recombination events can be divided into radiative and non-radiative events [4]. The outcome of such events could be either a photon (light) or a phonon (lattice vibration). The photons generated within the active region of the device have spontaneous directions and have to travel through several dielectric layers to emerge into the surrounding medium. Due to total internal reflection, some portion of these photons traveling get trapped with the layers and results in a poor extraction efficiency. The condition for the trapped light to escape is dependent on the angle of the incidence at the interface. The collection of angles at the interface defines the escape or emission cone [4]. Due to the spontaneous nature of the light generation in an LED, there exist multiple escape cones in a device as shown in the Figure 1.3 [7]. This escape cone gives an estimate of the light that is extracted ($\boldsymbol{F_T}$) to the total light that is generated and is dependent on the refractive indices of the materials at the interface denoted by the equation 1.2 [5], [4].

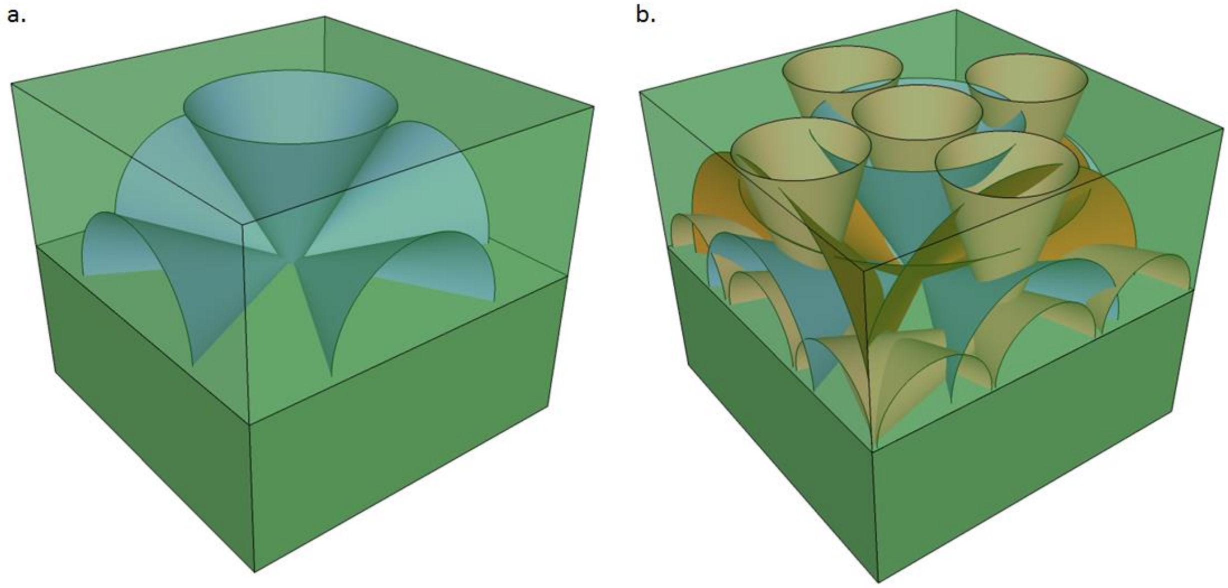

Figure 1.3 Escape cone for an ideal single source of illumination, b. Escape cones for different points of illumination in a real LED

$$F_T = \frac{1}{4} \cdot \left(\frac{n_{air}}{n_{semi}}\right)^2 \cdot \left[1 - \left[\frac{n_{semi} - n_{air}}{n_{semi} + n_{air}}\right]^2\right] \qquad (1.2)$$

This fraction of light ($\boldsymbol{F_T}$) extracted at the interface of GaN and air is ~ 4% and explains the low extraction efficiencies of the devices involving such materials. To extract the trapped light within the dielectric layers, necessary physical changes to the shape and structure of the device are to be done. In the recent years, several extraction methods have been developed and improved to address this problem. Techniques like chip shaping [8], [9], encapsulation [10], surface roughening [11], [12], [13], [14], patterned substrates [15], [16], [17], [18], integration of DBRs and photonic crystals [19], [20], [21] and the combination of them are usually deployed to improve the extraction in the LEDs. Each of these techniques has a unique approach and addresses a particular segment of the issue. With the incorporation of such extraction methods, the light extraction efficiency has been improved and lies between ~73% - 85% to date [6], [22].

1.2. At West Virginia University

Our group here at WVU, has immense research experience in the areas of material growth, fabrication methods and nanophotonics. The material growth and characterization group led by Dr. Dimitris Korakakis is primarily invested in the growth of high-quality epitaxial substrates using metal-organic vapor phase epitaxy (MOVPE) [23], [24], [25]. The substrates with the epi-layers of LEDs are fabricated into devices in a cleanroom environment. Previous efforts in growth and fabrication of LEDs have resulted in an optimized device structure (shown in the Figure 1.4 a.). With the precise control of the epitaxial growth and fabrication methods, the device-level characteristics (shown in the Figure 1.4 b.) are optimized for repeatable and stable devices [26], [27].

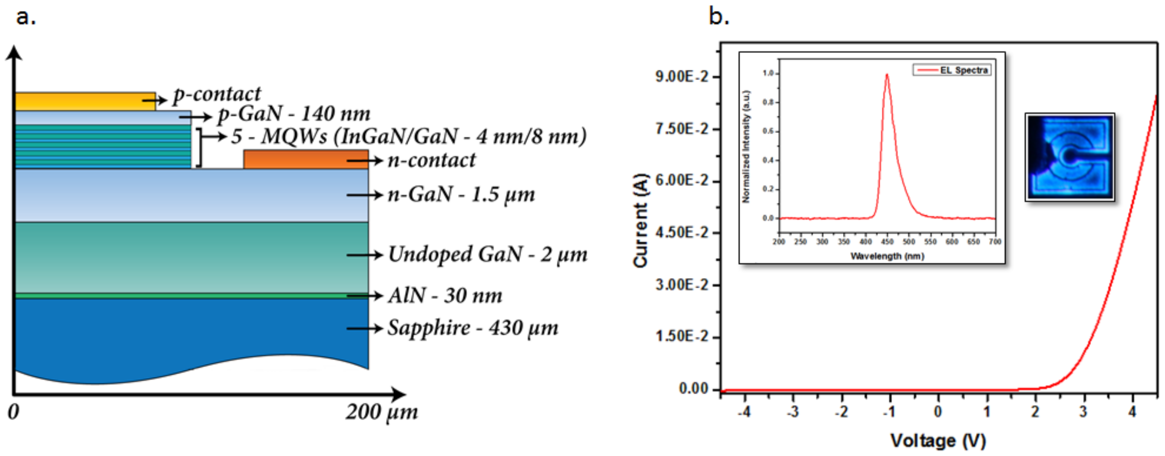

Figure 1.4 a. Optimized LED structure, b. Device-level characteristics of LEDs grown at WVU (Inset: Electroluminescence spectra and optical image)

To address the issue of the extracting the trapped light from the devices, the nanophotonics group is conducting research in the optical modeling, fabrication and characterization of photonic crystals and its applications. Photonic Crystals (PhCs), by definition are periodic dielectric structures with unique optical properties to reflect, manipulate or confine the propagation of light [28], [29]. The periodic arrangement of dielectric high and low media leads to a photonic band gap that is analogous to the electrical band gap possessed by semiconductor materials. With appropriate combination of critical parameters of the PhC, the photonic band gap is tuned to reflect, confine or transmit a group of wavelengths. Due to their unique diffraction and band gap properties, PhCs can be used as an integral part of an LED to block and direct a band of wavelengths that contribute in the extraction of the emission wavelength from the device as shown in the Figure 1.5.

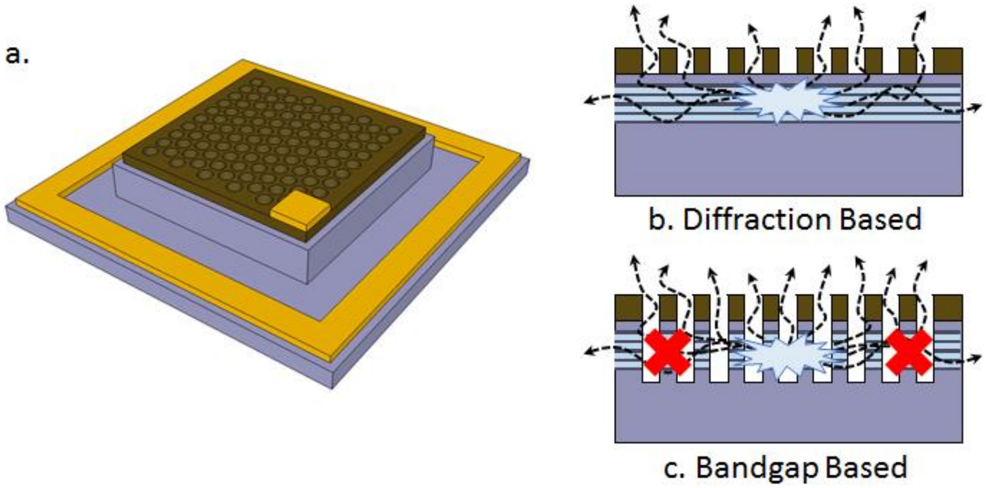

Figure 1.5 a. Illustration of a PhC LED, b. PhC in a diffraction based design and c. PhC in a band gap based design

1.3. Research Goals

The main goal of this research is to fabricate and integrate a PhC structure into an LED structure without degrading its physical and electrical characteristics and help improve the extraction efficiency. The specific tasks relating to this goal are listed below.

- *Theoretical Modeling* – Finite element time domain modeling software will be used to design an optimal lattice structure for improving the light extraction of an LED
- *Fabrication Process Development* – Novel materials and non-invasive fabrication methods based on both-e-beam lithography and large-scale nanosphere patterning will be developed for integration of PhCs into an LED

- *Characterization* – Bench-top optical methods, spectroscopy, I-V measurements will be used to optimize designs and quantify the improvement achieved

A brief summary of these individual goals is provided in the following sub-sections.

1.3.1. Theoretical Modeling

The theoretical design of the PhC helps in understanding the characteristic changes that light as an electromagnetic wave undergoes when it travels through any material. These changes in the behavior of an electromagnetic wave in any medium could be well understood by the classical electromagnetism concepts. The interactions of the PhC system are better understood by solution of the Maxwell's equations. Software engines like MPB, MEEP, OptiFDTD etc. are used to analyze the interactions with PhC structures.

MIT Photonic Bands (MPB), is a freely available Eigen solver that solves the interactions of an electromagnetic wave with a defined material [28]. A periodic arrangement of features like pillars or holes made of materials like Indium Tin Oxide (*ITO*), and Gallium Nitride (*GaN*) are defined in the CAD environment and simulated to obtain photonic band diagrams. These band diagrams are similar to electronic band diagram for a semiconductor and provide information about the photonic band gap of that structure as illustrated in Figure 1.6.

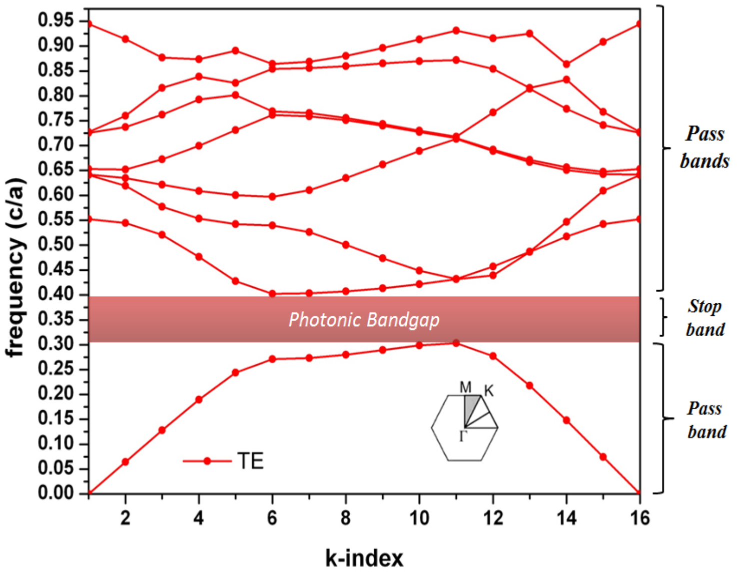

Figure 1.6 Band diagram of a triangular lattice of silicon pillars showing stop and pass bands

Using these band diagrams that possess a photonic band gap, a central frequency is chosen to extract the physical parameters of the PhC structure. This central frequency or wavelength is usually the emission wavelength of the LED. The PhC structures for band gap based extraction are chosen and the physical parameters are extracted to block and enhance the emission wavelength of the device. Apart from the band gap based extraction, a time domain evolution of electromagnetic waves within a PhC structure are simulated to obtain the optimal PhC structure that is best suited for diffraction based extraction improvement. Using Optiwave's Finite Difference Time Domain (FDTD) simulations, the respective field patterns as shown in the Figure 1.7, are extracted and optimal device parameters are then determined based on the overall intensities and comparison between different lattice configurations.

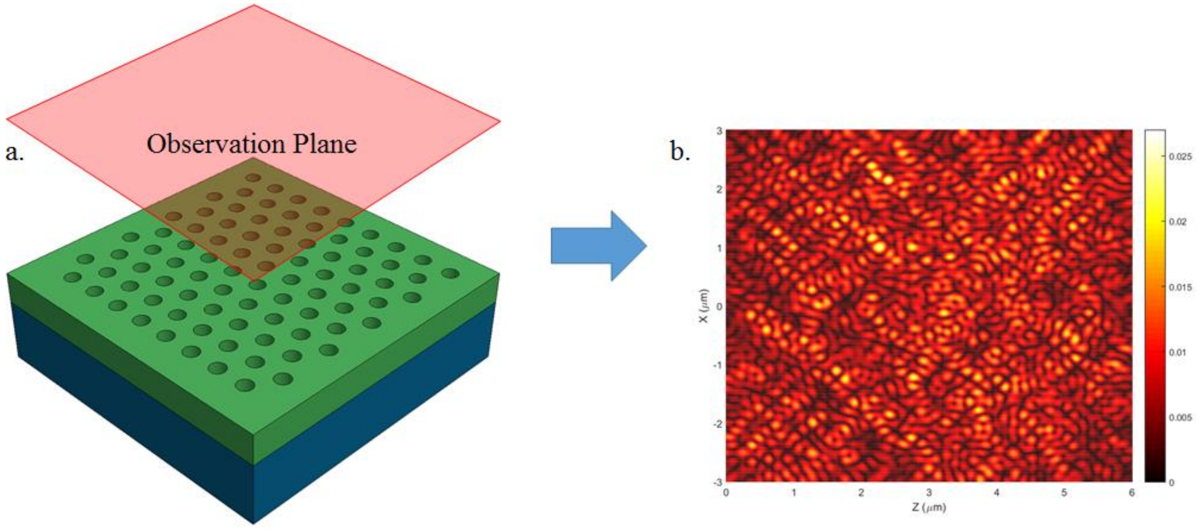

Figure 1.7 Finite Difference Time Domain simulations a. simulation model, b. Near-field distribution

In this work, two types of PhC structures are investigated, viz. typical and hybrid structures. A typical PhC is one with a periodic change in the refractive index (n_{high}, n_{low}), whereas the hybrid PhC structure is one with an intermediary dielectric media introduced (n_{high}, n_{med}, n_{low}). A detailed study of the photonic properties was done using both the MPB and Optiwave's software. The results give an insight into the optical improvement that can be achieved using the PhC structures integrated into LEDs.

1.3.2. Fabrication Process Development

Utilizing traditional micro-/nano- fabrication techniques to transfer the PhC pattern into the device presents a challenging task as it requires some materials to be sacrificially etched. Due to these etch processes, harsh chemical reactions might etch unintended materials or introduce defects into the structure causing etch damage [30], [31], [32] and altering electrical properties of the device. Although, there are various methods developed to recover from the etch damage by thermal annealing, chemical [33] and plasma treatments [34], [35]. Even with such recovery techniques, there still exists traces of the induced etch damage in the form of large amounts of leakage currents [30]. The solution to this problem, is to prevent these redundant etching steps is to implement lift-off techniques or other pattern transfer techniques that are non-invasive.

A typical fabrication process involves the use of photolithography for pattern transfer to a photo sensitive polymer (photoresists), followed by an etch process to transfer the pattern to the semiconductor material. This process flow has its limitations such as the type of polymers used, fixed mask patterns, minimum feature size achieved, etch resistance and limitation in aspect ratios. A new group of polymers that are sensitive to electron energy called electron beam resists have the answer to some of these limitations. Electron Beam Lithography (EBL) is the lithography technique used to expose such resists that has the ease in layout designing, wide range exposure times and the ability to achieve nano-scale features.

Fabrication of periodic nanoscale structures using both traditional and advanced lithography techniques have been previously studied and implemented. In most cases, the processing parameters were developed for common semiconductor materials like silicon and the processes cannot be easily transferred to materials from the III-V nitride family. Further process development and optimization has to be done to adapt the fabrication parameters to materials involved in PhCs and LED structures. Additionally, there is decline in benefit-cost ratio as the cost involved to use such complex and accurate technologies increases. In such cases, the most effective way to fabricate and integrate periodic structures into LEDs is achieved by one of two methods: utilizing least number of/eliminating processing steps or by developing cost effective methods.

In this work, novel materials that have high etch resistance and are capable of being dissolved in chemical solutions that enable lift-off were investigated. Spin-on-dielectrics, like Hydrogen Silsesquioxane (HSQ), typically used as an insulator in the semiconductor industry, has been identified as an electron beam resist. Using EBL and HSQ, research groups have achieved high resolution and high-density nano-scale features in various applications [36], [37], [38]. Previous experimentation by our group with a variant of HSQ supplied by DOW Corning [39] has proven to be a promising etch resistant electron beam resist. This led to the use of HSQ in creating nano-scale features [40] for light extraction and biosensing applications. Another variant of HSQ is investigated for its use in association with EBL to integrate PhC structures into the device structure. Utilizing HSQ for integration of PhC structures into LED shows a significant reduction in processing steps and improving the light extraction without affecting the electrical characteristics.

Although, EBL has proven its potential in fabricating micro- and nano-scale features for various applications, yet it has its own limitations like limited area of exposure, cost of equipment, focus and proximity issues, and low yield. In addition to top-down approaches like EBL, bottom-up methods such as nanosphere lithography (NSL) [41], [42], an inexpensive methodology was investigated to pattern transfer over a large area. A cost effective method to fabricate and integrate periodic structures into LEDs which has a high yield was developed. In this method, suspensions of polystyrene or silica microspheres were used as the mask for transferring the pattern to the material of interest. A thorough investigation into utilization of NSL to LED applications is performed along with development of the integration process into an LED. With the state-of-the-art processing tools available at WVU, three processing methods for integration of PhCs into III-V nitride materials are developed and implemented to significantly improve the light extraction from the devices.

1.3.3. Characterization

The conclusive and feedback step in the course of designing and developing the fabrication processes for integrating PhCs into various materials is to check for the material properties as designed versus as fabricated. Both electrical and optical properties of the essential layers of the LED is performed under the characterization of materials. Optimization of additional layers like ITO as a transparent conducting layer (TCL) is critical for the overall electrical and optical characteristics of the device. Current-voltage characteristics, specific contact resistivity, carrier concentration, electroluminescence, and radiation patterns are the electrical and optical properties that are studied for various configurations and processing parameters. These results are used as a form of feedback to adjust and fine tune growth and fabrication of the devices.

When PhCs are to be integrated within TCLs or any other dielectric layers, the optical properties are subjected to change. Methods to measure these characteristic changes in the optical properties were developed and tested.

1.4. Summary and Organization of Dissertation

This research will help understand and develop methods of light extraction that can be used as the structural components of LEDs without affecting the performance of the device. The improvements in the extraction due to the integration of certain extraction methods will help in increasing the quantum efficiencies of the devices which in turn improves the efficiency of the light source. The benefits following this dissertation are listed below.

- Designing an optimal PhC structure to help improve the light extraction in LEDs
- Investigate a novel class of hybrid PhC structures for improvement in light extraction in LEDs
- Exploring and implementation of novel materials like Hydrogen Silsesquioxane for fabrication and integration of PhCs
- Detailed integration process development and execution of PhCs into the LED structures without any performance degradation using HSQ and EBL
- Methods to facilitate large scale fabrication of PhCs using self-assembly techniques
- Spin coating and thermal evaporation techniques for large-scale patterning using NSL
- Electrical and Optical characterization setups for quantizing performance of LEDs with and without PhCs

The work explained through the next five chapters of this document focuses on fabrication and integration of PhC structures in LEDs. A detailed theory behind the functionality of both LEDs and PhCs is laid out in the Chapters 2 and 3. Design and modeling results of various PhC structures for improving the light extraction efficiency in LEDs using frequency and time domain simulation software will be demonstrated in Chapter 4. The results from these simulations point to an optimal PhC structure that can be utilized for fabrication and integration into the LED structure. In Chapter 5, several fabrication process flow using typical and novel ebeam resist are shown along with respective results. Additionally, an insight into methods like bilayer processing and Nanosphere Lithography to fabricate PhC structures is shown. This chapter also includes a sub-chapter that is dedicated on the topics of integration of PhCs using above mentioned methods. Chapter 6 discusses the characterization results of the devices containing hybrid PhC structures. A detailed summary and future direction of this research is laid out in the Chapter 7. Finally, all the supplemental information involved in the design, fabrication and characterization of PhC LEDs are summarized in the Appendices.

2. Light Emitting Diode Theory

The following chapter discusses the operation of a semiconductor light emitting diode and the challenges of achieving higher efficiency for solid-state lighting.

2.1. LED Basics

Light Emitting Diode is a semiconductor p-n junction diode that has revolutionized the conventional lighting methods. Over the past four decades, there has been good technical progress in the field of LEDs. Group III-Nitrides like AlN, GaN and InN along with their alloys have been responsible for a giant leap in this field. These nitrides and alloys are the few semiconductors that have wide and direct band gaps in the range of 3.4eV to 6.2eV. With these continuous and direct band gaps, semiconductor alloys are producing low wavelengths devices. Light Emitting Diodes and Laser Diodes based on GaN are capable of generating photons from deep ultraviolet (UV) through visible to the far infrared (IR) region as shown in the Figure 2.1. This extended range of photon wavelengths could not have been achieved by the group III-V semiconductor materials.

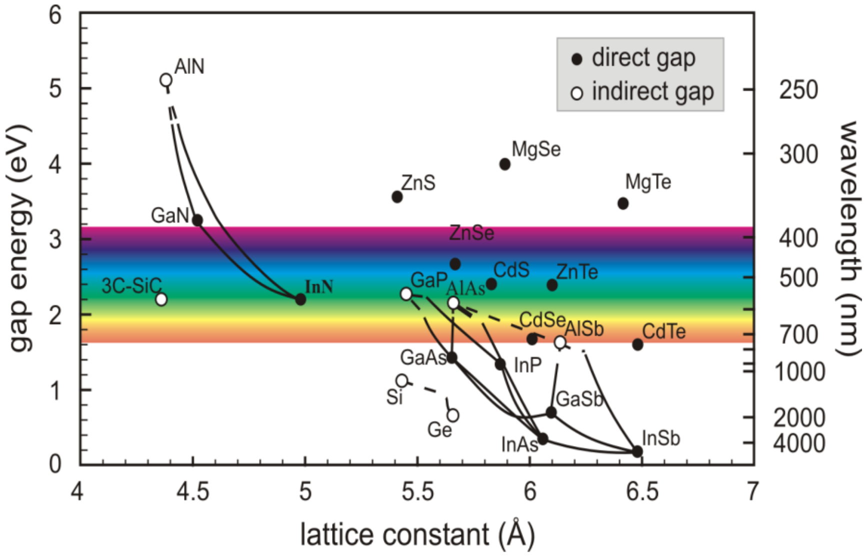

Figure 2.1 Bandgaps of the most important elemental and binary cubic semiconductors versus their lattice constant at 300 K. The right-hand scale gives the light wavelength λ, corresponding to the band gap energy [4]

As discussed earlier, there has been a great effort towards the development of efficient and reliable semiconductor based LEDs. And the group III-V based nitride semiconductors was the place for the research in this field. Today, there are many applications that make use of GaN based LEDs from display panels to traffic lights.

2.1.1. Direct and Indirect Bandgap Semiconductors

All semiconductor materials are mainly divided into two categories called the direct bandgap and indirect bandgap materials. The band structure of any material consists of two main bands called the conduction band and valence band. The conduction band is a band of electron energies that are free to move around the atomic lattice of the material while the valence band contains the occupied electrons. In a direct bandgap material, the electrons with same momentum undergo band to band radiative transition. This results in a more conservative recombination and a high probability of the transition. In case of an indirect bandgap material, the transition is generally due to a third component called a phonon, which results in a less probable transition of the electrons as shown in Figure 2.2.

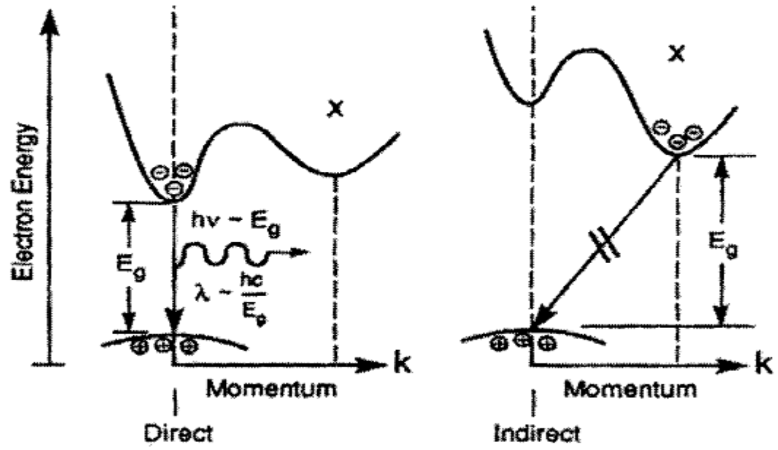

Figure 2.2 Energy band diagram of direct (GaN) and indirect bandgap (SiC) semiconductors.

This is very clear when comparing the direct and indirect bandgap LEDs. GaN being direct bandgap material, the LEDs based on this material exhibit higher efficiency (up to 12%) when compared to indirect bandgap SiC LEDs (0.02%).

Group III-nitride family contains mostly materials with direct bandgap and by creating ternary or quaternary alloys using Indium and/or Aluminum; the bandgap range can be swept from 0.7eV to 6.2eV. This range of the bandgap could possibly cover the entire visible spectrum including parts of deep UV and infrared as shown in Figure 2.1. However, as the In or Al content of InGaN and AlGaN films increases the difficulty in the growth of high quality material.

2.1.2. Fundamentals of LED operation

An LED is basically a p-n junction diode that is formed at the interface of a p-type (hole carriers) and n-type (electron carriers) materials. By creating an interface of two heavily doped materials with charge carriers that nullify each other, a depletion region is formed which is nonconductive. By applying voltage to the p and n type regions, the depletion region is manipulated and allows the flow of the carriers after certain voltage called turn-on voltage. When the electrons and holes recombine, they generally fall into lower energy levels radiating a photon. The wavelength of the photon is generally dependent on the bandgap of the materials forming the junction.

The transition of electrons and holes would either result in a radiative or a non-radiative recombination. Radiative recombinations happen mainly due to inter-band transitions, while non-radiative recombinations happen due to defects or auger recombination. In an LED, for maximum light output the probability for radiative recombination should be higher than the probability for non-radiative recombination.

It is found that under continuous injection of carriers an excess carrier density is built up. To nullify this excess electron density, excess holes are created. These excess carriers exponentially decrease with time called the recombination life time. The exponential decrease is combination of radiative and non-radiative recombinations. The recombination life time is defined by the equation.

$$\frac{1}{t} = \frac{1}{t_r} + \frac{1}{t_{nr}} \tag{2.1}$$

where, t_r is the radiative recombination lifetime and t_{nr} is the non-radiative recombination lifetime. The radiative recombination rate (R_r) is the ratio of the excess carriers to the radiative recombination life time. Likewise, the non-radiative recombination (R_{nr}) rate is the excess carriers to the non-radiative recombination life time.

$$R_r = \frac{\Delta n}{t_r}, R_{nr} = \frac{\Delta n}{t_{nr}} \tag{2.2}$$

These recombination rates are responsible for determining the Internal Quantum Efficiency or recombination efficiency which is defined as the ratio of the radiative recombination rate to the total recombination rate.

$$\eta_r = \frac{R_r}{(R_r + R_{nr})} \rightarrow \frac{1}{(1 + t_r/t_{nr})} \tag{2.3}$$

This internal quantum efficiency is entirely dependent on the ratio t_r/t_{nr} and by keeping this ratio small the efficiency could be maximized. Growing materials with low defect densities and eliminating impurities that cause non-radiative deep levels are critical material properties that increase the quantum efficiency.

The internal quantum efficiency does not specifically give the efficiency measure of the LED. The best method to rate the efficiency of the LED is see how much light is generated for the injected current. This measure is called the external quantum efficiency (η_o) defined by the ratio of photons out per injected electron:

$$\eta_o = (photons - out)/(electrons - in) \tag{2.4}$$

which is also expressed as a product of the recombination efficiency (η_r) and optical or light extraction efficiency (η_{ext}).

$$\eta_o = \eta_r \times \eta_{ext} \tag{2.5}$$

Light generated by the LED may be incident on a metallic contact surface and be absorbed by the metal. Here the ability of the light to escape into free space from the air-semiconductor interface is reduced by the fact that light is trapped within the material. This phenomenon is referred to as *total internal reflection*, or *trapped light phenomenon*. The optical extraction efficiency is thus defined by the ratio of the photons emitted into free space to the photons emitted in the active region.

$$\eta_{ext} = \frac{(num. of\ photons\ emitted\ into\ free\ space)}{(num. of\ photons\ emitted\ in\ the\ active\ region)} \tag{2.6}$$

As mentioned above, the light generated inside the LED cannot escape without undergoing total internal reflection (trapped). This phenomenon generally is observed if the angle of incidence of the light ray to the normal is far away from the normal and true vice-versa. So there is a range of angles that allow the light rays to escape at the air-semiconductor interface. An angle called the critical angle defined the Snell's Law defines the maximum limit of the angles at which the light rays would not undergo the total internal reflection as shown in Figure 2.3.

$$\theta_c = \sin^{-1}\frac{n_{air}}{n_{sc}} \approx \frac{n_{air}}{n_{sc}} \tag{2.7}$$

where, n_{air}, n_{sc} are the refractive indices of air and the semiconductor.

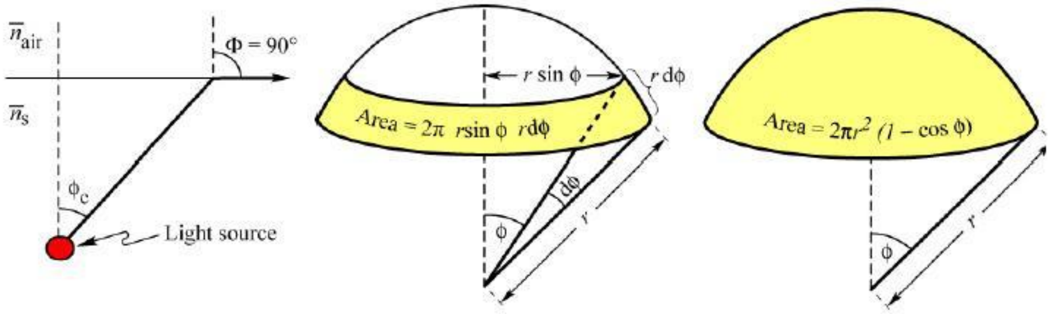

Figure 2.3 Definition of Critical Angle and the Escape Cone

And this condition is valid only when the light ray is traveling from semiconductor material into air. Hence, total internal reflection reduces the optical extraction efficiency significantly, in particular for the LEDs consisting high-refractive index materials. This loss of light due to critical angle limitation is accounted by the critical loss efficiency (η_C).

Adding to this, contribution to the loss associated with the reflection at the semiconductor/air interface is called the Fresnel loss (η_F). Assuming smooth interface, this loss is given in the case of normal incidence by

$$R = \left(\frac{n_{sc} - n_{air}}{n_{sc} + n_{air}}\right)^2 \qquad (2.8)$$

The Fresnel-loss efficiency can thus be defined as $\eta_F = (1-R)$ representing the fraction of photons escaping the semiconductor surface. The surface of the LED might be roughened and/or packaged with an epoxy dome to increase the Fresnel-loss efficiency. And also there should be an Absorption efficiency (η_A) to account to the fact that some part of the light is absorbed by the material.

On the whole, the optical extraction efficiency can also be expressed as:

$$\eta_{ext} = \eta_A \times \eta_F \times \eta_C \qquad (2.9)$$

Taking these losses and the efficiency issues into account, the LED structure of the modern day has evolved by incorporating many optical technologies to improve the efficiency both optically and electrically.

2.1.3. LED Structures

The basic LED structure is formed by the design of the early p-n junction diode. This pn-junction based LEDs forms a homojunction and has performed well so far. In homojunction LEDs, the p and n materials are composed of the same energy gap semiconductor. The minority carriers (holes) tend to diffuse into the majority carrier (electrons) region under forward bias conditions and this diffusion of charge carriers results in recombinations that are not highly beneficial.

A new structure is designed by combining wide bandgap semiconductors with narrow bandgap semiconductor forming a "heterojunction", which is found to be having extremely desirable properties unattainable in homojunction structures [4]. This structure allows the LED structures to achieve higher luminous efficiencies than the conventional homojunction LEDs. The two major benefits of heterojunction LEDs are the increased minority carrier injection efficiency and the ability to use wide-gap material. Due to the new the carriers are now confined to the active region by the barriers and the thickness of the region in which carriers recombine is given by the thickness of the active region rather than the diffusion length [4].

This ideal single-sided injection of electrons into the active layer makes the heterostructure *GaN/InGaN*, and *AlGaInP/InGaP* LEDs highly efficient. The energy gap differences also minimize the effect of the doping level on the injection efficiency, which dominated the homojunction LED efficiency.

Further, a special class of heterojunction LEDs called Quantum Well LEDs (QW) were designed to overcome the issue of carrier overflow in single and double heterostructures. In the QW LEDs, the thickness of the active region is less than the deBroglie wavelength adapted from Quantum Mechanics [4]. In particular, quantum-well structures active regions have an inherently small volume. At a certain current density, the active region is filled with carriers, and the injection of additional carriers will not lead to an increase in the emitted light intensity. A typical LED structure with a multi quantum well active region is as shown in the Figure 2.4.

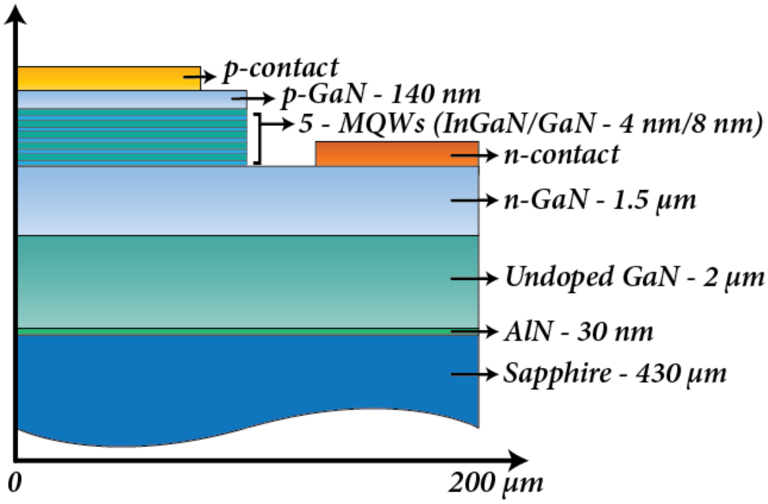

Figure 2.4 A typical MQW LED structure

2.2. LED Extraction Issues

As mentioned in the above sections, an LED structure usually contains layers of n-type and p-type semiconductor layers sandwiching an active region for light generation. These layers are arranged in basic p-n junction configuration forming a diode as shown in the Figure 2.5. The active region contains quantum wells made of InGaN/GaN layers that are designed to have a band gap energy required to produce an appropriate emission wavelength. Under certain bias conditions, the abundant electrons from the n-type layer recombine with the holes from the p-type layer releasing energy in the form of photons or non-radiatively. This process is called electron-hole recombination and contributes to the recombination efficiency (η_r). The rate of recombination of electrons and holes depends on the number of available electron and holes in the conduction and valence bands.

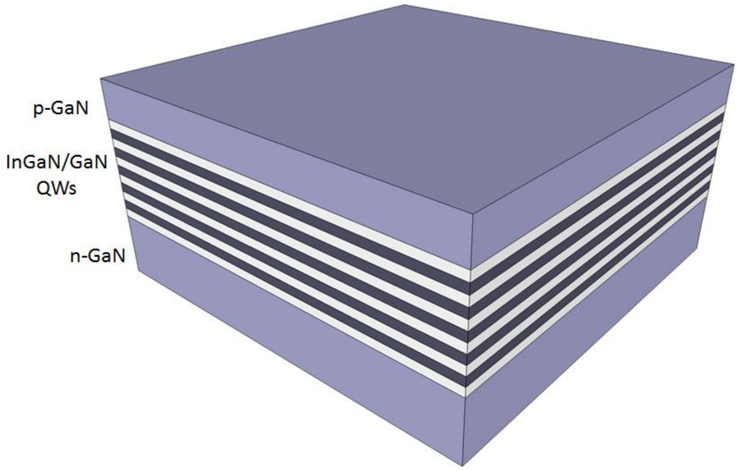

Figure 2.5 LED structure

The recombination events can be divide into radiative and non-radiative events and the result is a photon or a phonon (lattice vibration) respectively. In an LED, radiative recombination is preferred over the non-radiative recombinations [4]. The photons generated within the active region by radiative recombination have spontaneous directions and have to travel through the p- and n-type dielectric layers to emerge into the surrounding medium. In this process, some percent of the photons will either get reabsorbed into the dielectric layers or get trapped within the layers due to total internal reflection. The fraction of the photons extracted from the device to the photons generated contributes to the extraction efficiency (η_{ext}).

Photons that have enough energy to excite another ground state electron get reabsorbed in the process of excitation and the result could either be a photon with a different wavelength or emitted as phonon vibration (heat). This type of reabsorption and recombination reduce the number of photons that are extracted. These type of non-radiative recombinations can be due to various reasons like interstitial defects, impurity atoms, dislocations, foreign atoms etc. On the other hand, the photons that manage not to be reabsorbed will either get trapped or emitted into the surrounding medium.

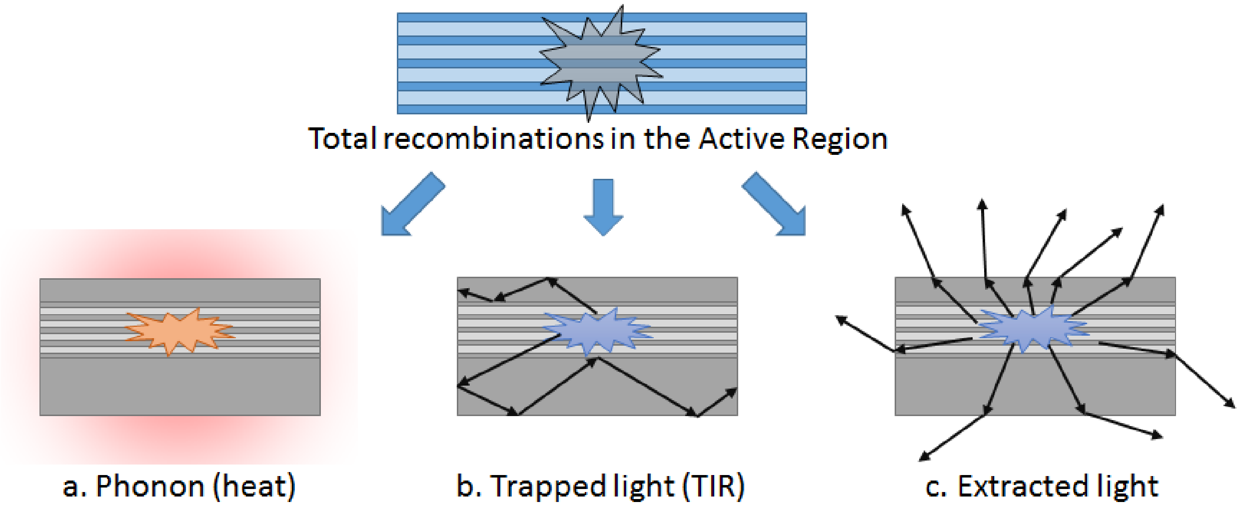

Figure 2.6 Illustration of total recombinations a. Lattice vibrations (phonons), b. Trapped light by total internal reflection and c. Extracted light

According to Snell's law, the light (collection of photons) passing through different isotropic media undergoes characteristic changes like change in the velocity and direction. At the interfaces, light is both reflected and refracted. Under certain conditions, the refracted will get trapped within the dielectric layers. This optical phenomenon is called total internal reflection and the critical conditions for this is obtained using the Snell's law. In summary, the total recombinations within an LED contribute to phonon vibrations, trapped light and extracted light as shown in the Figure 2.6. This dissertation concentrates on the extracting the trapped light and improve the amount of extracted light and in the following sections, how passive optical methods like photonic crystals can be utilized for extraction of light in an LED will be emphasized.

3. Photonic Crystal Theory

Photonic Crystals (PhCs) are periodic arrangement of two or more dielectric materials. They are analogous to the electronic semiconductor crystals. Like the semiconductor crystals have an electronic band gap between conduction and valence band (range of energies where no electron can exist), the PhCs also do have a band gap region called the photonic band gap (PBG) (range of frequencies where no photon can exist). Any material that possesses a photonic band gap is referred to as photonic band gap material.

Light as an electromagnetic wave undergoes characteristic changes when it travels through any material. These changes in the behavior of an electromagnetic wave in any medium could be well understood by the classical electromagnetism concepts. PBG materials when encountered by electromagnetic waves exhibit their unique property of bandgap i.e. either allowing all the frequencies of the wave to pass through (no bandgap - passband) or stopping a certain range of frequencies (band gap - stopband).

3.1. Electromagnetic Theory Applied to Photonic Crystals

We begin with Maxwell equations to study the electromagnetic behavior within a PhC. The four macroscopic Maxwell equations in SI units as known to us are:

$$\nabla \cdot \mathrm{B} = 0 \tag{3.1}$$

$$\nabla . \mathrm{D} = 4\pi\rho \tag{3.2}$$

$$\nabla \times \mathrm{E} + \frac{1}{\mathrm{c}}\frac{\partial \mathrm{B}}{\partial \mathrm{t}} = 0 \tag{3.3}$$

$$\nabla \times \mathrm{H} - \frac{1}{\mathrm{c}}\frac{\partial \mathrm{D}}{\partial \mathrm{t}} = \mathrm{J} \tag{3.4}$$

where E is the electric field, B is the magnetic field, D is the displacement field (also called as electric flux density), H is the magnetic field strength, ρ represents free charges, and J represents free currents. PBG materials are generally dielectric materials for which there are no free charges and currents and hence ρ = J = 0:

$$\nabla . \mathrm{D} = 0 \tag{3.5}$$

$$\nabla \times \mathrm{H} - \frac{1}{\mathrm{c}}\frac{\partial \mathrm{D}}{\partial \mathrm{t}} = 0 \tag{3.6}$$

By definition, the magnetic field (B) can be expressed in terms of relative magnetic permeability and the magnetic field strength (H) as $B = \mu_o\mu(r)H(r,t)$. And the displacement field (D) in terms of dielectric permittivity and electric field (E) as $D = \varepsilon_o\varepsilon(r)E(r,t)$. The relative magnetic permeability μ(r) is close to unity when it's the case of dielectric materials which simplifies the magnetic field to B= μ_oH. The dielectric permittivity (ε) is a closely approximated as the square of the refractive index *n* of the material. Using the above assumptions, Maxwell's Equations then can be re-written as follows:

$$\nabla \cdot \mu_o \mathrm{H} = 0 \rightarrow \nabla \cdot \mathrm{H}(\mathrm{r}, \mathrm{t}) = 0 \quad (3.7)$$

$$\nabla \cdot [\varepsilon_o \varepsilon(r) E(r, t)] = 0 \rightarrow \nabla \cdot [\varepsilon(r) E(r, t)] = 0 \quad (3.8)$$

$$\nabla \times \mathrm{E}(\mathrm{r}, \mathrm{t}) + \mu_o \frac{\partial\, \mathrm{H}(\mathrm{r}, \mathrm{t})}{\partial \mathrm{t}} = 0 \quad (3.9)$$

$$\nabla \times \mathrm{H}(\mathrm{r}, \mathrm{t}) - \varepsilon_o \varepsilon(\mathrm{r}) \frac{\partial \mathrm{E}(\mathrm{r}, \mathrm{t})}{\partial \mathrm{t}} = 0 \quad (3.10)$$

The electric field (E) and magnetic field strength (H) are functions of time and space, but due to the linearity of the Maxwell's equations, they can be separated into time and space dependent functions. Using Fourier analysis, the decomposition of a function into a number of sinusoidal functions of different frequencies can be done and then recombined to obtain the original function [43]. Therefore, E and H can be expanded as follows:

$$\mathrm{H}(\mathrm{r}, \mathrm{t}) = \mathrm{H}(\mathrm{r}) \mathrm{e}^{-\mathrm{i}\omega \mathrm{t}} \quad (3.11)$$

$$\mathrm{E}(\mathrm{r}, \mathrm{t}) = \mathrm{E}(\mathrm{r})\, \mathrm{e}^{-\mathrm{i}\omega \mathrm{t}} \quad (3.12)$$

The equations governing the mode profiles for a given frequency (ω) are derived by inserting the above equations into the simplified Maxwell's equations. The two divergence equations give the condition [43]:

$$\nabla \cdot \mathrm{H}(\mathrm{r}, \mathrm{t}) = \nabla \cdot \mathrm{H}(\mathrm{r}) \mathrm{e}^{-\mathrm{i}\omega \mathrm{t}} = \nabla \cdot \mathrm{H}(\mathrm{r}) = 0 \quad (3.13)$$

$$\nabla \cdot [\varepsilon(\mathrm{r}) \mathrm{E}(\mathrm{r}, \mathrm{t})] = \nabla \cdot \left[\varepsilon(\mathrm{r}) \mathrm{E}(\mathrm{r}) \mathrm{e}^{-\mathrm{i}\omega \mathrm{t}}\right] = \nabla \cdot [\varepsilon(\mathrm{r}) \mathrm{E}(\mathrm{r})] = 0 \quad (3.14)$$

This implies that there are no magnetic fields and displacement fields existing in the medium. And the two curl equations relate E(r) to H(r) as:

$$\nabla \times \mathrm{E}(\mathrm{r}) - \mathrm{i}\omega \mu_o \mathrm{H}(\mathrm{r}) = 0 \quad (3.15)$$

$$\nabla \times \mathrm{H}(\mathrm{r}) + \mathrm{i}\omega \varepsilon_o \varepsilon(\mathrm{r}) \mathrm{E}(\mathrm{r}) = 0 \quad (3.16)$$

By dividing above equation B by ε(r) and then taking the curl, equation A then can be used to eliminate E(r). Using the relation between the speed of light and ε_o and μ_o given by

$$c = \frac{1}{\sqrt{\varepsilon_o\, \mu_o}} \quad (3.17)$$

The result is:

$$\left[\nabla\times\left(\frac{1}{\varepsilon(\mathrm{r})}\nabla\times\mathrm{H}(\mathrm{r})\right)=\left(\frac{\omega}{\mathrm{c}}\right)^{2}\mathrm{H}(\mathrm{r})\right]\text{ or,}\tag{3.18}$$

$$\left[L\mathrm{H}(r)=\left(\frac{\omega}{\mathrm{c}}\right)^{2}\mathrm{H}(\mathrm{r})\right],\text{where } L\mathrm{H}(r)\equiv\nabla\times\left(\frac{1}{\varepsilon(\mathrm{r})}\nabla\times\mathrm{H}(\mathrm{r})\right)\tag{3.19}$$

This equation is called the *master* equation and L represents a differential operator. The master equation can be solved first to find the modes H(r) and the corresponding frequencies then equation 2.25 can be used to recover E(r) as follows:

$$\mathrm{E}(\mathrm{r})=\frac{\mathrm{i}}{\omega\varepsilon_{\mathrm{o}}\varepsilon(\mathrm{r})}\nabla\times\mathrm{H}(\mathrm{r})\tag{3.20}$$

The reason why the problem was formulated in terms of H(r) and not E(r) is mainly due to mathematical convenience.

The master equation (2.27) gives a result which will be of the form of the original function multiplied by a constant. This is an example of an eigenvalue problem in mathematical physics where the constant is known as eigenvalue and the function $\mathrm{H}(\mathrm{r})$ is known as an Eigen function.

The most important implications of the master equation is the scaling property. Suppose we scale the photonic crystal structure by a factor of *s*, so that,

$$\varepsilon'(r)=\varepsilon(r/s)\tag{3.21}$$

Then, by performing a change of variable with $r'=sr$ and, $\nabla'=\nabla/s$, master equation transforms to,

$$\nabla'\times\left[\frac{1}{\varepsilon'(r')}\nabla'\times\mathrm{H}\left(\frac{r'}{s}\right)\right]=\left(\frac{\omega}{cs}\right)^{2}\mathrm{H}\left(\frac{r'}{s}\right)\tag{3.22}$$

We get the same master equation, with eigenvector $(r)=(r'/s)$ and eigenvalue $\omega'=\omega s$.

Here we observe that even after scaling the structure by a factor of *s*, both the frequency and the field profile are scaled by the same factor. This concludes that in the design of a photonic crystal, the wavelengths of certain features can be controlled by adjusting the lattice constants of the photonic crystals.

3.1.1. The Concept of Photonic Bandgap

Like in semiconductor crystals, the range of energies in which no electrons are found is called the energy bandgap (E_g). Photonic crystals by definition have a discrete translational symmetry along one, two or three dimensions. The basic structural design concepts of PhCs take us back into the concepts of solid state physics. Any crystal with translation symmetry in the spatial directions is made of a foundation structure called the lattice. This lattice defines a theoretical construct of an infinite array of points with certain geometrical periodic characteristics. To mathematically define this construct, a set of vectors defined in space called the Basis or Lattice Vectors are used. Using these basis vectors, the entire lattice could be reproduced by extrapolating the basis vectors w.r.t. the previous lattice point as shown in Figure 3.1.

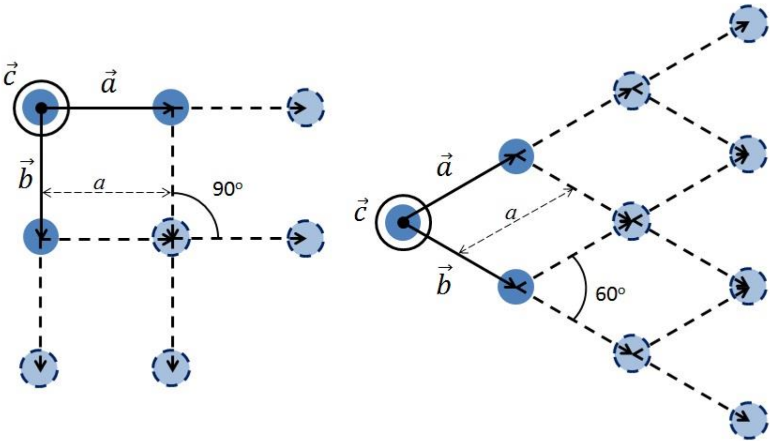

Figure 3.1 Illustration of lattice vectors and lattice generation (Left) Square lattice and (Right) Triangular lattice

In this way, a whole lattice could be generated starting from an initial point and knowing the characteristics of the lattice. All the lattice points in the lattices shown are separated by a fixed step length called lattice constant (a), which is the magnitude of the basis vectors. The basis vectors not only give the information of the lattice constant, but the angle between the vectors gives the information about the geometry of the lattice. The above two lattices are basically observed in a 2D plane only and hence creating a 2D lattice only. If this 2D lattice is also repeated in the third dimension then the lattice is considered a 3D lattice.

A PhC by definition is a periodic arrangement of dielectric highs and lows. This could be realized by replacing the lattice point of the lattice with an object of a certain dielectric material. For example, assuming the default material is air (n_{air}=1) and the lattice point is replaced by a slab of refractive index n. And if the lattice point is repeated in one direction alone creates a simple PhC, a 1D PhC as shown in the Figure 3.2.

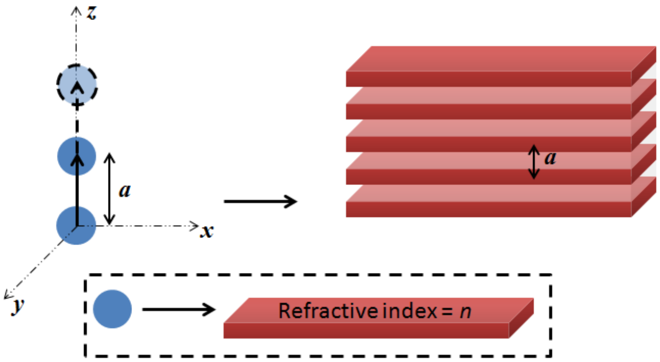

Figure 3.2 1D photonic crystal with varying dielectric constant in the z direction. Red layers can represent high refractive index regions while white/empty layers can represent low refractive index regions

The above 1D PhC has a continuous translational symmetry in x and y directions and in the z direction, we observe a discrete but translational symmetry. In other words, the dielectric constant of the system is only varying along the z direction. The discreteness in the dielectric constant could be expressed in terms of the lattice constant (*a*) as follows: [43]

$$\varepsilon(r) = \varepsilon(r \pm a) \tag{3.23}$$

3.1.2. The Reciprocal Lattice

Consider a periodic function $f(r) = f(r + R)$ for all vectors R that connect one lattice point to the next. Let R be an ensemble of the entire lattice vectors as follows: $R = l\vec{a} + m\vec{b} + n\vec{c}$, where l,m,n are integers and $\vec{a}, \vec{b}, \vec{c}$ are the primitive lattice vectors. Then for a periodic system, there exists a set of vectors called the reciprocal lattice vectors G such that the product $G \cdot R$ is some integer multiple of 2π for every R. These reciprocal lattice vectors G form a lattice of their own with a set of primitive vectors $\overrightarrow{a^*}, \overrightarrow{b^*} and\ \overrightarrow{c^*}$. And since these reciprocal lattice is also periodic, any point in the reciprocal space could be written as $G\ = l\overrightarrow{a^*} + m\overrightarrow{b^*} + n\overrightarrow{c^*}$.

Therefore, the reciprocal space vectors $\overrightarrow{a^*}, \overrightarrow{b^*} and\ \overrightarrow{c^*}$ can be found using the following recipe:

$$\overrightarrow{a^*} = \frac{2\,\pi\,\vec{b}\,\times\,\vec{c}}{\vec{a}\,\cdot(\vec{b}\times\,\vec{c})} \tag{3.24}$$

$$\overrightarrow{b^*} = \frac{2\,\pi\,\vec{c}\,\times\,\vec{a}}{\vec{a}\,\cdot\left(\vec{b}\times\,\vec{c}\right)} \tag{3.25}$$

$$\overrightarrow{c^*} = \frac{2\,\pi\,\vec{a}\,\times\,\vec{b}}{\vec{a}\,\cdot(\vec{b}\times\,\vec{c})} \tag{3.26}$$

From equation 2.32, we observe that for any R, $\varepsilon(r) = \varepsilon(r + \mathrm{R})$ is true and hence periodic in nature. This dependency of the dielectric constant on the z direction forces H to be dependent on z i.e. simply the product of a plane wave with a *z*-periodic function. The plane wave is similar to that in free space but modulated by a periodic function because of the periodic lattice as shown [43]

$$\mathrm{H}(\dots,\dots,\mathrm{z}) \quad \alpha \quad \mathrm{e}^{\mathrm{i}k_z\mathrm{z}}.\,\mathrm{u}_{\mathrm{k_z}}(\mathrm{z},\dots) \tag{3.27}$$

The modes can then be written as follows

$$\mathrm{H}_{\mathrm{k_z}}(\mathrm{r}) = \mathrm{e}^{\mathrm{i}k_z\mathrm{z}}.\,\mathrm{u}_{\mathrm{k_z}}(\mathrm{r}) = \mathrm{e}^{\mathrm{i}k_z\mathrm{z}}.\,\mathrm{u}_{\mathrm{k_z}}(\mathrm{r}+\mathrm{R}) \tag{3.28}$$

The above result is commonly referred to as Bloch's theorem which states that any Bloch state with a wave vector k_z and that of a wave vector k_z+mb are identical. Also it states that the $\mathrm{k_z}$'s are identical in a periodic manner with a period of $2\pi/a$. This allows us to consider only $\mathrm{k_z}$'s that exist in the range $-\pi/a < k_z \leq \pi/a$ which is the region of non-redundant values of $\mathrm{k_z}$. This region is commonly known as the Brillouin zone.

3.1.3. The Brillouin Zone

It is found that based on the periodic nature of the real space and the reciprocal space, the solution for the entire lattice structure could be just characterized by the behavior in a small region called the Brillouin zone. For example, a mode with wave vector k and a mode with a wave vector k+G are considered the same mode, if G is a reciprocal lattice vector. This means that there is a redundancy in the label k [4]. To eliminate this redundancy, a finite zone in reciprocal space must be found in which adding increments of G will not lead to the same mode. The zone that is closest to k = 0 is called the (first) Brillouin zone. Brillouin zone is best realized using similar concepts of the Wigner-Seitz cell in Bravais lattices.

For a square lattice with a lattice constant a, the lattice vectors are $\vec{a} = a\hat{x}, \vec{b} = a\hat{y}$ and $c = \hat{z}$. The reciprocal lattice vectors are found using the above mentioned governing equations 2.33, 2.34 and 2.35. The results are

$$\overrightarrow{a^*} = \frac{2\,\pi}{a}\hat{x} \tag{3.29}$$

$$\overrightarrow{b^*} = \frac{2\,\pi}{a}\hat{y} \tag{3.30}$$

The reciprocal lattice is also a square lattice, but with spacing $2\pi/a$ instead of a and hence the name *reciprocal lattice* suits this fact very well. And also we observe that the reciprocal lattice vectors for a triangular lattice also forms a triangular lattice but rotated by 90° as shown in the Figure 3.3.

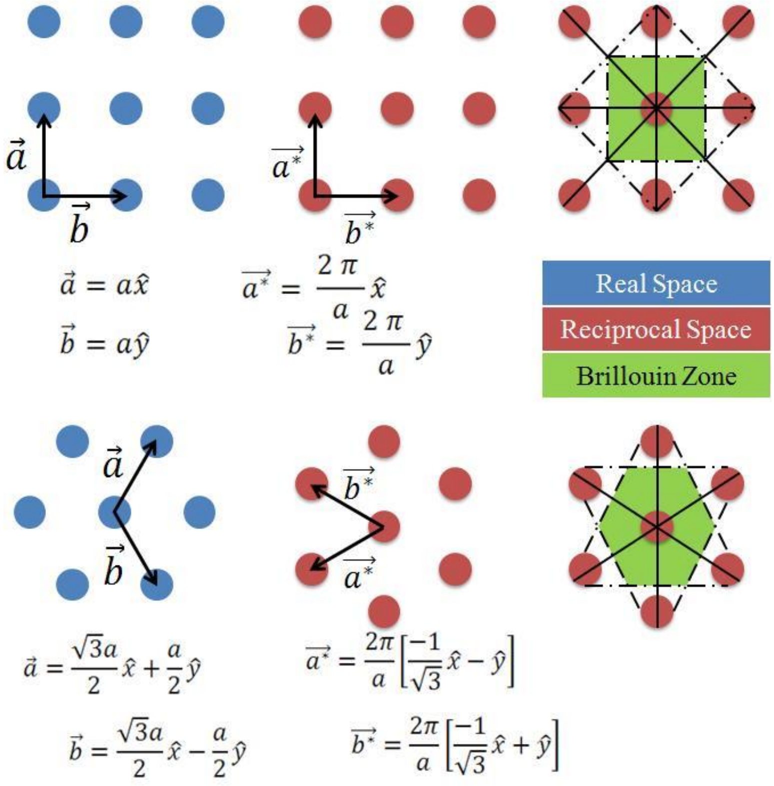

Figure 3.3 Brillouin Zone Calculation for a Square Lattice (Top) and Triangular Lattice (Bottom)

Wigner-Seitz cell of the bravias lattice as mentioned before in the reciprocal space is the Brillouin zone. Geometrically, this can be accomplished by drawing perpendicular bisectors of the lines connecting every lattice point. Each bisector divides the line joining lattice points into two half-planes and the intersection of all the half-planes that contain origin is the Brillouin zone. The square and triangular lattice Brillouin zones are shown in Figure 3.3 as the green shaded region. Due to the high symmetry of the lattice points both in the real and the reciprocal space, we need not consider every point of k inside the Brillouin zone. So the smallest region within the Brillouin zone that could be repeated to form the whole reciprocal lattice is called the Irreducible Brillouin Zone. A photonic crystal with the symmetry of a simple square lattice and a square Brillouin zone center at k = 0, the irreducible zone is a triangular wedge with 1/8 the area of the full Brillouin zone; the rest of the Brillouin zone consists of redundant copies of the irreducible zone.

Continuing ahead with the origin of the photonic bandgap, the modes of a three-dimensional periodic system are Bloch states that can be labeled by a Bloch wave vector $\mathrm{k} = k_1\overrightarrow{a^*} + k_2\overrightarrow{b^*} + k_3\overrightarrow{c^*}$ where k lies within the Brillouin zone. Each value of the wave vector k inside the Brillouin zone identifies an eigenstate of *L (differential operator of the master equation)* with frequency ω(k) and an eigenvector $\mathrm{H_k}$ of the form:

$$\mathrm{H_k(r)} = e^{i\mathrm{k.r}} u_k(\mathrm{r}) \tag{3.31}$$

Where u_k(r) is a periodic function on the lattice $\mathrm{u_k(r)} = u_k(\mathrm{r} + \mathrm{R})$ for all lattice vectors R. This equation demonstrates how the electromagnetic modes of a PhC with discrete periodicity can be written as Bloch states. All of the information about these modes is given by the wave vector k and the periodic function $\mathrm{u_k}$(r). To solve for $\mathrm{u_k}$(r), the Bloch state can be inserted into the master equation to get the following:

$$\hat{L}_k\, \mathrm{u_k(r)} = \left(\frac{\omega(\mathrm{k})}{c}\right)^2 \mathrm{u_k(r)} \tag{3.32}$$

where $\hat{L}_k$ is the new Hermitian operator defined as

$$\hat{L}_k = (i\mathrm{k} + \nabla) \times \frac{1}{\varepsilon(\mathrm{r})}\, (i\mathrm{k} + \nabla) \times \tag{3.33}$$

The function *u* and the mode profiles are determined by the eigenvalue problem which is restricted to a single unit cell of the PhC lattice to create a discrete spectrum of eigenvalues. There are infinite number of eigenvalues (modes) found from the above equation for each value of k. These modes are considered to have distinct frequencies for each k position labeled by a band index n. Therefore, these modes of a PhC are simply a set of continuous functions ω_n(k) indexed in the order of increasing frequency by the band number. This information gathered from the eigenvalue problem, is called band structure of the PhC, which gives more insight of the optical properties of the crystal. This band structures or simply referred to as band diagram of the PhC is very similar to the band structure of a semiconductor crystal. As we know in semiconductors, there exists a conduction band and a valence band and the energy separation between these two bands is the energy bandgap of that crystal.

The origin of the photonic bandgap can be explained by the Variational theorem. The theorem states that electrical field energy of any mode tends to be concentrated in high dielectric regions while remaining orthogonal to the modes below it in frequency [43].

In a PhC band diagram, the lowest band is known as *dielectric* band whereas the rest of the bands are known as *air* bands. These dielectric and air bands are analogous to the conduction and valence bands in the semiconductors. In the air bands, energy is concentrated in lowest dielectric regions to maintain orthogonality as mentioned in the Variational theorem principle and thus creating a gap between the bands. There exists no real eigen value solution for the master equation for any k in this bandgap region, similar to that of the concept of energy bandgap in the semiconductor crystal.

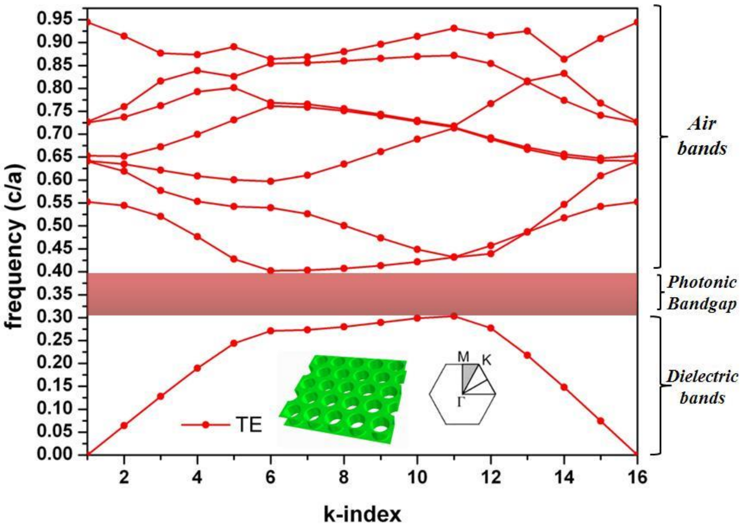

Figure 3.4 Photonic Band diagram of a 2D PhC of air holes in *GaN* substrate.

The figure 2.10 shows a typical band diagram of a 2D PhC made of ***air holes*** in ***GaN*** substrate. It is very clear from the figure, that the lower frequency dielectric bands have their electric field energy mostly concentrated in higher dielectric regions, while higher frequency air bands have the electric field energy of their modes concentrated in lower dielectric regions.

3.2. PhC Application in LEDs

As mentioned earlier, photonic crystals (PhCs) are periodic dielectric structures with high and low dielectric media. They possess a photonic band gap that is analogous to the electrical band gap possessed by semiconductor materials. The range of wavelengths that are allowed to propagate through these structures are known as “modes,” and collectively known as “pass-bands”. Bands that are prohibited from passing comprise the “stop band,” or the photonic band gap, of the PhC. As shown in the Figure 3.5, the PhCs can be utilized to control the behavior of light in one, two or three spatial dimensions.

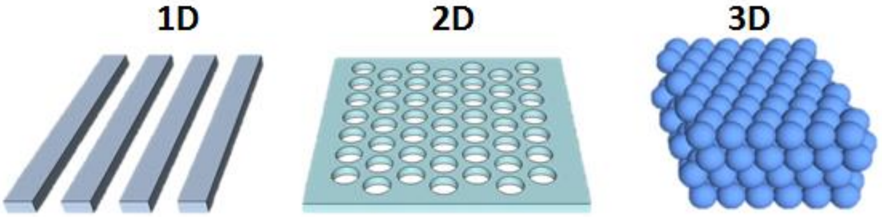

Figure 3.5 One, two and three dimensional photonic crystals

Technical advancements in the micro- and nano-fabrication techniques have enabled the integration of these nano-photonic structures into a wide range of devices and applications. With a wide selection of dielectric materials and the ease of designing the PhCs in multiple dimensions, novel applications are being extensively investigated. These applications include: PhC waveguides [44], beam splitters, nano-cavity resonators, LEDs [19] [45], biosensors [46], chemical sensors [47], and many others. With the addition of such PhC structures designed to diffract or block the emission wavelength, the light extraction from an LED can be increased.

3.2.1. Band Gap Based

The band gap of the PhC is a similar concept as the band gap of any semiconductor. The band gap in PhC comprises the range of wavelengths that are not allowed through the plane of propagation. A properly designed PhC can be used to block a specific range of wavelengths and hence can be used in applications to either block or enhance the desired wavelength. Several research groups have invested in this area of the PhCs and developed various applications like waveguides [48], lasers [49], LEDs [50], [51], biosensors [52], [53]and various others.

In the current context of LEDs, band gap based PhCs can be used for improving the light extraction. To do this, PhC structures should be properly designed to block the propagation of the light across the structure as shown in the Figure 2.4. An LED equipped with a PhC in the light-emitting region designed to block the emission wavelength of the device can be a potential solution to the light extraction problem.

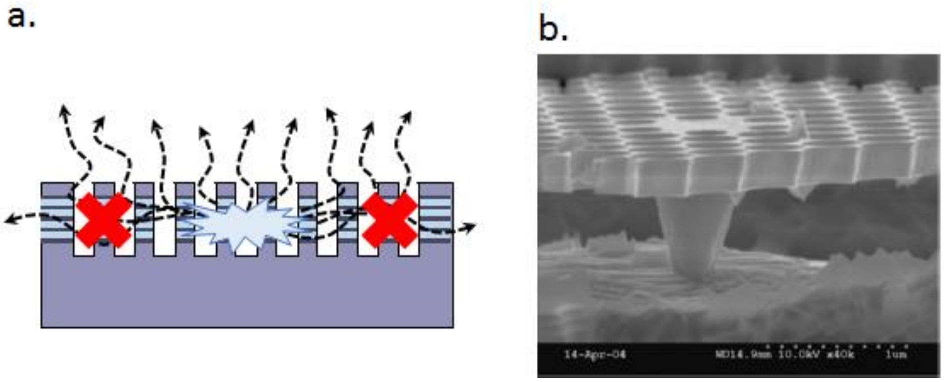

Figure 3.6 a. Illustration of an LED with a PhC in the light-emitting region b. SEM image of a PhC through the active region [54].

Using this method, several groups have tried and succeeded in improving the light extraction using the photonic band gap property of the PhCs [50], [55], [56]. However, all these methods require the PhCs are etched all the way through the active region of the device. This requirement of the PhC to be etched into the active region arises the issue of increasing leakage currents [30] and other electrical issues. Another issue is that most of these works used photoluminescence for characterizing the improvement in light extraction. This way there is no information on the effects on electrical characteristics, thermal characteristics and internal quantum efficiency due to the PhC structures fabricated [57].

3.2.2. Diffraction Based

Due to the aggressive approach for fabrication of PhC structures possessing a band gap, an alternate method is to use PhC patterns to diffract the trapped portion of the light. Diffraction refers to the phenomena of light bending around objects in the direction of propagation. With the use of the random features as diffraction elements, the light emission can be improved as the trapped modes are diffracted out of the plane [57]. The most common type of diffraction pattern to improve the light extraction in the devices is by using some fashion of surface roughening or use a generic periodic pattern to help diffract portion of trapped light as shown in the Figure 2.5. However, the surface roughening techniques yield an improvement in the extraction is very low. On the other hand, with the help of diffraction based PhCs, the improvement of the light extraction is comparatively higher than that of the former method. Additionally, use of PhCs to diffract any amount of trapped light can be possible solution without affecting the electrical characteristics drastically.

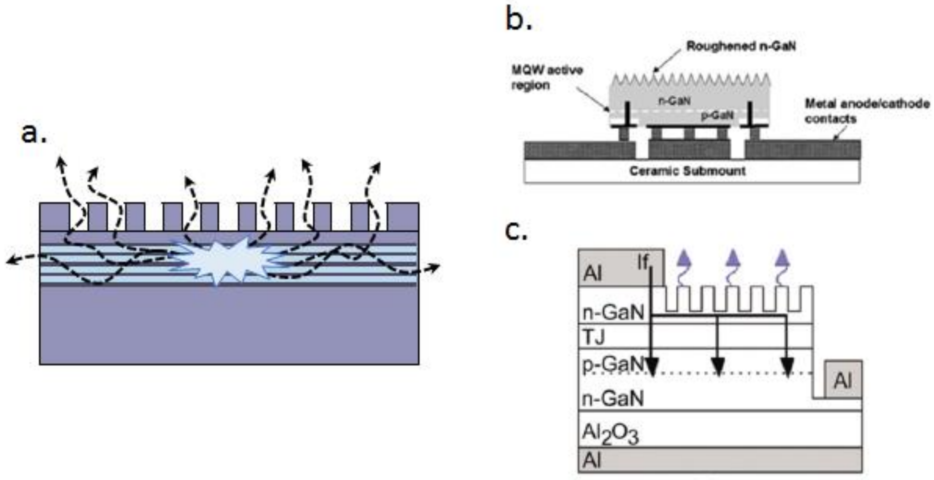

Figure 3.7 a. Illustration of diffraction based PhC, b. Surface roughening on an LED [58] c.PhC structure on an LED [59]

4. Photonic Crystal Modeling

Design of a photonic crystal (PhC) structure in a material of interest can be performed using a variety of software tools available (MPB, OptiFDTD etc.). Most of these software tools utilize plane wave expansion method to compute the definite Eigen states of the periodic structure [60]. This method is effective in most cases where the PhC structure is to be used in a band gap based configuration. However, PhC structures are not limited to the band gap configuration but are also being utilized for their diffractive properties. These diffractive properties of the PhC structures can be thoroughly understood by the light interaction that is off axis to the plane of the PhC as shown in the Figure 4.1.

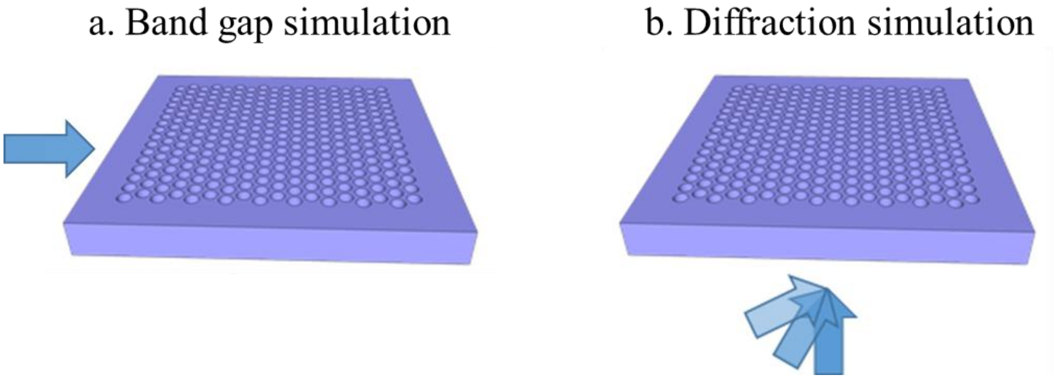

Figure 4.1 Light interaction with a PhC (a.) Band gap simulation and (b.) Diffraction simulation

This chapter lays the theoretical modeling of various photonic crystal structures which are then used to determine the optimal PhC structure that can be used for improving the light extraction within an LED. The study here contains both frequency and time domain simulation of photonic crystal lattice structures viz. square and triangular lattices.

4.1. Frequency Domain

As mentioned in the second chapter, the band gap of the photonic crystal is derived from an appropriate combination of the substrate material (ε_s), size of the feature (r), lattice constant (a), feature height (h) and the type of lattice configuration a.k.a. the critical parameters of the PhC as shown in the Figure 4.2. In order to solve the Eigen value problem of the master equation, powerful software engines are utilized and are used to extract the band gap information of the PhC.

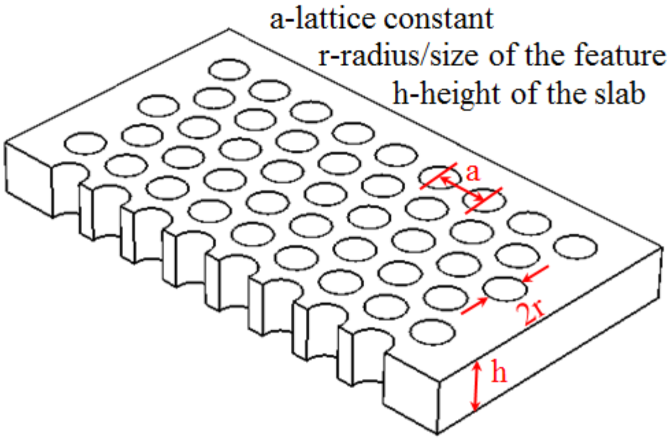

Figure 4.2 Critical parameters of a PhC structure

For this study, PhC lattices of holes and pillars are simulated using MIT Photonic Bands (MPB), a freely available software that solves the complex Eigen value problem described earlier. MPB is a frequency domain software program that directly computes the eigenstates and eigenvalues of Maxwell's equations. Here, MPB is used to solve the master equation for allowed frequencies and corresponding fields. Due to the periodicity of the photonic crystal lattice, MPB invokes Bloch's theorem (plane wave expansion method) and solves for the master equation listed in the second chapter or Equation 4.1

$$\left[\nabla \times \left(\frac{1}{\varepsilon(\mathrm{r})} \nabla \times \mathrm{H(r)}\right) = \left(\frac{\omega}{\mathrm{c}}\right)^2 \mathrm{H(r)}\right], \tag{4.1}$$

$$\text{where } \mathrm{H(r)} = \mathrm{e}^{\mathrm{ikz}}.\mathrm{u_k(r)}$$

To solve for the eigenstates for the master Eigen value problem, the magnetic field component is expanded in a plane wave basis as shown. Since the computation is being performed in a periodic space, the above mention plane wave is expanded using the Fourier approximation.

$$u_k(r) = \sum_G h_G e^{iG\cdot r} \tag{4.2}$$

Where G is the reciprocal lattice vectors and h_G is the amplitude. Now the basis is discretized into a finite number of points. By substituting Equation 4.2 into equation 4.1 and taking the Fourier Transform of both sides results in an equation that is similar to a matrix equation of the form $A\vec{x} = \omega^2\vec{x}$. MPB solves this equation using an iterative Eigen solver approach to diagonalize the matrix to find the eigenvalues (frequencies) and eigenvectors (magnetic fields). An initial guess value of the eigenvector has to be used to solve for the eigenvalues using iterative methods.

MPB, to perform the simulations, takes the set of critical parameters normalized with respect to the lattice constant *(a)*. All the solutions to the master equation are normalized and the output frequency has the units of *(c/a)* or frequency = 1 *(c/a)*, where c is the speed of light, $3\text{x}10^8$ m/s. Since frequency = (c/λ), this implies (c/a) = (c/λ). Therefore, MPB's units for frequency are approximated to the normalized wavelength (a/λ). This allows the solutions to Maxwell's equations at one wavelength (a/λ_o) to be scaled to determine the solutions at a different wavelength (a/λ_1). This scalable property is very useful in the field of photonics, where larger scale crystals can be studied to understand the behavior of the photonic crystal that can be difficult to fabricate.

Another property of the photonic crystals is that due to the periodic nature of the real space and the reciprocal space, the solution for the entire lattice structure can be understood by the behavior in the Brillouin zone. Hence computing the interactions of the electromagnetic waves for each point within the smallest volume, called irreducible Brillouin zone yields discrete solutions. Utilizing these solutions from the Maxwell's equations, the critical parameters (a - lattice constant, r - radius, h - height) for a PhC to block a certain range of wavelengths can be determined.

Moving ahead, the results obtained from MPB simulations for triangular and square lattice of holes and pillars in materials like Gallium Nitride (GaN) and Indium Tin Oxide (ITO). The band gap information is extracted for these materials is analyzed and the optimal structures for light extraction in an LED will be extracted.

4.1.1. Gallium Nitride PhC Simulations

As mentioned earlier, gallium nitride (GaN) is one of the binary group III-V nitride which is most commonly used in blue LEDs. The refractive index for GaN is taken from our materials group as ***n=2.4738*** and has been used throughout the simulations. As shown in the Figure 4.3, GaN constitutes most of the LED structure and the light extracted from the LED is trapped in the GaN layers due to the total internal reflection.

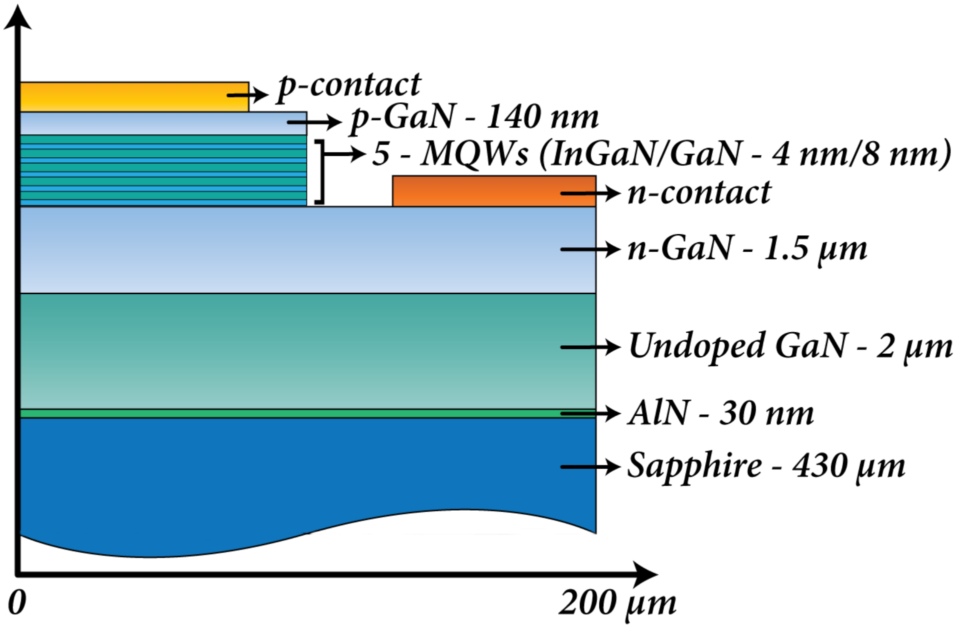

Figure 4.3 LED structure showing the various materials involved

To understand the behavior of light in a GaN slab, MPB simulations are performed on a plain GaN slab. The simulation result is shown in the Figure 4.4 and it is very clear that there exists not bandgap for the GaN slab which implies that all the modes are guided within the slab. This is a fundamental proof that the light from the active region of the LED tends to be guided in the GaN layers and not escape out of the layers.

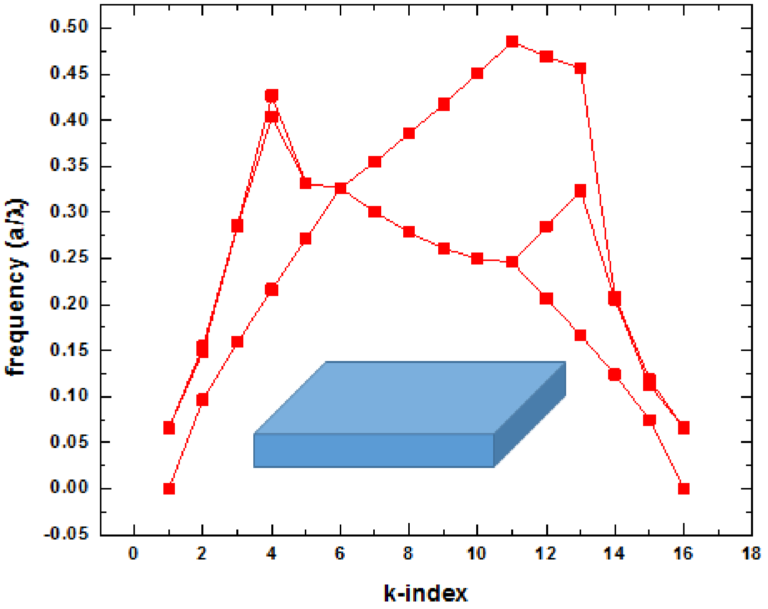

Figure 4.4 Band gap diagram for a GaN slab

To find the optimal PhC structure with a band gap, a series of simulations need to be performed. First, the radius (r) of the unit cell shown above is varied from ***0.2a*** to ***0.4a*** in steps of ***0.01a*** and the simulation for the band diagrams were done. For these set of simulations, the height of the slab is set to infinity to reduce the complexity as shown in the Figure 4.5. This step is done to reduce the number of iterations and yield a quicker result.. The band diagrams for the above mentioned structures are analyzed for bandgaps and are calculated using the formula stated in the Equation 4.3.

$$\begin{aligned} &Band\ gap\ (\%) \\ &= \frac{Lowest\ frequency\ of\ higher\ order\ band - highest\ frequency\ of\ lower\ order\ band}{Mid\ gap\ frequency} \end{aligned} \qquad (4.3)$$

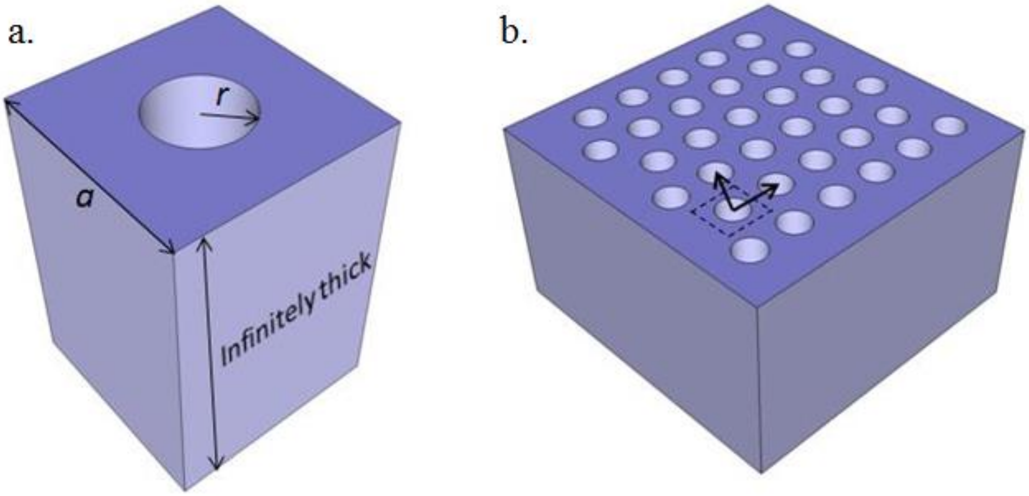

Figure 4.5 Infinitely thick (a.) unit cell, and (b.) triangular lattice of holes

As a result, the band gap diagrams for all radii are extracted and analyzed to find the optimal radius of the hole that has the maximum band gap. The respective band gap information is plotted with respect to the radius of the hole and is shown in the Figure 4.6 and is referred to as the band gap map. The band gap map shows that there is steady increase in the band gap as the radius increases. The plot shown in Figure 4.6 also shows the radii of the features that are feasible to fabricate using standard microfabrication techniques. Figure 4.7 and Figure 4.8 show the TE and TM band diagrams for the triangular lattice of air hole with radius r=0.33a and height h=infinity. It is observed that for the given lattice structure, a triangular lattice of holes, the TE bandgap is prominent and TM bandgap is very low and insignificant. A TE band gap of 25.21% is found to be the prominent band gap for this particular configuration and is highlighted in the respective figure.

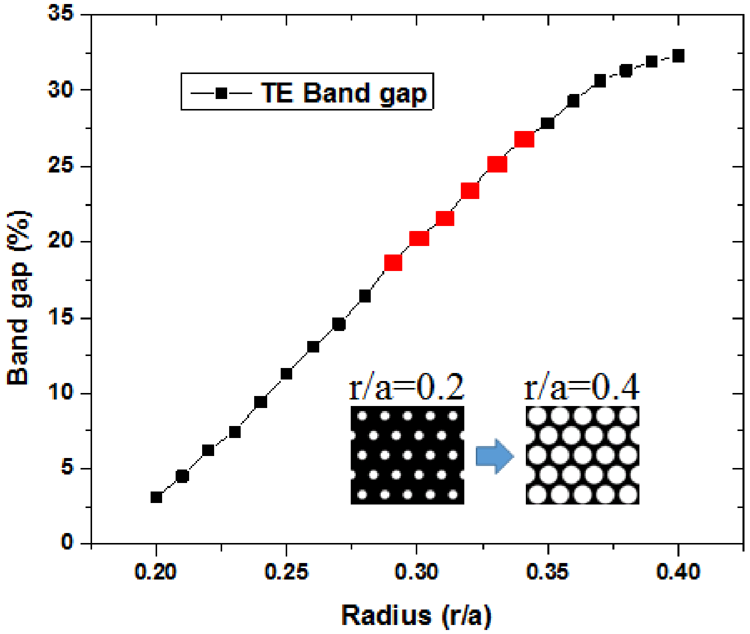

Figure 4.6 Band gap map of the triangular lattice of holes in gallium nitride (Red dots are feasible to fabricate)

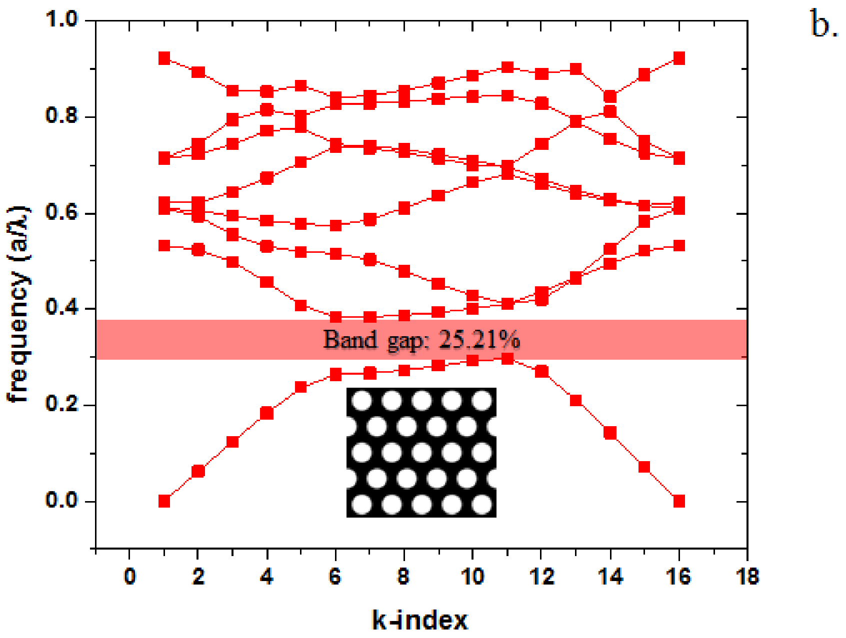

Figure 4.7 TE band diagram of GaN holes for r=0.33a

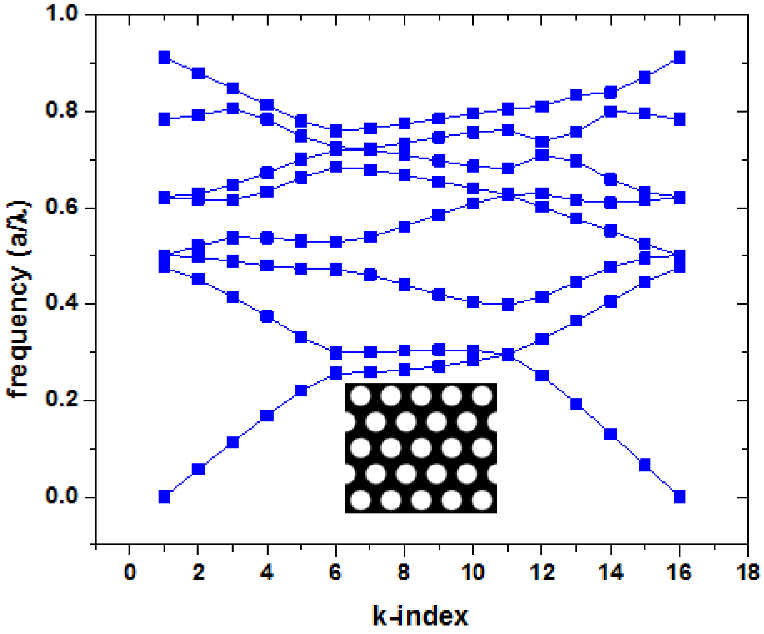

Figure 4.8 TM band diagram of GaN holes for r=0.33a

A radius (r=0.33a) with a wide bandgap is identified from the bandgap map and the thickness of the slab is reduced to a finite thickness For the next series of simulations, the thickness (h/a) of the slab is then varied from 0.65 to 1.2 in steps of 0.05 and the TE (zeven) and TM (zodd) band diagrams for the finite thick PhC slabs are analyzed. A similar process is used to find the band gaps in these set of diagrams, except the band gap edges are the intersection of the band and the light cone. The light cone is the set of Eigen solutions of the Maxwell's equations found at the edge of the brillouin zone of the given lattice. These solutions mark the boundary of the modes that are either guided or radiative. Figure 4.9 shows the guided and radiative modes of a finite thickness PhC slab shaded under orange and green areas. The band gap trend of triangular lattice of holes showing how the band gap varies as the height of the slab increases is shown in the Figure 4.10.

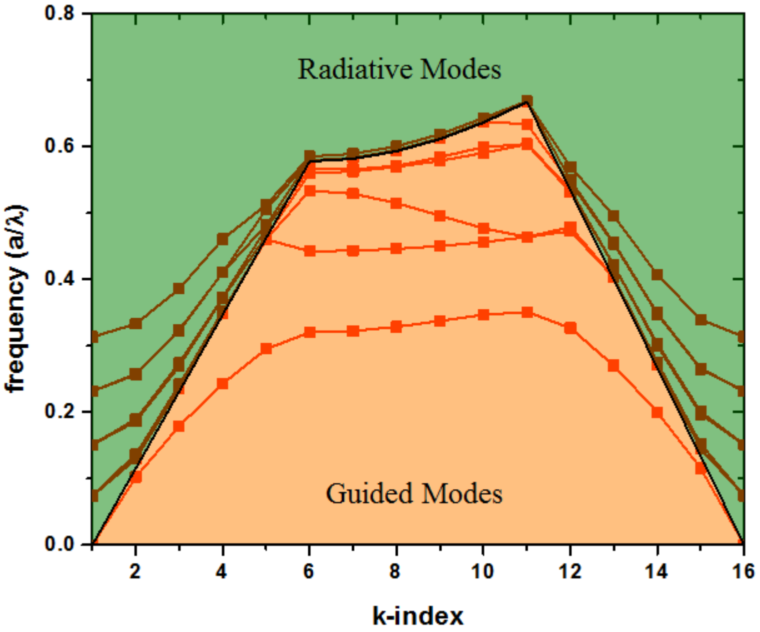

Figure 4.9 Band diagram highlighting the guided (orange) and radiative modes (green)

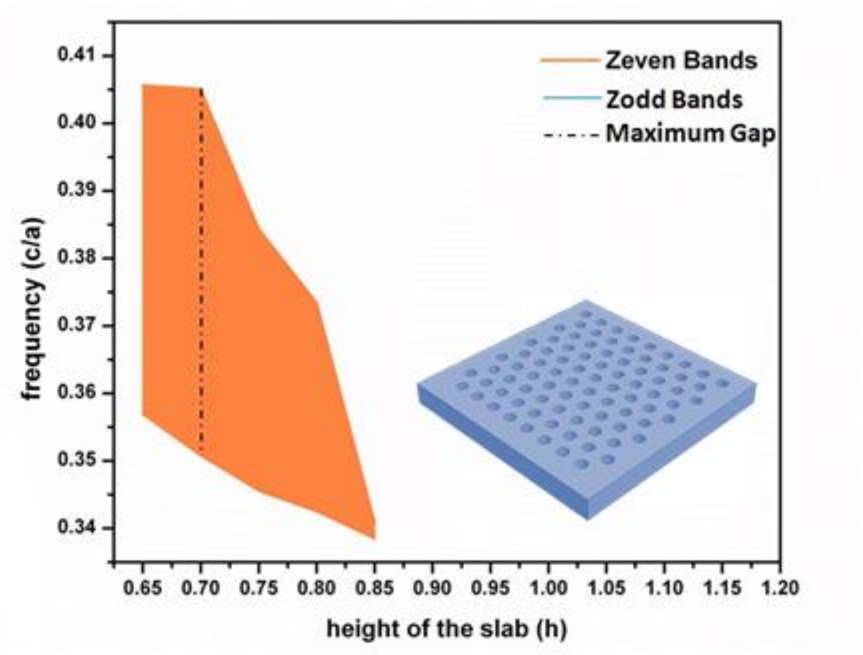

Figure 4.10 Band gap trend for GaN holes w.r.t. height of the slab and radius r=0.33a

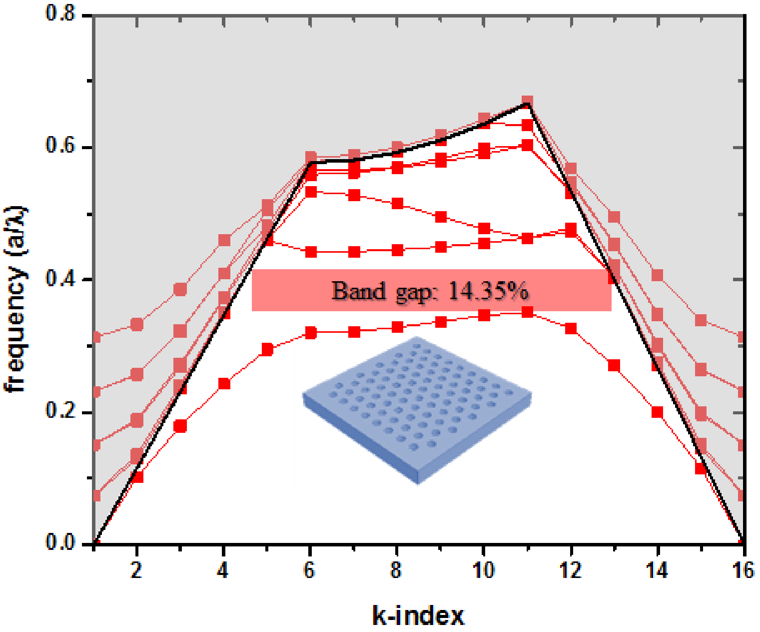

Figure 4.11 ZEven band diagram of GaN holes for r=0.33a and h=0.7a

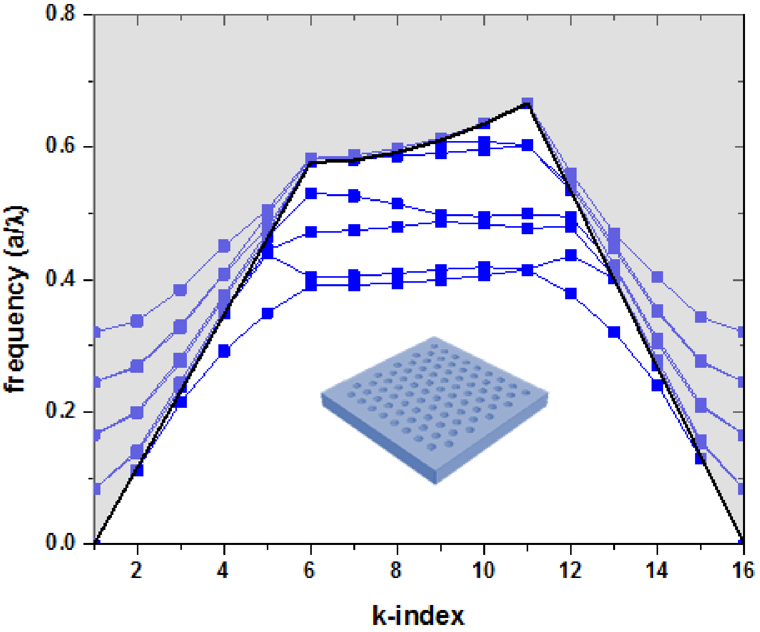

Figure 4.12 ZOdd band diagram of GaN holes for r=0.33a and h=0.7a

A maximum bandgap of 14.35% has been observed in this structure with air hole radius of 0.33a and height of 0.7a. The band diagrams (zeven and zodd) for a finite thick slab of air holes of radius (0.33a) and height (0.7a) is shown in the Figure 4.11 & 4.12. From the band diagram, the mid-gap frequency of (0.3780 c/a) is extracted and the physical dimensions for 2D PhC structures are calculated and presented in Table 4.1.

Table 4.1 Physical parameters of triangular lattice of air holes in GaN

Mid Gap frequency	f	*0.3780*
Wavelength of operation	λ	*465 nm*
Lattice constant	$a=f\lambda$	*175.77 nm*
Radius	$r=0.33a$	*58.00 nm*
Thickness	$h=0.7a$	*123.03 nm*

4.1.2. Indium Tin Oxide PhC Simulations

Indium Tin Oxide (ITO), is commonly used as a transparent conductive layer in an LED structure due to its unique optical and electrical characteristics. Studies have shown PhCs in ITO improve directional emission and light extraction in LEDs [61]. ITO PhCs are simulated using MPB in a similar fashion as described in the GaN PhC section. The refractive index of ITO is extracted from experimentation done using ion beam assisted deposition in a Temescal evaporator and characterizing the thin films using white light ellipsometry and the index is ***n=2.02207***.

The band diagram map shown in the Figure 4.13 shows the steady increase in the TE band gap as the radius of the feature increases. The plot also highlights the radii that are feasible to be fabricate using microfabrication techniques. The TE band diagram for the infinite PhC of triangular lattice of air holes (r=0.33a) is shown in the Figure 4.14 with a bandgap of 35.55% and TM band diagram is shown in the Figure 4.15.

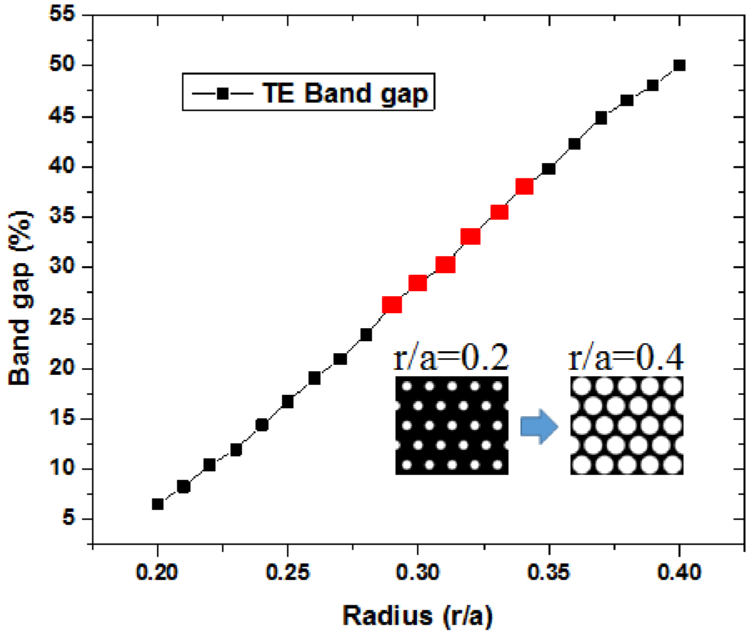

Figure 4.13 Band gap map of the triangular lattice of holes in indium tin oxide (Red dots are feasible to fabricate)

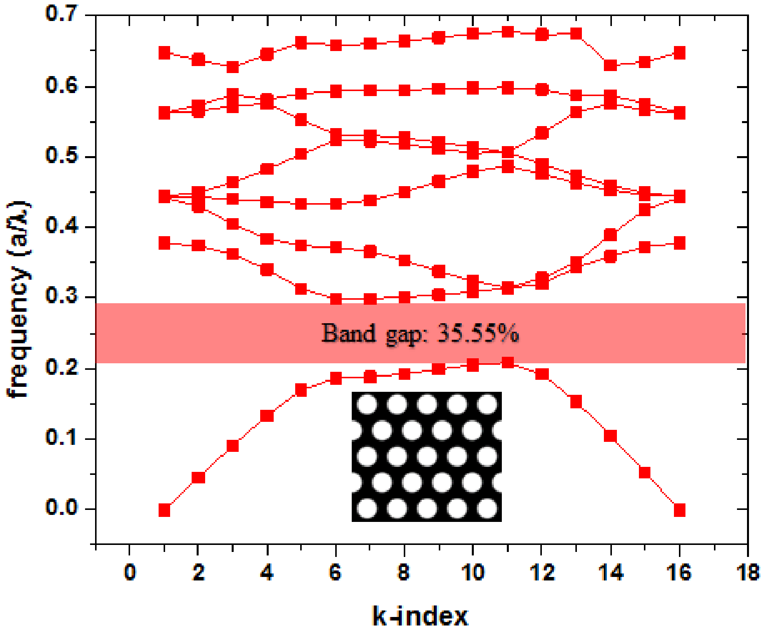

Figure 4.14 TE band diagram of ITO air holes for r=0.33a

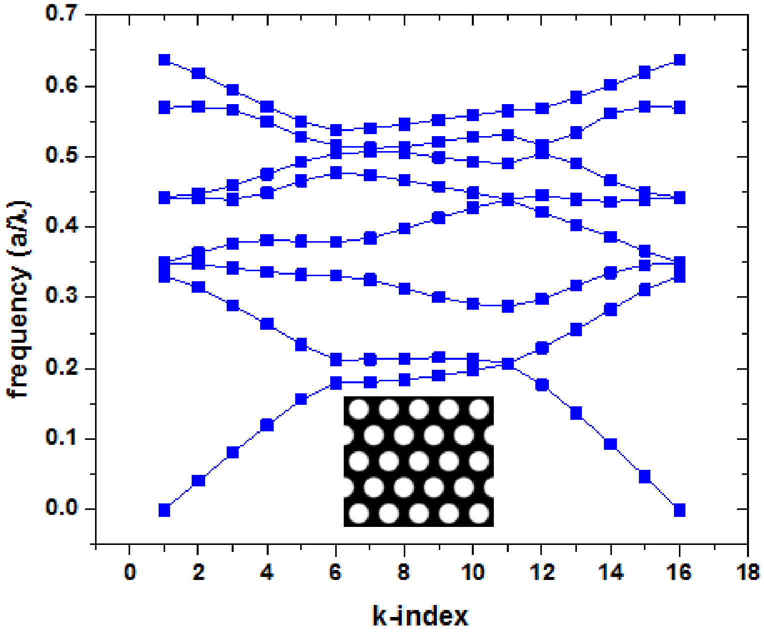

Figure 4.15 TM band diagram of ITO air holes for r=0.33a

From the results obtained, the radius r=0.33a is fixed and height of the slab is varied from 0.65a to 1.2a in steps of 0.05a. The zeven and zodd band diagrams for the finite thick PhC slabs are extracted and analyzed. A similar process is used to find the band gaps in these set of diagrams, except there were no band gaps found as the height of the slab was confined. This is due to the lower refractive index of the material compared to that of GaN. However, there exists a directional band gap between the k-points 6 and 11. This states the PhC lattice is effective, when the light is passing through the lattice in a particular direction only. But as the triangular lattice is a highly symmetric lattice with both translational and rotational symmetries, even the directional band gap can be considered as a full band gap. Figure 4.18 shows the band gap trend of the directional band gap of the triangular lattice of holes with fixed radius and the height varied from 0.65a to 1.2a. The band diagram (zeven and zodd) for a finite thick slab of air holes of radius (0.33a) and height (1.2a) is shown in the Figure 4.19 & 4.20.

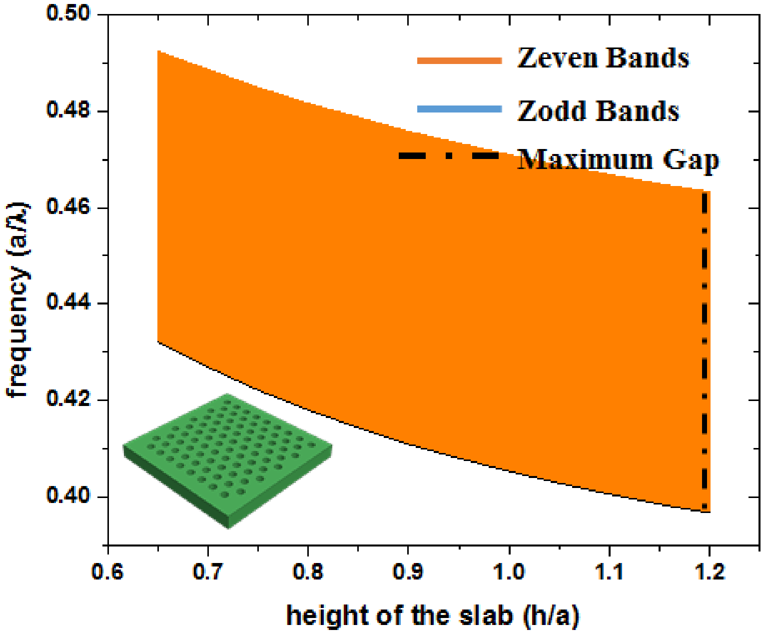

Figure 4.16 Directional band gap map of triangular lattice of holes in ITO for r=0.33a

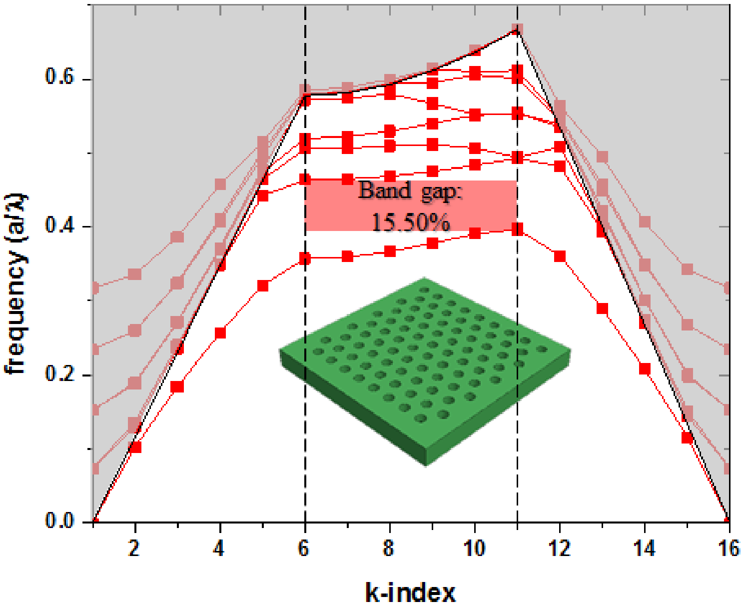

Figure 4.17 Zeven band diagram of ITO holes for r=0.33a and h=1.2a showing the directional band gap

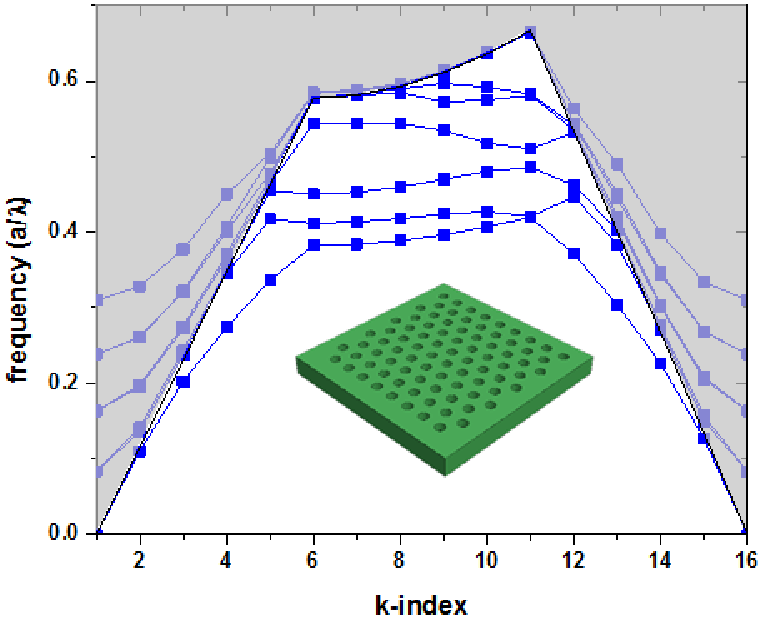

Figure 4.18 ZOdd band diagram of ITO holes for r=0.33a and h=1.2a

A maximum directional band gap of 15.50% has been observed in this structure with air hole radius of 0.33a and height of 1.2a. From the band diagram, the mid-gap frequency of (0.42995 c/a) is extracted and the physical dimensions for 2D PhC structures are calculated and presented in Table 4.2.

Table 4.2 Physical parameters of triangular lattice of air holes in ITO

Mid Gap frequency	*f*	*0.4299*
Wavelength of operation	*λ*	*465 nm*
Lattice constant	*a=fλ*	*199.92 nm*
Radius	*r=0.33a*	*65.9 nm*
Thickness	*h=1.2a*	*239.9 nm*

4.1.3. More Simulations

Of the two materials discussed earlier, ITO PhCs are the most commonly used type for LEDs and light extraction improvement. Considering how LEDs are grown layer by layer in a metal organic chemical vapor deposition chamber, it is fundamentally tedious and difficult to pre-pattern the GaN layers. Hence, the only probable way to fabricate PhC structures in a GaN layer will be post growth and through micro-fabrication techniques. These post fabrication techniques will most likely induce structural damages previously reported by several groups [30], [31]. As ITO is a thin-film that is deposited over the LED structure, it is relatively safer to fabricate PhC structures in this material than in GaN without any performance degradation. Therefore, moving forward all simulations will be concentrated on ITO material and how a PhC lattice in this material affects the light extraction from the LED. In this sub-section, other variations of the ITO PhC lattices will be explored like air holes in square lattice configuration and also a special case of PhCs called hybrid PhCs.

As described earlier, MPB simulations were performed first by varying the radius of the hole r=0.2 to 0.4 in steps of 0.01 to find the optimal radius that is both easy to fabricate and has a relatively wide band gap. Figure 4.19 shows the band gap map of square holes configuration as the radius of the feature is varied. This plot shows that there are two band gaps with this configuration and are only existent when the radius of the feature is greater than 0.32a. The band gap diagrams extracted for TE and TM polarized light are shown in the Figure 4.20 and Figure 4.21. As it was discussed earlier, the radii that are feasible to fabricate are in between 0.31a and 0.35a. So, for the next series of simulations, the radius r=0.35a is fixed and the height of the PhC is confined and varied from 0.65a to 1.2a.

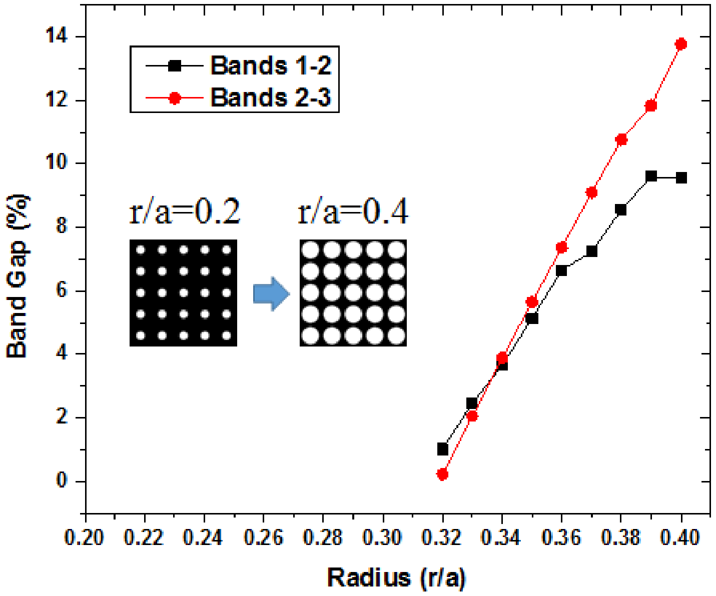

Figure 4.19 Band gap map for square lattice of holes

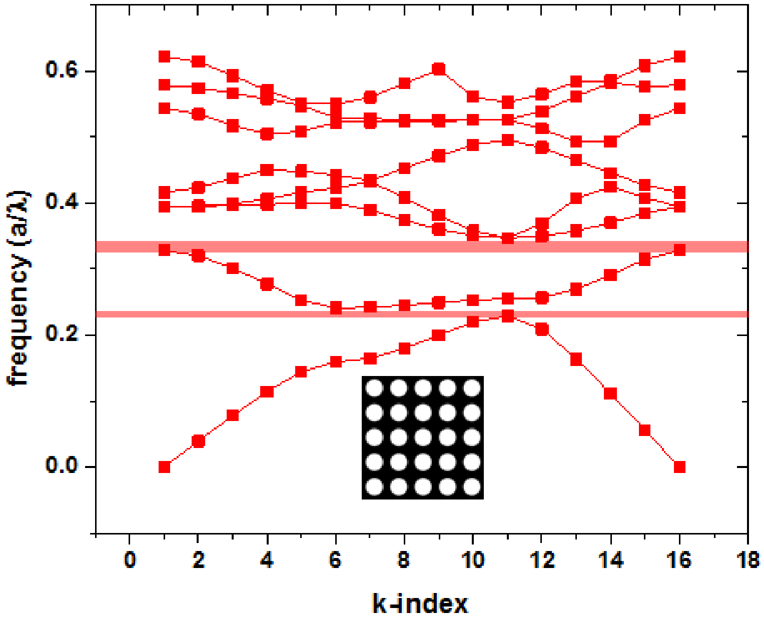

Figure 4.20 TE band diagram of square lattice of air holes for r=0.35a

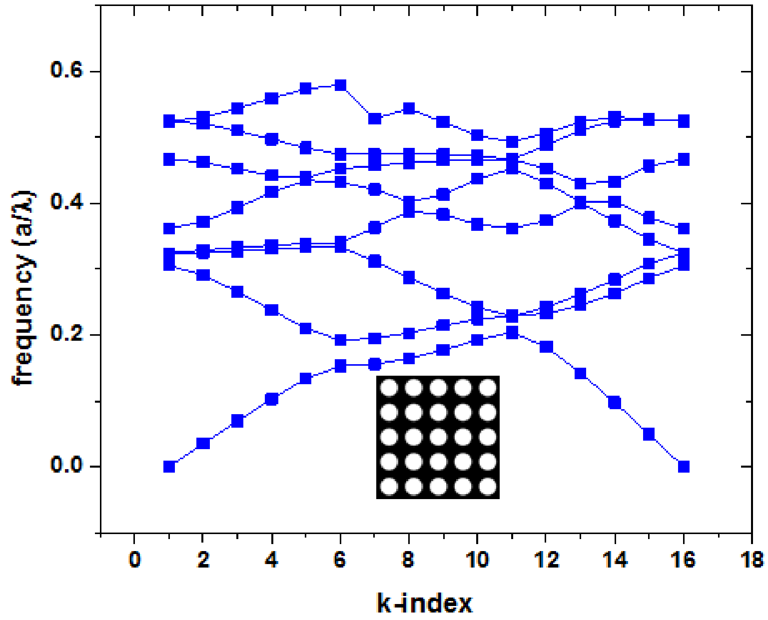

Figure 4.21 TM band diagram of square lattice of air holes for r=0.35a

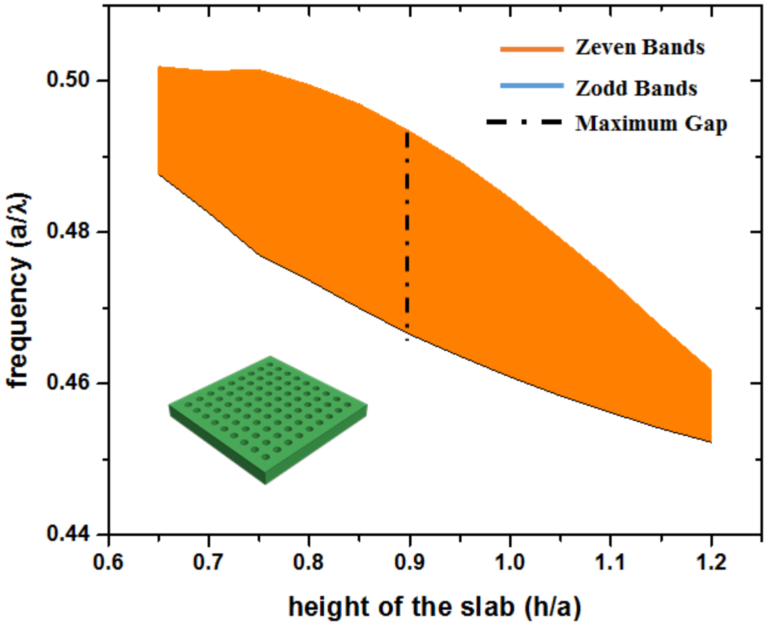

Figure 4.22 Directional band gap map of square lattice of holes in ITO for r=0.35a w.r.t. height

As the thickness of the PhC slab is confined, the bands collapse and reduce the possibility of having a band gap. It is found that a directional band gap exists between zeven bands 2 and 3 for square lattice of holes in ITO material. The band gap map for ITO square holes of radius r=0.35a with respect to the height of the slab is shown in the Figure 4.22. Zeven and zodd band diagrams for the PhC structure with square lattice of holes of radius r=0.35a and height h=0.9a are shown in the Figures 4.23 and 4.24. A maximum directional band gap of 5.59% has been observed in this structure with air hole radius of 0.35a and height of 0.9a. From the band diagram, the mid-gap frequency of (0.47994 c/a) is extracted and the physical dimensions for 2D PhC structures are calculated and presented in Table 4.3.

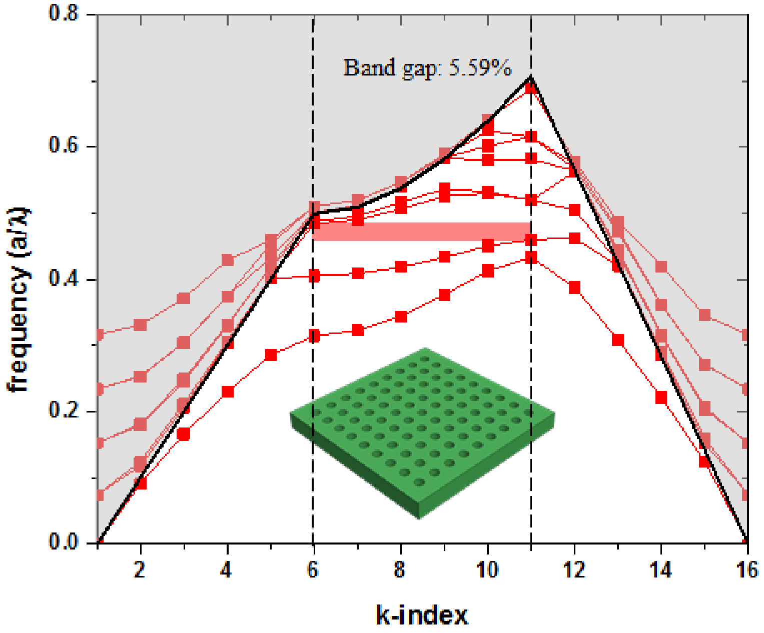

Figure 4.23 Zeven band diagram of ITO holes for r=0.35a and h=0.9a showing the directional band gap

Furthermore, a parametric sweep was done to find how the directional band gaps in both square and triangular lattice of holes is affected by the radius and the height. To do this, the radius is swept from 0.33a to 0.38a and the height is swept from 0.65a to 1.2a. For each of the parameter, the band gap is extracted and plotted as a contour map to see the trend.

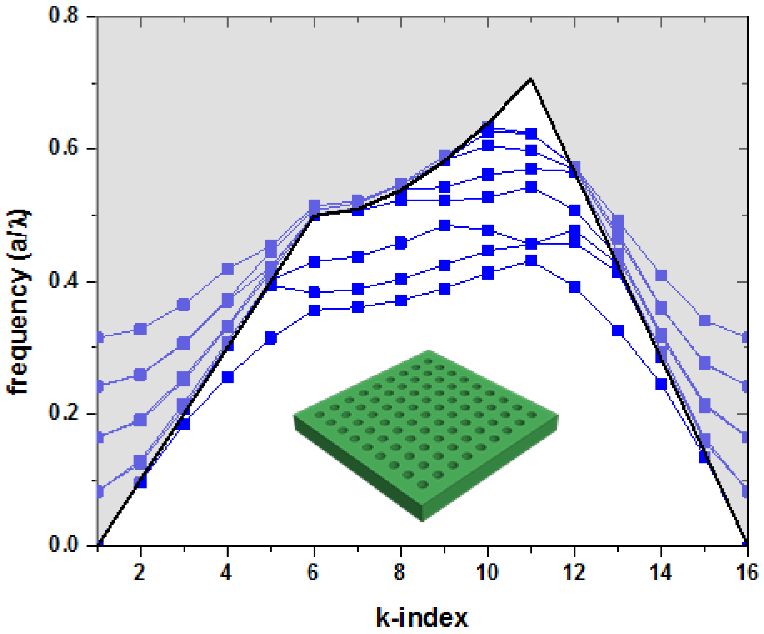

Figure 4.24 Zodd band diagram for a square lattice of air holes with radius r=0.35a and height h=0.9a

Table 4.3 Physical parameters of square lattice of air holes in ITO

Mid Gap frequency	*f*	*0.47994*
Wavelength of operation	*λ*	*465 nm*
Lattice constant	*a=fλ*	*223.17 nm*
Radius	*r=0.35a*	*78.11 nm*
Thickness	*h=0.9a*	*200.85 nm*

As observed in the earlier simulations, the triangular lattice has a directional band gap that exists between bands 1 and 2. While the square lattice also has a directional band gap that exists between bands 2 and 3. From the results extracted, it is thus found that for triangular lattice of holes, the directional band gap steadily increases as the radius and height increases.

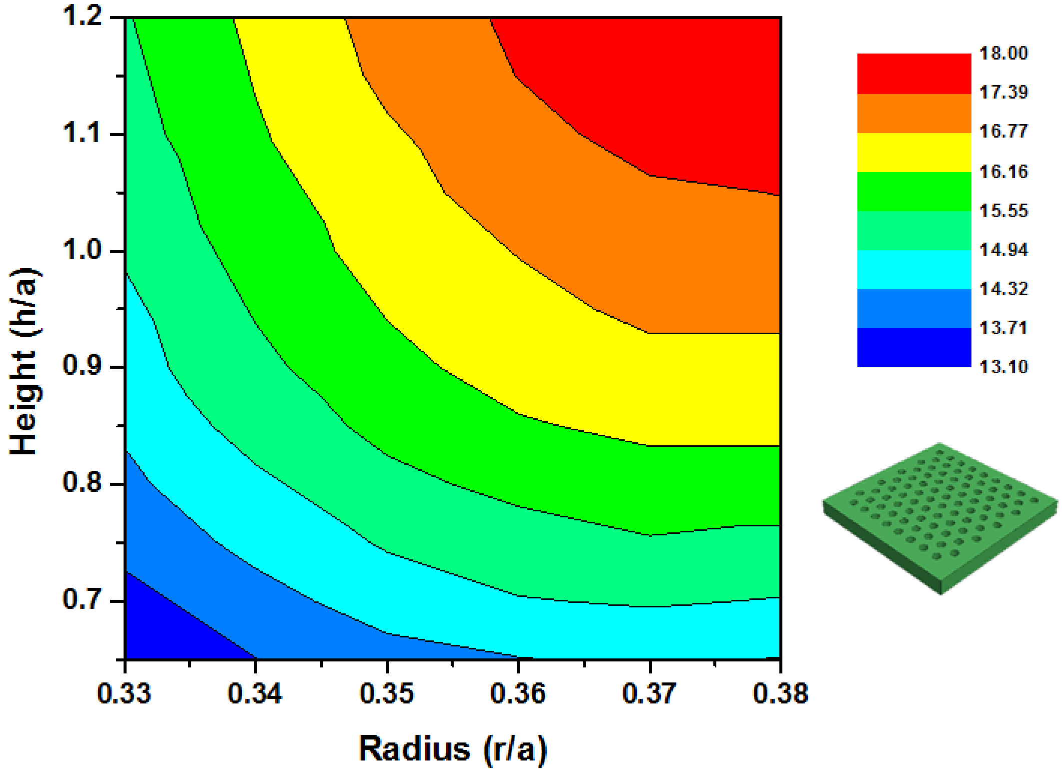

Figure 4.25 Band gap trend of triangular lattice of holes w.r.t. radius and height

As for the square lattice of holes, the directional band gap is particularly high at lower radius and decreases as the radius is increased. Figure 4.25 and Figure 4.26 shows the band gap trend with respect to the radius and height parameters of the triangular and square lattices of holes.

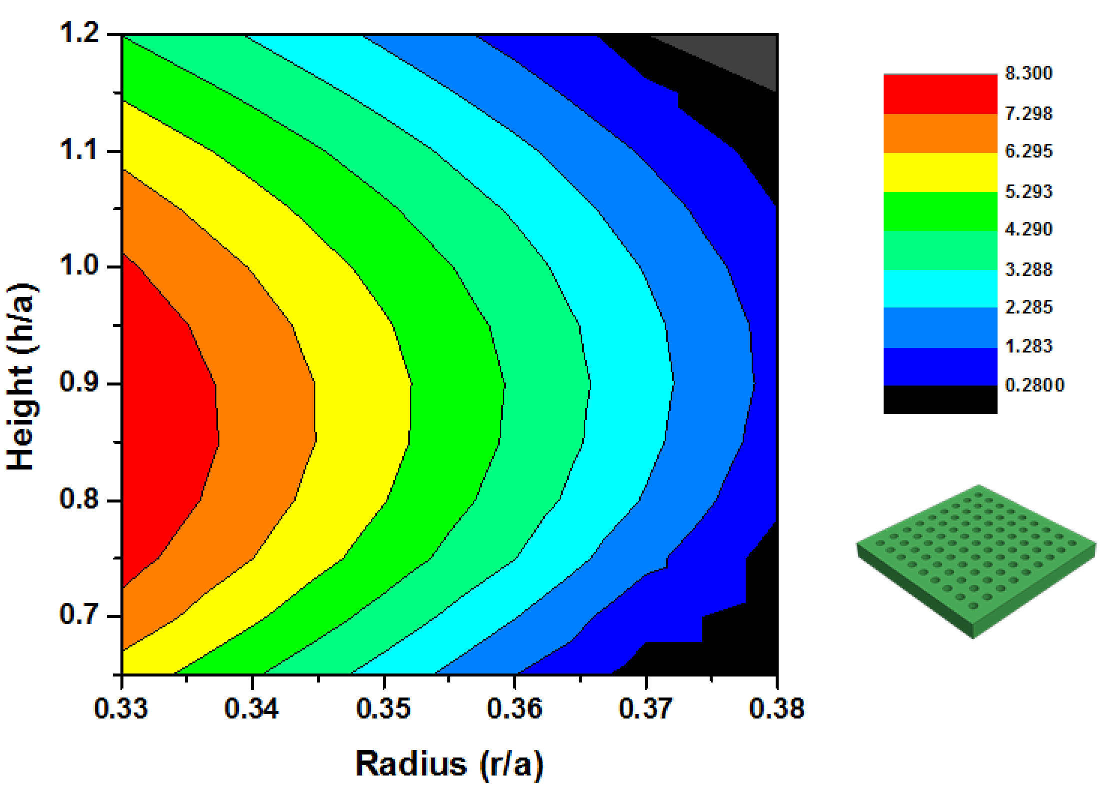

Figure 4.26 Band gap trend of square lattice of holes w.r.t. radius and height

4.1.4. Hybrid PhCs

Traditionally, a PhC is defined as a periodic structure with a high and a low dielectric media. Here we define a hybrid PhC as a periodic structure as a periodic structure with more than two dielectric materials and contribute to a result in a collective effect. In the illustration shown in Figure 4.27, the concept of a hybrid photonic crystal is visualized, involving materials like SiOx and ITO. This particular type of hybrid PhC design is a result to accommodate one of the side effects of integrating PhC structures into LEDs. In the integration process of PhCs into an LED, SiOx is used as a mask to pattern the ITO layer. However, the SiOx masking pattern can only be removed by means of corrosive acid etchants. Attempts to remove the SiOx patterns using acids has resulted in partially etching away the underlying materials (in this case the LED layers). As a result, the SiOx features used for realizing the PhC patterns that are now an integral part of the PhC structure resulting in a hybrid PhC.

Frequency domain simulations were done in a similar fashion as described in the earlier sections. From the simulations performed, it was observed that by the addition of this third material, the directional band gaps that were present in the case of square and triangular lattices of holes collapsed and resulted in typically insignificant band gaps (<1%).

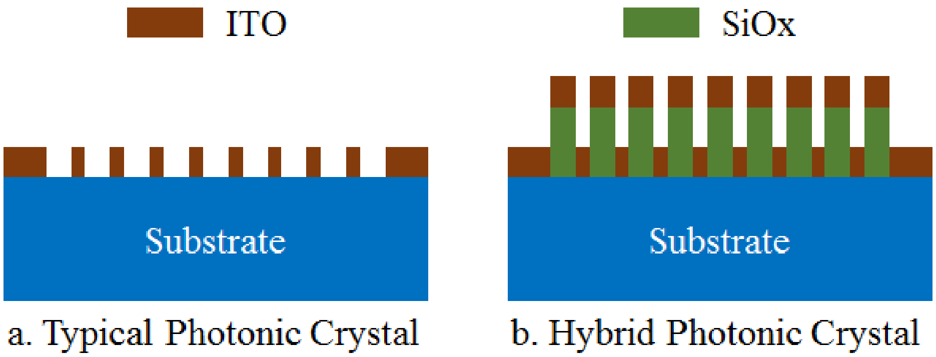

Figure 4.27 Illustration of (a.) Typical and (b.) Hybrid photonic crystal

As the band gaps in these configurations are insignificant, the zeven and zodd band diagrams are plotted for radius r=0.33a and height h=1.0a for simplicity. Figures 4.28 and 4.29 show the zeven and zodd band diagrams of triangular lattice of hybrid PhCs, and Figures 4.30 and 4.31 show the zeven and zodd band diagrams of square lattice of hybrid PhCs. To better understand the effect of having a hybrid PhC for improving the light extraction from an LED, simulations need to be performed to understand their diffractive properties.

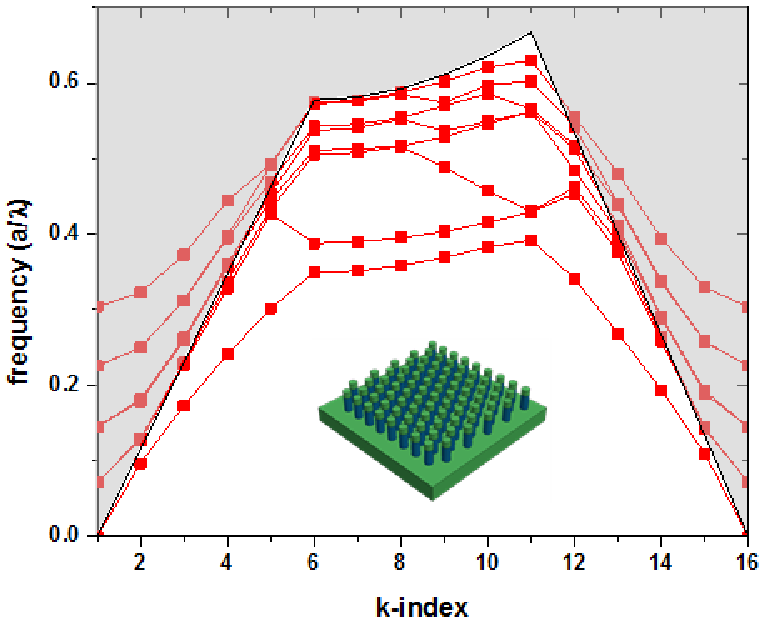

Figure 4.28 Zeven band diagram for triangular lattice of hybrid PhC r=0.33a, h=1.0a

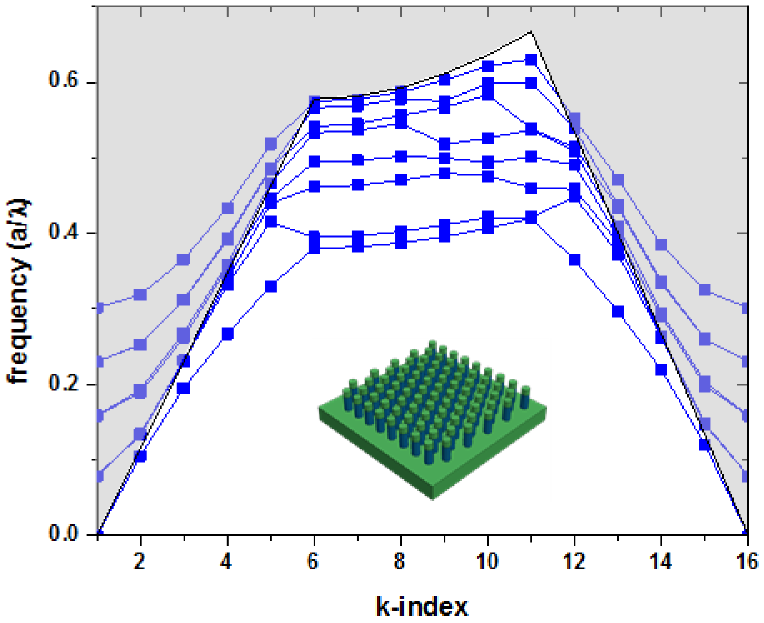

Figure 4.29 Zodd band diagram for triangular lattice of hybrid PhC r=0.33a, h=1.0a

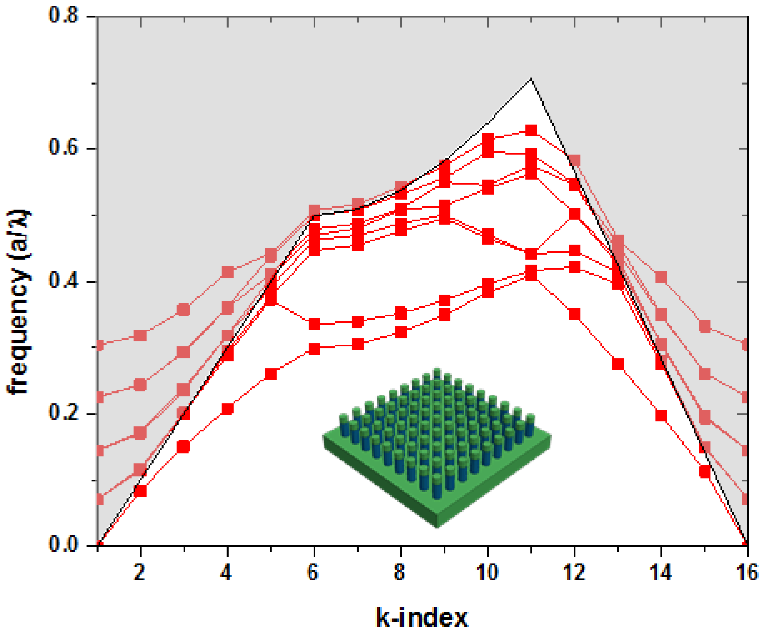

Figure 4.30 Zeven band diagram for square lattice of hybrid PhC r=0.33a, h=1.0a

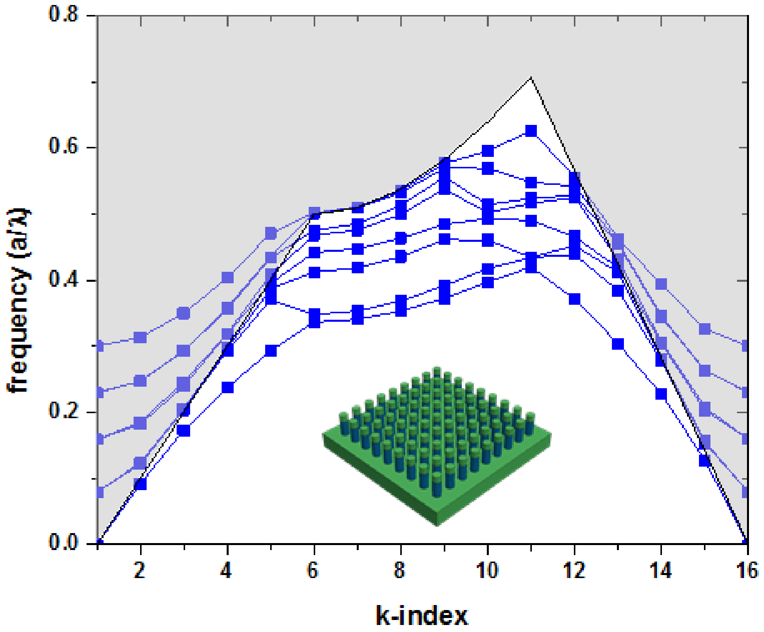

Figure 4.31 Zodd band diagram for square lattice of hybrid PhC r=0.33a, h=1.0a

4.2. Time Domain

Time-domain methods are well-suited to computing the electromagnetic field evolutions with respect to time for a particular structure. Optiwave’s finite difference time domain (FDTD) is one such time domain software that allows computer aided design and simulation of advanced passive photonic components. FDTD method is a powerful engineering tool for understanding integrated and diffractive optics device simulations. The software has features such as ability to model light propagation, scattering, and diffraction, and reflection and polarization effects.

The FDTD approach is based on a direct numerical solution of the time-dependent Maxwell’s equations. As the name implies, FDTD divides the whole computation space and simulation time into a uniform grid of discrete points and approximates the derivatives of the Maxwell’s equations by finite differences. First, the simulation model is designed in the X-Z plane and the simulation space is divided into discrete cells of dimensions Δx, Δy, and Δz (referred to as Yee’s cell) as shown in the Figure 4.32. Each mesh point is associated with a specific type of material and contains information about its properties such as refractive index, and dispersion parameters. The propagation of light through these discrete cells are used to understand the evolution of the electromagnetic field within these cells. The result of the first cell is used an input to the next cell and further computations are performed. In this way, the time dependent Maxwell’s equations are computed for the entire simulation space.

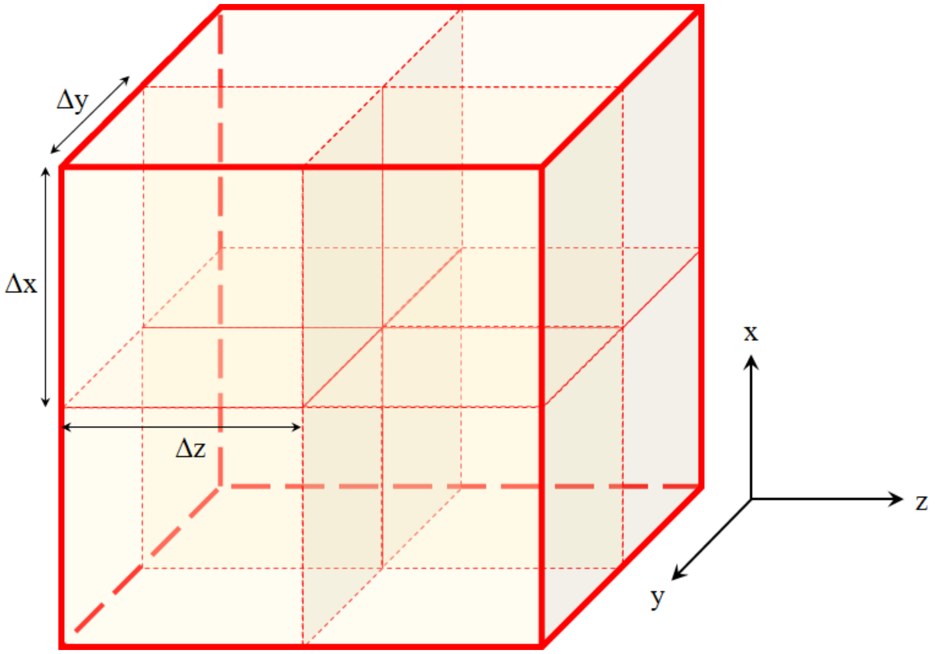

Figure 4.32 Yee's cell illustration of the simulation space

As mentioned earlier, the most widely used PhC structures for enhancing the light extraction in LEDs are diffraction based structures [62], [63]. With the addition of such PhC structures, a maximum improvement of 73% was observed [64]. However, this enhancement is due to a combination of diffractive PhC structure, vertical cavity resonance and reflective metal backing. To understand the impact of having a periodic structure configuration, a composite structure containing PhC on the LED has to be simulated. A major limitation to the frequency domain simulation software is that the light source is usually parallel to the plane of the PhC. Due to this limitation, software engines with the flexibility to change the angle of incidence of the source need to be utilized. Software like Optiwave FDTD (Finite-difference time-domain) allow the flexibility of modeling in a computer-aided design (CAD) environment. With this flexibility, an appropriate model for simulation with a light source normal to the plane of PhC can be designed.

4.2.1. Setting Up the Simulation Space

In this current scenario, the LED structure with a PhC structure is as shown in the Figure 4.33 (a). Light generated within the active region of the LED has to travel through the dielectric layers to be extracted into the environment. In order to simulate the extraction from the LED, all the materials involved in the structure and their properties need to be taken into consideration. Due to computing restrictions, all the individual layers of the LED are condensed into a single layer with an effective refractive index of the entire LED (nLED~2.44). To further simplify the simulations, only a 6x6 μm^2 area of the LED with a different PhC configurations were simulated. Finally, on top of this LED layer, a transparent conducting layer like indium tin oxide (ITO) is patterned with a periodic pattern as shown in the Figure 4.33 (b).

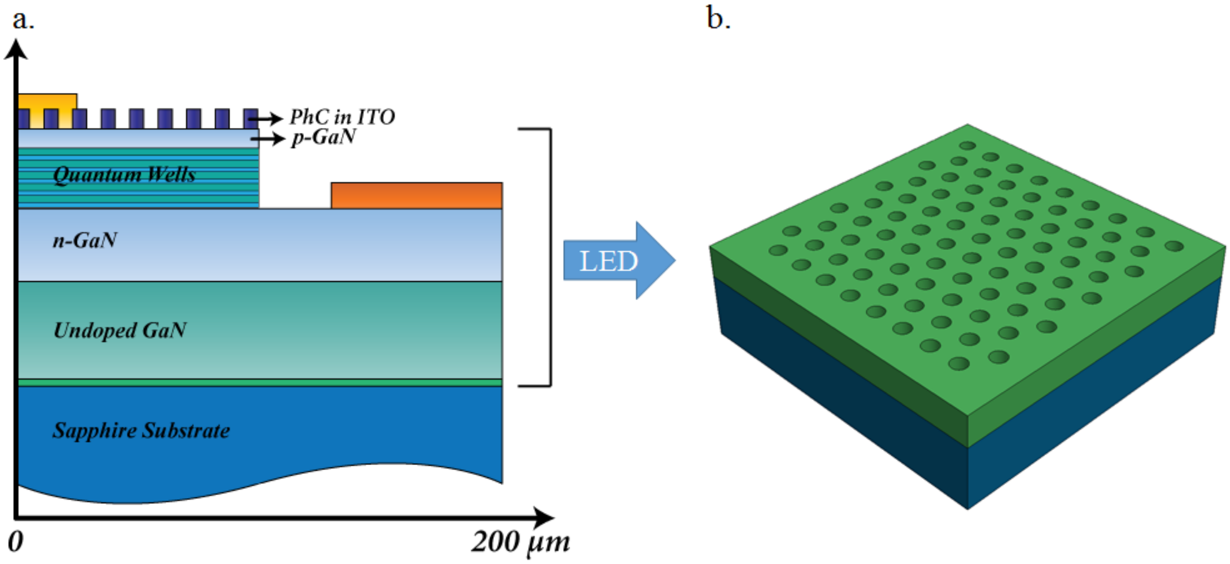

Figure 4.33 (a) PhC LED structure (b) CAD model of the PhC LED

Various configurations of PhCs like triangular and square lattice of holes and hybrid structures are incorporated into the ITO layer and simulated. The simulation space is surrounded by a perfectly matched layers and point sources with peak wavelength of 465 nm are used to emulate the behavior of the photons generated within an LED. An observation plane is used to record the field patterns at a constant distance away from the surface of the ITO layer. Figure 4.34 shows the layout of the simulation space.

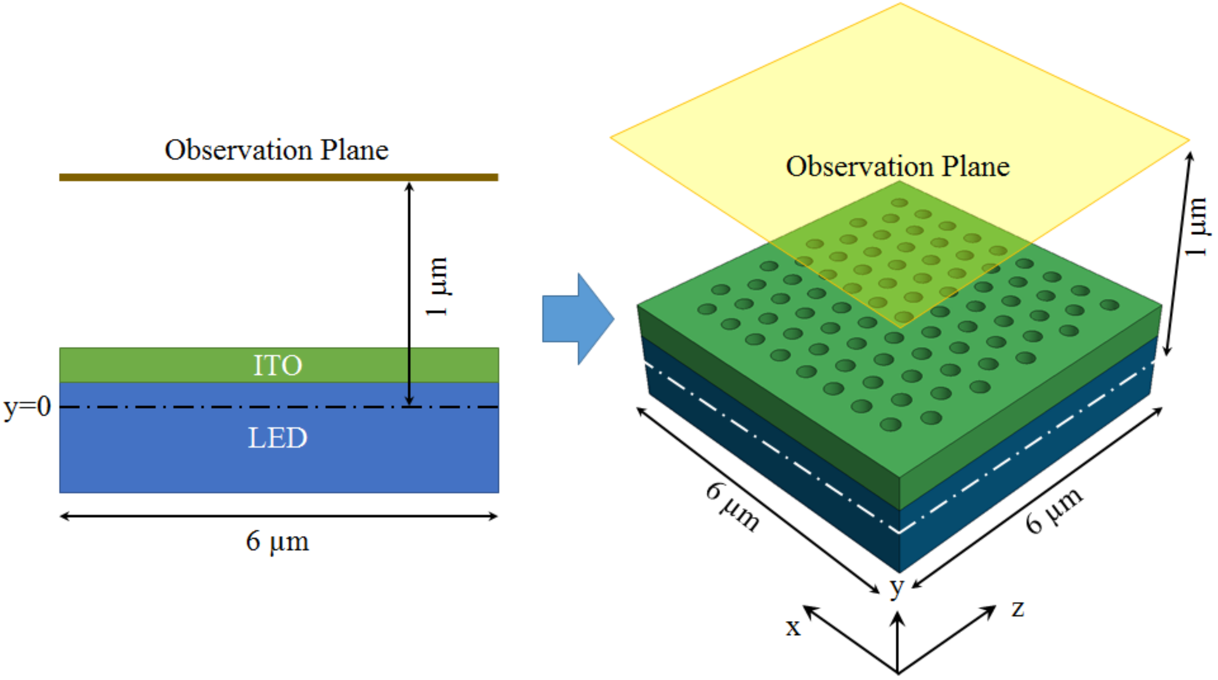

Figure 4.34 2D and 3D illustration of the simulation space

4.2.2. Point Sources

In order to effectively mimic the photons generated in an LED, the sources for these simulations need to be spontaneous and should have emission characteristics of an LED. For this study, point sources in various configurations are simulated to find the optimal point source configuration to emulate an LED. The ITO layer is left unpatterned to observe the field distributions and determine an efficient point source configuration. The observation plane for these simulations is set at a height of 250 nm, right above the ITO layer. The point sources are arranged in triangular, square and random patterns as shown in the Figure 4.35 (a, b, & c). All the point sources used in these simulations have a random starting point to mimic the spontaneous emission nature of the LED.

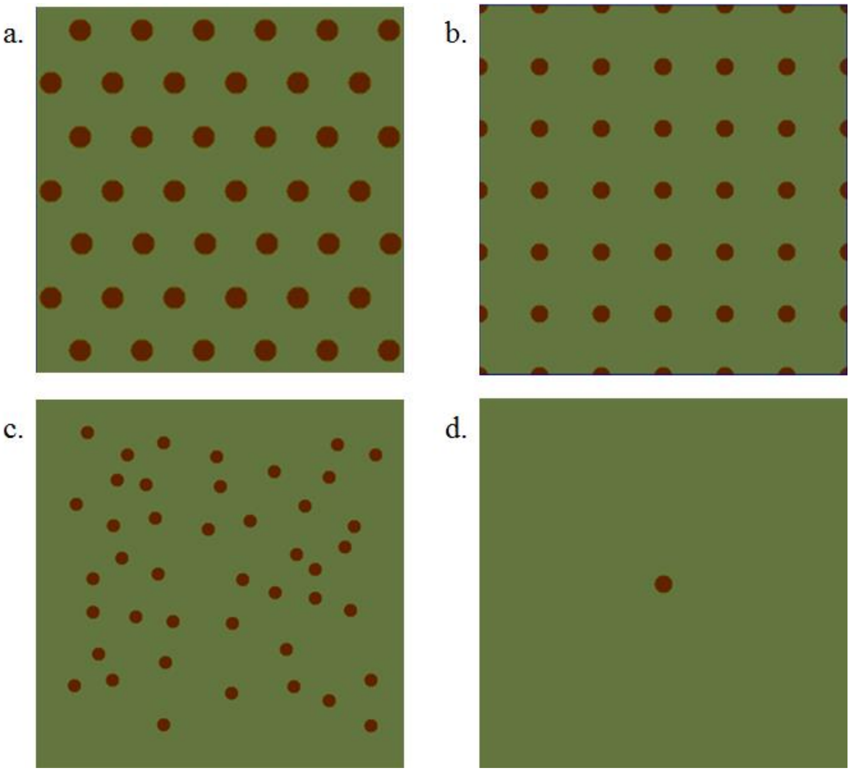

Figure 4.35 Point sources arranged in (a.) triangular, (b.) square, (c.) random, and (d.) single

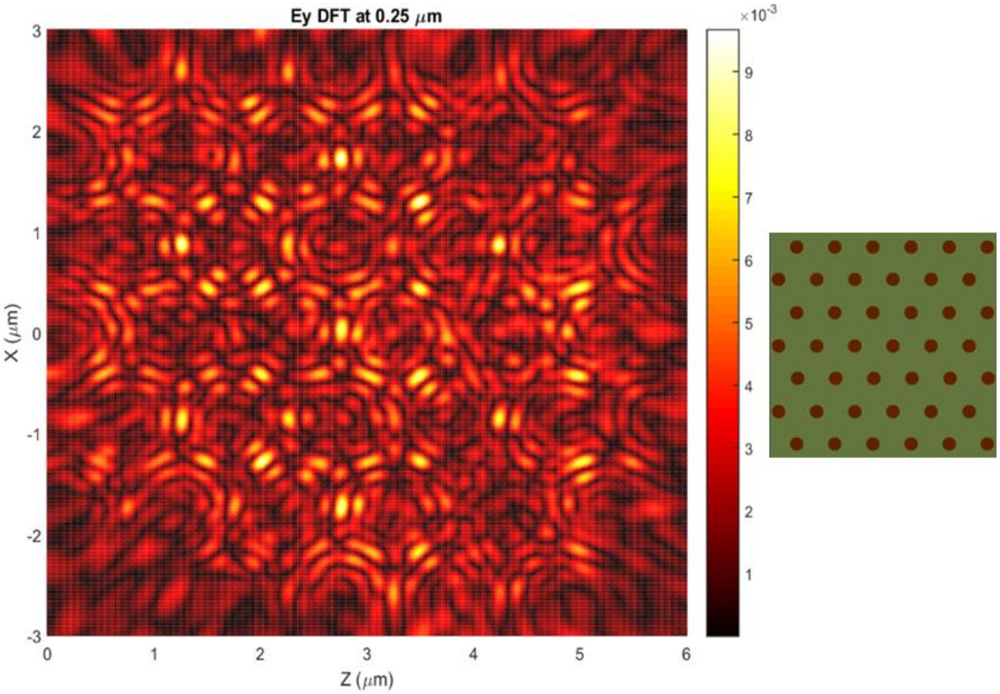

Figure 4.36 Ey DFT field pattern observed for a triangular arrangement of the point sources.

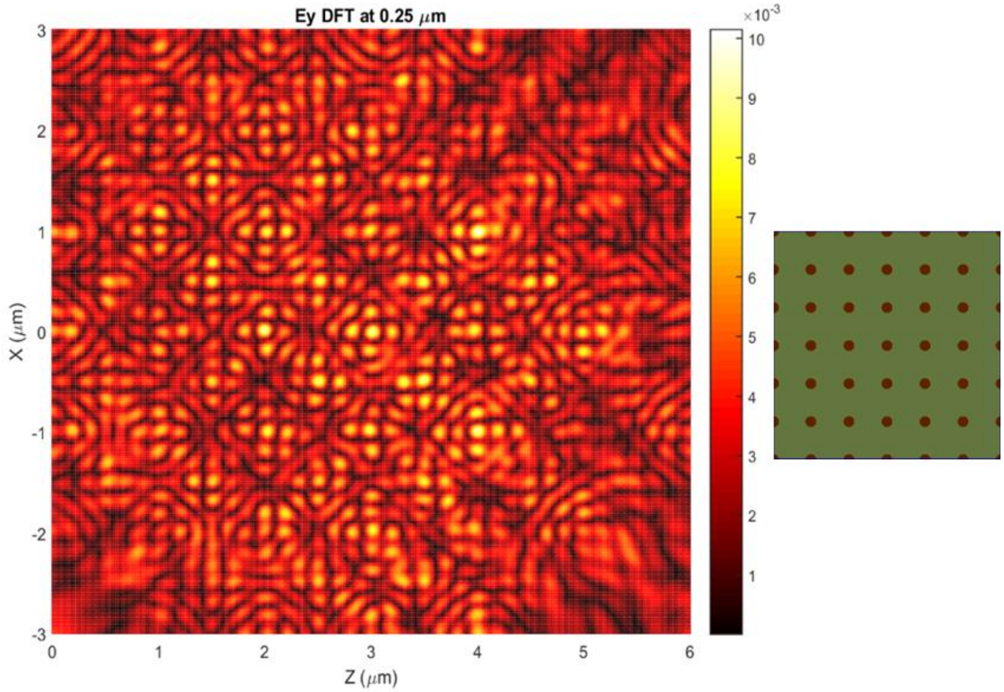

Figure 4.37 Ey DFT field pattern observed for a square arrangement of the point sources.

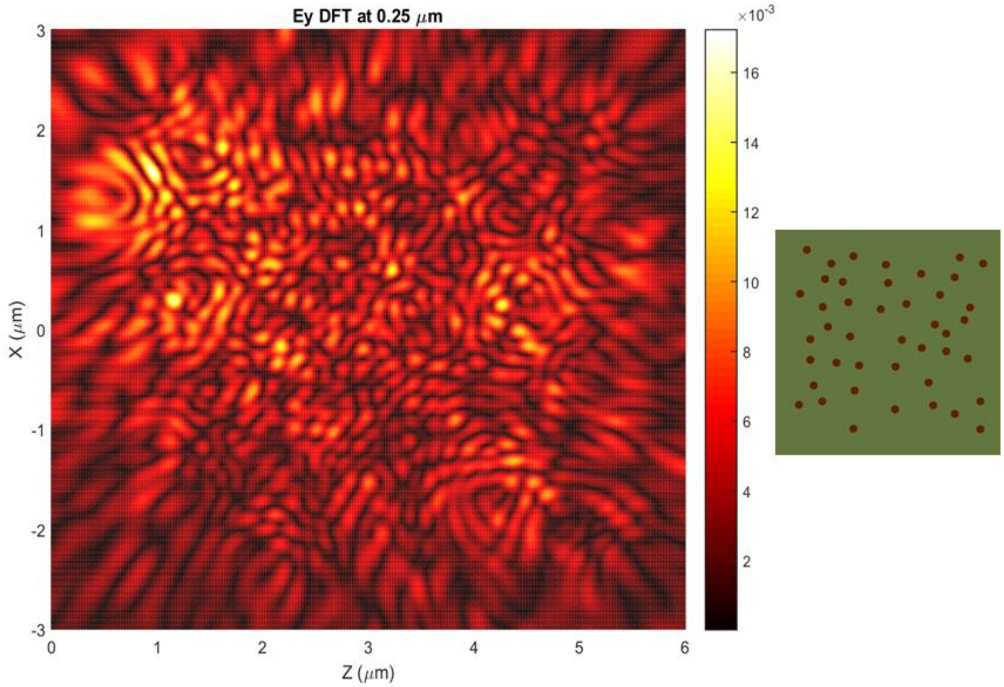

Figure 4.38 Ey DFT field pattern observed for a random arrangement of the point sources

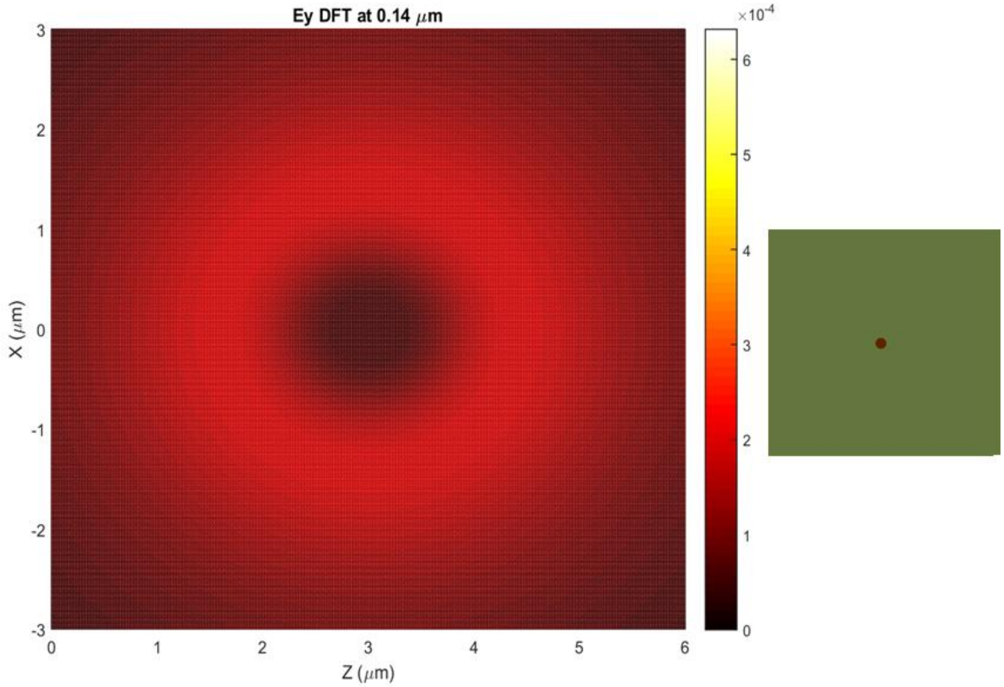

Figure 4.39 Ey DFT field pattern observed for a single point source

A single point source was also simulated to observe the effect of the single point source shown in the Figure 4.35 (d.). The respective electric field patterns (Ey DFT) were extracted and plotted shown in the Figures 4.36, 4.37, 4.38 and 4.39. From the field patterns extracted, it is observed that the point sources arranged in a periodic pattern have a periodic field distribution and represent the diffraction patterns of the periodic arrangement. While the random arrangement does not portray any trend as expected and the single point source on the other hand shows a uniform field pattern. Due to the periodic nature of the field distributions extracted from the periodic configurations, it is deduced that periodic arrangement has its own effect due to multiple point sources and the way they are setup. The random arrangement on the other hand doesn't result in a consistent result and hence the single point source configuration is decided to be most apt configuration for emulating the photons from an LED.

4.2.3. Diffraction Simulations

For this study, PhC structures in square and triangular lattice configurations with cylindrical features with radii ranging from 50 nm to 500 nm separated by a pitch of 1 μm are simulated. Along with these, square and triangular lattices with hybrid pillars intact are also simulated. An unpatterned LED was also simulated to be used as a control device for comparison. The simulated models are shown in the Figure 4.40. As mentioned earlier, due to computing restrictions, only a portion of the LED is chosen for simulations. From the previous study done on the various configurations of point sources, a single point source is used for these simulations. The point source emission characteristics are shown in the Figure 4.41. The point source has a peak emission at 465 nm and a full width half maximum (FWHM) bandwidth of ~20 nm. The start time for the point source is set at 40E-15 seconds mimicking the delay in turning on an LED.

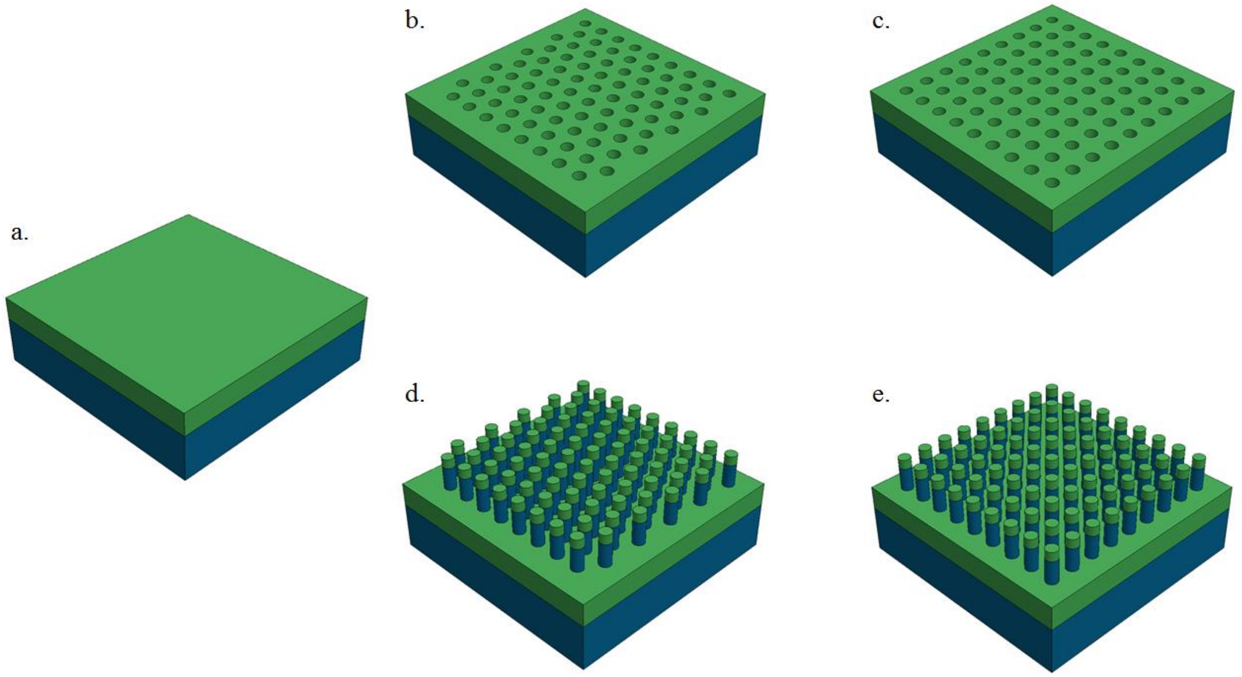

Figure 4.40 CAD models of the simulated structures (a) Control, (b) Triangular air holes, (c) Square air holes, (d) Triangular Hybrid pillars, and (e) Square Hybrid pillars

After the 3D FDTD simulations were performed on these models and their respective electric field patterns were extracted from the observation plane set at a constant distance (~1 µm). The extracted slice is only few multiples of the wavelength away and hence these field patterns are considered to be near field patterns. From these field patterns, the intensity per unit area for each model is extracted and compared.

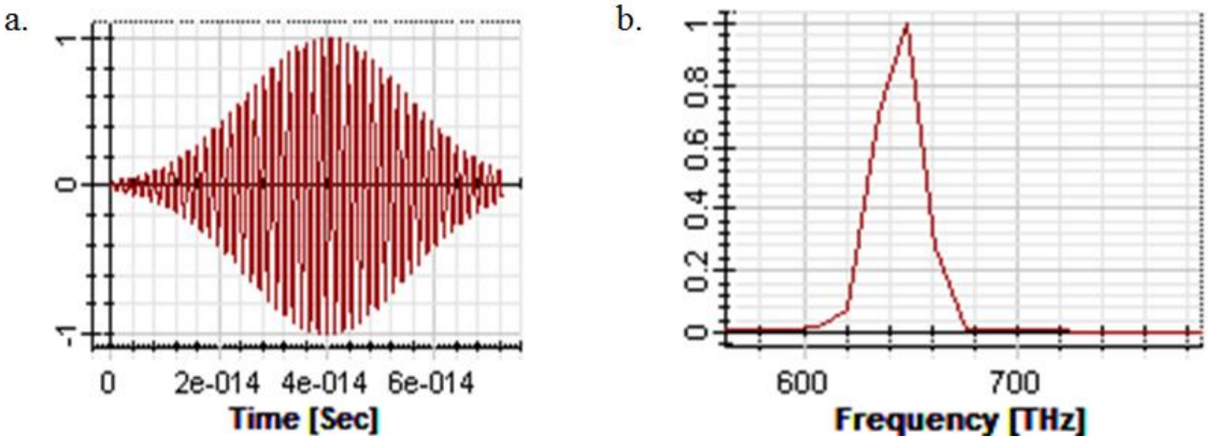

Figure 4.41 Emission characteristics of the point source (a.) Start time, and (b.) Emission spectrum

The near field patterns for the triangular holes with the feature size varying from 50 nm to 500 nm are shown in the Figure 4.42. Similarly, near field patterns for triangular hybrid pillars, square holes and square hybrid pillars are shown in the Figures 4.43, 4.44 and 4.45 respectively. The intensity per unit area for each of the near field patterns is extracted and plotted with respect to the radius of the feature for each of the lattice configurations is shown in the Figure 4.46.

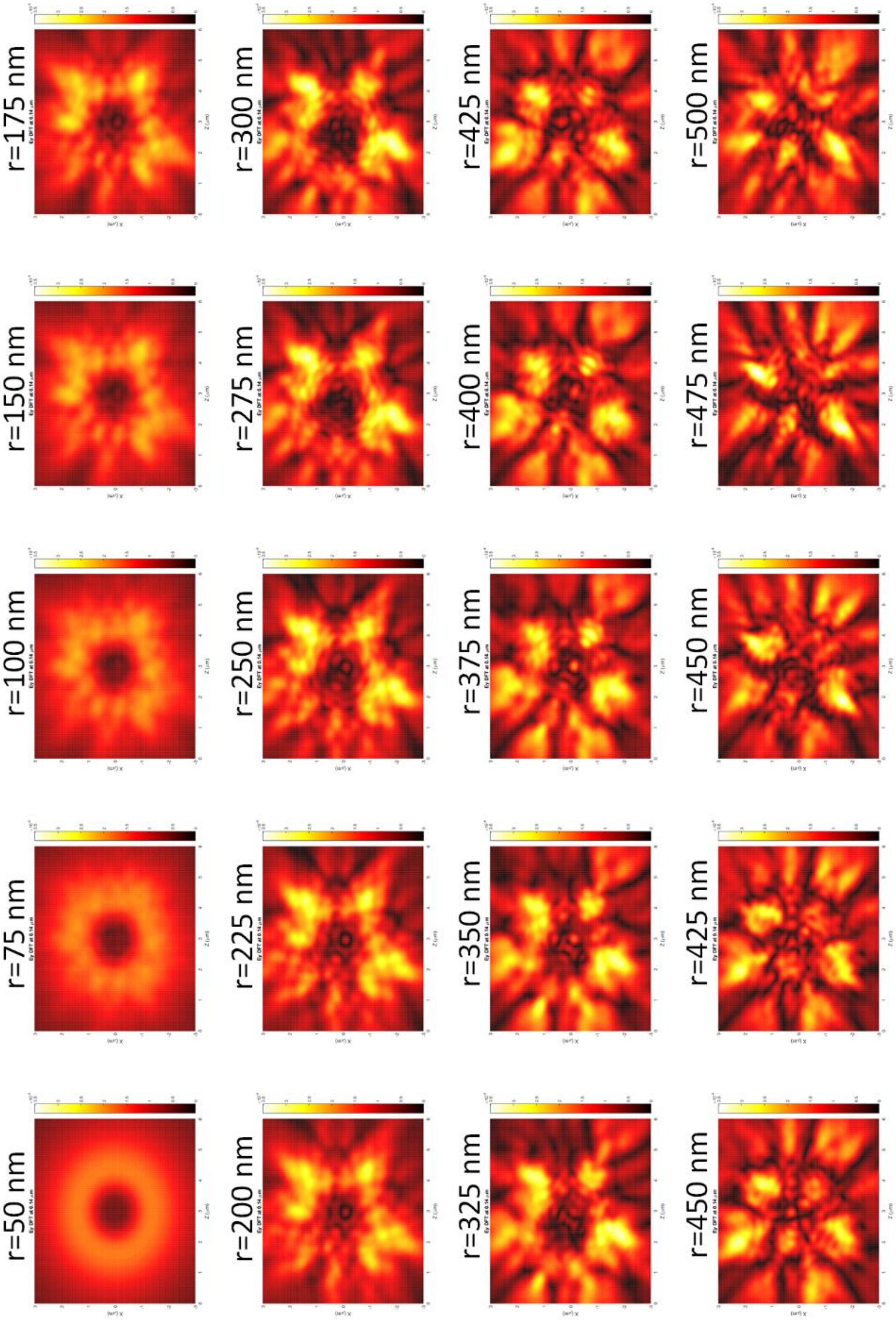

Figure 4.42 Electric field patterns (Ey) extracted from FDTD simulations of triangular lattice of holes of radius ranging from 50 nm to 500 nm

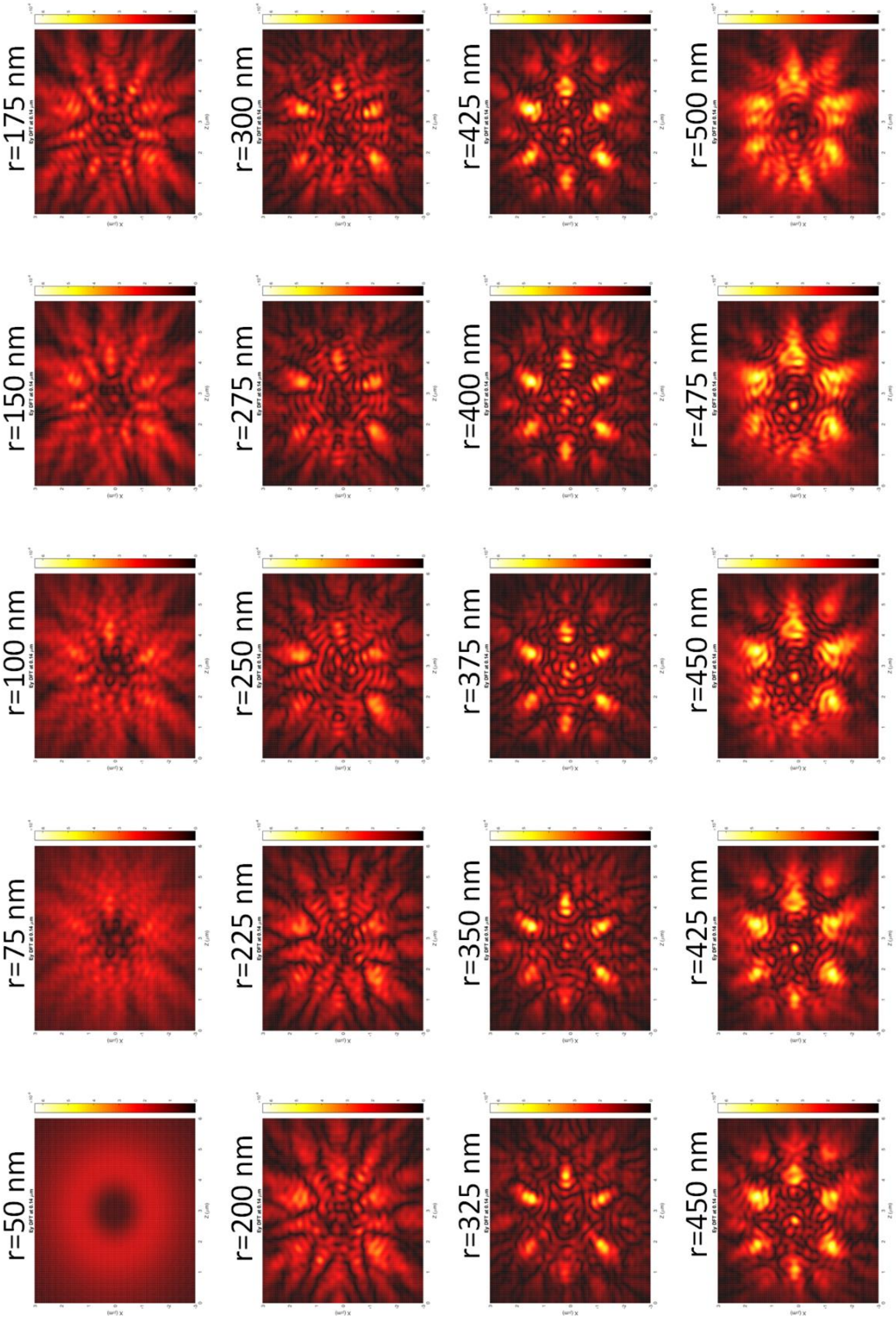

Figure 4.43 Electric field patterns (Ey) extracted from FDTD simulations of triangular lattice of hybrid pillars of radius ranging from 50 nm to 500 nm

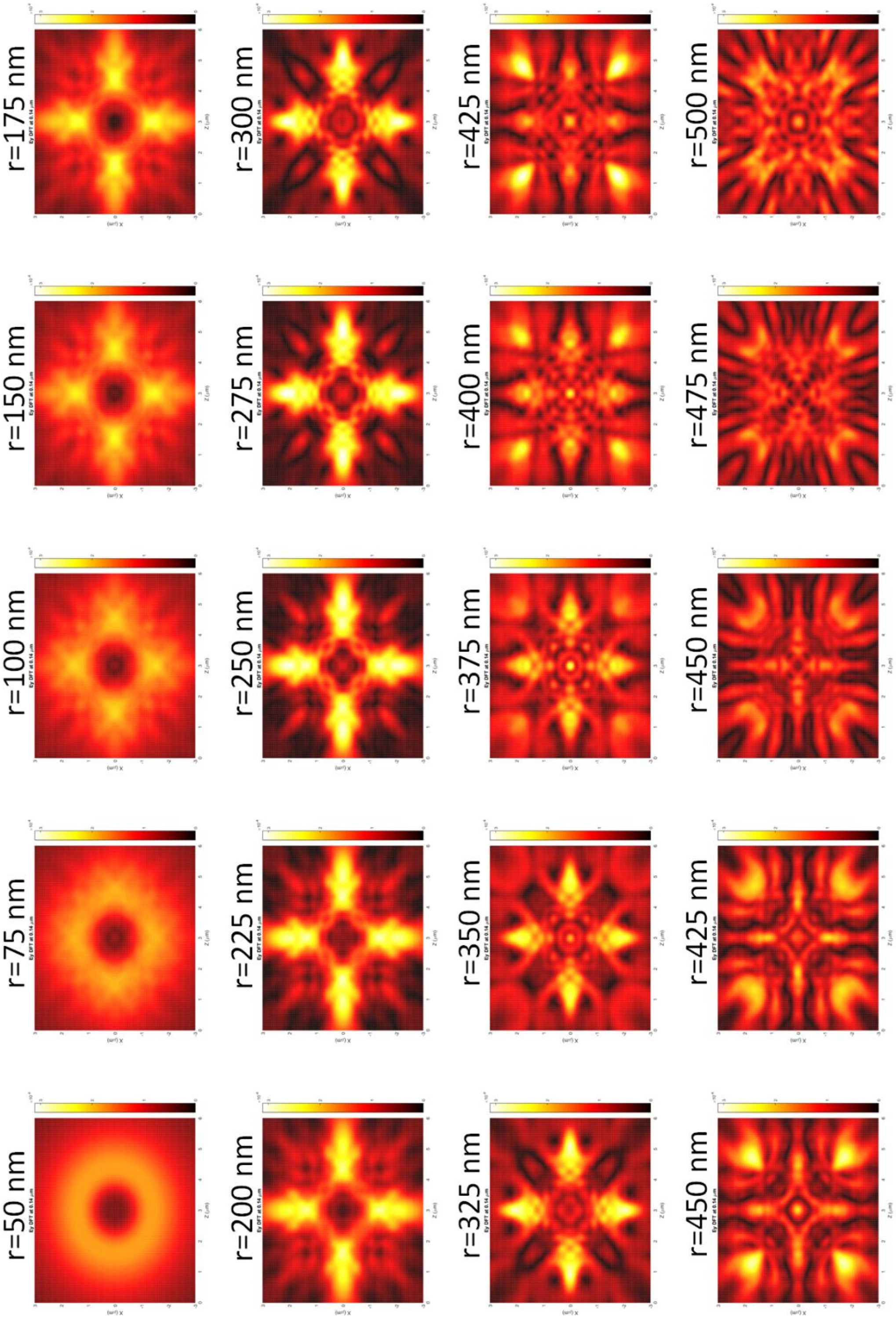

Figure 4.44 Electric field patterns (Ey) extracted from FDTD simulations of square lattice of holes of radius ranging from 50 nm to 500 nm

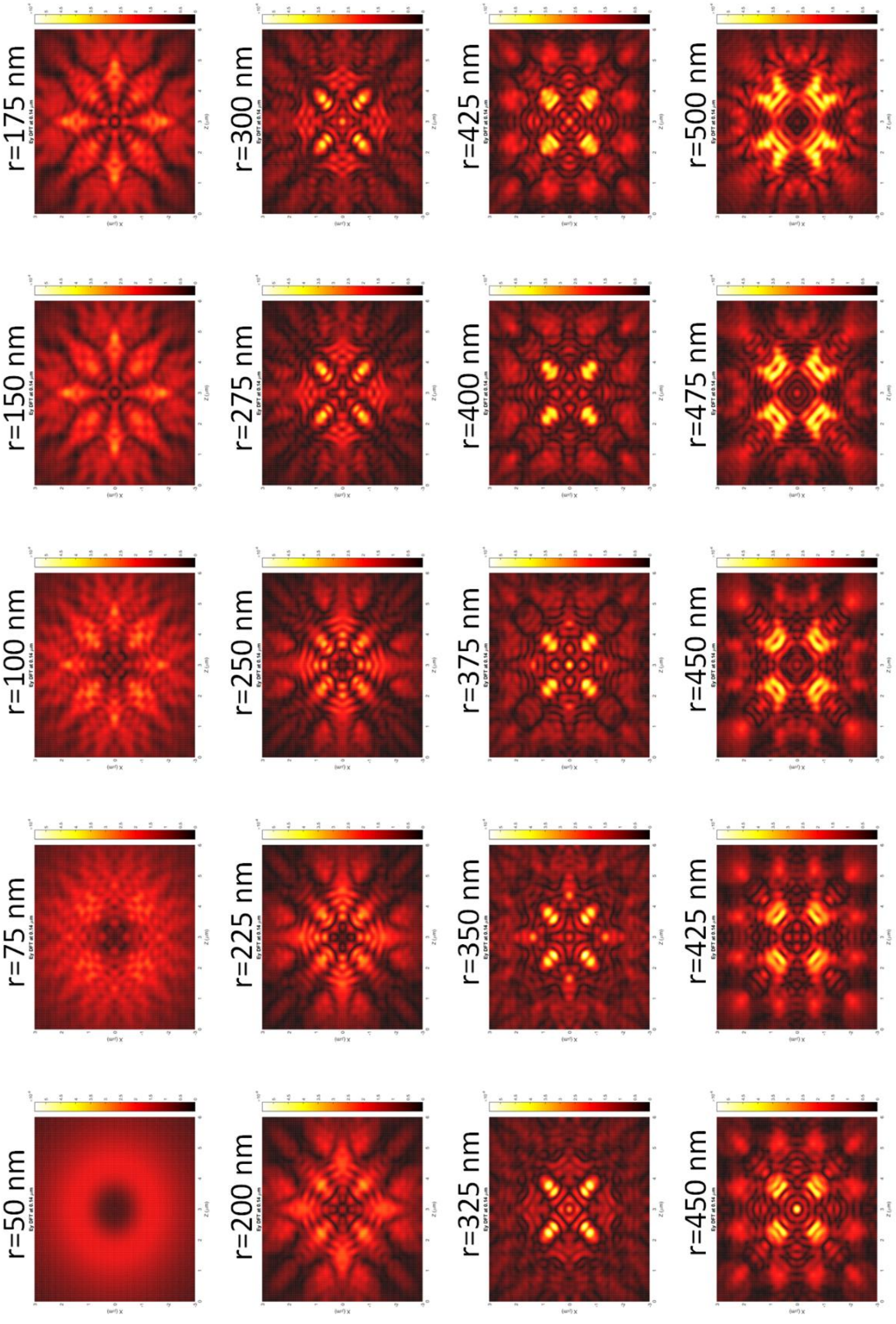

Figure 4.45 Electric field patterns (Ey) extracted from FDTD simulations of square lattice of hybrid pillars of radius ranging from 50 nm to 500 nm

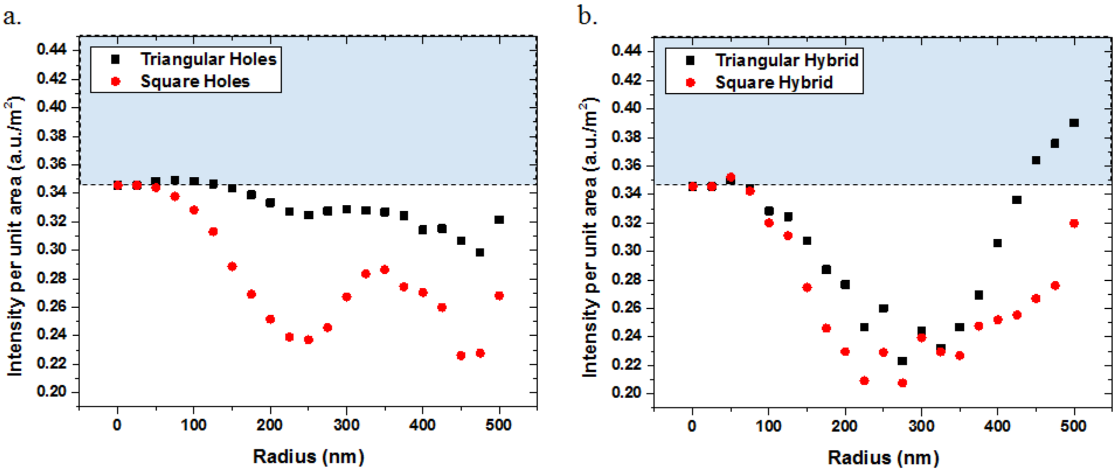

Figure 4.46 Near Field Intensity per unit area for triangular and square lattice of (a.) Holes, and (b.) Hybrid pillar patterns observed at 1µm

The near field data is exported and then used for calculating the far-field distributions using convolution of the free-space transfer function of the extracted field as shown in the Figure 4.47. Figures 4.48, 4.49, 4.50 and 4.51 show the far field fields calculated using the convolution program of triangular lattice of holes and hybrid pillars, and square lattice of holes and hybrid pillars respectively. The intensity per unit area is calculated from each of the far field distributions and plotted with respect of the radius of the feature as shown in the Figure 4.52.

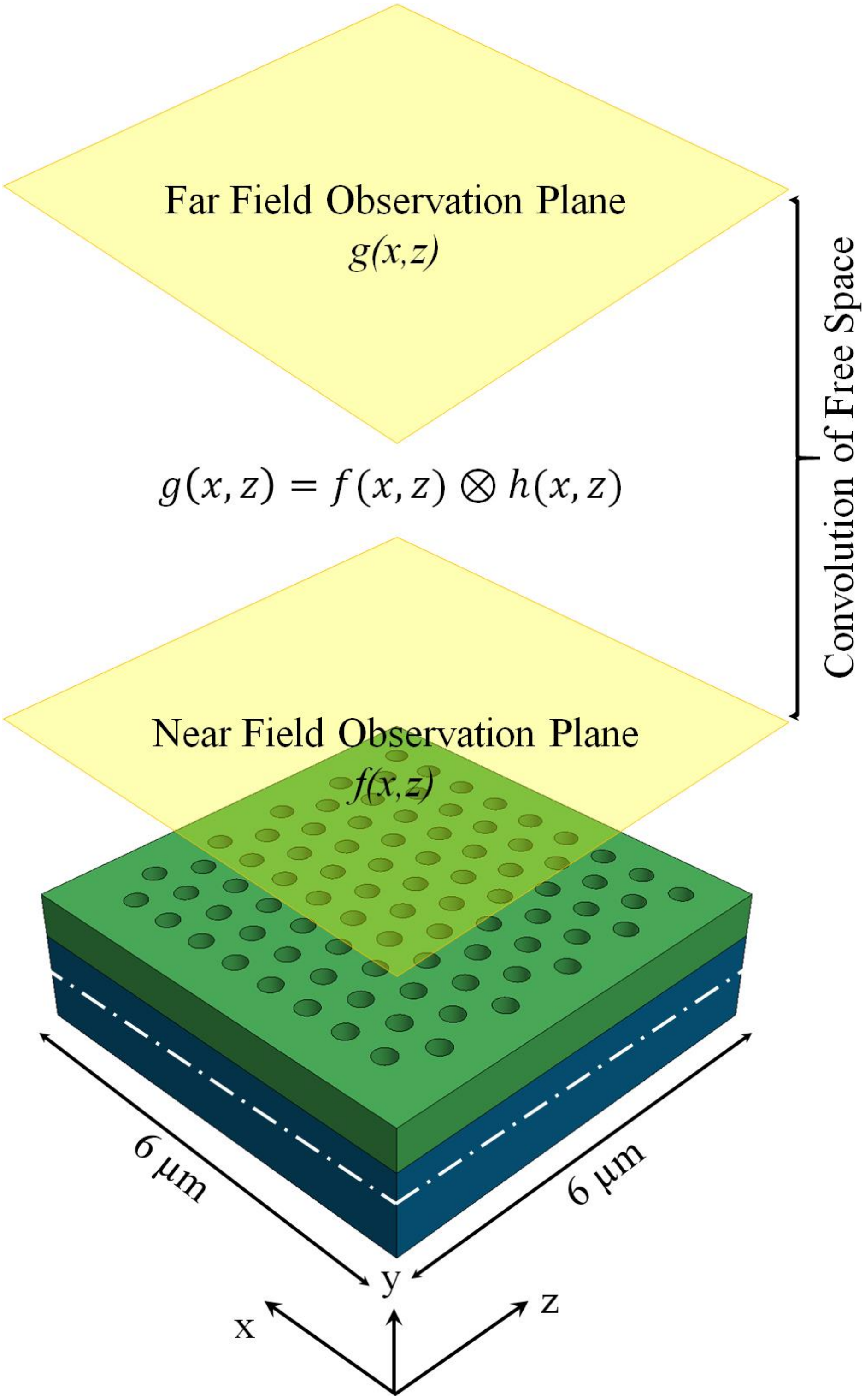

Figure 4.47 Generation of far field patterns through convolution of free space transfer function and near field data

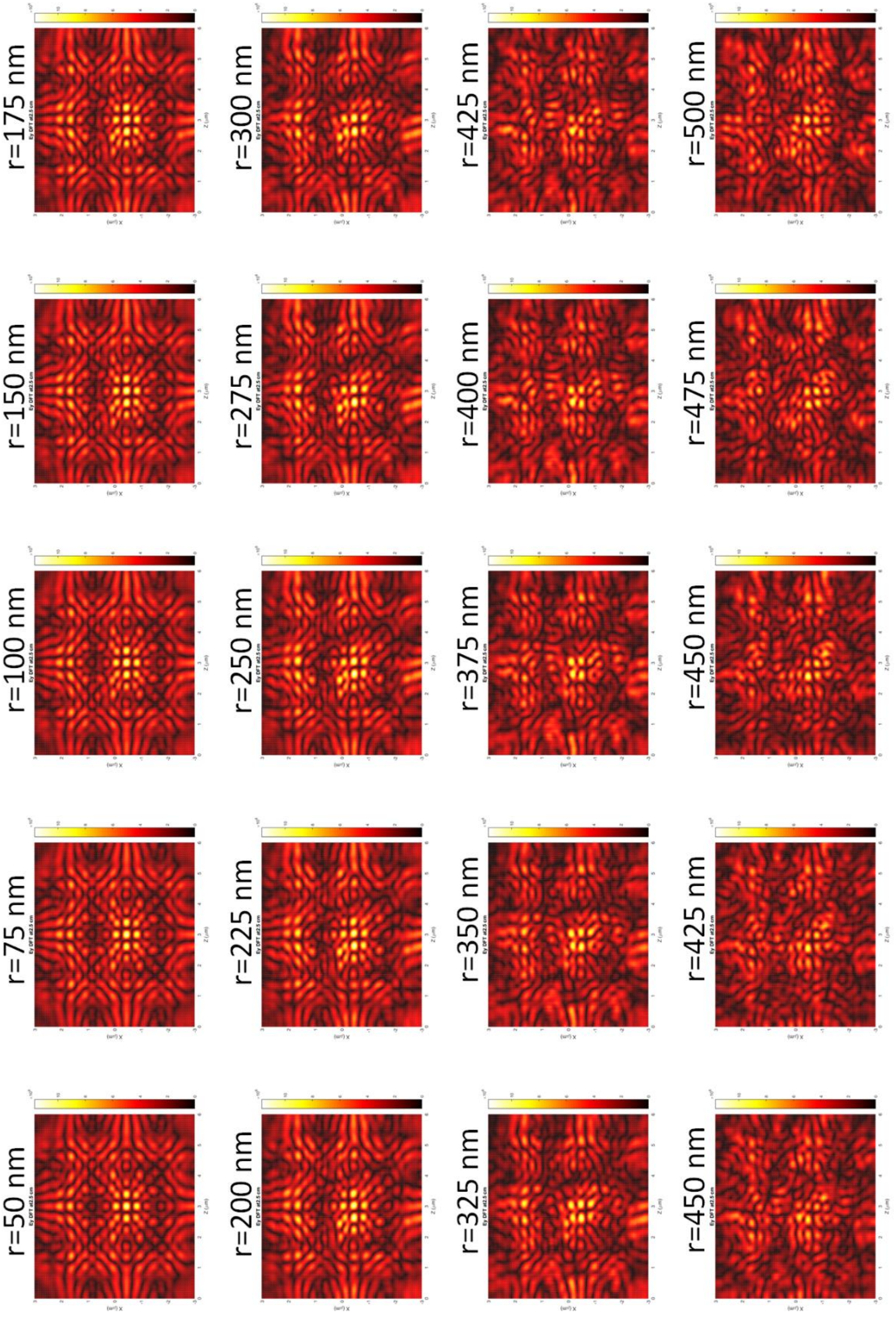

Figure 4.48 Far field electric field patterns (Ey) extracted from FDTD simulations of triangular lattice of holes of radius ranging from 50 nm to 500 nm

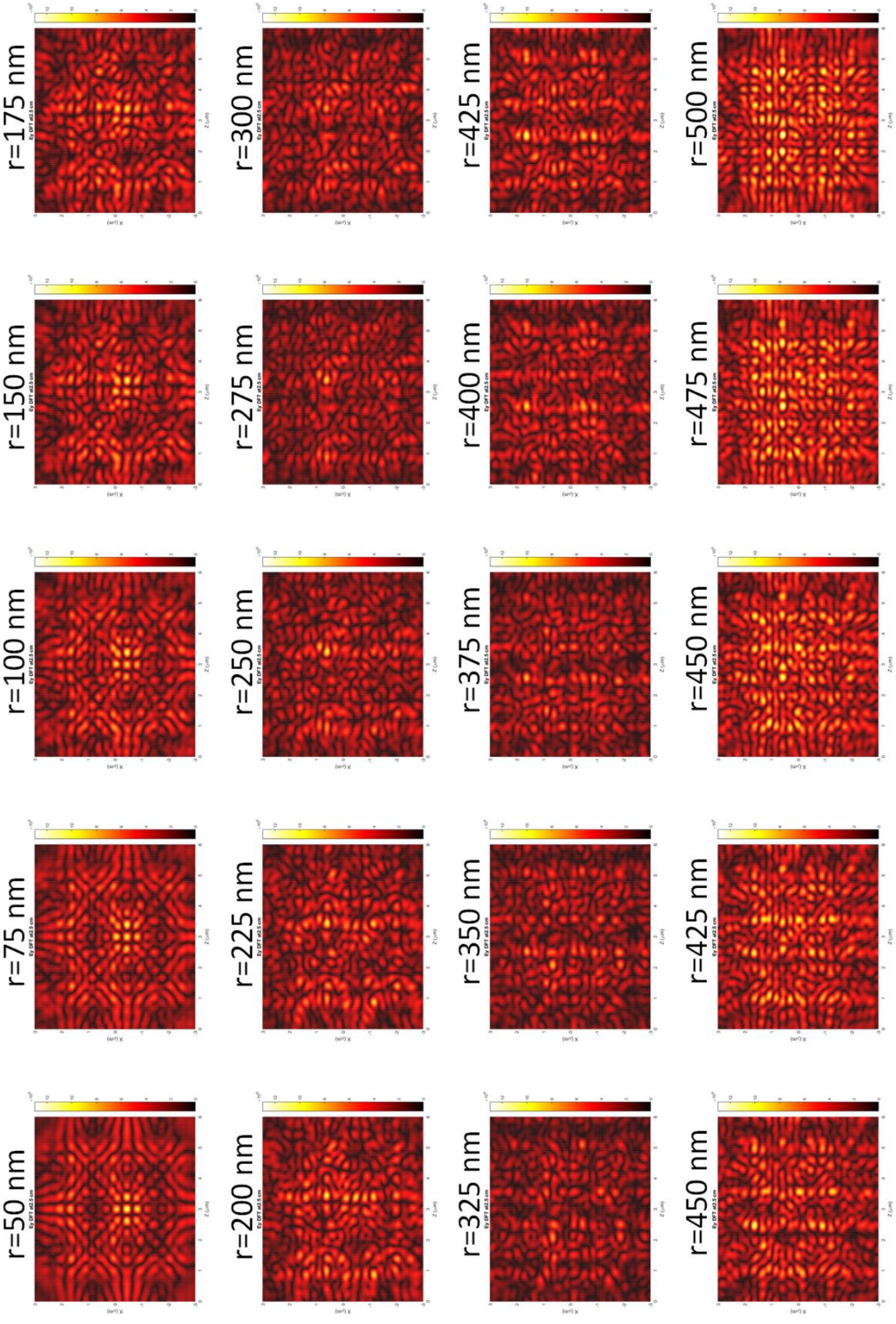

Figure 4.49 Far field electric field patterns (Ey) extracted from FDTD simulations of triangular lattice of hybrid pillars of radius ranging from 50 nm to 500 nm

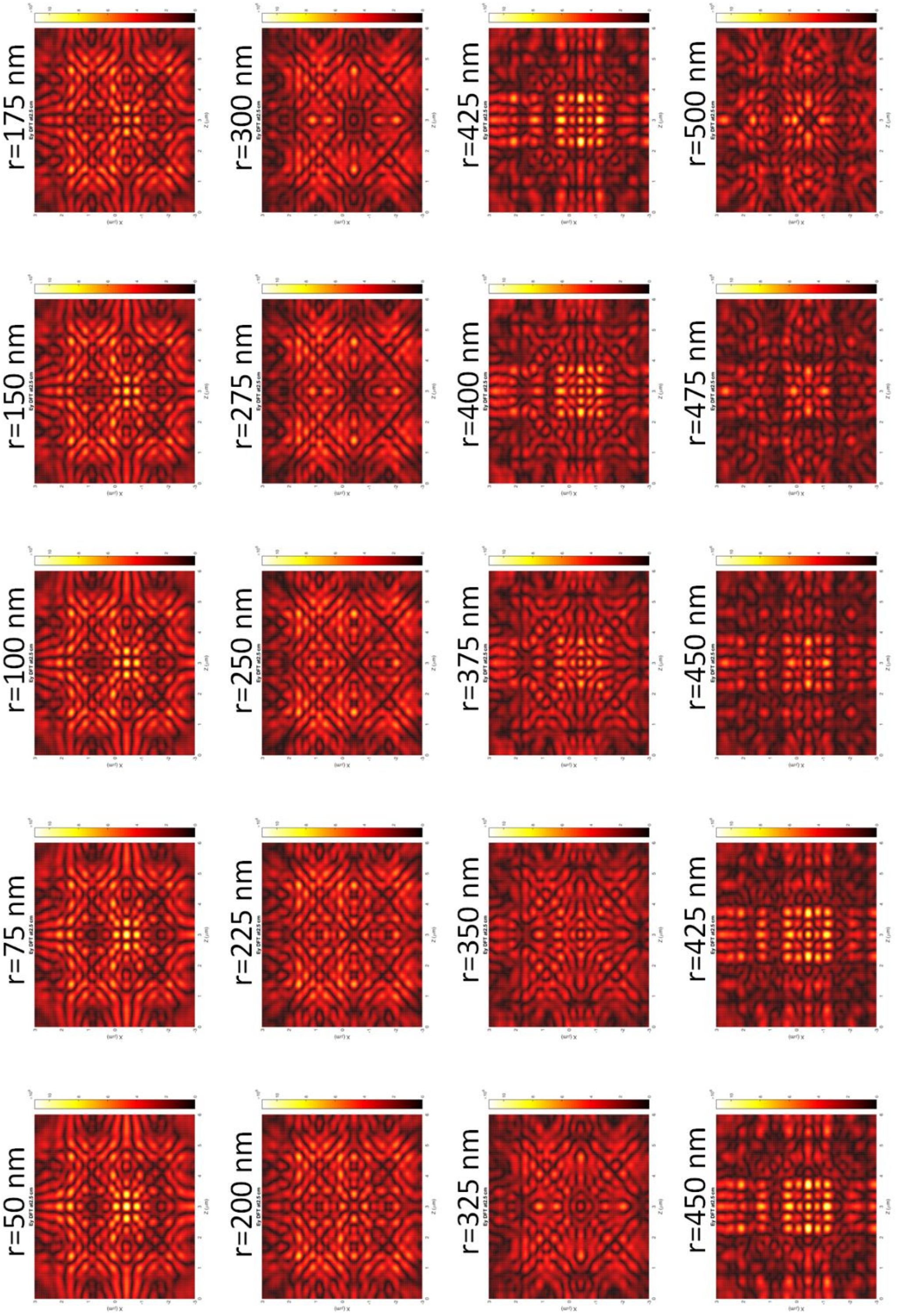

Figure 4.50 Far field electric field patterns (Ey) extracted from FDTD simulations of square lattice of holes of radius ranging from 50 nm to 500 nm

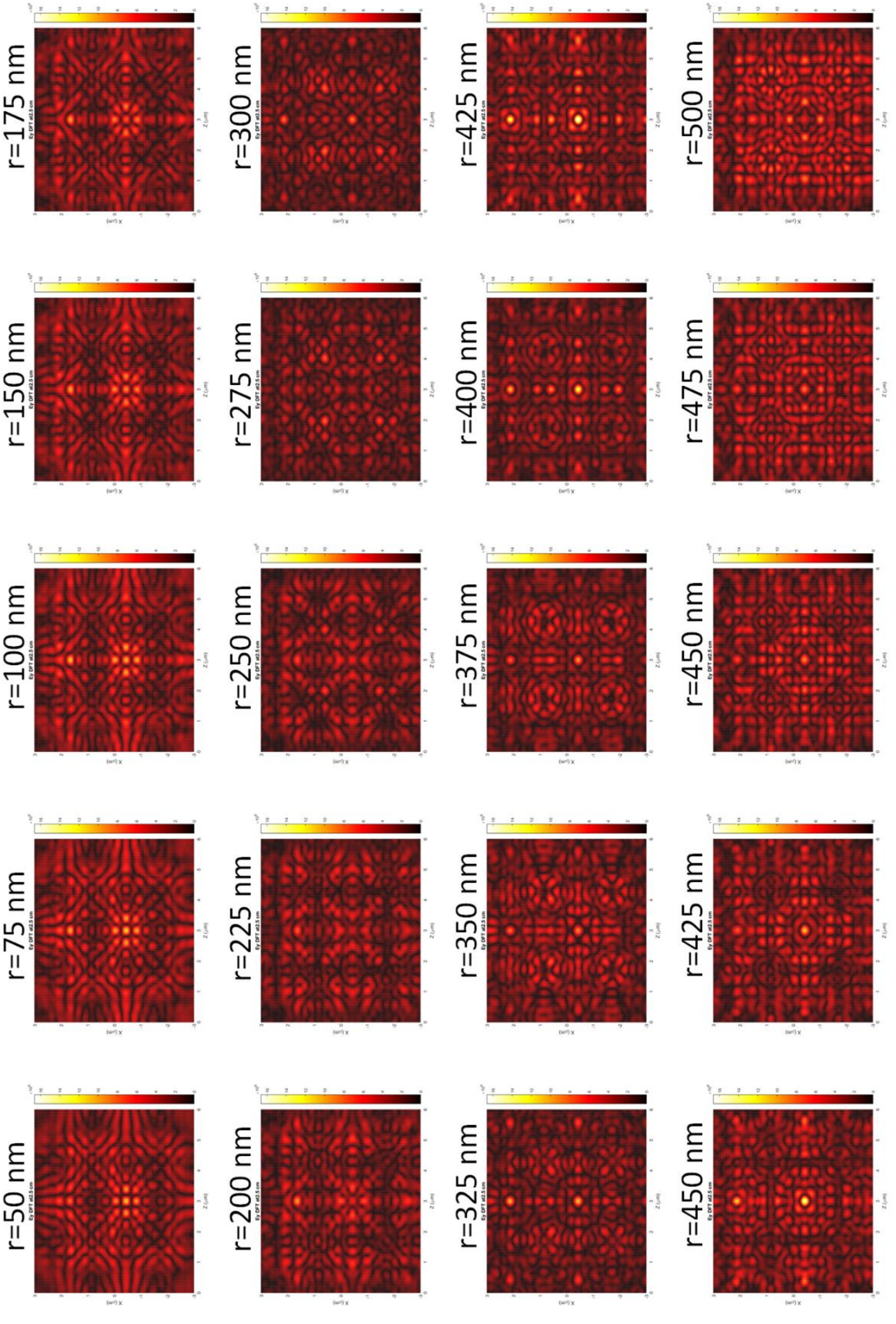

Figure 4.51 Far field electric field patterns (Ey) extracted from FDTD simulations of square lattice of hybrid pillars of radius ranging from 50 nm to 500 nm

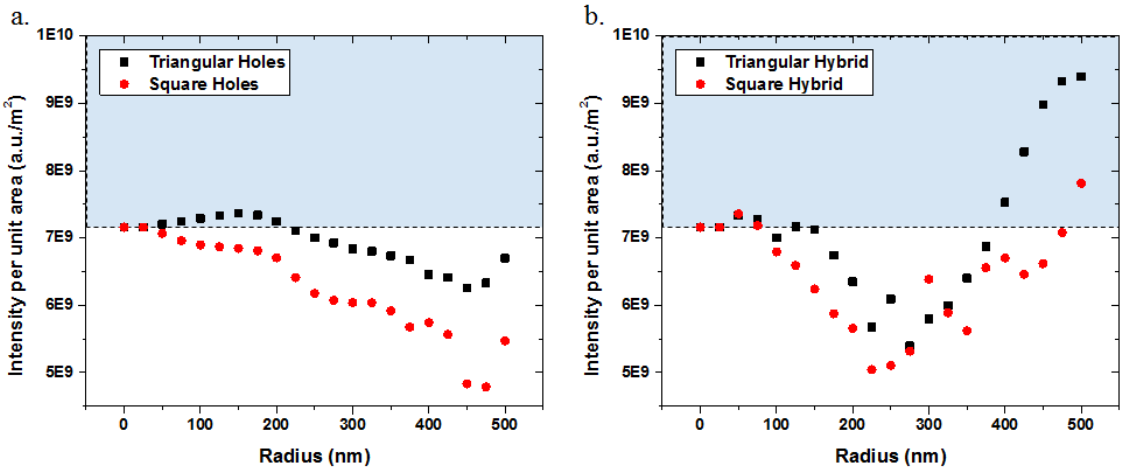

Figure 4.52 Far Field Intensity per unit area for triangular and square lattice of (a.) Holes, and (b.) Hybrid pillar patterns observed at 25 mm

From the results obtained through the various simulations performed, it can be observed that by adding a PhC pattern to the LED structure, there seems to be an improvement in the respective intensities when compared to the control structure. However, not every PhC structure that was simulated resulted in an improvement of the intensities as observed in the Figure 4.52. There were structures that actually reduce the intensity per unit area and this could be a result of the light being guided into the device layers and leaking through the cross-section of the device. By observing the trends in the intensity per unit area versus the radius of the feature, the triangular lattice of holes seem to have a steady improvement when the radius of the feature lies in between 50 nm and 200 nm. The triangular hybrid PhC structures seem to have an improvement in the intensities when radius of the feature is 75 nm and above 400 nm. On the other hand, square lattice structures do not produce a significant improvement as seen in the case of the triangular lattice.

Based on the current study, an optimal PhC structure for improving the light extraction in a blue InGaN/GaN based LED would have to be triangular lattice of hybrid pillars with radius greater than 350 nm with a pitch of 1 μm. The improvement observed with this configuration is close to and above 30%. Similarly, a PhC structure with holes in triangular lattice configuration with radius of the feature less than 200 nm yielded an improvement of less than 5%. However, this improvement can be further increased by implementing the PhC based light extraction along with other extraction methods. To understand the effects of other parameters like the lattice constant, simulation area etc. and further studies need to be conducted. Other simulation engines will need to be explored to incorporate the effects of both electrical and optical phenomena that happen within an LED.

5. Fabrication

This chapter is divided into sections that are focus on the fabrication techniques of LEDs, PhCs and PhC LEDs. These sections will talk about the integration of the two technologies without affecting the performance of the devices. Fabrication techniques targeting large-scale integration of PhCs into LEDs will also be discussed.

5.1. Fabrication Process for LED

5.1.1. Planar LEDs

The fabrication starts with the growth of layers that make up the LED active regions using MOVPE techniques [65], [66]. The LED structure is grown on a sapphire substrate (430µm thick) and is shown in the Figure 5.1 [66], [65]. InGaN/GaN -based quantum wells with a periodicity of 11.90 nm (QW ~ 4 nm, Barrier ~ 8 nm) were grown with 16% indium concentration ($In_{0.16}Ga_{0.84}N$) on n-type (Silicon doped) GaN and followed by p-type (Magnesium doped) GaN. The thicknesses of each layers of the structure are indicated in the Figure 5.1. The targeted emission wavelength of this LED structure is around 440 to 470 nm depending on the several factors including indium concentration, processing parameters, to name a few. For this project, LEDs were grown with above mentioned layers over sapphire substrates. The fabrication process for the LED mainly follows many steps of micro-fabrication techniques like photolithography, reactive ion etching, thin film deposition, annealing, etc.

The first step in the fabrication process right after growth is to degrease the surface of the LED by using solvents like Acetone and Methanol in an ultrasonicator. Then the LED sample goes through an annealing process at 800 ^{o}C for 5 minutes in Nitrogen ambient to mobilize the charge carriers and reduce the resistivity of the p-type GaN films [67]. After the initial annealing, there is a probability of formation of native oxide layers on the surface. In order to remove these native oxide layers, the sample is cleaned in a sequence of acidic baths like buffered oxide etchant (BOE) for 3 minutes, DI water rinse cycle for 2 minutes, diluted hydrochloric acid (1:1) for 1:30 minutes, and finally rinse in DI water for another 2 minutes. After the surface clean, the sample is then dehydrated in a box oven for about 20 minutes.

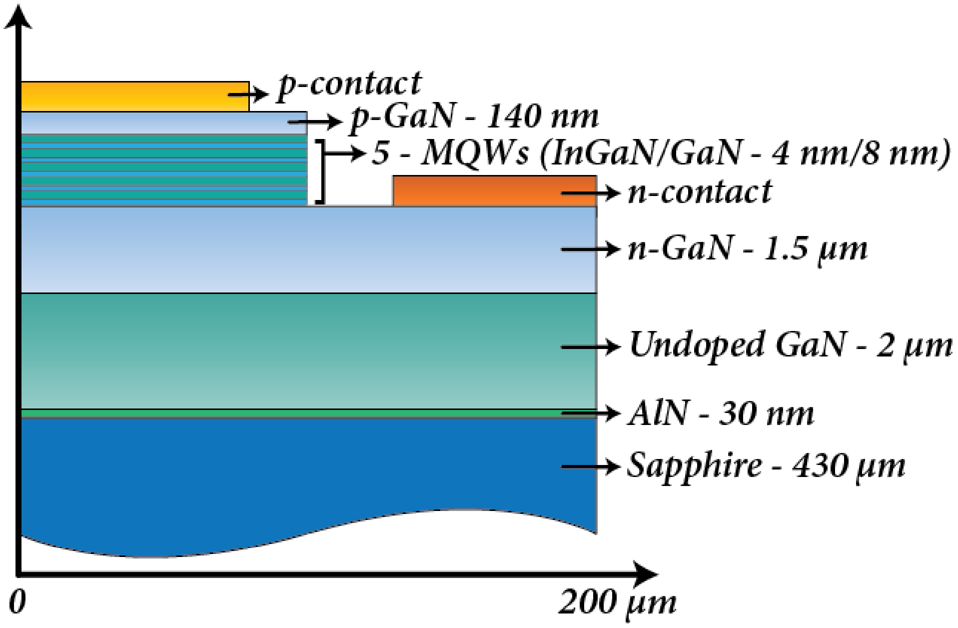

Figure 5.1 LED structure

The cleaned and dehydrated sample is spun with AZ 4400 photoresist at 4000 rpm for 30 seconds required for the mesa patterning and etch. Solvent evaporation is done by placing the sample on hot plate set at 95°C for 1 minute. Photolithography is done using a mask aligner to expose a pattern in the photoresist at 250 mJ/cm^2 energy. AZ 400K developer is diluted with DI water in a 1:3 ratio and developed the exposed resist for about 1:30 minutes. Since AZ 4400 is a positive photoresist, the exposed pattern should be an exact replica of the photomask. Figure 5.2 shows an illustration of the patterning process required for mesa pattern on the LED. The developed pattern is then hard baked at 120°C to convert the photoresist into the hard mask required for the next step, reactive ion etching.

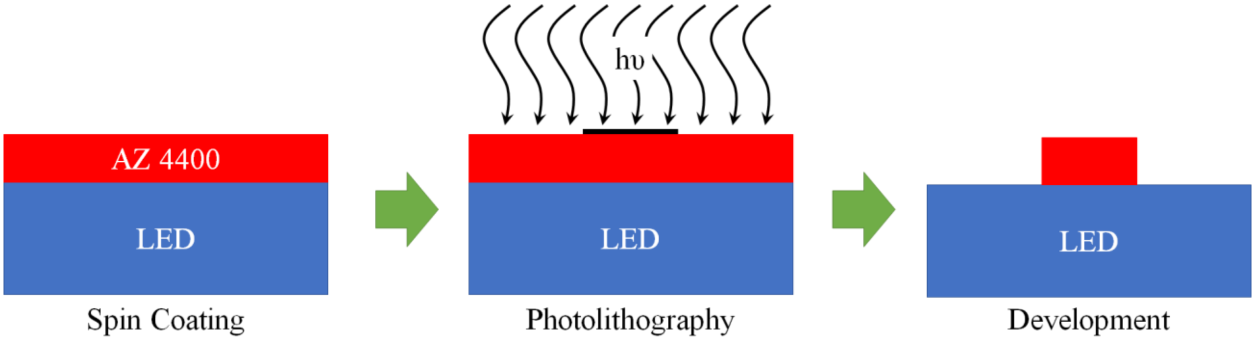

Figure 5.2 Mesa patterning step

The mesa structures in the photoresist are used as hard mask to etch sacrificially into the LED layers. Inductively coupled plasm reactive ion etching is the technique that is used to etch the III-V nitride materials. The etch chamber is flown with boron trichloride (BCl_3) and chlorine (Cl_2) at 10 and 20 sccm flow and a constant pressure of 10 mT is maintained. ICP and RIE powers are applied to the gas chamber to generate a plasma that facilitates etching of the materials. This step is performed for about 120 seconds to achieve an etch depth of ~500 nm. The photoresist on the sample is then stripped by cleaning the sample for 1 hour in AZ 300 T stripper solution set at a temperature of 100^{o}C. Figure 5.3 shows the illustration of the mesa etching and stripping process.

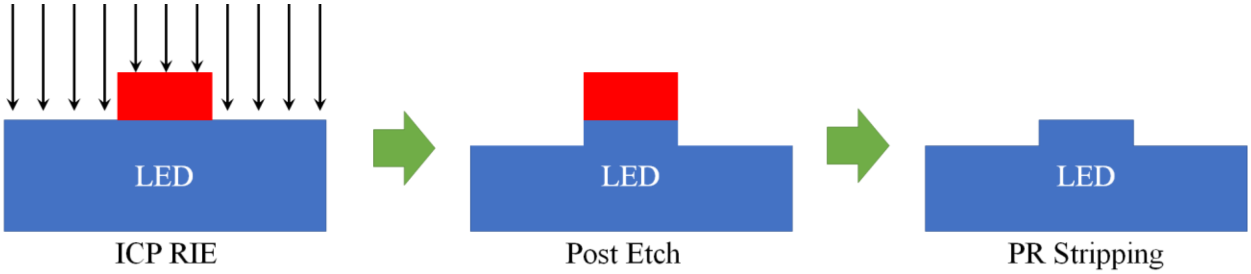

Figure 5.3 Mesa etch process and photoresist stripping

The sample is then degreased and dehydrated for further processing. AZ 5214 E-IR photoresist is spun on the etched sample at 4000 rpm for 30 seconds required for metal contact patterning. After spinning, solvent evaporation is done on a 95^{o}C hot plate for 1 minute. Photolithography is done on sample using a mask aligner at an exposure energy of 50 mJ/cm^2. The exposed sample is baked on a 120^{o}C hot plate for 2 minutes to enable crosslinking of the polymer. After post-exposure bake, the sample is exposed using a flood exposure at an exposure energy of 2000 mJ/cm^2. The second exposure step is used as the image reversal step. AZ 300 MIF developer is used for developing the exposed pattern for about 35 seconds. Figure 5.4 shows the illustration of the metal contact patterning.

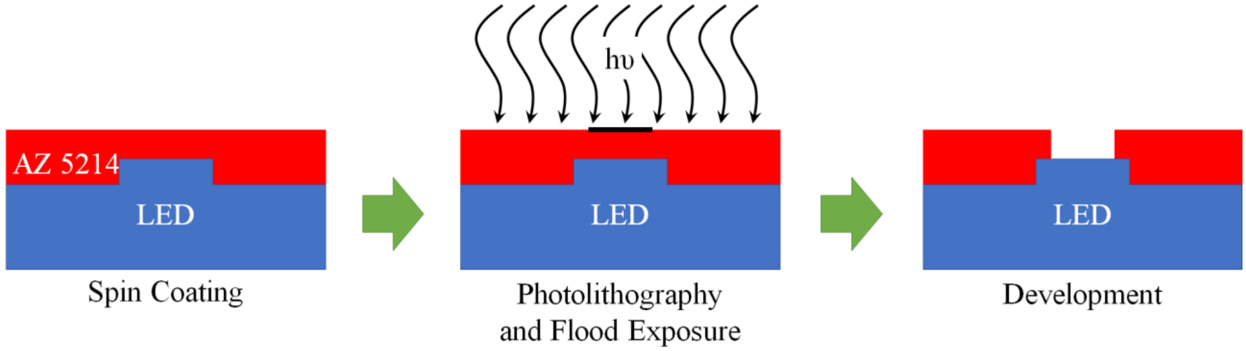

Figure 5.4 Photolithography process for metal contact patterning

The pattern now exposes the sample for metal contact deposition. Electron beam evaporation is used for evaporating the ohmic p-metal contact containing nickel and gold metals of thicknesses 30 and 150 nm respectively. The thicknesses of the metals were previously optimized to behave like an ohmic metal contact with p-type GaN material [68]. The sample with evaporated metal is left in an acetone bath to facilitate the lift-off procedure and expose the contact on the sample as shown in the Figure 5.5.

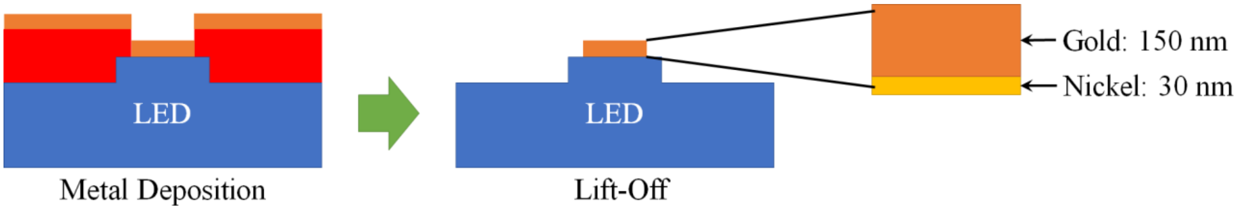

Figure 5.5 p-metal contact evaporation and lift-off process

The sample is once again degreased and dehydrated to remove any residues from the lift-off procedure. AZ 5214 E-IR is spun again on the sample for n-contact patterning at 4000 rpm for 30 seconds. Similar lithography parameters are used on the resist except the exposed region is now covering the n-contact region. N-contact metals containing layers of titanium (2 nm), aluminum (100 nm), titanium (30 nm) and gold (150 nm) are evaporated in an electron beam evaporator and lifted off using acetone. The lift-off process exposes the deposited n-contact on the LED as shown in the Figure 5.6.

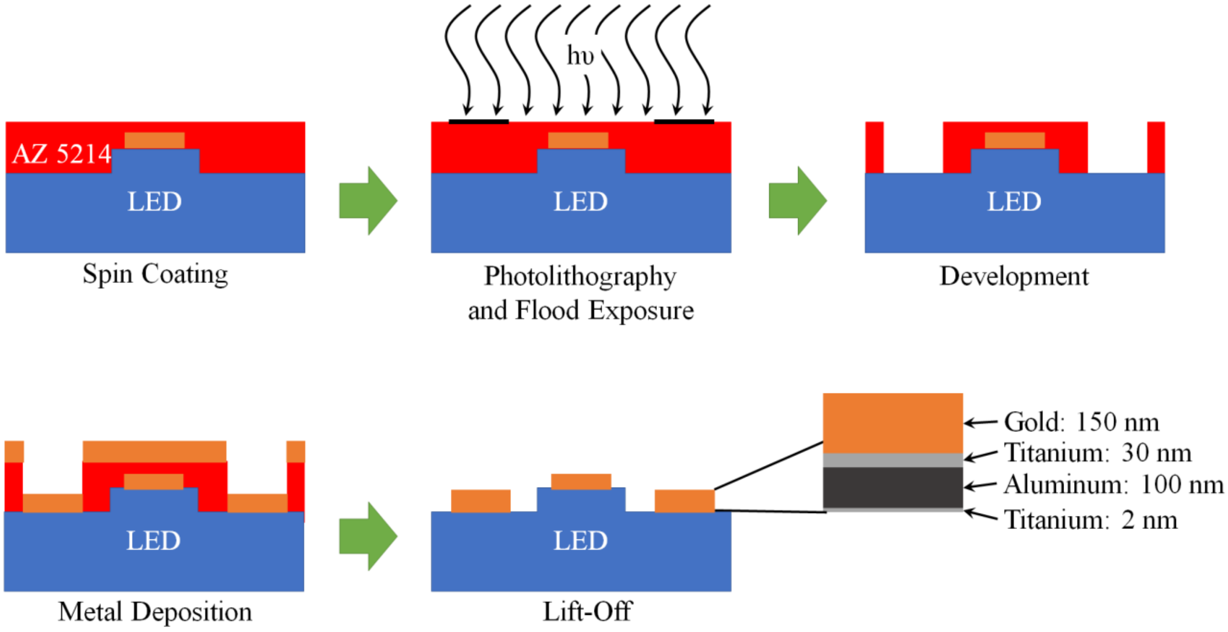

Figure 5.6 n-contact patterning and deposition

At this stage, the LED has both the p-type and n-type contacts deposited and ready for post annealing. The annealing process is done at 600°C for 3 minutes in air and is done to anneal the contacts. The LED is now considered operational, however, further processing steps like oxide isolation and bonding pad depositions can be done depending on the application. A 3D illustration of the final form of the LED and an optical image of several devices fabricated using the above mentioned process are shown in the Figure 5.7 (a&b).

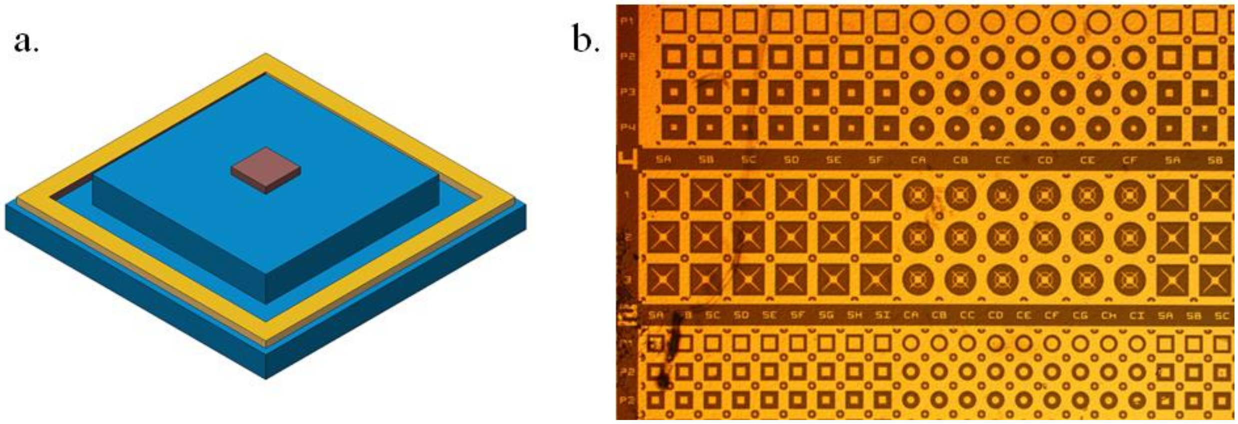

Figure 5.7 (a.) A 3D illustration of the fabricated LED (b.) Optical image showing various LEDs fabricated on a substrate

As described in this section, it takes at least 7 steps of microfabrication techniques to envision a working LED from a substrate with active layers. In the next section, the fabrication and characterization of indium tin oxide (ITO) thin films for ITO LEDs.

5.1.2. ITO thin film deposition

ITO thin film as previously known, are used as transparent contacts on LEDs both to improve optical and electrical characteristics of the devices. There are several ways to realize thin films of ITO like electron beam evaporation, RF sputtering, pulsed laser deposition, and bottom-up methods [69], [70], [71]. ITO is also known for its high transmission in the visible spectrum [71]. We have chosen to use electron beam evaporation for depositing the thin films of ITO for LEDs. Electron beam evaporation is a process of evaporating metals and dielectrics using a high energy electron beam to heat and evaporate material gradually. The main components of an electron beam evaporator are shown in the Figure 5.8. A tungsten filament is applied with a high voltage (10 kV) and by flow of current through it start ejecting electrons. Strong magnetic fields are used to confine and focus the beam on to the material. The material is placed in a crucible (graphite) and the electron beam is used to evaporate or sublimate the material on the substrate. The entire deposition process is done in a chamber that is maintained at a very low pressure in the order of 10^{-5} Torr. Since ITO has oxygen bonds that eventually break up during the sublimation process, the chamber needs to be replenished with oxygen ions. This is facilitated by an ion beam generator which creates a sea of oxygen ions that are in the path of the evaporating material. This method is called ion beam assisted deposition (IBAD) and ensures that a uniform deposition of the material. A plasma of ions is generated with the use of the ion beam and a neutralizer filament is used to neutralize the negative charge developed due to the plasma.

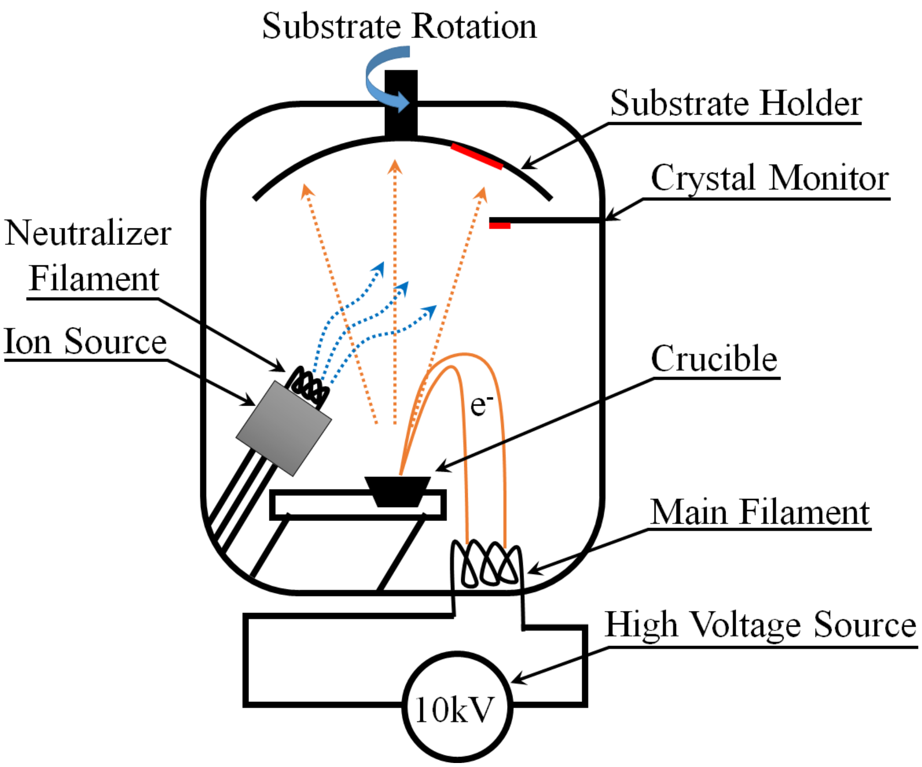

Figure 5.8 Electron beam evaporator components

Other factors influencing the deposition of the thin films are the deposition rate, temperature of the chamber, and the tooling factor. The deposition rate is a parameter that is controlled by a deposition controller and a piezo electric crystal monitor provides the feedback of the film thickness that is deposited. As the crystal monitor provides just an approximation of the film thickness based on the density of the material of interest, a parameter called tooling factor is used to compensate the error between the measured thickness (T_m) and crystal monitor thickness (T_x) and they are related to the initial tooling factor ($TF_{initial}$) as shown in the Equation 5.1. The tooling factor is one such processing parameter that needs several iterations of the deposition so the final deposited thickness is consistent with the crystal monitor thickness.

$$TF_{new} = TF_{initial} \times \frac{T_m}{T_x} \qquad (5.1)$$

It is found that the deposition rate and tooling factor are dependent on the temperature of the chamber and so in order to maintain uniformity, the chamber temperature is set at 200°C using heater bulbs inside the chamber. With all the conditions set, the ITO thin films can be produced consistently for use in LEDs.

5.1.3. Critical Characteristics of ITO

Incorporating the ITO films as contacts into LED structures require both optimal electrical and optical characteristics. It is very well known that there is a tradeoff between the two properties and the ideal option would be to obtain best of the two properties. To find the optimal thickness, a Matlab based simulation was performed to find the total transmission of a stack of dielectric slabs. Figure 5.9 shows the simulation setup of the dielectric stack with refractive indices n1, n2, and n3. In the current scenario of the blue LEDs, the three layers are air, ITO and GaN respectively and the material of interest is the ITO layer. Equations 5.2, 5.3, show the reflectivity at each interfaces of the dielectrics. Equation 5.4 is a constant and 5.5 show the calculations behind the total reflectivity observed from the stacked dielectric slabs. After calculating the reflectivity due to the ITO layer, the transmittance is calculated by performing ***t=1-r***

$$r_{12} = \frac{n_1 - n_2}{n_1 + n_2} \tag{5.2}$$

$$r_{23} = \frac{n_2 - n_3}{n_2 + n_3} \tag{5.3}$$

$$\beta = \frac{2\pi n_2 t}{\lambda} \tag{5.4}$$

$$r_{tot} = \frac{r_{12}^2 + r_{23}^2 + 2r_{12}r_{23}\cos(2\beta)}{1 + r_{12}^2 + r_{23}^2 + 2r_{12}r_{23}\cos(2\beta)} \tag{5.5}$$

(5.6)

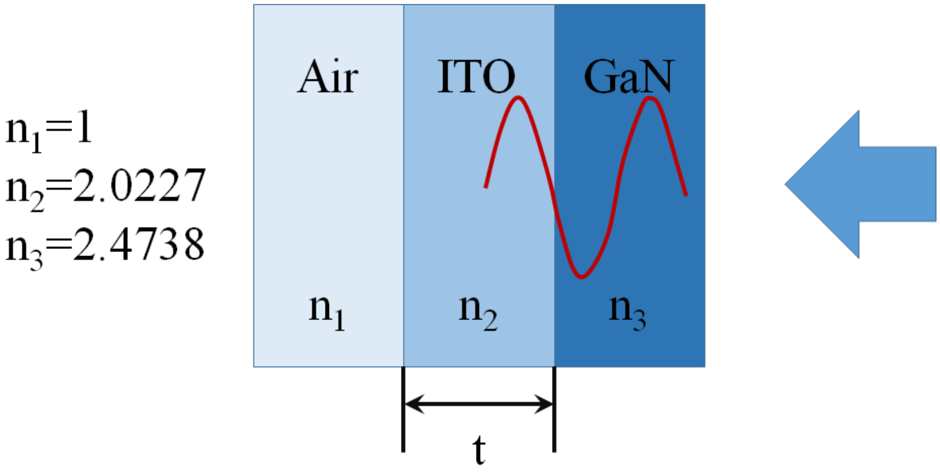

Figure 5.9 Dielectric stack simulations for maximum transmission.

Simulations were done to yield the optimal thickness of the ITO film that has the maximum transmittance. These simulations were done for different emission wavelengths ranging from 440 to 470 nm to find the optimal thicknesses for different emission wavelengths. Figure 5.10 shows the simulation result showing the transmittance at various thicknesses for the emission wavelength of 445 nm. It is found from the simulations that the ITO layer has a maximum transmittance of 93% for thicknesses in the 55, 165, and 275 nm. Figures 5.11 shows the transmittance percentage plotted against the emission wavelength for the ITO layer thickness of 165 nm. It is clear that on an average the transmittance across all wavelengths is above 93% and so the optimal thickness for maximum transmittance can be deduced as 165 nm or in the range of 160-170 nm.

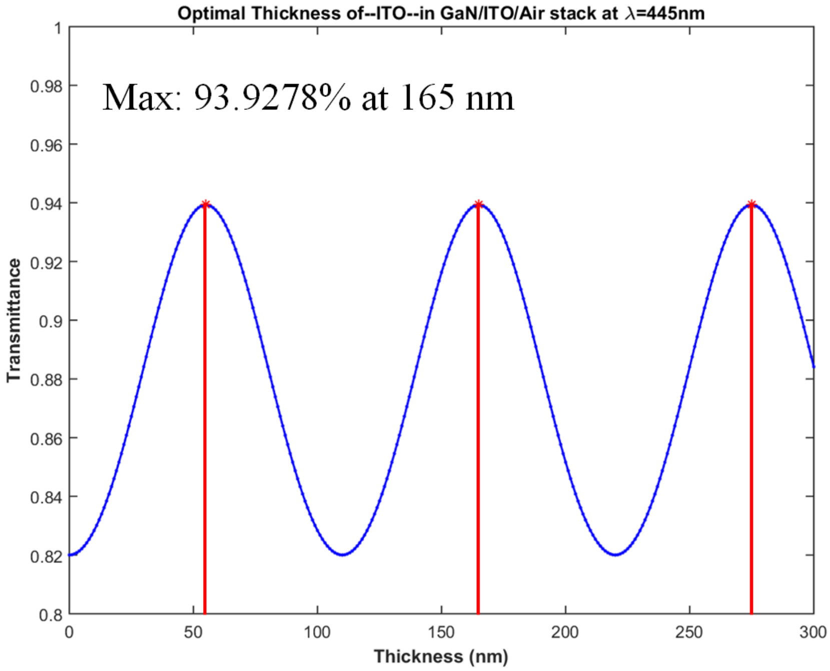

Figure 5.10 Matlab simulation result for finding the optimal thickness for maximum transmittance from ITO at λ=445 nm

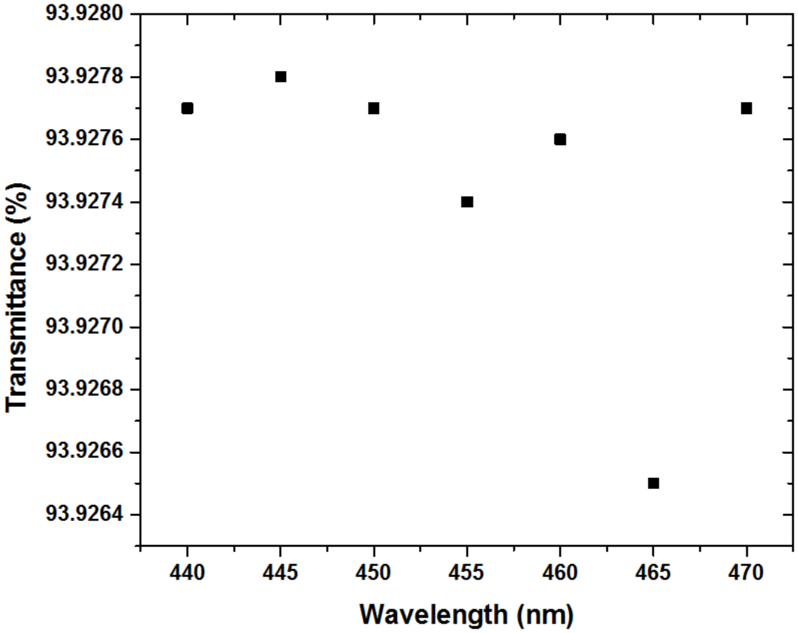

Figure 5.11 Transmittance versus the emission wavelength for ITO layer thickness of 165 nm

After finding the optimal thickness for maximum transmittance, ITO thin films were deposited targeting 165 nm using electron beam evaporator. The initial tooling factor was set at 50 and several iterations of depositions were done to optimize the tooling factor. The final tooling factor obtained from the several depositions and optimization is around 75. Using this optimized tooling factor, ITO thin films were deposited with ±5 nm tolerance.

Once the optimal thickness for maximum transmittance is found, ITO thin films were deposited on glass substrates to find the transmittance in practice. These films were annealed at different temperatures to study how the transmittance is affected by the temperature. Figure 5.12 shows the transmittance observed over visible range of wavelengths and different annealing temperatures. Figure 5.13 shows the transmittance plotted with respect to the wavelengths in the blue spectrum (440-470 nm).

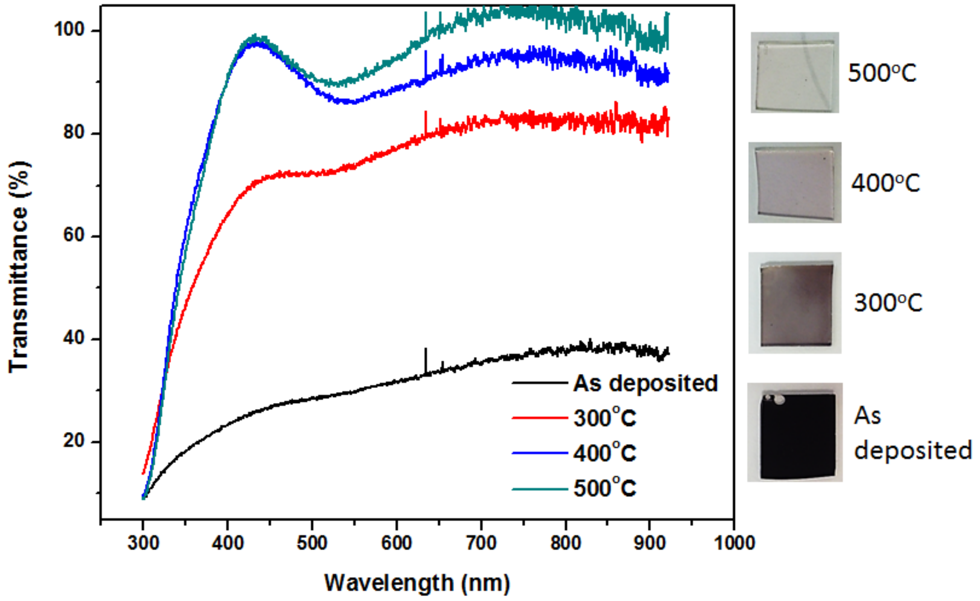

Figure 5.12 Transmittance of ITO thin films versus plotted against wavelength annealed at different temperatures

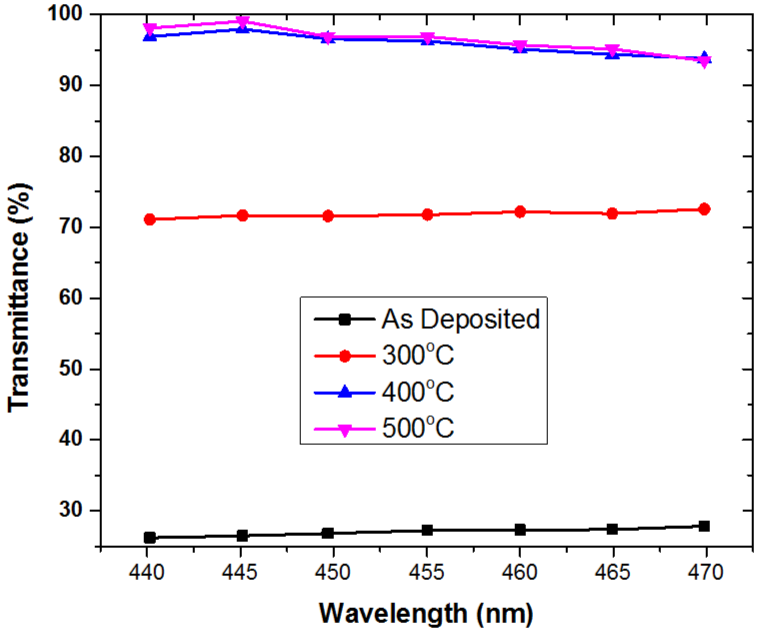

Figure 5.13 ITO transmittance plotted against the blue spectrum for different annealing temperatures

The plot shows that for the thin films that were not annealed, the transmittance is significantly low and cannot be used in an LED. Annealing process has enabled the transmittance of the thin film to increase significantly. It is observed that the transmittance of films annealed above 400°C were similar showing less deviation. It is also seen that the transmittance percentages exceeded the simulation predictions and were found to be >98% transparent in the blue spectrum. Hence, the ITO thin film for maximum transmittance is found to be a 165 nm film annealed at temperatures 400°C or above.

The next step is to study the electrical characteristics of this thin film that is optimized for > 98% transmittance. For this, transmission line method (TLM) and Hall Effect measurements were done to find the specific contact resistivity and resistivity of the thin film. ITO thin films (165 nm) were deposited on undoped GaN substrates and annealed at different temperatures (300-600°C) for Hall effect measurements. Figure 5.14 summarizes the Hall Effect results and shows that a lowest film resistivity (~9E-4) was observed from the thin film annealed at 600°C.

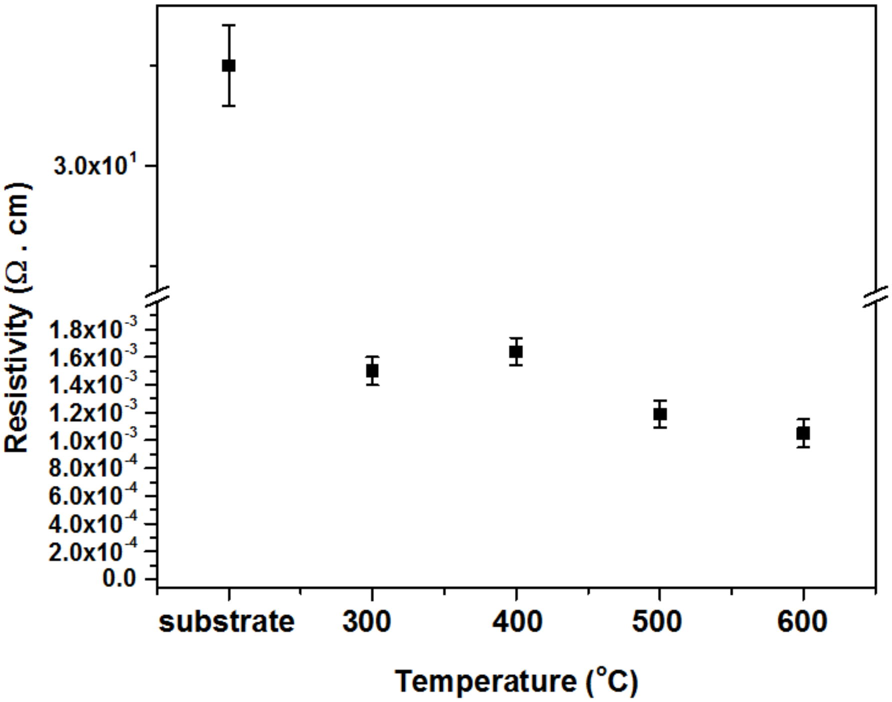

Figure 5.14 Hall Effect measurements for resistivity of the ITO thin films

The Hall Effect results for the ITO thin film annealed at 600°C are summarized in the Table 5.1.

Table 5.1 Summary of Hall Effect Measurements for ITO thin film (~165nm) annealed at 600°C

Carriers	Electrons (n-type)
Mobility (μ_n)	19.2 cm^2/Vs
Resistivity (ρ)	9E-4 Ω cm
Concentration (n)	-3.1E20 cm^{-3}

To find the specific contact resistivity, ITO thin films were deposited on p-type GaN substrates with a pattern as shown in the Figure 5.15 (a). Current-voltage (IV) characteristics were extracted from each pair of contacts and the respective slopes give the resistance of the film observed as a contact to the substrate. These resistances are plotted against the distance between the contacts and fitted as a linear curve to find the X (L_T) and Y (R_c) intercepts. Using the equation 5.6, the specific contact resistivity is calculated. Figure 5.16 shows the contact resistivity as a function of annealing temperatures. The plot shows that the lowest contact resistivity of 9.57E-4 Ωcm^2 was observed with the ITO thin film annealed at 600°C.

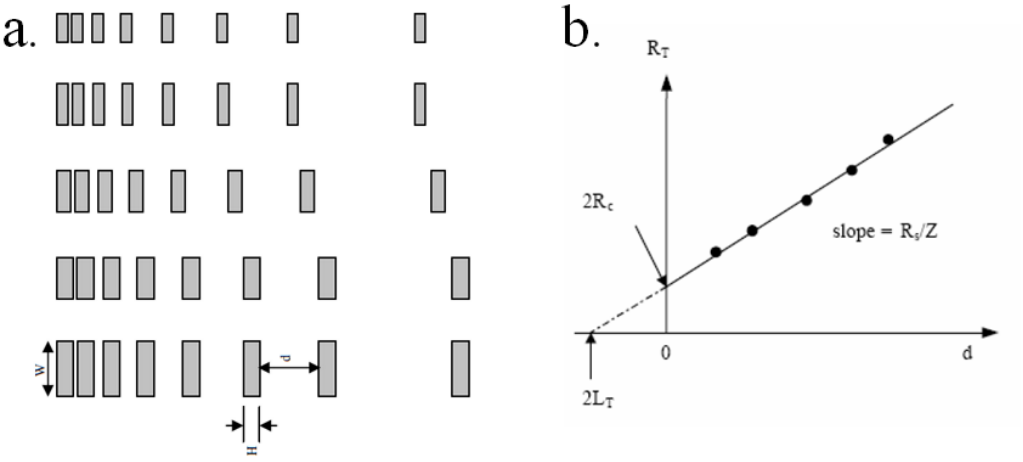

Figure 5.15 (a.) Photolithography pattern used for TLM (b.) Resistance vs. distance between contacts

$$\rho_c = L_T \times R_c \times W \ (\Omega . cm^2) \qquad (5.7)$$

As a result of these series of experiments performed to obtain optical and electrical characteristics of ITO, a 165 nm thin film annealed at 600°C is found to have the optimal characteristics. A summary of the electrical and optical characteristics is shown in the Table 5.2.

Table 5.2 Ideal characteristics of ITO thin film required for an LED

Thickness	Annealing Temperature	Transmittance	Resistivity	Mobility	Contact Resistivity
165 nm	600°C	98%	9E-4 Ωcm^2	19.2 cm^2/Vs	9.57E-4 Ωcm^2

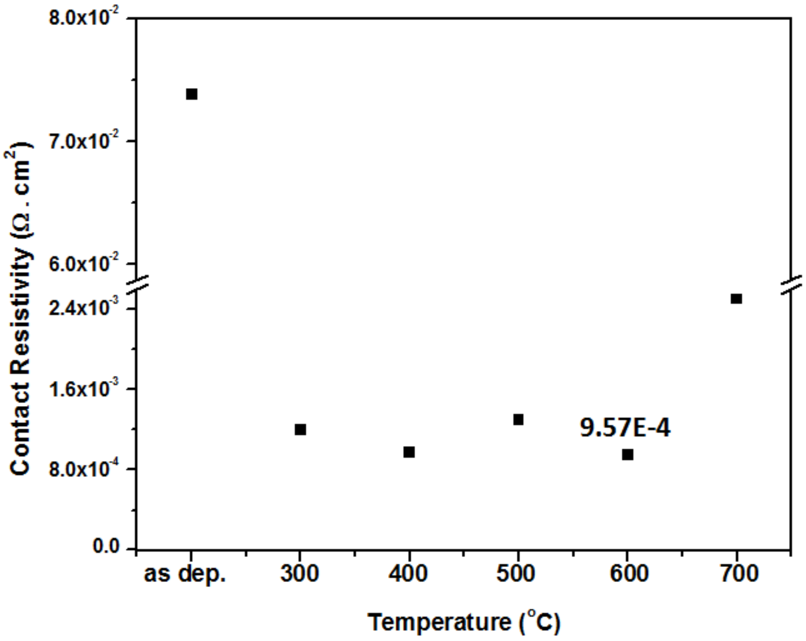

Figure 5.16 Specific contact resistivity of ITO thin film annealed at different temperatures

5.1.4. ITO LEDs

As deduced earlier, ITO layer is an n-type material with electrons as majority carriers. Figure 5.17 shows the process of adding ITO to the LED fabrication process. The ITO layer replaces the p-metal contact step in the LED fabrication process. However, to interface with the ITO layer, an ohmic contact designed for an n-type material is required. It was established earlier that the metal stack containing titanium, aluminum, titanium and gold forms a good ohmic contact with the n-type GaN layer. In this case, as ITO is an n-type material, similar metal stack can be used as an ohmic contact. Annealing temperatures need not be changed as it was found that ITO film produced at 600°C to have the best characteristics. A 3D illustration and optical image of ITO LEDs are shown in the Figure 5.18.

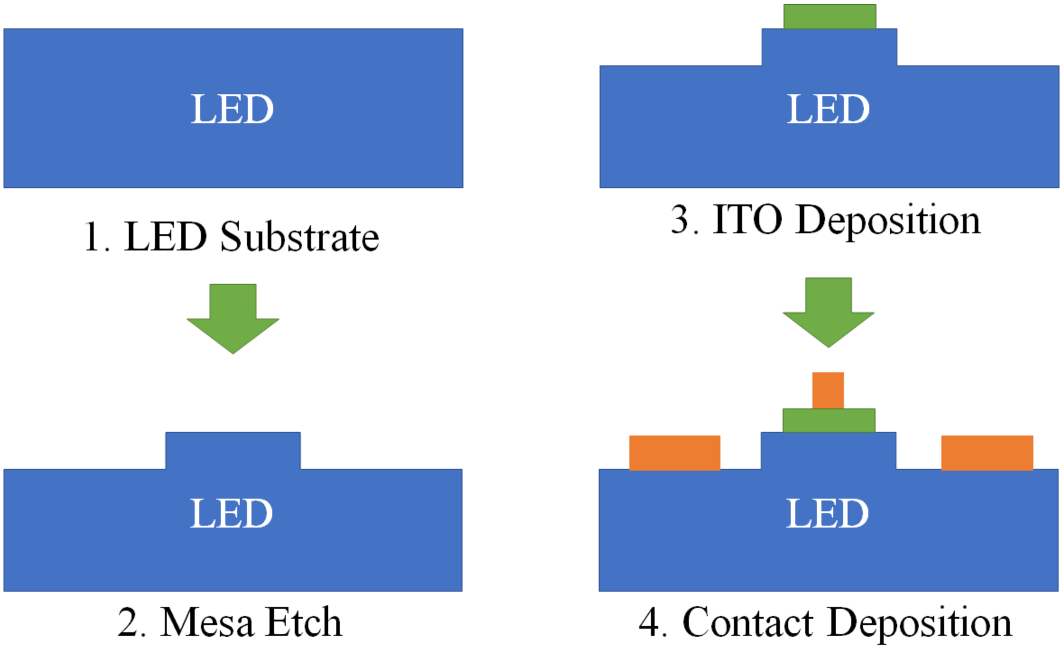

Figure 5.17 Simple process flow showing the ITO LED fabrication process

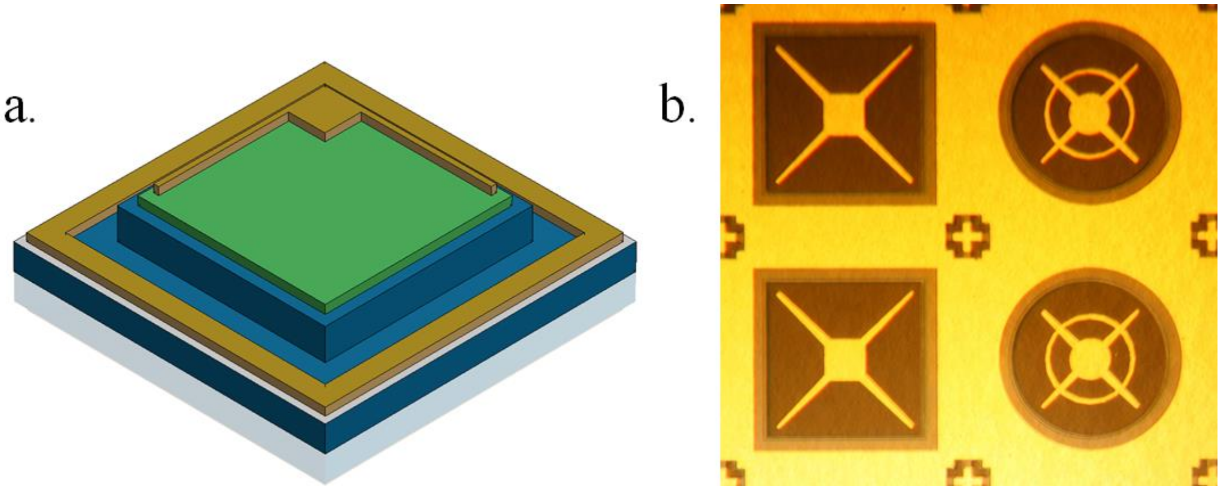

Figure 5.18 (a.) 3D illustration of an ITO LED, (b.) Optical image of ITO LEDs

Initial attempts of adding ITO layer to the LED structure has resulted in peeling off of ITO thin film from the GaN surface and as a result yielded in poor electrical characteristics. To address this, a thin layer of metal needs to be added to improve the adhesion of the ITO films on to the GaN surface. Dr. Hornak's group has done research in this area in regards to transparent contacts and found a 2-5 nm thick layer of Nickel metal improves the adhesion and also acts as a tunneling contact between the semiconductors [72]. Figure 5.19 shows the SEM image of the section of the

ITO layer that peeled off of the substrate. 3 nm of nickel layer was chosen for improving the adhesion of the ITO layer onto the GaN surfaces.

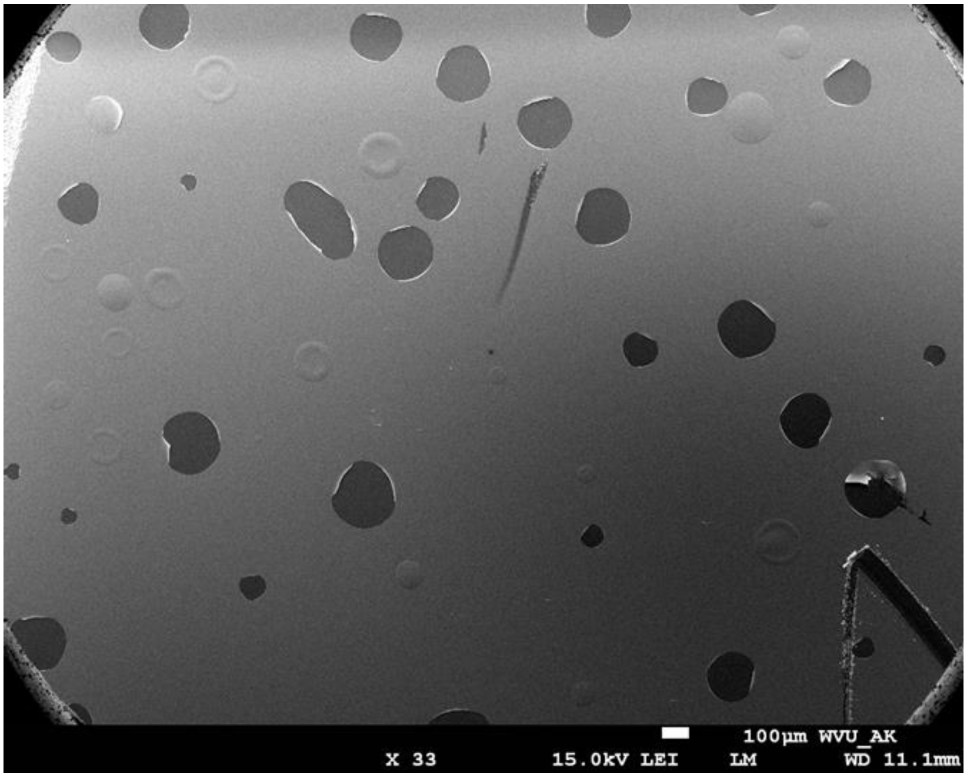

Figure 5.19 SEM micrograph showing the peeling of the ITO layer on the LED

5.2. Fabrication Methods of PhCs

The goal of this research is to develop and efficiently integrate PhCs into LEDs that help in light extraction and improve the overall efficiency. Various research groups have worked previously in this area and have interesting outcomes. This section concentrates on fabrication of PhCs using typical and novel methods for integrating into the devices.

5.2.1. Electron Beam Lithography

Typically PhCs designed for wavelengths in the visible spectrum have feature sizes are considered sub-micron features. Traditionally photolithography has the resolution as low as 1 μm and depending on the wavelength of the light source used, the resolution can be reduced. Therefore, photolithography processes can no longer be used due to the diffraction limit of light at these sub-micron scales. In order to achieve these sub-micron features, electron beam lithography technique (EBL) is used instead. In this section, the process to fabricate PhC structures and then later discuss the issues and limitations of using traditional resists and EBL.

Electron beam lithography (EBL), as the name suggests uses high energy electrons to expose an electron beam resist, commonly referred as ebeam resist. As it is known, waves associated with electrons have wavelength in the range of angstroms, which drastically reduces the resolution of the lithography [73]. The electron beam is focused down to a spot size of ~ 20 nm using electrostatic and magnetic lenses inside the scanning electron microscope (SEM). The main components of an EBL/SEM column are demonstrated in the Figure 5.20 [74], [75].

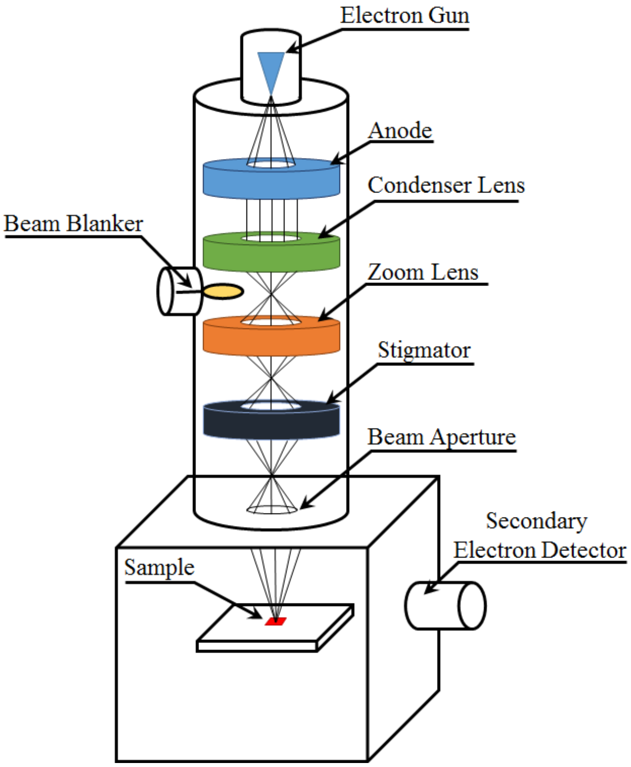

Figure 5.20 Main components inside the EBL/SEM column

The electrons are generated from an electron gun that is set at a high accelerating voltage (usually 10-100 kV) to provide enough kinetic energy to the electrons. The main purpose of the electrostatic and magnetic components is to converge and condense the emitted electron beam from the cathode. All these electro optical components are used to align the electron beam to be focused on the plane of the sample. A beam blanker is used in the column to turn the beam ON/OFF while exposing.

EBL is one such technique that enables direct patterning of the electron beam resist. A CAD software is used to design the patterns of the PhC structures. Nanometer Pattern Generation System (NPGS) is used to control the beam and beam blanker to expose the designed PhC structure. Once the EBL/SEM is aligned, the sample spun with an ebeam resist is loaded in and NPGS software takes over the control and exposes the pattern. Figure 5.21 shows a screenshot of the CAD environment with PhC pattern.

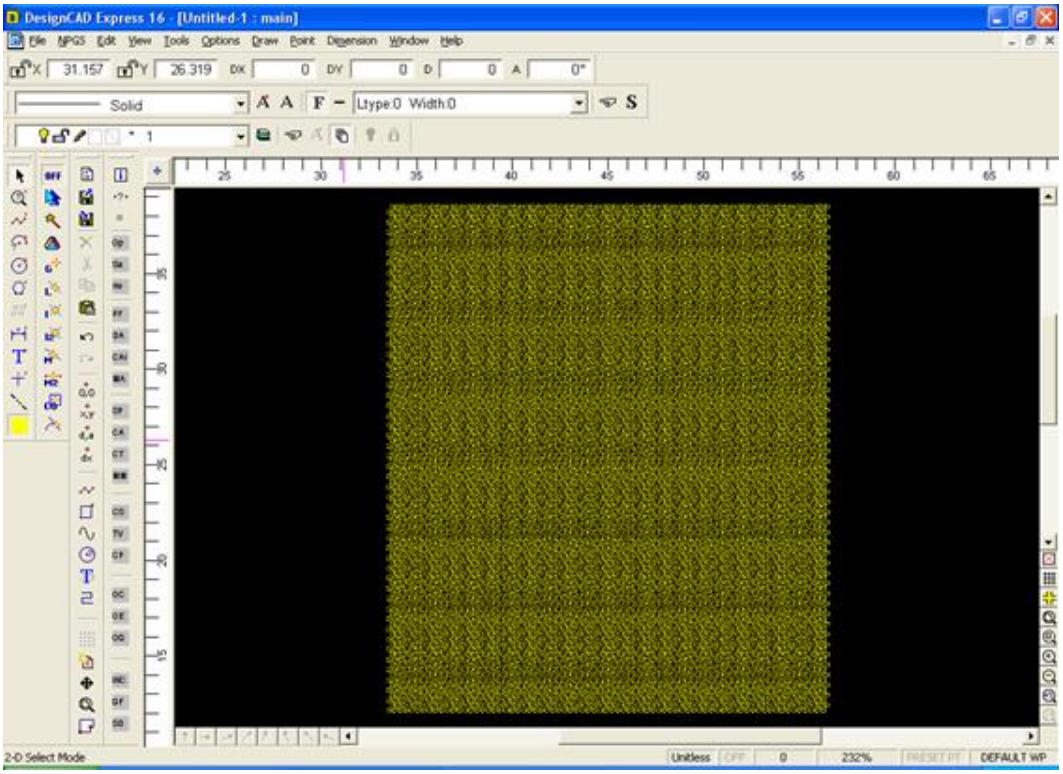

Figure 5.21 CAD software screenshot with a PhC pattern

Just like photoresists, there are two types of ebeam resists (positive and negative tone) and are categorized based on the final pattern yielded upon exposure and development. 950 PMMA A3 (Polymethyl methacrylate) and maN-2403 are positive and negative tone ebeam resists that are used in this section for fabricating PhC structures. PhC patterns for the LED light extraction are fabricated using both the resists and the respective process development and parameters are discussed in this section.

5.2.2. PhC Fabrication using PMMA (Positive Resist)

The following process is for a positive tone resist like 950 PMMA A3. First, a sample is prepared by degreasing the surface in acetone and methanol solvents (5 minutes each) in an ultrasonicator. Once the sample is degreased, the sample is rinsed in DI water, blown dry with nitrogen and baked in an oven for dehydration at 120^{o}C for 20 minutes. The sample is then spun with 950 PMMA A3 at 5000 rpm for 50 seconds followed by a solvent evaporation bake at 180^{o}C for 3 minutes. The sample is then exposed using EBL technique at an acceleration voltage of 30 kV. The optimal exposure dosages for PMMA range from 280 μC/cm^2 to 350 μC/cm^2. After exposure, the sample is developed in a MIBK:IPA (1:3) for 70 seconds followed by rinsing in DI water to stop the development process. The development procedure dissolves the exposed area of the ebeam resist and leaves with holes in the ebeam resist. Figure 5.22 shows the process flow for patterning PMMA.

Following the EBL exposure, the PhC pattern needs to be transferred into the substrate material and this is facilitated by means of micro-fabrication techniques. Use of metal deposition and reactive etching techniques, the pattern is transferred into the substrate material. The sample is deposited with a thin layer of nickel using electron beam evaporation and lifted off using acetone. The sample now contains a pattern of pillars of nickel which can be used as hard mask for etching into the substrate. Finally, the residual nickel is removed using nickel etchant to reveal PhC crystal structures containing pillars. This process flow is shown in the Figure 5.23 is a continuation of the process shown in Figure 5.22 and as this process results in pillars, a sacrificial layer has to be used to fabricate PhC structures containing holes.

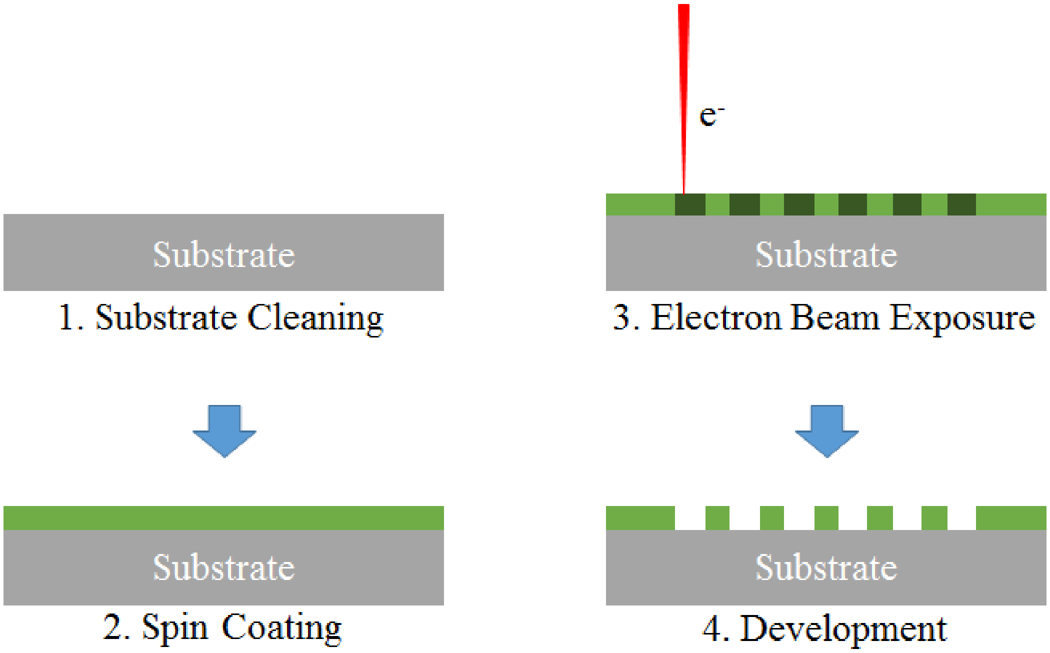

Figure 5.22 Fabrication process flow for 950 PMMA A3 using EBL

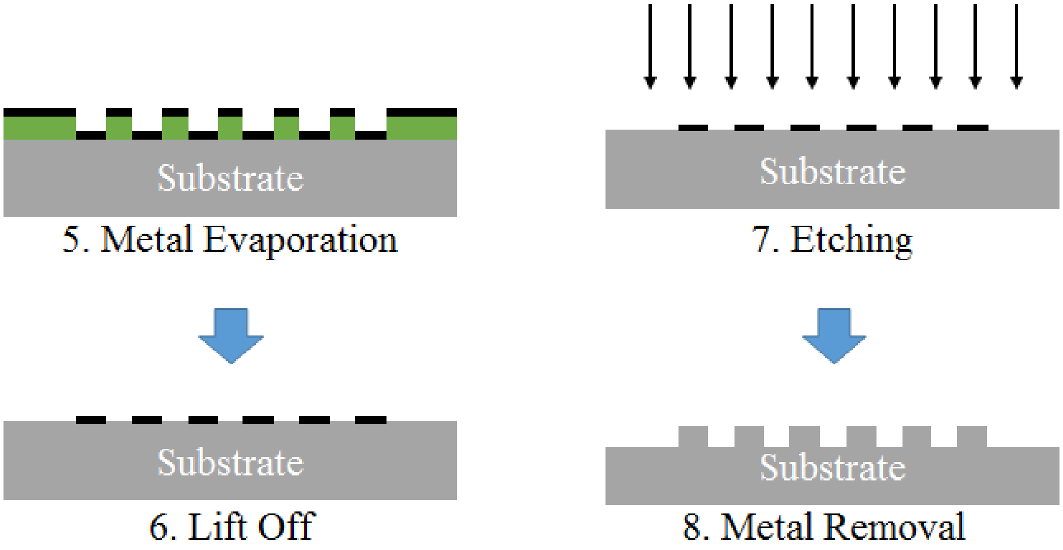

Figure 5.23 Continuation of fabrication process for transferring pattern into the substrate

Figure 5.24 shows a 3D illustration of PhC pillars in the substrate and an SEM micrograph of a PhC pattern of pillars fabricated using the above mentioned process.

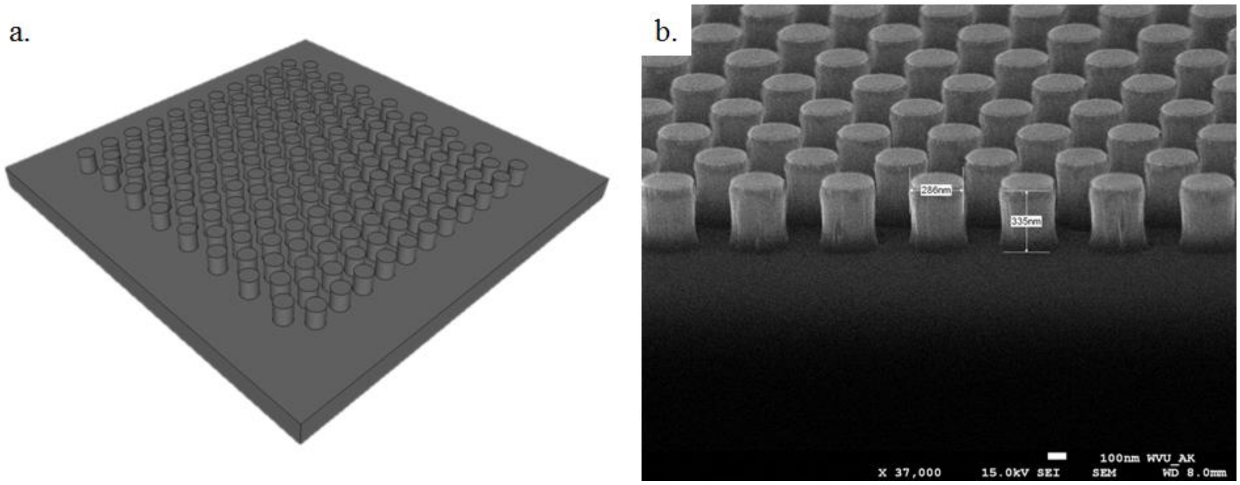

Figure 5.24 (a.)3D illustration of PhC pillars, (b.) SEM micrograph of PhC pillars fabricated in silicon

5.2.3. PhC Fabrication using maN (Negative Resist)

The following process is for a negative tone resist like maN-2403.The sample is prepared by degreasing the surface in acetone and methanol solvents (5 minutes each) in an ultrasonicator. Once the sample is degreased, the sample is rinsed in DI water, blown dry with nitrogen and baked in an oven for dehydration at 120°C for 20 minutes. The sample is then spun with maN-2403 at 5000 rpm for 50 seconds followed by a solvent evaporation bake at 95°C for 1 minute. The sample is then exposed using EBL technique at an acceleration voltage of 30 kV. The optimal exposure dosages for maN range from 75 μC/cm^2 to 85 μC/cm^2. After exposure, the sample is developed in a maD-525 for 70 seconds followed by rinsing in DI water to stop the development process. The development procedure dissolves the ebeam resist except the exposed area of the ebeam resist and leaves with pillars in the ebeam resist. Figure 5.25 shows the process flow for patterning maN-2403.

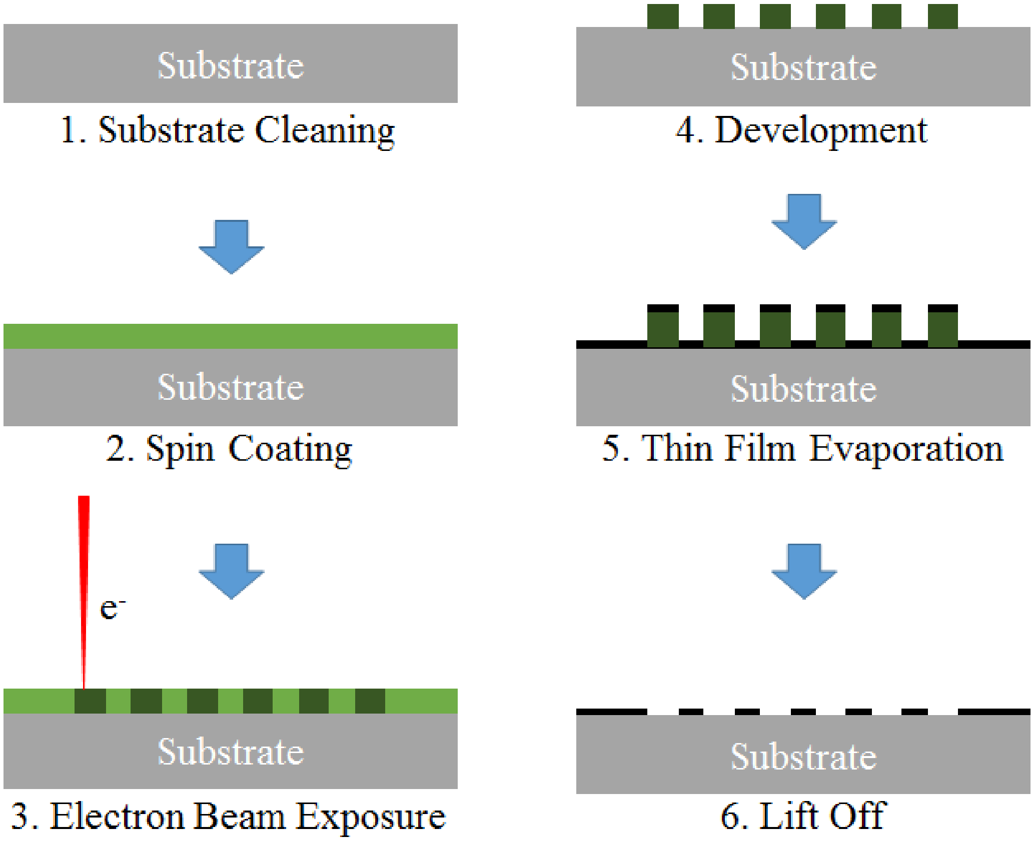

Figure 5.25 Fabrication process flow for maN-2403 using EBL

Following the EBL exposure, the PhC pattern needs to be transferred into the substrate material and this is facilitated by means of micro-fabrication techniques. Thin films can be deposited using electron beam evaporation and lifted off to yield a PhC structure of holes as shown in the Figure 5.25. However, the thickness of the ebeam resist is only 100 nm and this allows lift-off of thin films that are ~1/3 the thickness of the resist. On the contrary, the sample can be deposited with a thin layer of nickel using electron beam evaporation and lifted off using acetone. Using the nickel layer as a hard mask and reactive ion etching, the PhC pattern can be transferred into the substrate material. This process is shown in the Figure 5.26 and Figure 5.27 shows a 3D illustration of PhC pillars in the substrate and an SEM micrograph of a PhC pattern of holes fabricated using the above mentioned process.

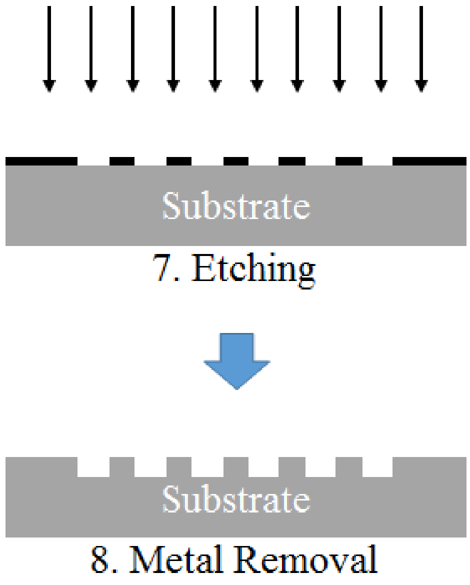

Figure 5.26 Continuation fabrication process for pattern transfer into substrate material

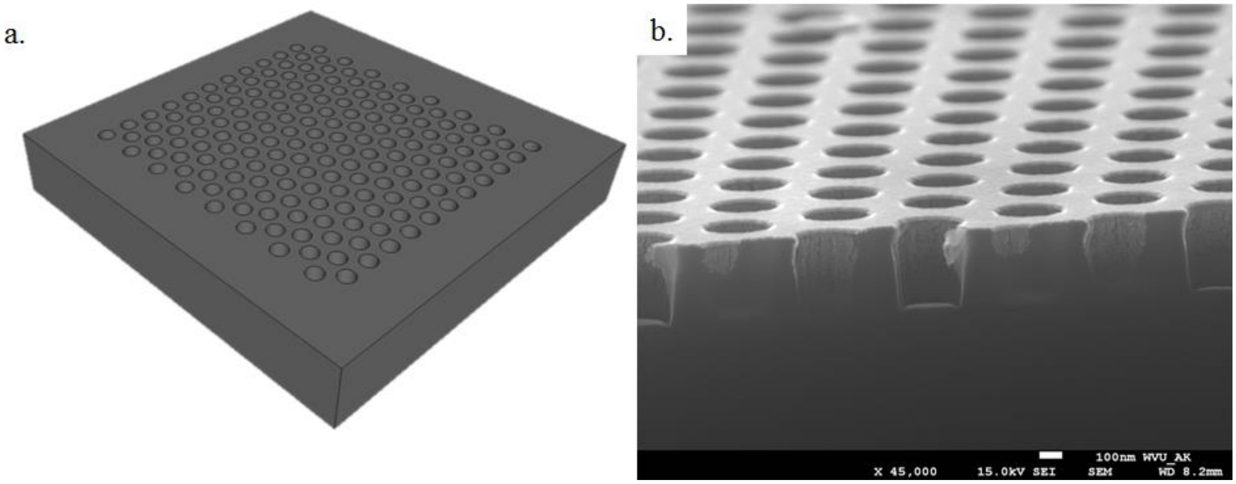

Figure 5.27 (a.)3D illustration of PhC pillars, (b.) SEM micrograph of PhC pillars fabricated in silicon

5.2.4. PhC Fabrication using Hydrogen Silsesquioxane (spin-on-dielectric)

Silsesquioxane refers to an organosilicon compound with empirical formula $\boldsymbol{RSiO_{3/2}}$ where ***R*** is either hydrogen or an alkyl, alkene, aryl, arylene group [76], [77]. Modifying the ***R*** group in Silsesquioxane results in materials that have properties ranging from an insulator to a semiconductor [78], [79]. The addition of polyhedral oligomeric groups enables for electroluminescence [80] and photoluminescence properties [81].

Hydrogen Silsesquioxane (HSQ), is a type of Silsesquioxane that has been modified to have a hydrogen in place of the ***R*** as shown in the Figure 5.28. HSQ has unique properties to be used in various interlayer dielectric applications. Extensive research was done by a number of commercial and academic institutions on HSQ to be used in semiconductor applications.

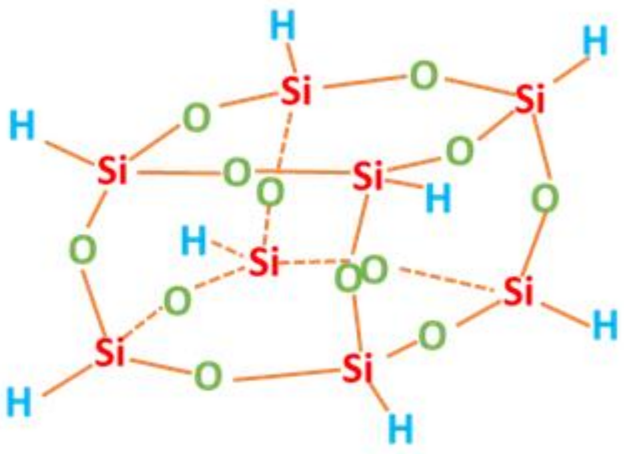

Figure 5.28 Cage structure of Hydrogen Silsesquioxane [82]

In recent years of using HSQ in a variety of semiconductor applications, it was discovered that this spin-on-dielectric can be cured by exposing it to electron beam energy [83], [84] , [85]. By the use of electron beam lithography and the computer-aided design, the resist can be exposed using any desired mask pattern. The exposure of the resist changes the solubility of the resist in a developer and this helps to realize a pattern in the resist. Previous studies show that the exposure of the resist yields in a pattern that is insoluble in the developer and this makes HSQ a negative tone resist. The electron beam exposure of the resist aids in breaking the Si-H bonds and resulting in crosslinking of the resist and forming Si-O bonds as shown in the reactions below [84].

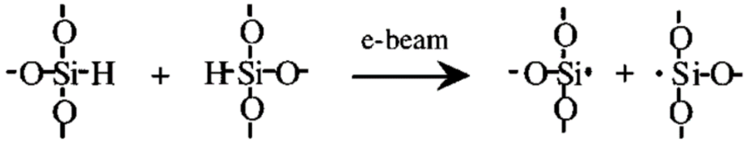

$$-O-\overset{\overset{|}{O}}{\underset{\underset{|}{O}}{Si}}-H + H-\overset{\overset{|}{O}}{\underset{\underset{|}{O}}{Si}}-O- \xrightarrow{\text{e-beam}} -O-\overset{\overset{|}{O}}{\underset{\underset{|}{O}}{Si}}\cdot + \cdot\overset{\overset{|}{O}}{\underset{\underset{|}{O}}{Si}}-O- \qquad (5.8)$$

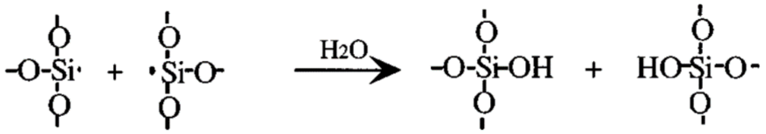

$$-O-\underset{O}{\overset{O}{Si}}\cdot + \cdot\underset{O}{\overset{O}{Si}}-O- \xrightarrow{H_2O} -O-\underset{O}{\overset{O}{Si}}-OH + HO-\underset{O}{\overset{O}{Si}}-O- \quad (5.9)$$

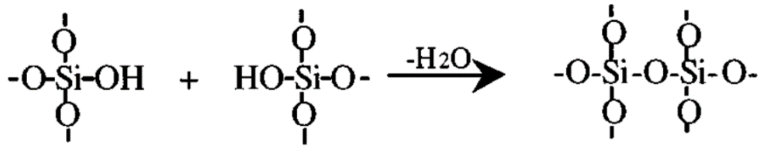

$$-O-\underset{O}{\overset{O}{Si}}-OH + HO-\underset{O}{\overset{O}{Si}}-O- \xrightarrow{-H_2O} -O-\underset{O}{\overset{O}{Si}}-O-\underset{O}{\overset{O}{Si}}-O- \quad (5.10)$$

Once exposed, the resist layer is developed in aqueous solution of tetramethylammonium hydroxide (*TMAH*) or potassium hydroxide (*KOH*) yielding in high contrast patterns [86], [87]. Although the chemical reactions (Equations 5.8, 5.9, 5.10) show the cross linking of the Si-O bonds from Si-H bonds, the homogeneity of this cross linking is not spread out across the pattern [84]. This inhomogeneity can be addressed by curing the exposed resist either in an oxygen plasma environment or thermally. These additional steps ensure the exposed regions are entirely crosslinked and can be used as effective etch masks [84], [40]. This ability of using the exposed resist as the etch masks opens an array of new applications.

Several groups have used HSQ and its variants along with electron beam lithography to be incorporated in a variety of applications. A lot of these applications exploit the curability of the material into SiOx for etch resistance [88], achieving high resolution features [89], ability to be used along with other resists to form high aspect ratio patterns [90] and Nanoimprint lithography [91]. These properties will be studied and develop a fabrication process for integrating PhCs into LEDs.

In the present scenario of integrating PhCs into LED structures, HSQ is used for its material properties. As described in the previous sections, integrating PhCs into an LED using traditional ebeam resists and micro-/nano- fabrication techniques involves etch process that can be damaging to the structure. The characteristics of the HSQ based resists allows for the reduction in the number of processing steps and achieve better results. The curable nature of HSQ to SiOx enables the resist to be used as an etch mask and to transfer the pattern into the substrate materials. The process flow for such a process using HSQ is shown in the Figure 5.29. Using this direct fabrication process, previous efforts by our group has shown promising results in producing high anisotropic structures in silicon as shown in the Figure 5.30 [40].

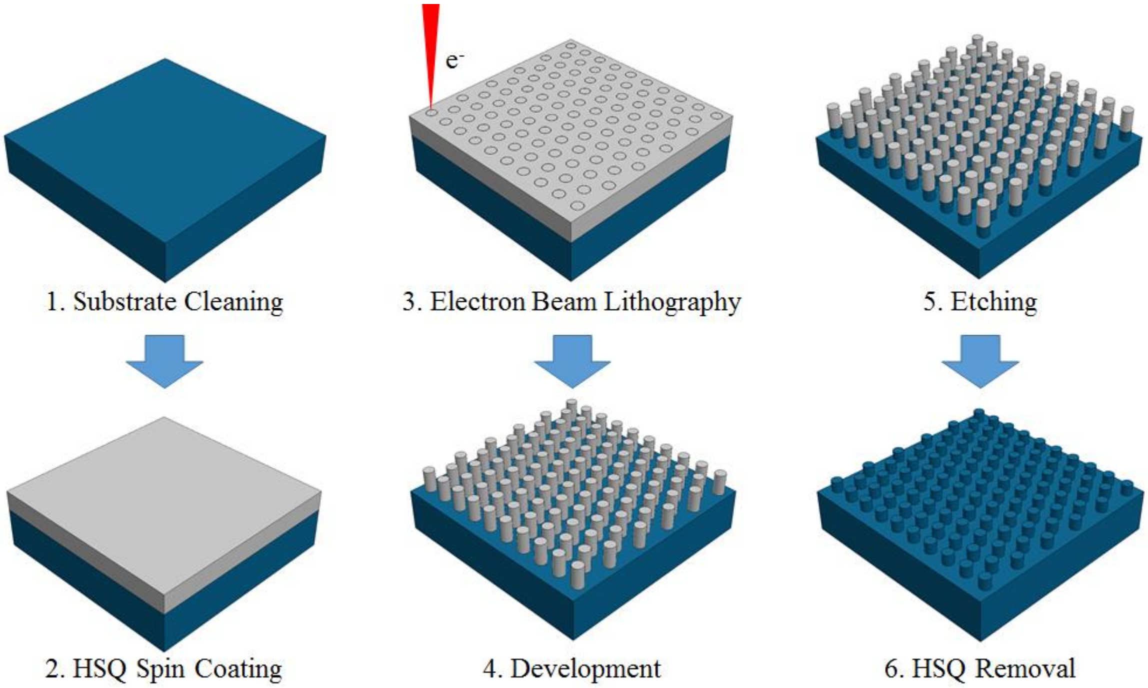

Figure 5.29 PhC fabrication process using HSQ and EBL

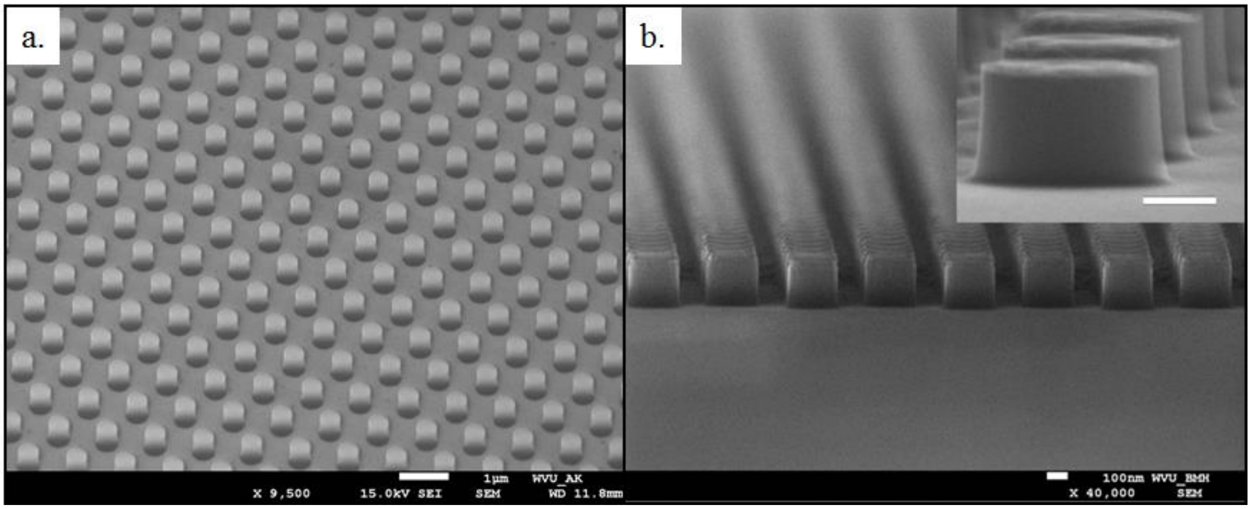

Figure 5.30 PhC patterns in silicon fabricated using direct fabrication process (a.) Developed HSQ pattern, (b.) PhC pattern etched into silicon [40]

5.2.5. PhC Fabrication using Nanosphere Lithography

Electron beam lithography, is known as an efficient technique when the target pattern is confined to a small area. However, to fabricate on a wafer scale, EBL would be time consuming and expensive, hence, not a suitable method for pattern transfer. Bottom up methods like NSL use suspended nanosphere solutions to self-assemble on the wafer creating a wafer scale pattern within less time and inexpensively [92]. NSL uses a combination of several solutions and suspensions to achieve large-scale self-assembly.

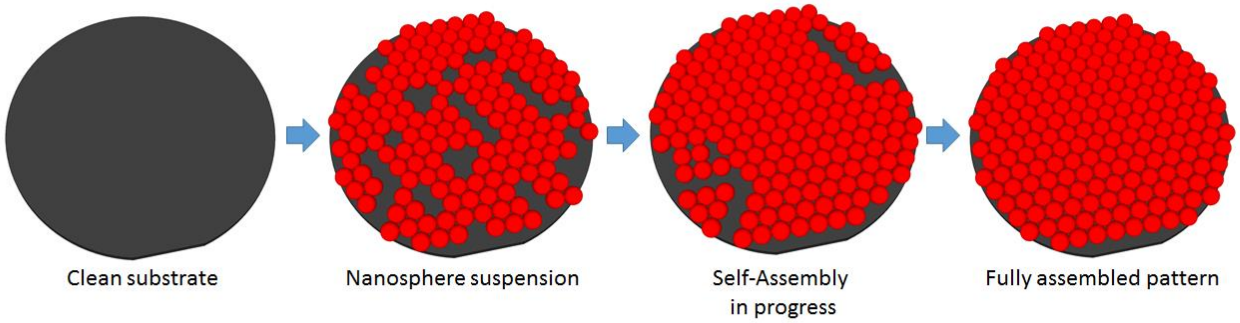

Figure 5.31 Typical Self-Assembly process

Self-Assembly is a process in which disordered components form an organized structure or pattern upon mutual attraction and local interactions [93]. There are two types of self-assembly processes, static (may require external stimuli) and dynamic (only happens when the process is dissipating energy) [93]. Exploiting the nature of self-assembly in nanoscale suspensions, large-scale patterning can be achieved. A typical self-assembly fabrication process involves a substrate coated with a suspension containing nanoscale components that assemble over time or with external stimuli as shown in the Figure 5.31.

NSL involves the use of micro-/nano- scale spheres that are suspended in a solution. There are three types of homogenous mixtures formed by the combination of the spheres and liquids used. They are categorized as Suspensions, Colloids and Solutions. These are differentiated by the size of the spheres that are mixed in the liquids. Suspensions are those with spheres large enough to form a sedimentation in the liquid. Colloids are those with spheres that are microscopically dispersed throughout the liquid forming a homogenous medium. Finally, a solution is one in which the solids are soluble in the liquid. Suspensions and colloids are the most appropriate candidates for use in NSL. The common types of solid particles used for NSL are either silica or polystyrene beads suspended in water or special solutions to make them a colloid. However, metal nanoparticles and other novel nanomaterials have been being explored in recent years expanding the NSL’s area of applications. Areas like bio-photonics [94], optics [95], photonics [96] and plasmonics [97] are utilizing the advantages of NSL and achieving a great deal of success.

For this study, polystyrene spheres have been chosen for a starting point to develop a method to uniformly self-assemble and form a large area pattern. The polystyrene spheres chosen are suspended in water and the mixtures are available at various concentrations. The development of the wafer scale fabrication was conducted on silicon substrates to prove the concept and later will be translated to suitable substrates for LEDs. Due to natural oxidation of materials, there exists a thin layer of oxide on the substrate and several non-polar bonds that tend to repel both water and any water based solutions [98]. This causes the surface to be hydrophobic (water hating) and repels the mixtures with polystyrene beads. In order to make the surface hydrophilic (water loving) and attract the aqueous suspensions, the surface has to be treated with chemical baths that remove the non-polar bonds. Several surface treatment methods have been developed to treat the surface to make the surface hydrophilic.

A variation of using both piranha bath and RCA clean have proven to be helpful in treating the surface to be hydrophilic [99], [100]. The fabrication process involves extensive cleaning of the substrate in acetone, methanol and DI water, followed by soaking the substrate in piranha bath (3:1 H_2SO_4:H_2O_2), RCA clean (5:1:1 DI H_2O:NH_4OH:H_2O_2) and in deionized water. Thorough study in variation of times for the cleaning methods have resulted in 30 minutes for each of the piranha and RCA cleans and 60 minutes in deionized water respectively. The effect of surface preparation methods on the contact angles of liquid to the surface before and after are shown in the Figure 5.32.

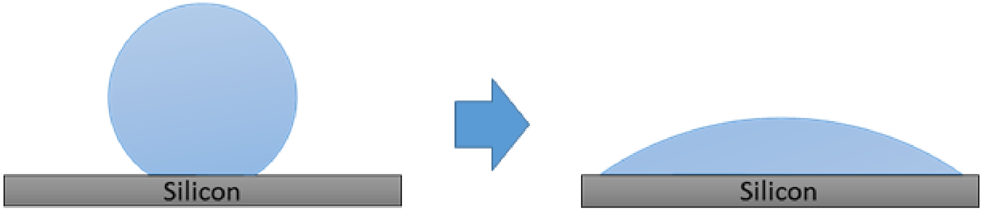

Figure 5.32 Contact angle change by surface preparation using piranha and RCA cleans

Following the surface treatment procedures, there are several methods to disperse the suspension containing the polystyrene beads reported in the literature viz. sedimentation [101], spin coating [102], [103], dip coating [104], evaporative dispersion [105], convective dispersion [106], [107] etc. Primarily, spin coating, and evaporative dispersion methods have been tested for dispersing a single layer of beads in this research.

Silicon samples were cut to the size of 1.5 x 1.5 cm^2 and cleaned using piranha bath and RCA clean. 40 µL of 500 nm polystyrene bead solution was spun onto the cleaned samples at 1400 rpm for 60 seconds. Optical images of the samples were taken using an optical microscope and a Canon digital camera. The images were taken at 5x magnification and the sample area is ~ 0.05 mm^2 in the images. Matlab based image analysis code was written and used to estimate the percentage coverage of the beads on the optical images. Figure 5.33 shows the optical image and the Matlab extracted coverage area.

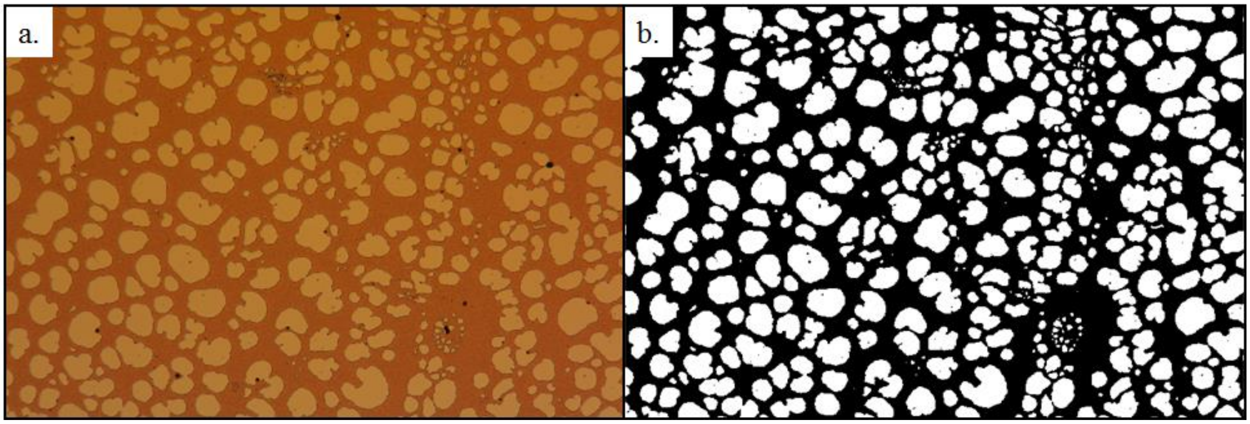

Figure 5.33 Initial spin coating result (a.) Optical Image, and (b.) Matlab image showing 43% coverage

The initial efforts with the spin coating technique showed significantly low coverage of the surface area of approximately 43%. By adding surfactants to the aqueous suspensions with the polystyrene beads have shown better assembly [99]. Sodium dodecyl sulfate (SDS) is one such surfactant that enables in reducing the surface tension in aqueous solutions [99]. Various concentrations of SDS are mixed with polystyrene suspensions and were tested on the surface treated substrates.

Additional to the surfactant solution, a new spin recipe was developed with a settling time step. The settling time step helps increasing the attracting forces between the hydrophilic surface and the polystyrene beads. The new spin recipe contains three spin steps of 400 rpm for 10 seconds, 800 rpm for 60 seconds and 1400 rpm for 10 seconds. Using this combination of settling time and a three step process, the coverage of the single layer of polystyrene beads has significantly improved from 43% to 81%. Four different setting times (3,5,7,9 minutes) have been tested with the three step spin process and found that 5 minute settling time has the best coverage of polystyrene beads. Figure 5.34 shows the coverage percentage plotted against the settling time.

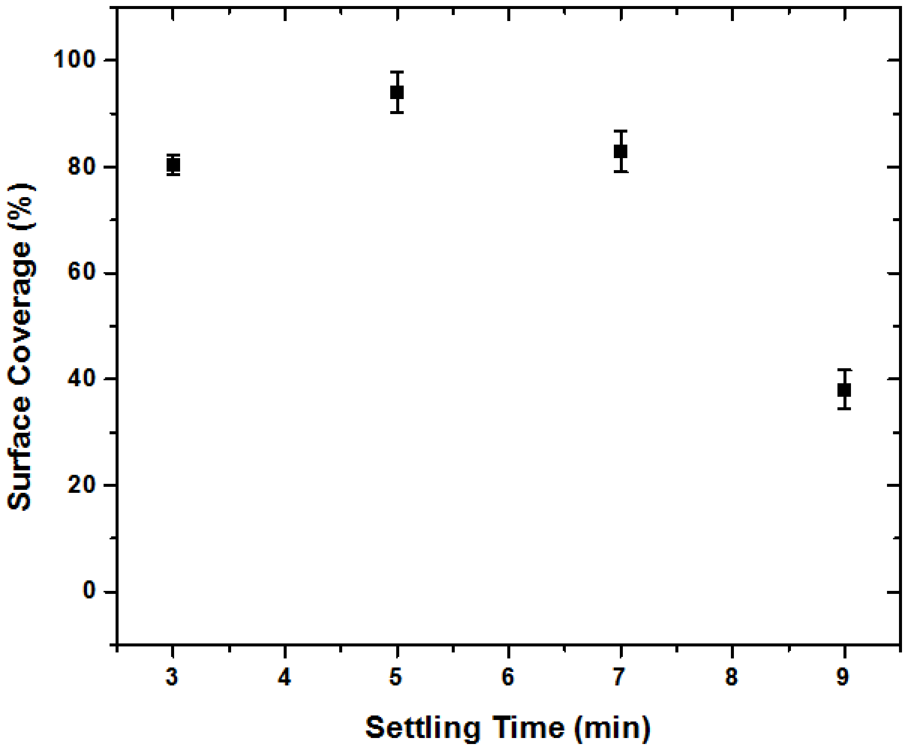

Figure 5.34 Settling time versus the percentage coverage

It is seen that the 5 minute settling time has resulted in the most coverage from using the three step spinning process. Figure 5.35 shows the optical image and the Matlab extracted coverage area.

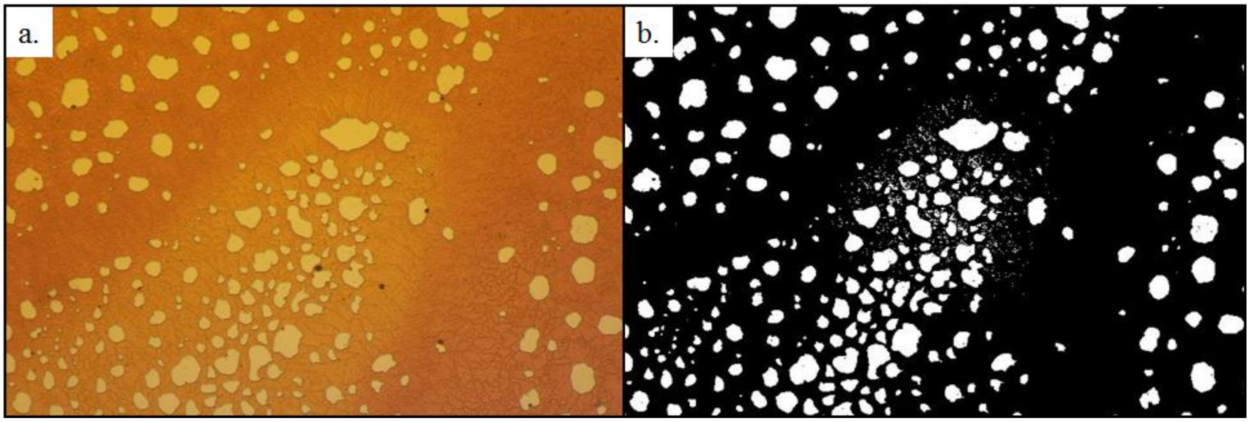

Figure 5.35 Spin coating result with 5 minute settling time (a.) Optical Image, and (b.) Matlab image showing 84% coverage area

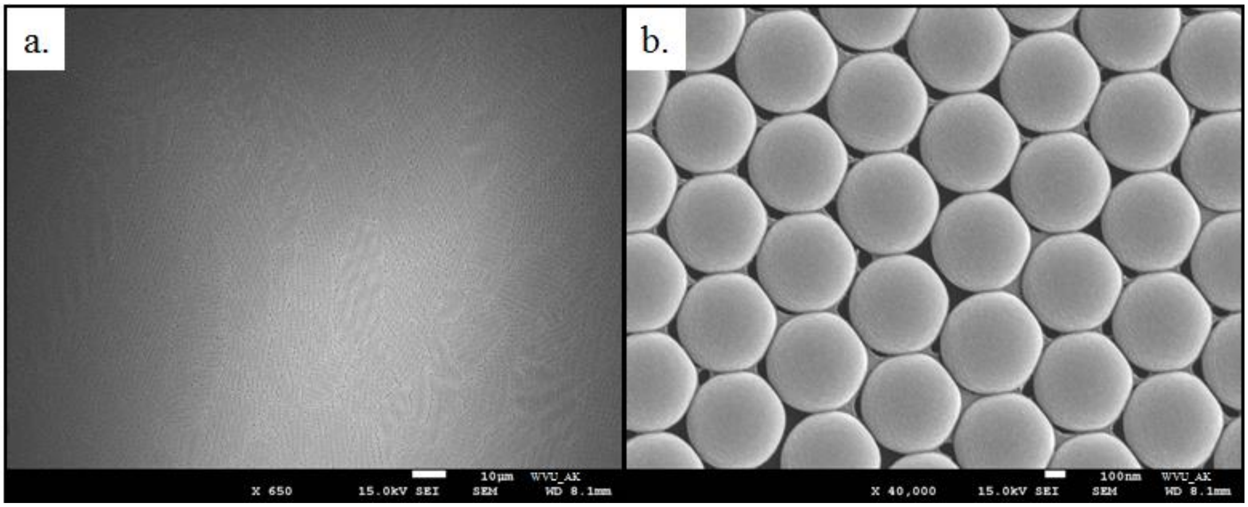

Figure 5.36 (a.) SEM image of spin coated polystyrene beads (b.) Close-up image showing a single layer of polystyrene beads

SEM images obtained from the spin coating method are shown in the Figure 5.36. On the other hand, to achieve better and uniform coverage of the beads on the surface, thermal evaporation method was developed. Figure 5.37 shows the setup for thermal evaporation method. The concept here is to control the evaporation of the aqueous solution containing the polystyrene beads steadily. Under the influence of gravity and steady evaporation, a uniform single layer of polystyrene beads should be self-assembled.

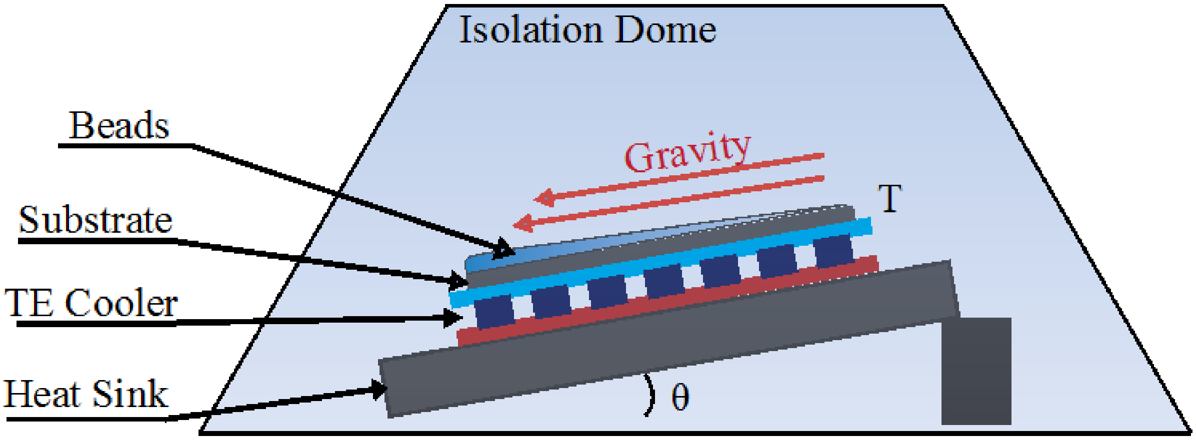

Figure 5.37 Illustration of thermal evaporation setup

This study involves two additional parameters, viz. temperature (T) and angle of inclination (θ), apart from the way the surface preparation methods. The study of the temperature and the angle of inclination both resulted in interesting results. As the angle of inclination was increased, there was a steady gradient in the number of layers self-assembled and as the temperature was increased, the aqueous solution evaporated quickly and resulted in multiple layers of beads. The results of temperature and angle of inclination is shown in the Figure 5.38.

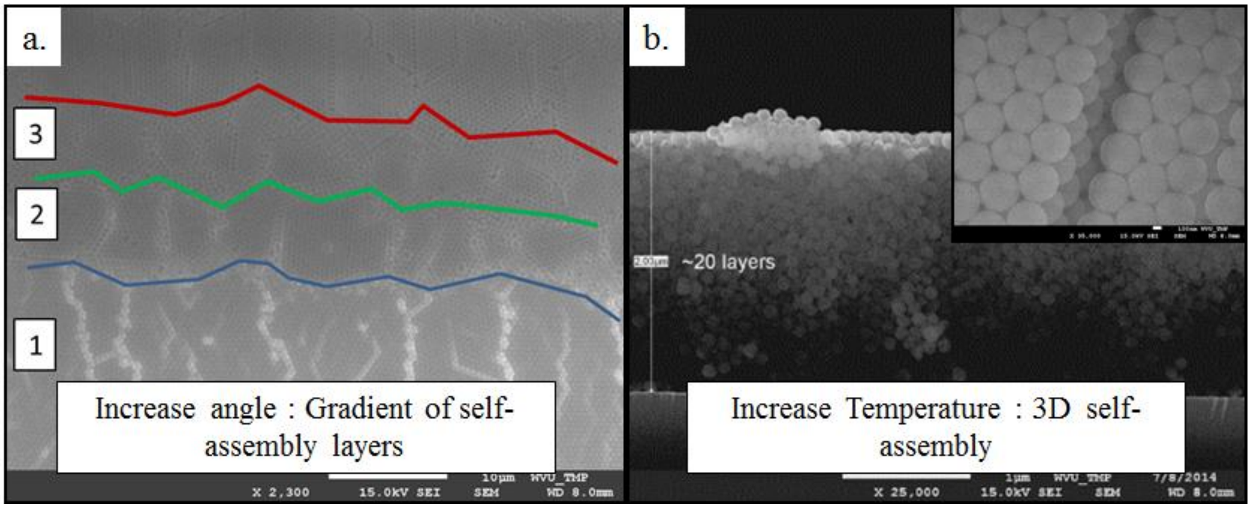

Figure 5.38 Thermal evaporation method results (a.) Variation in angle of inclination, (b.) Variation in temperature

By tuning the temperature and angle of incidence, a steady consistent process was developed to produce a single layer of polystyrene beads. 40 µL of polystyrene beads were dispersed on the hydrophilic sample which is set on a thermoelectric cooler maintaining a constant temperature of 21.5^{o}C and at an angle of 10^o. These settings have resulted in almost 98.5% surface coverage obtained from the optical images as shown in the Figure 5.39.

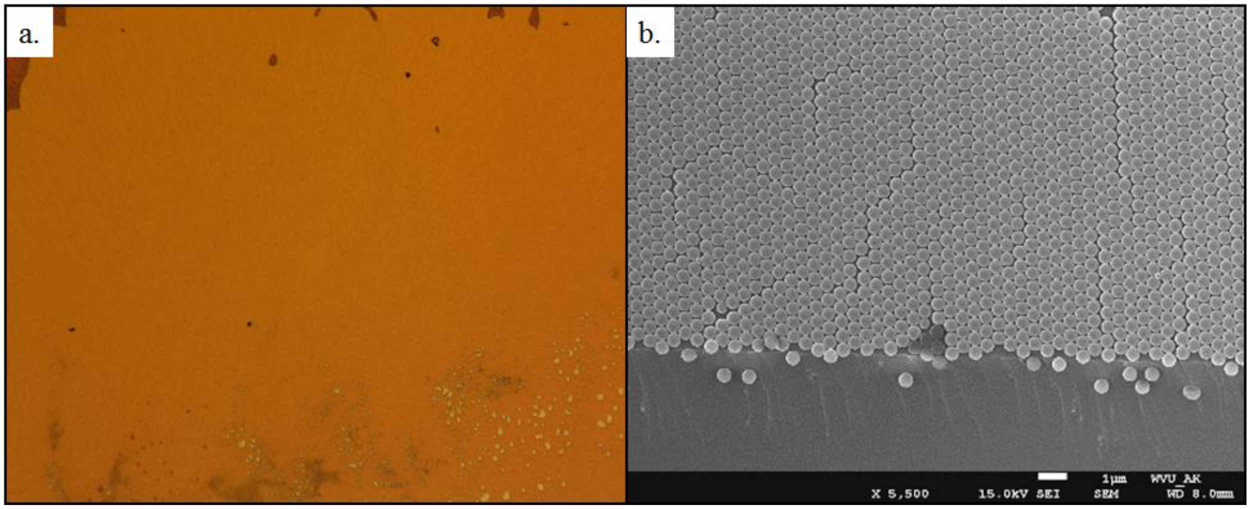

Figure 5.39 Thermal evaporation results (a.) Optical image (b.) SEM image

Of the two methods discussed in this section, the thermal evaporation method seems to have the best coverage of a single layer of beads. Proceeding forward, the fabrication process to transfer a pattern into the substrate material requires to the use of a sacrificial template and in this case, the self-assembled layer of polystyrene beads will be used for pattern transfer. The spheres can be shrunk in an oxygen plasma environment and can be used as the template for PhCs. The fabrication process detailed in the Figure 5.40 allows fabrication on a large area with lesser efforts compared to the traditional fabrication methods.

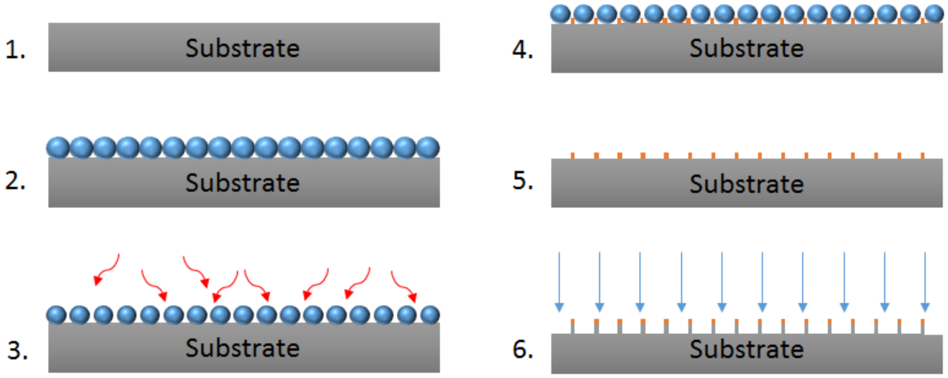

Figure 5.40 Fabrication process using Nanosphere Lithography to pattern on a large-scale 1. Clean substrate, 2. Self-assembly of beads, 3. Shrinking in oxygen plasma, 4. Metal mask deposition, 5. Lift-off, 6. Reactive ion etch

Utilizing the above processing parameters, we achieved large-scale patterning on substrates that are 1.5x1.5 cm^2 area. The results obtained after all the steps including the etching are summarized in Figure 5.41. Further study in this area will concentrate on using this process of patterning in the LED fabrication process.

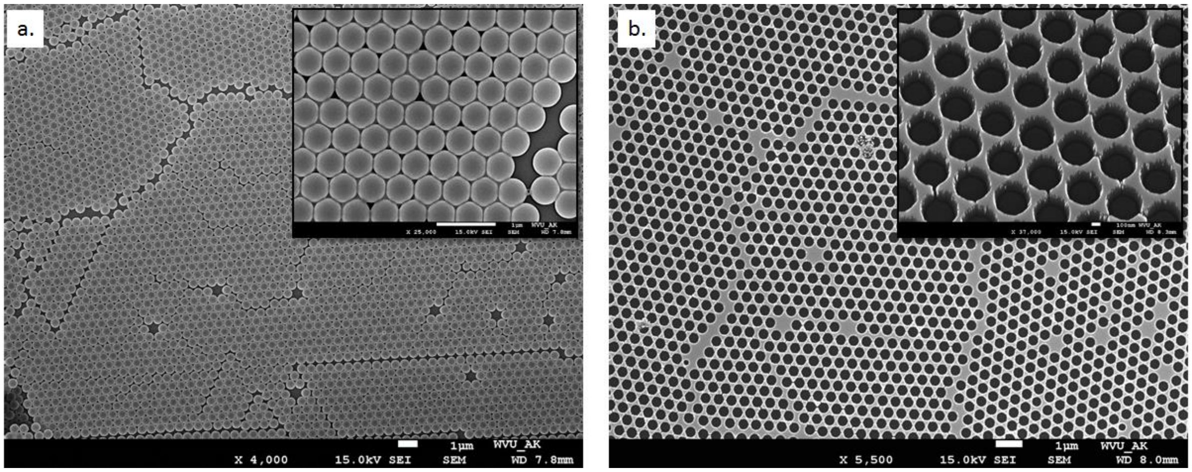

Figure 5.41 (a.) Spin-coated polystyrene beads (Inset: Magnified view), (b.) After reactive ion etch (Inset: Angle view)

5.3. Photonic Crystal LEDs

This section mainly focusses on the integration of the PhC structures into the LED structure. The processes described earlier in the above sections, only lay the ground for fabrication of the PhC structures. Some of those processes cannot be directly used for integrating PhCs into LEDs as the LED fabrication process itself has 6 to 7 additional processing steps. The following sub-sections show the integration processes using above mentioned methods and the respective results from those processes.

5.3.1. Integration using PMMA

In order to fabricate holes using PMMA ebeam resist, a sacrificial layer has to be used to result in a PhC structure with holes. These sacrificial layers could be any dielectric or polymer materials that do not have any chemical effects on the underlying substrate materials. For this fabrication process, a silicon dioxide layer was deposited using electron beam evaporation and ion beam assisted deposition. The entire process flow using a positive tone resist for fabricating PhC holes is as shown in the Figure 5.43.

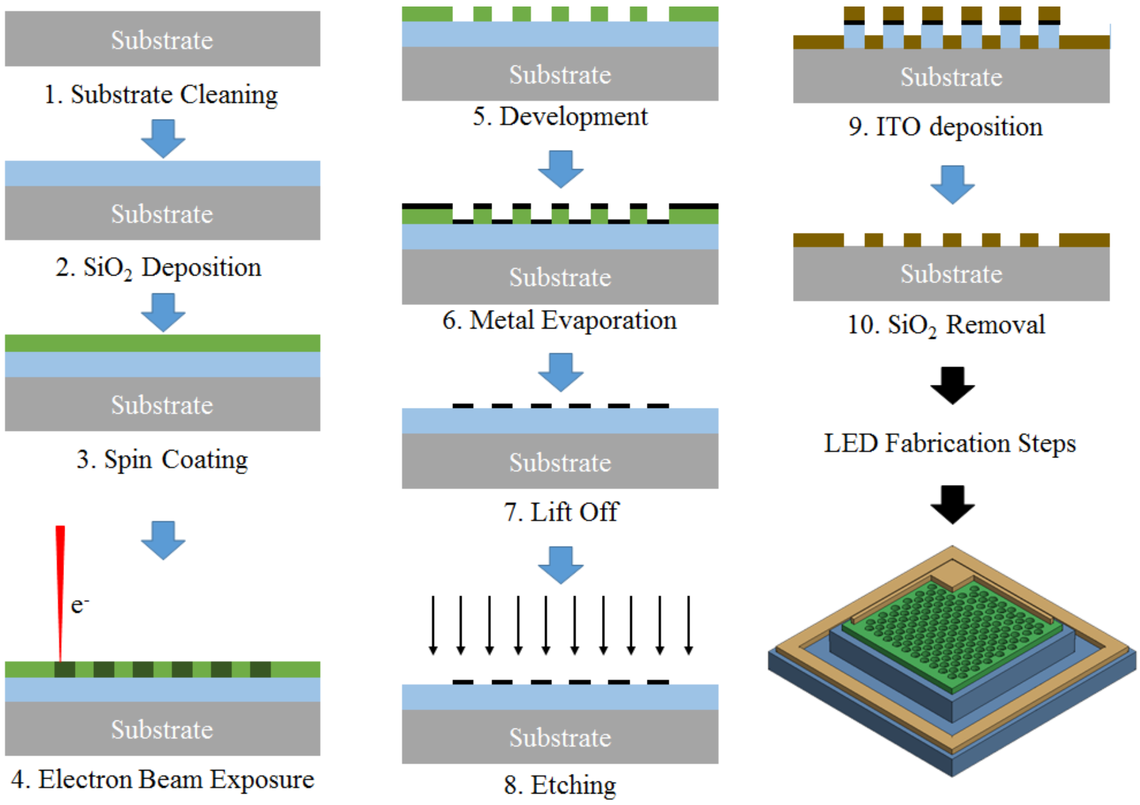

Figure 5.42 Process flow for fabricating PhCs of holes in ITO

Utilizing the above process, LEDs were fabricated to have patterned p-metal and ITO contact layers. For patterning contact layers, a 400 nm of SiO2 layer was deposited using electron beam evaporation. EBL was done on the PMMA layer to produce 300 nm (dia.) holes with a pitch of 500 nm in a triangular lattice configuration. A 25 nm nickel layer was deposited using electron beam evaporation and lifted off using acetone bath. Reactive ion etching with a CF_4/O_2 plasma was performed to transfer the pattern into the sacrificial layer. Etch recipe parameters are listed in Appendix C. Figure 5.44 shows the stages of the fabrication process up to pattern transfer into the sacrificial layer. After this step, both p-contact metal stack (Ni/Au) and ITO layers were deposited on separate LED samples. As the SiO_2 (sacrificial) layer was removed using corrosive etchant (hydrofluoric acid), there were adverse effects on the contact layers, especially on the ITO layer. Figure 5.45 (a.) shows the result of patterning metal contacts and removal of the SiO_2 layer. However, the metal pillars above the SiO_2 layer settled down on the metal contact. Additional cleaning was done with sonication to remove the residual pillars as shown in the Figure 5.45 (b.).

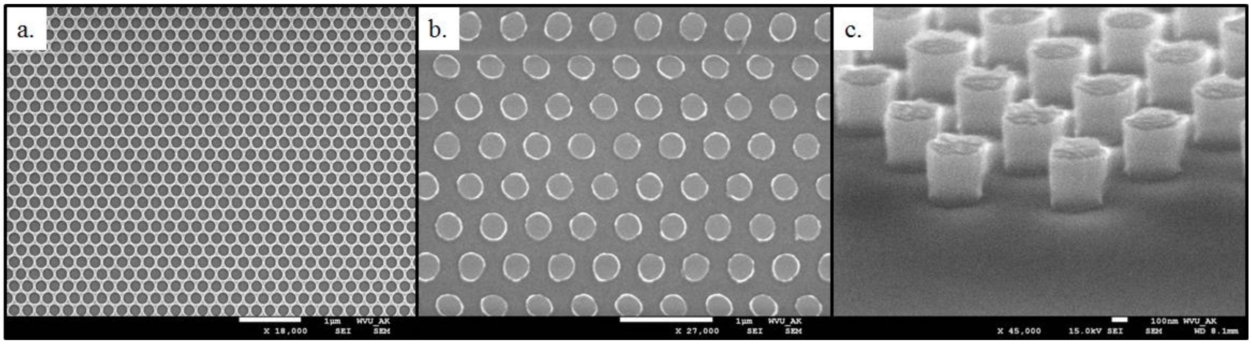

Figure 5.43 SEM images of the fabrication process showing (a.) holes in PMMA, (b.) Nickel pillars after lift-off, and (c.) Pillars etched into the SiO_2 layer

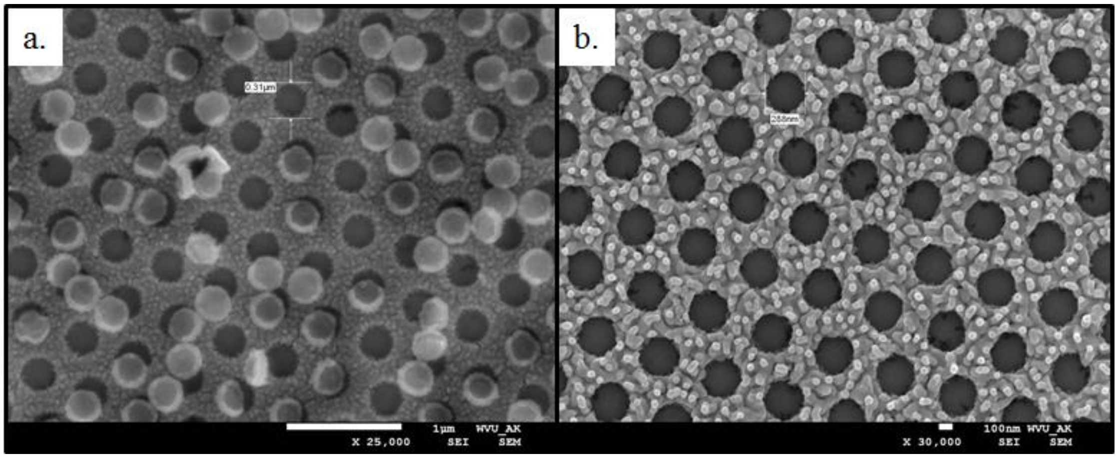

Figure 5.44 SEM images of patterned metal contact (a.) right after etching, (b.) after cleaning with sonication

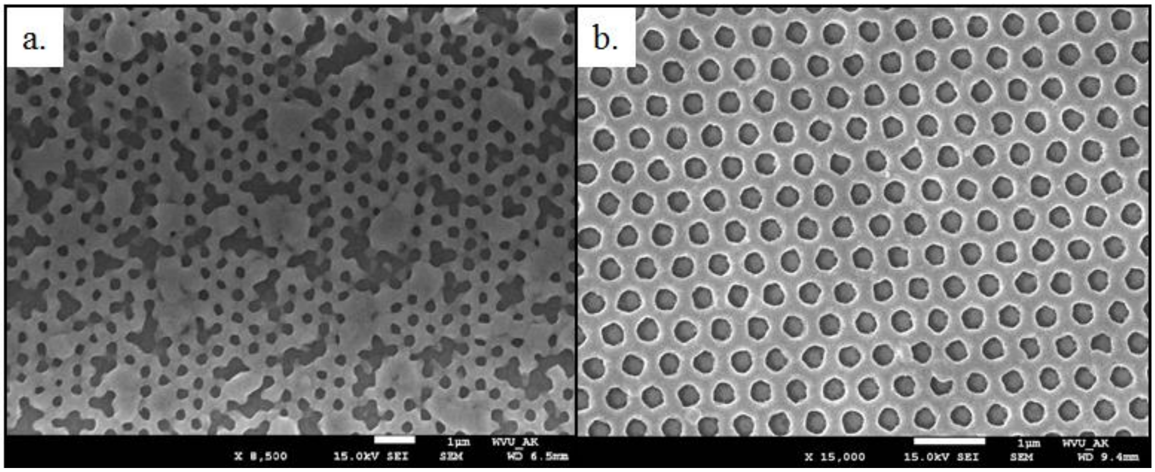

Figure 5.45 Effect of annealing step on contacts that had SiO_2 removed (a.) before, and (b.) after

As part of the fabrication of LED, the contacts need to be annealed at 600°C and this step reflows the metal contact and disrupts the integrity of contact as shown in the Figure 5.46 (a.). Hence the removal of the SiO_2 is done after the contact annealing step and the final result is shown in the Figure 5.46 (b.).

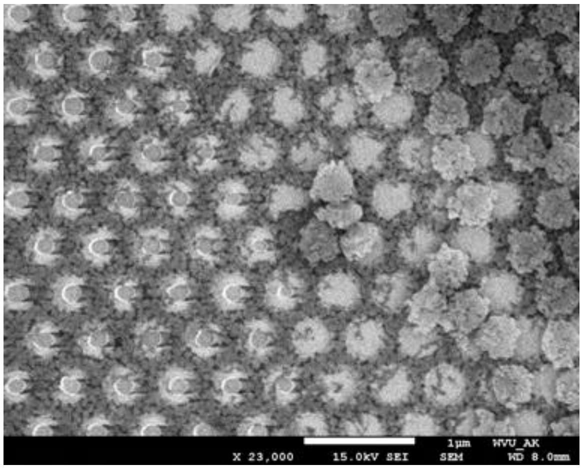

Figure 5.46 SEM image of ITO PhC after removal of SiO_2 layer

Similar processing method was used to pattern ITO layer, however, the acid etchant has corroded the ITO layer as shown in the Figure 5.47. Furthermore, the reactive ion etching step of silicon dioxide layer induces etch damage into the LED layers and resulted in poor current-voltage characteristics shown in Figure 5.48. As the additional etch steps and corrosive etchants have degrading effects, this fabrication process cannot be used for integration of ITO PhCs into LEDs.

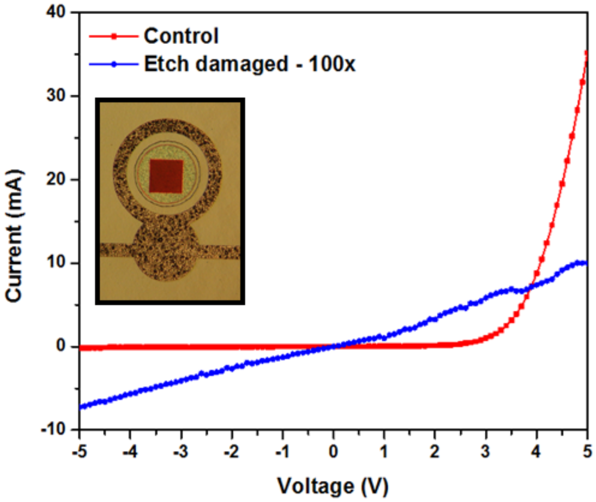

Figure 5.47 Comparison of control and etch damaged current-voltage characteristics of LEDs (Inset: Optical Image of PhC LED with patterned metal contact)

5.3.2. Integration using maN-2403

The process described in section 5.2.3 yields in PhC structures containing holes required for light extraction improvement in LEDs. However, due to the thickness of the resist and lift-off limitation, this process can only result in ~100 nm ITO thin film with holes. As it was deduced in the earlier sections, the thickness of ITO thin film required for optical transmission is about 165 nm. In order to fabricate holes using maN-2403 ebeam resist, the ITO thin film has to be deposited on before the EBL step followed by a reactive ion etching step to transfer the pattern into ITO. The entire process flow using a negative tone resist for fabricating PhC holes is as shown in the Figure 5.49.

Utilizing the above process, LEDs were fabricated to have patterned ITO contact layer. For patterning contact layers, a 165 nm of ITO layer was deposited using electron beam evaporation. EBL was done on the maN-2403 layer to produce 300 nm (dia.) holes with a pitch of 500 nm in a triangular lattice configuration. A 20 nm nickel layer was deposited using electron beam evaporation and lifted off using acetone bath. Reactive ion etching with a $BCl_3/Cl_2/CF_4$ plasma was performed to transfer the pattern into the sacrificial layer. Etch recipe parameters are listed in Appendix C. Figure 5.50 shows the SEM images at different stages of the fabrication process for pattern transfer into the ITO layer.

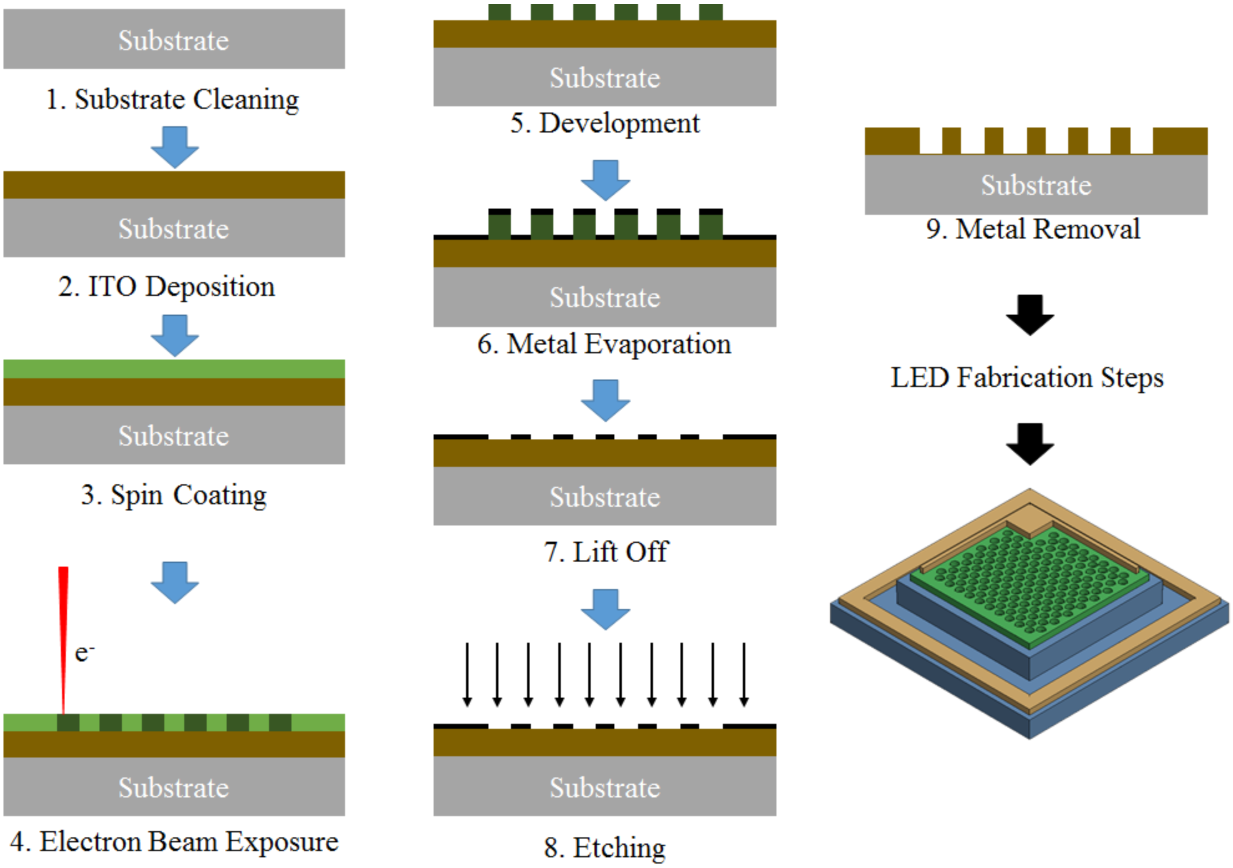

Figure 5.48 Process flow for fabricating PhCs of holes in ITO

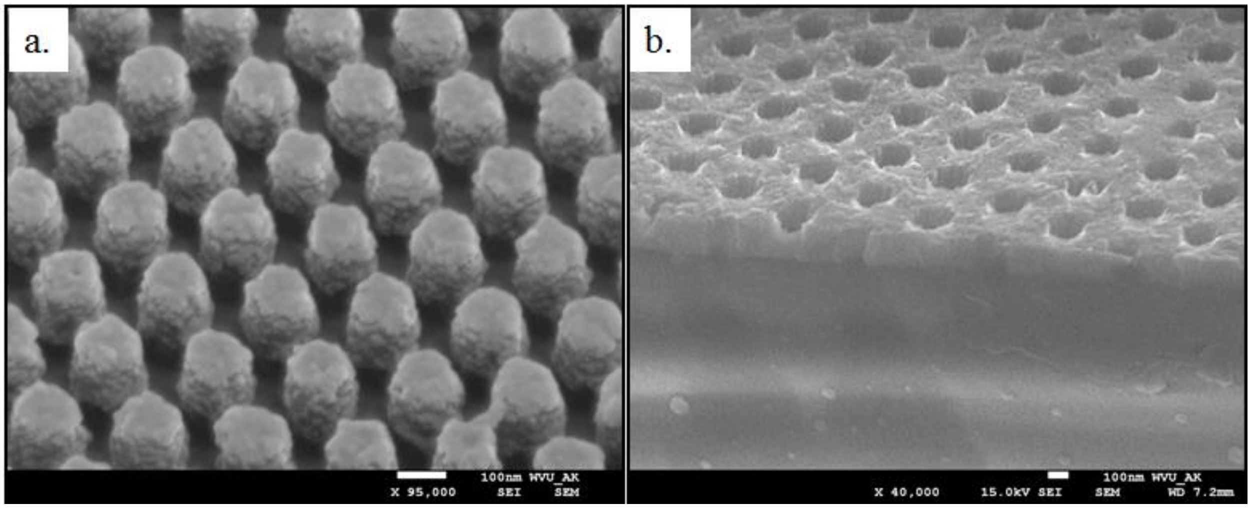

Figure 5.49 SEM images of (a.) maN-2403 pillars, (b.) PhC in ITO after etching

To facilitate the removal of the metal layer, corrosive acid etchants are required and as mentioned earlier the additional reactive ion etching step induces etch damage into the LED layers. Hence, this process also adds degrading effects and cannot be used for integration of PhCs into LEDs. An alternate to the issues mentioned in this and earlier section, is to utilize novel materials and methods that are less damaging to the structure and do not affect the performance of the LED.

5.3.3. Integration using Hydrogen Silsesquioxane

As previously introduced in previous section 5.2.4, HSQ can be used to reduce the number of processing steps to produce similar results produced using traditional ebeam resists. As it was seen in the PhC fabrication section, HSQ is also considered to be a negative tone resist and follows a similar process flow as the maN-2403 resist. Following the similar process flow, aggressive chemical etchants need to be used for lifting off the cured form of HSQ. This resulted in similar results as seen in the Figure 5.47. Due to the chemical properties of HSQ, the resist could be preferably used for realizing the aforementioned hybrid PhCs structures. The process flow using HSQ for integrating hybrid PhC structures is as shown in the Figure 5.50.

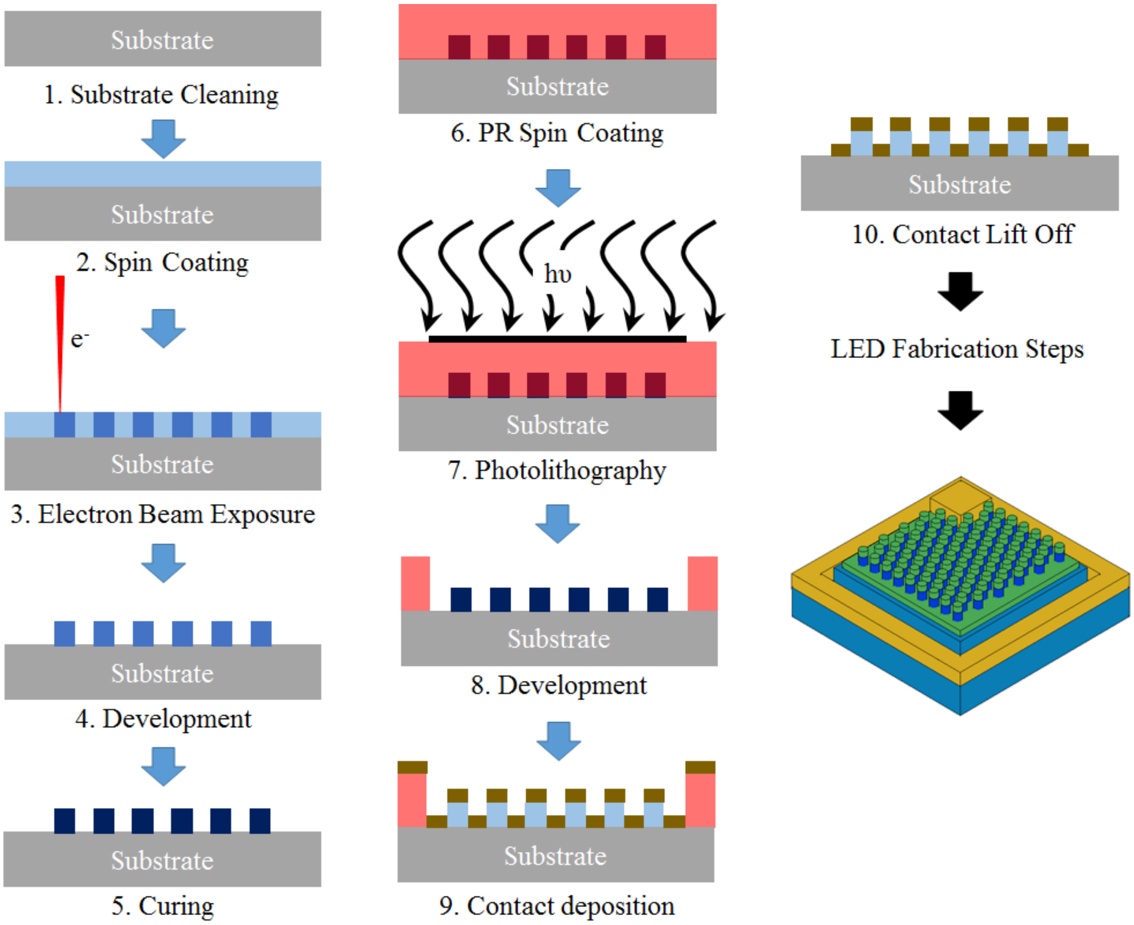

Figure 5.50 Process flow for fabricating hybrid PhCs in ITO

Utilizing the above process, LEDs were fabricated to have patterned metal and ITO contact layer. For patterning metal contact layers, FOx-16 from Dow Corning was spun at 3000 rpm for 1 minute. The sample is soft baked on a hot plate set at 95ºC for 4 minutes. The spun sample is then exposed using ebeam lithography with 6500 μC/cm^2 exposure dosage. After exposure, the sample is developed in AZ 400K developer diluted in DI water (1:1) for 150 seconds. The exposed pattern is then cured using a temperature treatment, by setting it on a hot plate at 400ºC for 1 hour. This step should ensure the conversion of the HSQ material into SiO_x. At this stage, the LED sample contains SiO_x pillars on the surface of the p-type GaN. Further steps involve multiple iterations of photolithography, etch, metal deposition and lift off techniques that are common for fabricating LEDs.

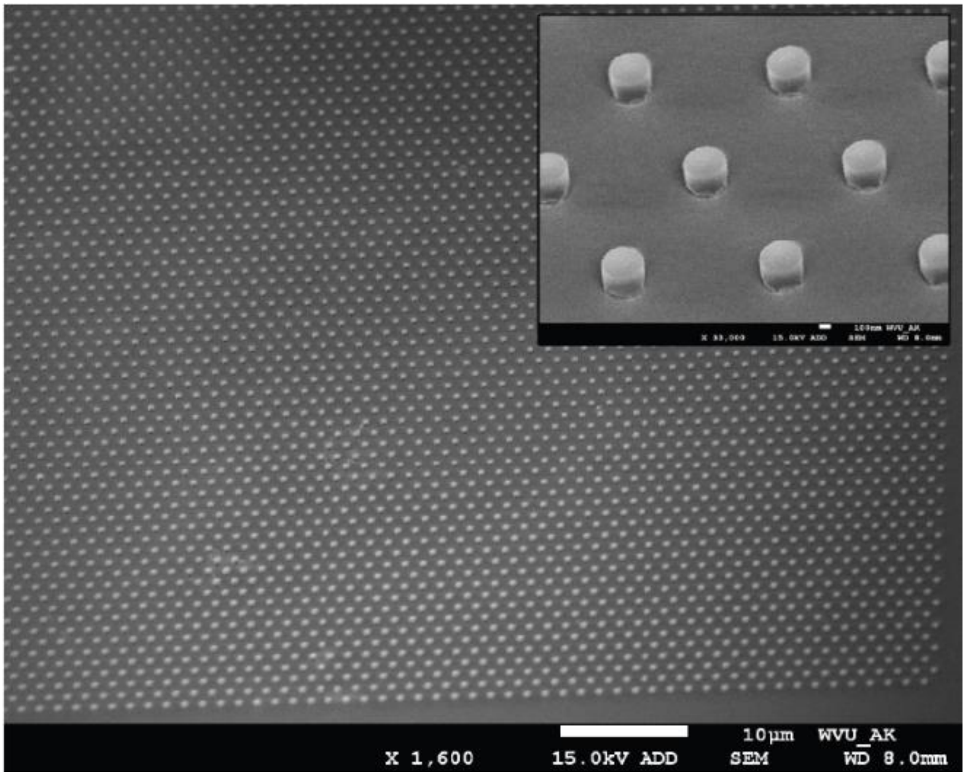

Figure 5.51 SEM image of Hydrogen Silsesquioxane (HSQ) pillars after development (Inset) Zoomed in SEM image of the pillars

Photolithography is performed using AZ-5214 E-IR for p-contact patterning. The p-type contact (Ni/Au – 30nm/50nm) is deposited using electron beam evaporation followed by lift-off revealing both unpatterned and patterned metal contacts. The patterned metal contacts have SiO_x pillars that were intentionally left within the contact to prevent collapsing of the patterned contact during the post-annealing process. The resulting p-metal contact is 160 μm in diameter with a patterned area of 80 x 80 μm^2. The patterned p-contact in its final state contains SiO_x pillars (cured HSQ) surrounded by the p-metal stack as shown in Figure 5.53.

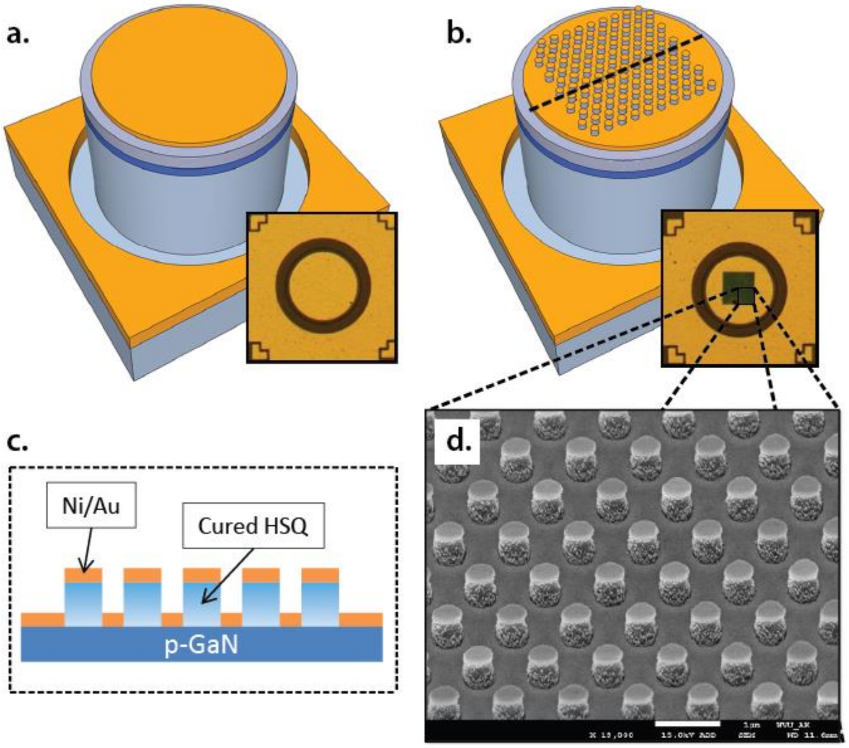

Fig. 5.52 a. Schematic of the final fabricated unpatterned device (Inset: Microscope image) b. Schematic of the final fabricated patterned device (Inset: Microscope image) c. Cross-section view of the patterned metal contact with cured HSQ pillars intact d. SEM image of the patterned metal contact with the cured HSQ pillars intact

Photolithography is then performed to create a protective layer of photoresist (AZ 4400) 200μm in diameter over the patterned p-contact area in preparation for the mesa etch. ICP RIE is then used to etch a mesa in GaN using the hard-baked photoresist as a mask. BCl_3/Cl_2 plasma was utilized to etch into the n-type GaN layer. An etch depth of 600 nm was achieved after 120 seconds of plasma etch. Afterwards, photolithography was used to pattern the n-contact region. The n-contact is created using e-beam assisted metal deposition (Ti/Al/Ti/Au – 2nm/100nm/30nm/50nm) followed by a lift-off. The fabrication process is completed with a post annealing process performed at 600°C for 3 minutes in air to anneal the contacts. The final fabricated devices with and without patterned metal contacts on p-type GaN are shown in Figure 5.52 (a. & b.).

Utilizing similar patterning process, ITO contact layers were are also patterned to have hybrid PhC structures. For ITO PhCs, both square and triangular lattice of hybrid PhCs were fabricated and Figure 5.53 shows the hybrid PhC patterns in ITO on the fully fabricated devices.

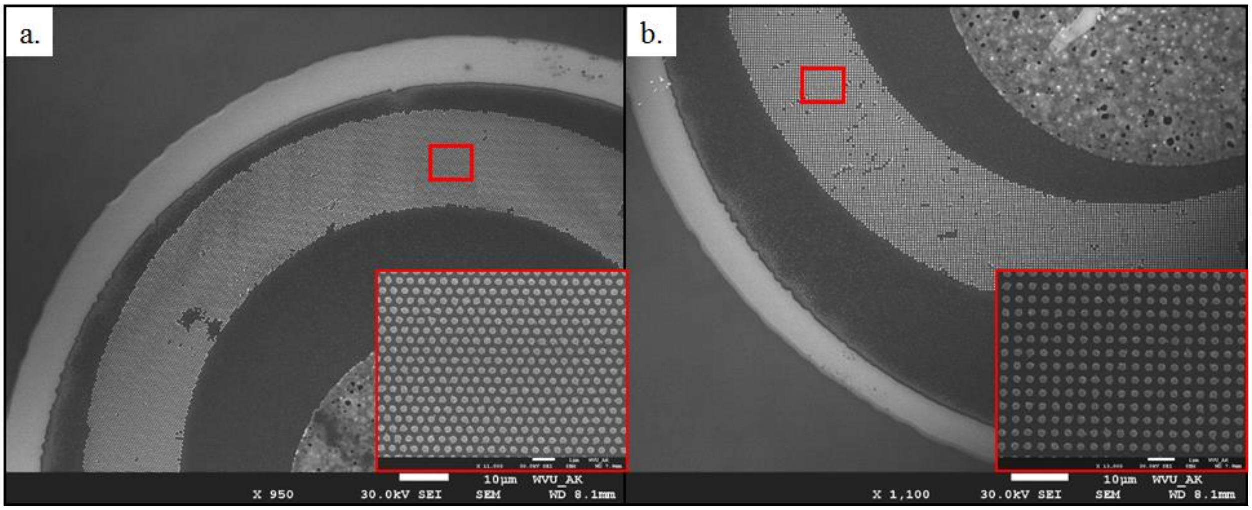

Figure 5.53 SEM image of hybrid PhC structures for ITO LEDs (a.) Triangular, (b.) Square (Inset) Zoomed in SEM image of the pillars

5.3.4. Integration using Nanosphere Lithography

As introduced in the above sections, NSL is the technique used for large-scale patterning with an intent to reduce processing costs. With the use of NSL, both PhC types containing holes and pillars can be achieved by tweaking the procedure. In this section, a process flow is shown that will possibly help in patterning the contacts (metal and transparent) on a larger scale (wafer size). The process flow is based on thorough literature survey performed [97], [102], [108] on large-scale self-assembly and contains a theoretical approach for integrating the PhC into the LEDs as shown in the Figure 5.54.

In this process, a substrate with LED active layers is cleaned in various solutions including acid baths to make the surface hydrophilic. Then polystyrene bead solution will be spun on the wafer allowing it to self-assembly a uniform layer. This layer of polystyrene beads are shrunk in a low energy oxygen plasma. The time for the plasma etch will have to be optimized to stop at the right dimensions of the spheres. These shrunk spheres are then used as a mask for evaporation of materials like metal or transparent contacts. Later, the polystyrene beads are removed by using a simple lift-off method. At this stage, the wafer should contain a large-scale pattern of the PhC in the selected material. From this point onwards, the fabrication steps for the LED are carried out to form a PhC LED wafer as shown.

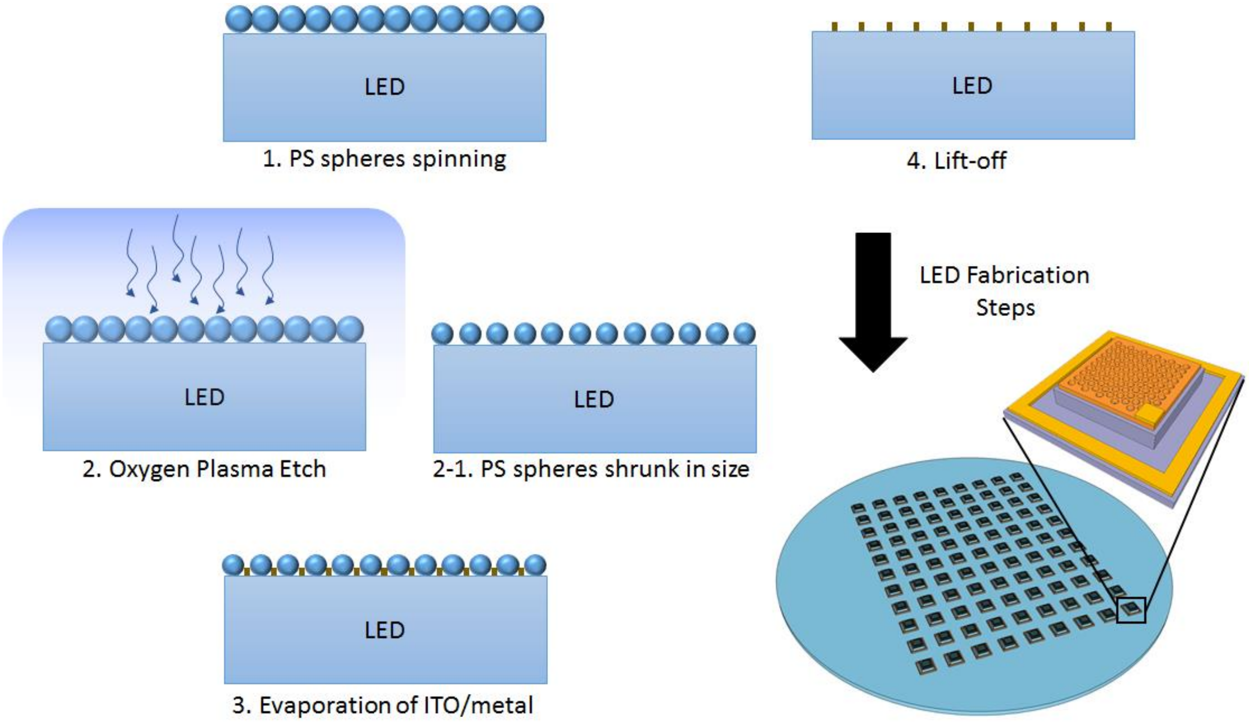

Figure 5.54 Large-scale patterning using nanosphere lithography

5.3.5. Bilayer Processing

In order to transfer the pattern to the layers of the LED like p-type GaN or ITO (transparent contacts), the above mentioned method using HSQ cannot be used. Since HSQ is a chemical that converts to SiOx after being exposed to an electron beam, traditional lift-off techniques are not effective. Acid baths are required to perform a successful lift-off for HSQ resists [109], which could be corrosive to the layers of the device including the transparent contacts. To avoid the use of corrosive acids for lift-off, a sacrificial layer can be added to the pattern transfer step that can be soluble in non-corrosive solvents.

Polymethylmethacrylate (PMMA) is a polymer electron beam resist that has been used in a variety of applications [110], [111]. One of the advantage of this polymer is that it is soluble in solvents like acetone even after the exposure to the electron beam. This allows to be used as a sacrificial layer for the current application. Several research groups have used similar approach of using sacrificial layers in conjunction with HSQ [112], [113], [114] for various applications. This approach has resulted in easier pattern transfer using HSQ and its variants.

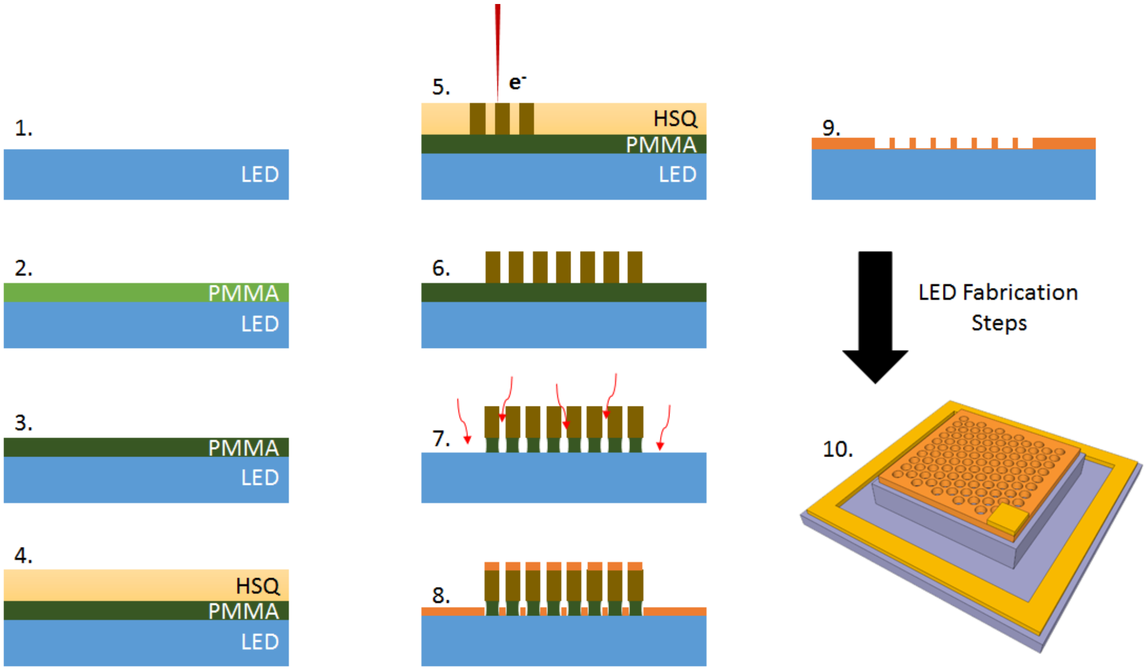

Figure 5.55 Process flow for bilayer patterning using HSQ and PMMA 1. Clean surface, 2. PMMA spin coat, 3. PMMA hard bake, 4. HSQ spin coat, 5. EBL on HSQ, 6. HSQ development, 7. Low power oxygen plasma etch, 8. Contact deposition (transparent or metal), 9. Lift-off, 10. Fully fabricated PhC LED

The process that will be used for patterning PhCs on LED structures using this bilayer patterning using HSQ and PMMA is as shown in the Figure 5.55. The process involves spin coating PMMA followed by hard baking the layer that evaporates any solvents. Then HSQ is coated over the PMMA layer followed by the electron beam lithography exposing the HSQ layer. The design for the mask is dependent on the materials and simulation results obtained. The exposed layer is developed to reveal the pattern seen in the Figure 5.56. The underneath layer of PMMA should be unaffected by either the EBL or the developing steps. The sample will be now etched using a low energy oxygen plasma asher to etch the sacrificial layer (For recipe see Appendix C). At this point, the sample should have HSQ pillars with a sacrificial PMMA pillar underneath it as shown in the Figure 5.57. Then the sample is deposited with either metal or transparent contacts (like ITO) followed by a simple lift-off as shown in the Figure 5.58. This process flow should have patterned the contact with designed PhC parameters. After patterning the contact layer, the regular steps to fabricate the LED structure are performed to finish the entire process of fabrication of PhC LED. Further processing needs to be done to complete the fabrication of the LED.

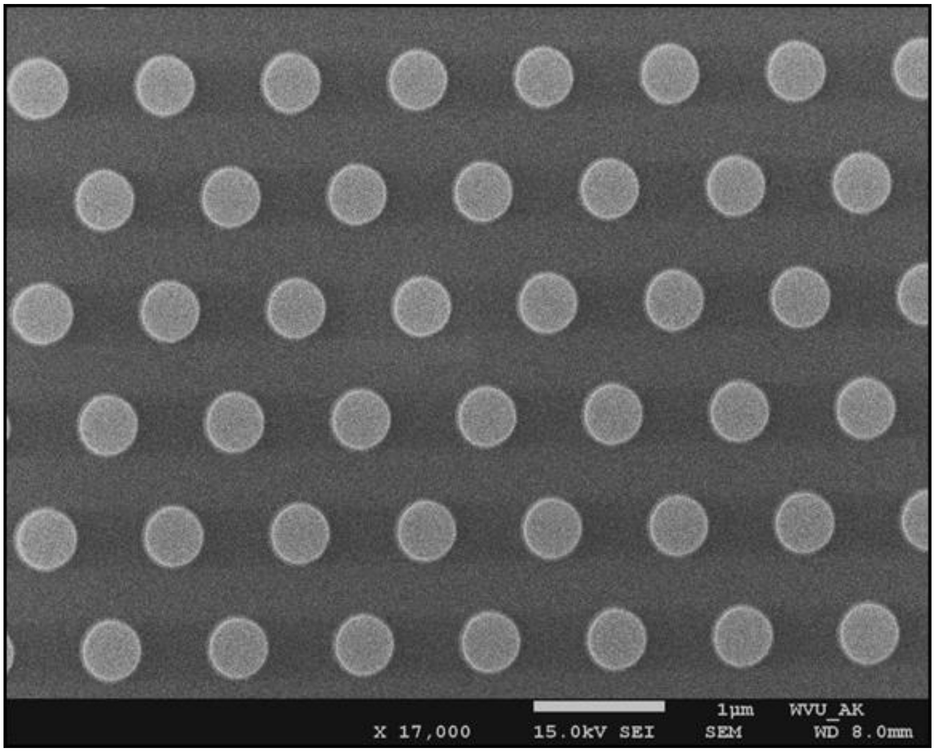

Figure 5.56 HSQ pillars developed atop the sacrificial PMMA layer

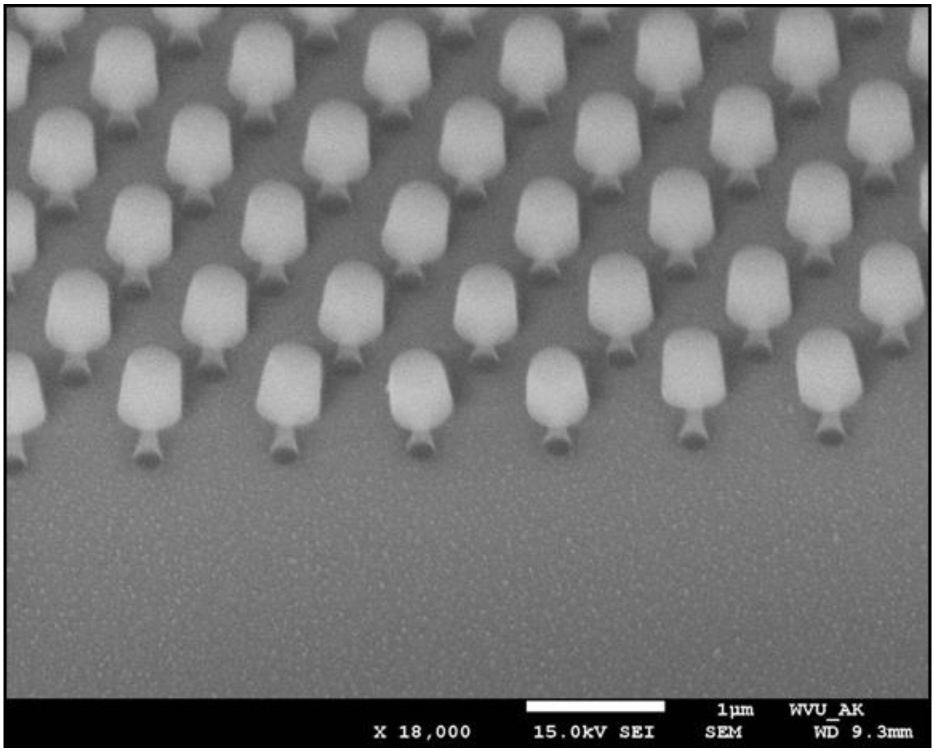

Figure 5.57 Tilted view SEM image of the HSQ pillars on top of the plasma etched PMMA pillars

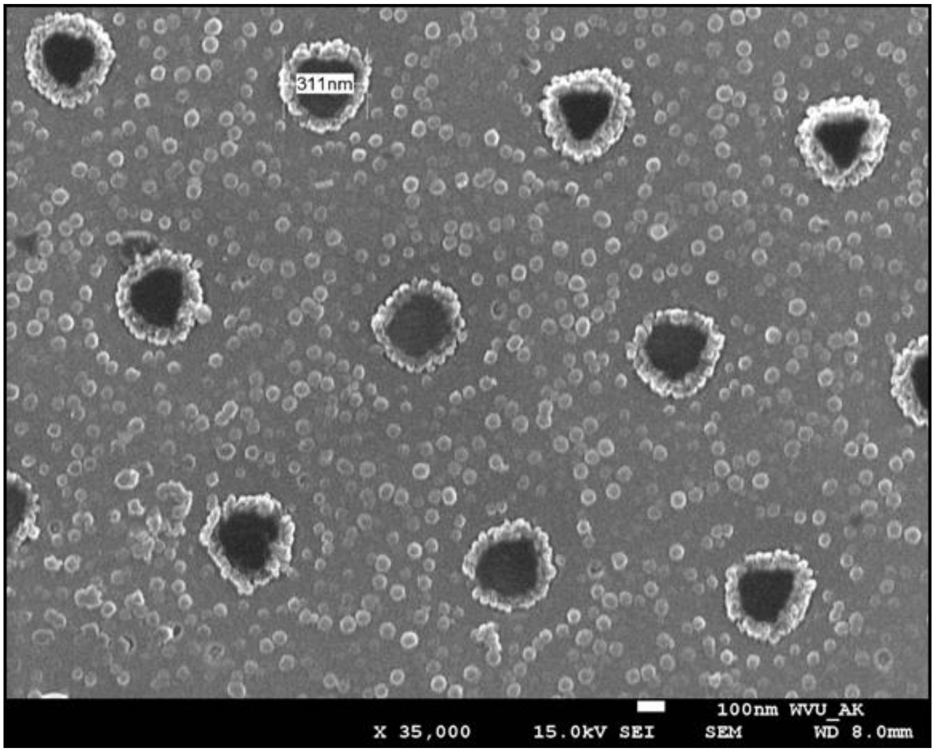

Figure 5.58 SEM image of PhC lattice of holes fabricated using bilayer processing

6. Characterization

To compare the performance of the devices with and without PhC structures, characterization techniques that assess the device both electrically and optically are needed. Current-voltage (IV) characteristics, and electroluminescence (EL) spectra of the aforementioned devices will used to compare their performance electrically. Radiation spectra and image processing techniques will be used to compare the optical improvements in those devices. The results obtained with these techniques will be used as a feedback in optimizing the process parameters and improving the integration process.

6.1. Hybrid Metal PhC LEDs

To fabricate these LEDs, HSQ (FOX® - 16 from Dow Corning) is spun on the sample at 3000 rpm for 1 minute resulting in a thickness of approximately 500 nm. Electron beam lithography was used to pattern an area of 80 x 80 μm^2 with features of 440 nm in diameter separated by a pitch of 1 µm. To compare the performance of the metal contacts with hybrid PhCs fabricated in the previous chapter, both planar and patterned devices were characterized. Figure 6.1 presents the current-voltage (IV) characteristics of the two device types. Four devices of each type were characterized and the average IV characteristics are shown with their respective error bars included.

The respective normalized electro-luminescence (EL) spectra for the devices are shown in the Figure 6.2 which were observed at an injection current of 60mA using a constant current source. These EL spectra of the planar and patterned devices were taken from the top side of the device using an optical fiber at a constant distance of 1 inch, as shown in the inset figure of Figure 6.2. The spectra are smoothed using that adjacent averaging method to remove any noise. It is observed from the plot that the peak wavelengths for all the tested devices are close to the expected emission wavelength (440nm). The peak wavelength for both planar and patterned devices at different injection currents was observed to be within the range of tolerance (<1%).

On the other hand, the radiation patterns of each device are compared to better understand the radial distribution of the light from the devices. Although, these measurements are traditionally done using an integrating sphere, for this work, an optical setup was constructed to measure the radiation pattern of each device as shown in the Figure 6.3.

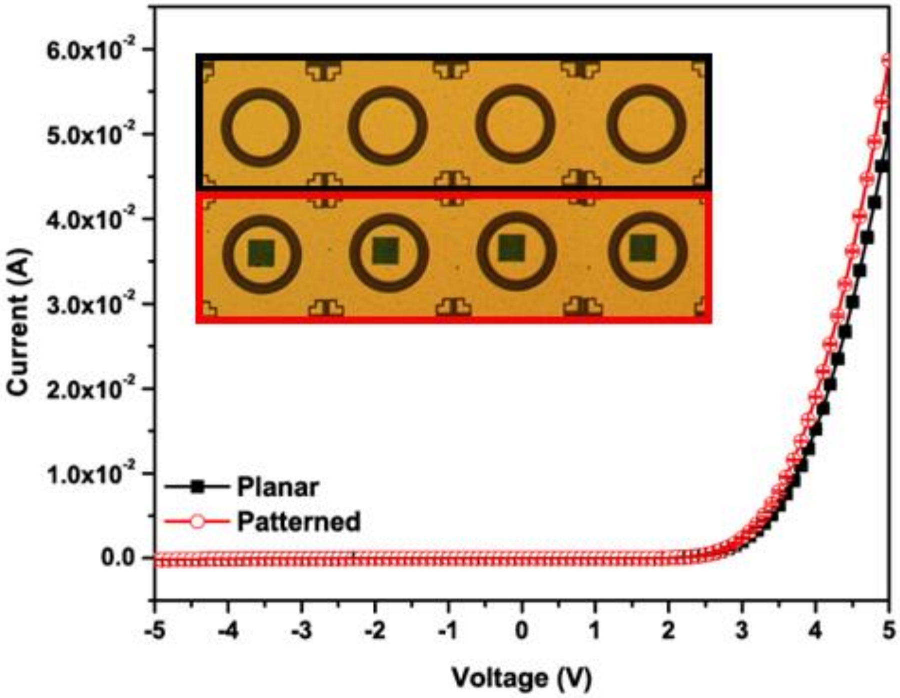

Figure 6.1 Current-Voltage Characteristics of 200µm Mesa Circular LEDs with error bars included

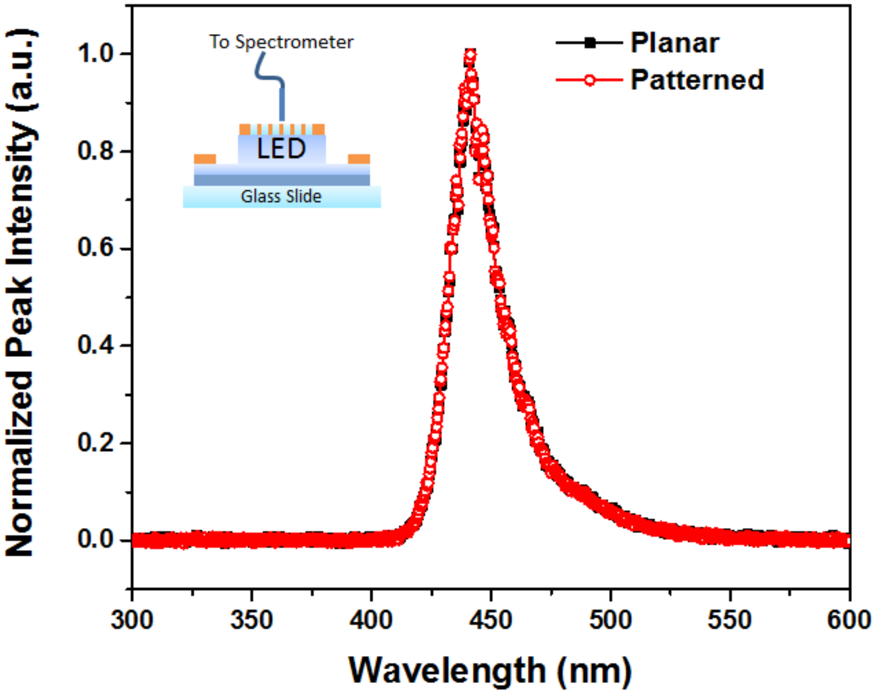

Figure 6.2 Normalized EL Spectra of planar and patterned LEDs

The EL spectra of each device is taken at angles varying from -60^o to 60^o at intervals of 5^o using a multi-mode optical fiber. The optical fiber is maintained at a constant distance (1 inch) from the surface of the LED and rotated about a fixed axis. The intensities at the peak emission wavelength (440 nm) are extracted from the respective EL spectra and normalized by dividing the maximum intensity observed at 0^o (surface normal). The normalized intensities are plotted with respect to the angles and summarized in Figure 6.4.

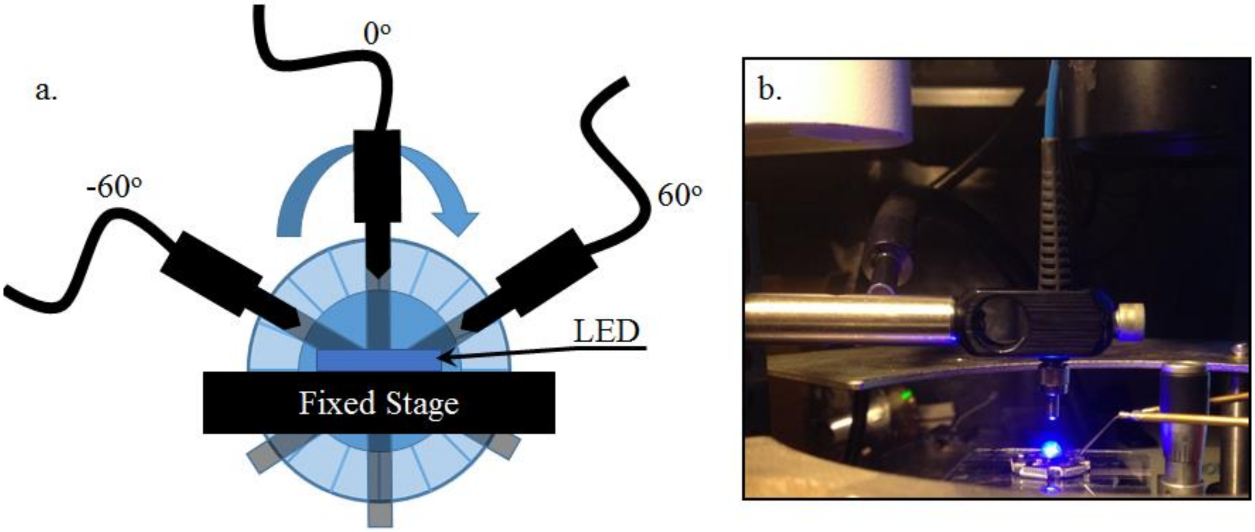

Figure 6.3 (a.) Radiation plot generation setup, (b.) Image showing the optical fiber positioned at 0^o above the LED

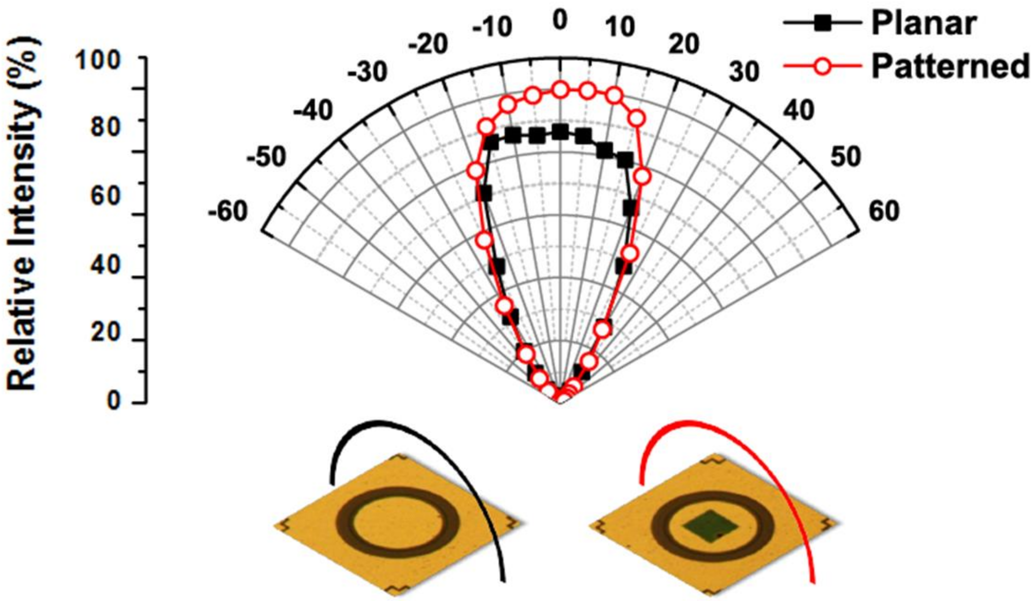

Fig. 6.4 Radiation plots of the planar and patterned LEDs with hybrid PhCs

From the radiation plots obtained, it is observed that the field of view for both the devices is ±20°. It is also seen the intensity of the patterned LED is approximately 15% higher than that of the planar LED directionally (surface normal). The radiation profiles shown here are constrained to a slice of the solid angle. Since the devices tested are symmetrical, the radiation profiles along any direction would be a replica of the shown result and hence the plots could be rotated to a solid angle perspective. To get more detailed information about the intensity extracted from the device, an alternate method for analyzing the intensity profile is adopted.

A Matlab-based image analysis tool was developed to characterize the top-side emission uniformity. For this analysis, both devices were separately driven with constant currents and images were captured using a Canon 5D Mark II camera mounted on a microscope with a 50x objective. External illumination sources were eliminated to reduce sources of unwanted emission intensity. Images for planar and patterned- LEDs were captured with the following camera settings: the sensitivity of the sensor (ISO) was set to 6400 to capture minimal amounts of generated light. A shutter speed of 1/160 second was chosen as the best setting for capturing unsaturated images. The characterization setup for the image capture and analysis is shown in the Figure 6.5. With the parameters set, images were taken at different injection currents 60 mA, 80 mA and 100 mA. Along with these images, a background image is also taken with the LED powered off to determine the background noise level.

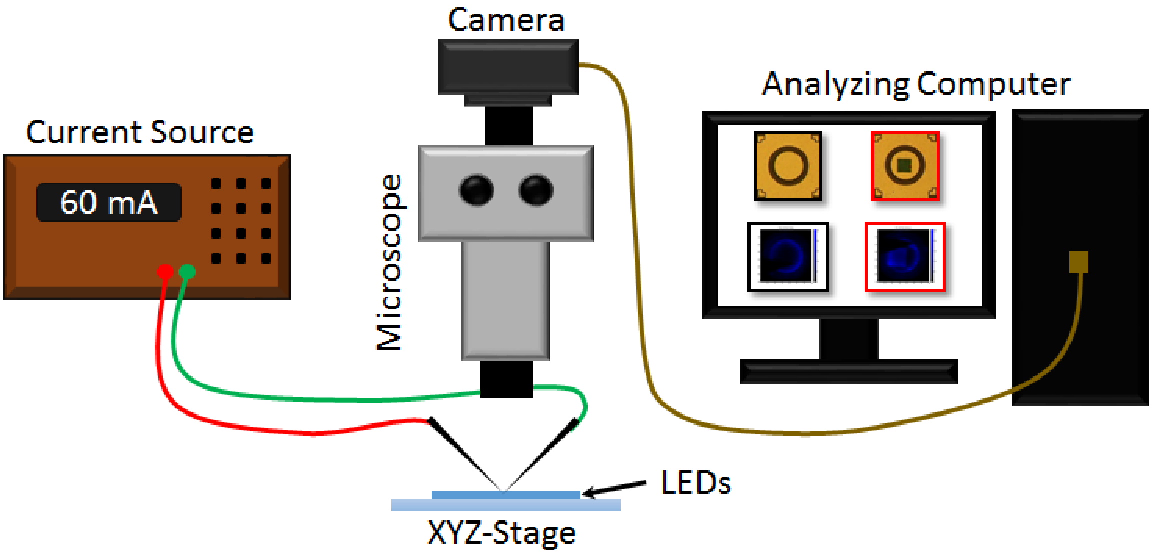

Figure 6.5 Characterization setup for image capture and analysis

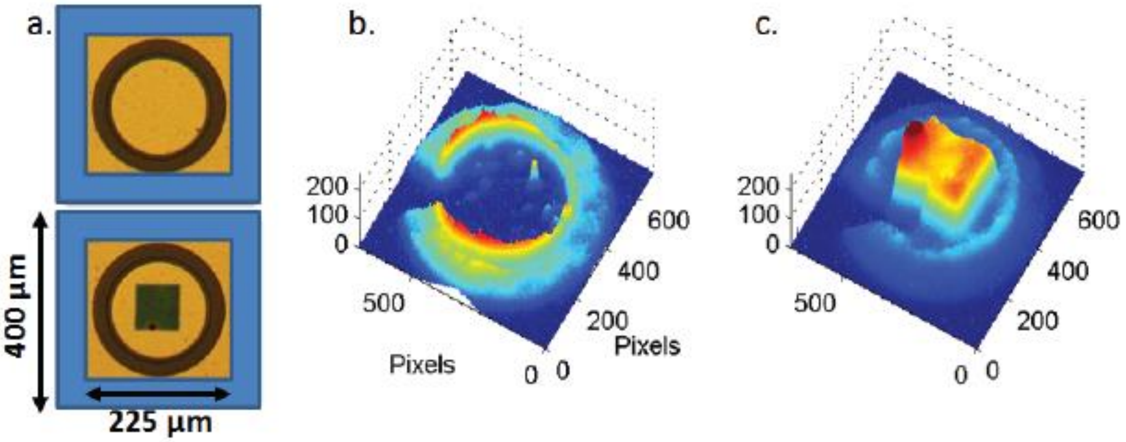

Fig. 6.6 (a.) Cropped areas of the unpatterned and patterned devices, Blue intensity images extracted from Matlab-based image analysis tool (b.) Unpatterned and (c.) Patterned devices

Once the parameters were set, images were taken at different injection currents 60mA, 80mA and 100mA. Along with these images, a background image is also taken with the LED powered off to determine the background noise level. Once the images are taken, they were cropped to the edge of the n-type contact of the LED with a cropping size of 700 px X 700 px as shown in the Figure 6.6. These cropped images are then input to the image processing tool to extract the red, green and blue pixels. Since the red and green pixel intensities have relatively insignificant intensities, only the blue pixels are chosen for further analysis as shown in Figure 6.6.

The image profiles along the horizontal axes of the images are extracted and the respective pixel intensities are compared, as shown in the Figure 6.7. These profiles are smoothed using the adjacent averaging method. The intensity profiles show an increase in the intensity in the patterned area while reducing the intensity around the edge of the contact. The averages of the pixel intensities over the area were also compared and the results are shown in Figure 6.8.

The results obtained from the Matlab image processing technique indicate that the patterned p-metal contact with hybrid PhC pillars acts as a passive optical component and helps in extraction of light from the top of the LED. This observation may also have been due to a change in the current distribution in the patterned contact, which will be studied in future efforts.

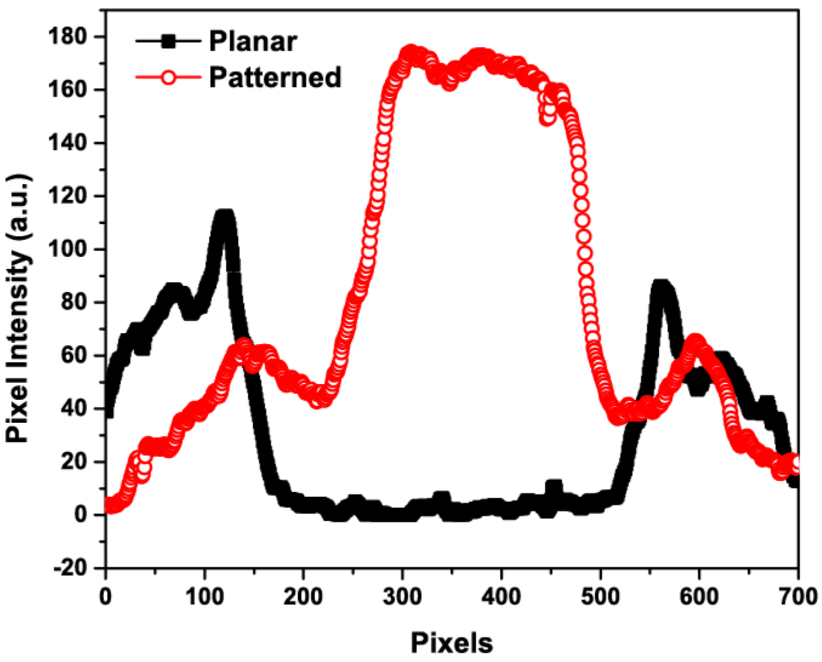

Fig. 6.7 Row intensity profiles of Planar and Patterned

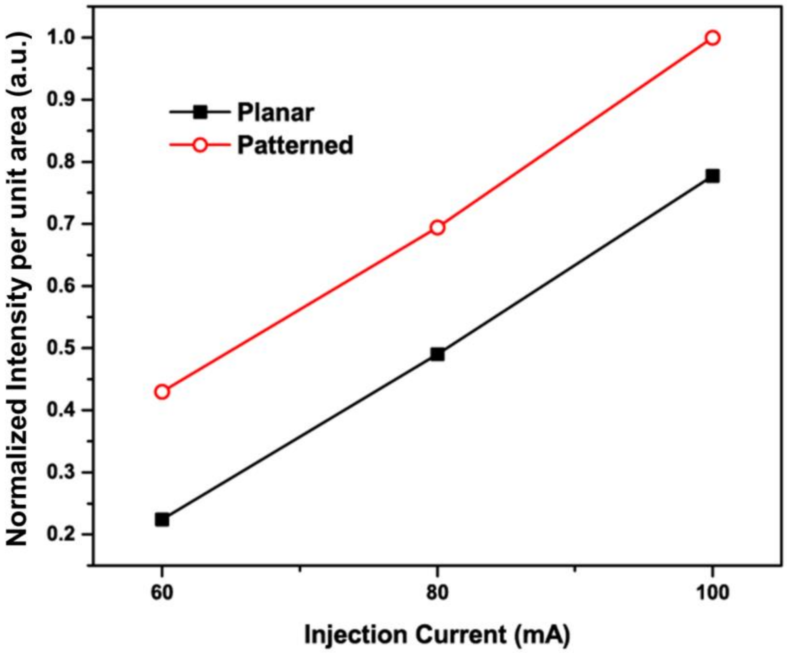

Figure 6.8 Normalized average intensities of the images of the two devices observed at injection currents 60mA, 80mA and 100mA

An improved extraction was observed from the patterned devices when compared with the unpatterned counterparts. Qualitatively, it is observed that the patterned LED has an average increase of the intensity of 30% when compared with its unpatterned counterpart. Although, this improvement is comparatively low relative to that of the extraction observed from other methods [115], [116], [117], [118], our process can be considered complementary to the existing methods and a means to achieve additional performance improvements.

6.1.1. Additional Improvements

As mentioned in the above section, additional performance improvements can be achieved by adding other light extraction methods like reflective metal coating or distributed Bragg reflectors (DBRs). This sub-section summarizes the characterization results obtained from the LEDs that had additional light extraction methods like a mirror and a DBR. A 6 period DBR designed for reflecting 440 nm wavelength consisting gallium nitride and aluminum gallium nitride (GaN/AlGaN) materials was grown using MOCVD. The LED structure is grown over the DBR and similar fabrication method was used to process the DBR LED and the patterned DBR LED. Figure 6.9 shows the devices and additional light extraction methods that can be added to improve the light extraction.

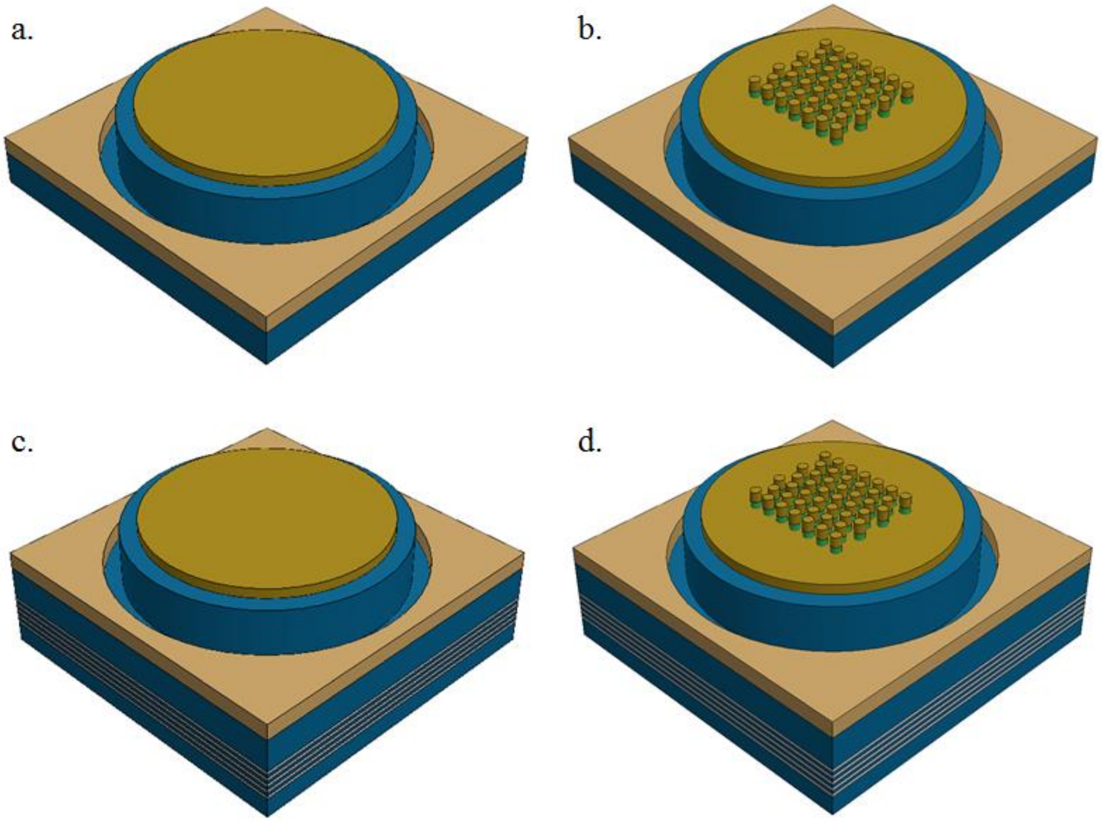

Figure 6.9 (a.) Planar, (b.) Patterned, (c.) DBR, and (d.)Patterned DBR

The IV characteristics of the DBR and patterned DBR LEDs were extracted from 4 individual devices. The averages of these IVs are shown in the Figure 6.10 and it shows there is a very small change in the characteristics. The respective normalized electro-luminescence (EL) spectra for the devices are shown in the Figure 6.11 which were observed at an injection current of 60mA using a constant current source. The spectra are smoothed using that adjacent averaging method to remove any noise. It is observed from the plot that the peak wavelengths for all the tested devices are close to the expected emission wavelength (440nm). The peak wavelength for both planar and patterned devices at different injection currents was observed to be within the range of tolerance (<1%).

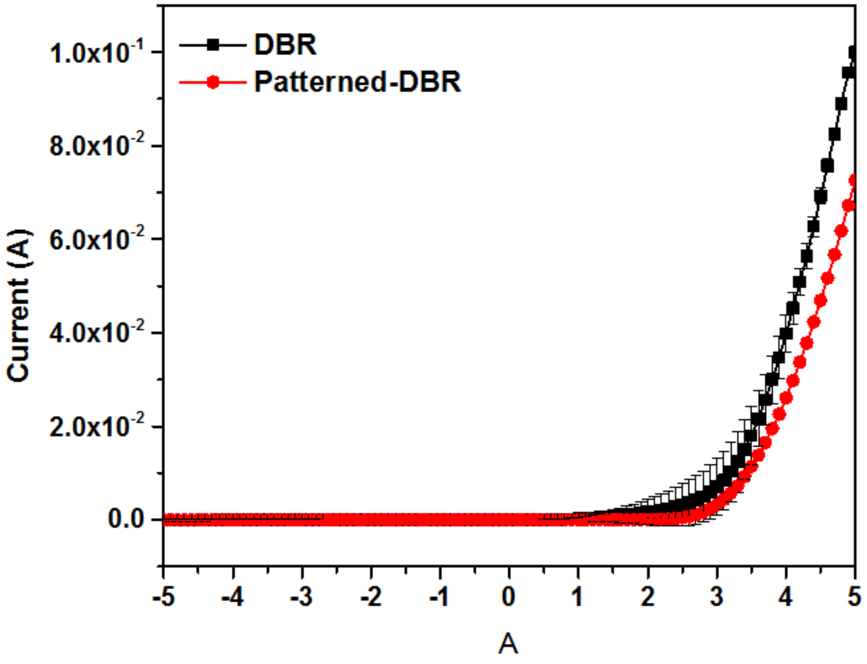

Figure 6.10 Current-Voltage Characteristics of 200µm Mesa Circular DBR LEDs

Images were taken using the camera setup with a shutter speed of 1/160 second and the Matlab image analysis program was used extract the blue intensities. Figure 6.12 shows the blue intensity profile of the DBR and the patterned DBR LEDs. The image profiles along the horizontal axes of the images are extracted and the respective pixel intensities are compared, as shown in the Figure 6.13. These profiles are smoothed using the adjacent averaging method. The intensity profiles show an increase in the intensity in the patterned area while reducing the intensity around the edge of the contact. The averages of the pixel intensities over the area were also compared and the results are shown in Figure 6.14. The results obtained from the Matlab image processing technique indicate that the patterned p-metal contact with hybrid PhC pillars acts as a passive optical component and helps in extraction of light from the top of the LED. This observation may also have been due to a change in the current distribution in the patterned contact, which will be studied in future efforts.

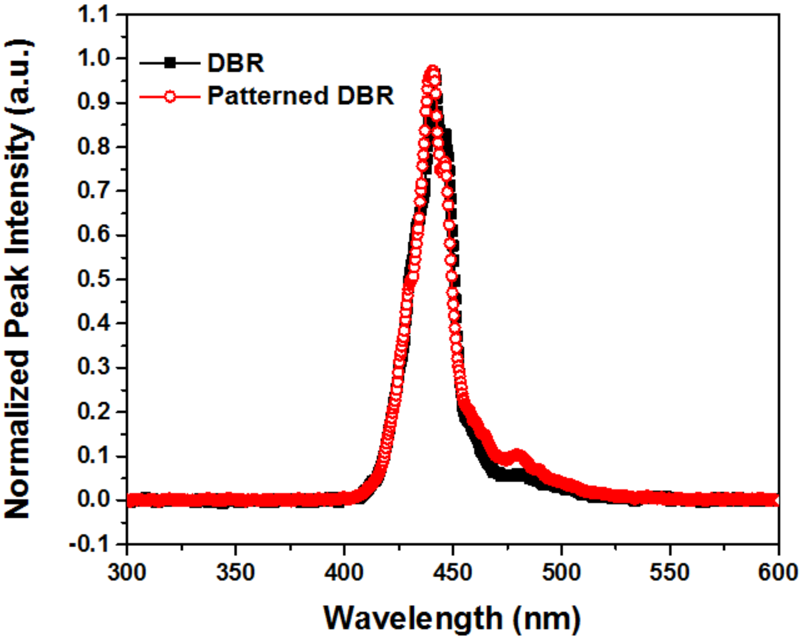

Figure 6.11 Normalized EL Spectra of DBR and patterned DBR LEDs

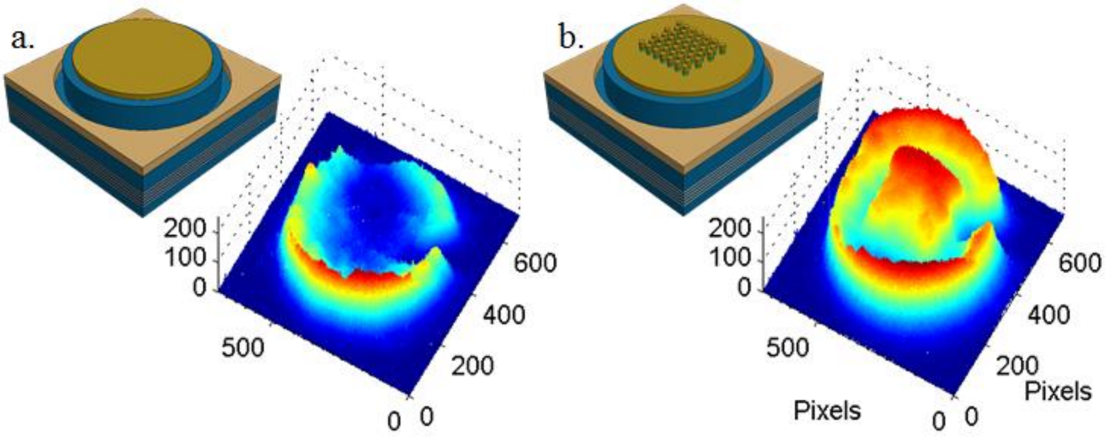

Figure 6.12 Extracted blue intensities of (a.) DBR and (b.) Patterned DBR LEDs

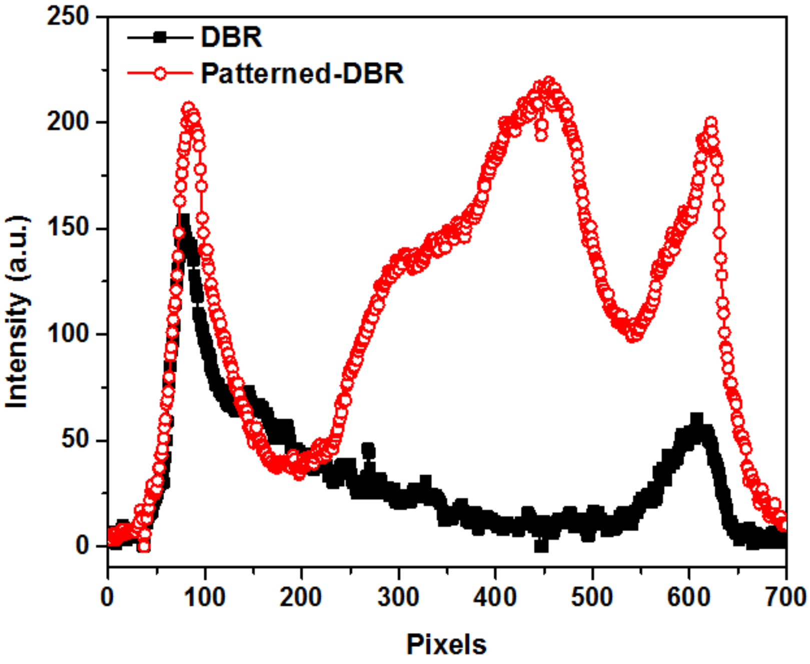

Figure 6.13 Row intensity profiles of DBR and Patterned-DBR

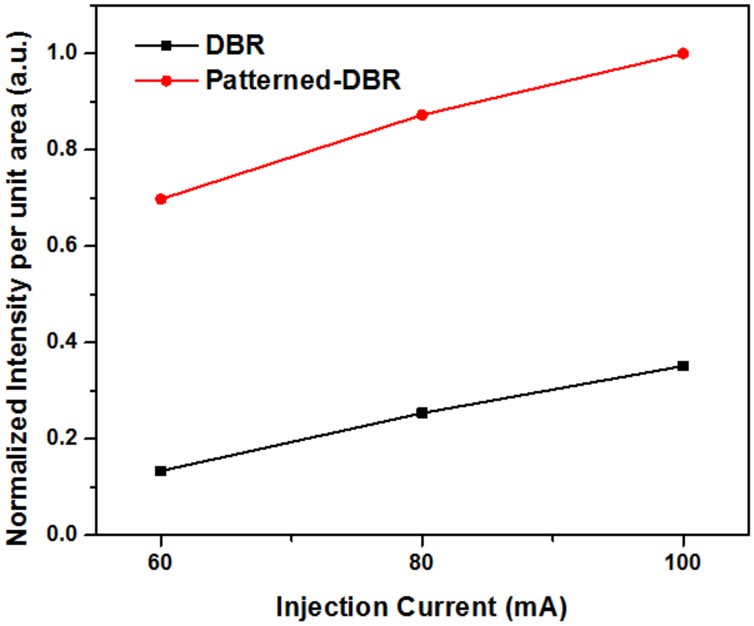

Figure 6.14 Normalized average intensities of the images of the two devices observed at injection currents 60mA, 80mA and 100mA

An improved extraction was observed from the patterned devices when compared with the unpatterned counterparts. Qualitatively, it is observed that the patterned DBR LED has 3x increase in the average intensity when compared with its unpatterned counterpart. A comparison of all the intensities including the planar and the patterned planar devices is shown in the Figure 6.15.

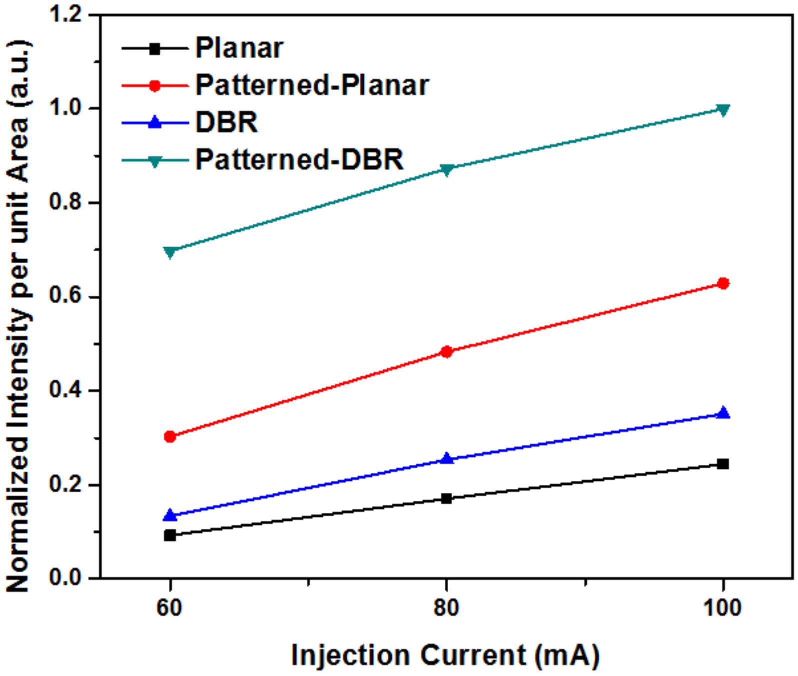

Figure 6.15 Normalized average intensities of the images of the planar, patterned, DBR and patterned-DBR devices observed at injection currents 60mA, 80mA and 100mA

In summary, the patterned DBR LEDs show a total improvement of 4.25x when compared to the planar devices. This shows that the integration of the PhC structures, in this case, the hybrid PhCs have improved the light extraction from the LEDs. In the following section, the characteristics of the hybrid PhCs ITO LEDs are summarized.

6.2. Hybrid PhC ITO LEDs

For this study, hybrid PhC structures in square and triangular lattice configuration were fabricated in ITO and characterized in a similar fashion as described in the above sections. PhC structures of 150 nm features with a pitch of 500 nm were designed in the CAD program and used for fabricating these LEDs. FOx-16 was used for fabricating these PhC structures exposed at 6000 μC/cm^2 using EBL and developed using AZ 400K diluted with water. A planar LED and control ITO LED were also fabricated along with the hybrid PhC LEDs. The fabricated structures for this study are shown in the Figure 6.16. This batch of LEDs were designed to have an emission wavelength of 455 nm. The IV characteristics of the planar, ITO, triangular hybrid and square hybrid LEDs were extracted from 2 individual devices respectively. The averages of these IVs are shown in the Figure 6.17 and as observed, the ITO layer has increased the series resistance for the LEDs. However, the increase in the series resistance compensates for the increase in photons produced at the same injection current. The respective normalized electro-luminescence (EL) spectra for the devices are shown in the Figure 6.18 which were observed at an injection current of 60mA using a constant current source. The spectra are smoothed using that adjacent averaging method to remove any noise. It is observed from the plot that the peak wavelengths for the planar and ITO LEDs differ by 5 nm and the ITO LEDs have the emission wavelength within 1% deviation from the target wavelength. The shift in the peak wavelength for the planar and ITO LEDs is due to the planar device being fabricated on a separate substrate.

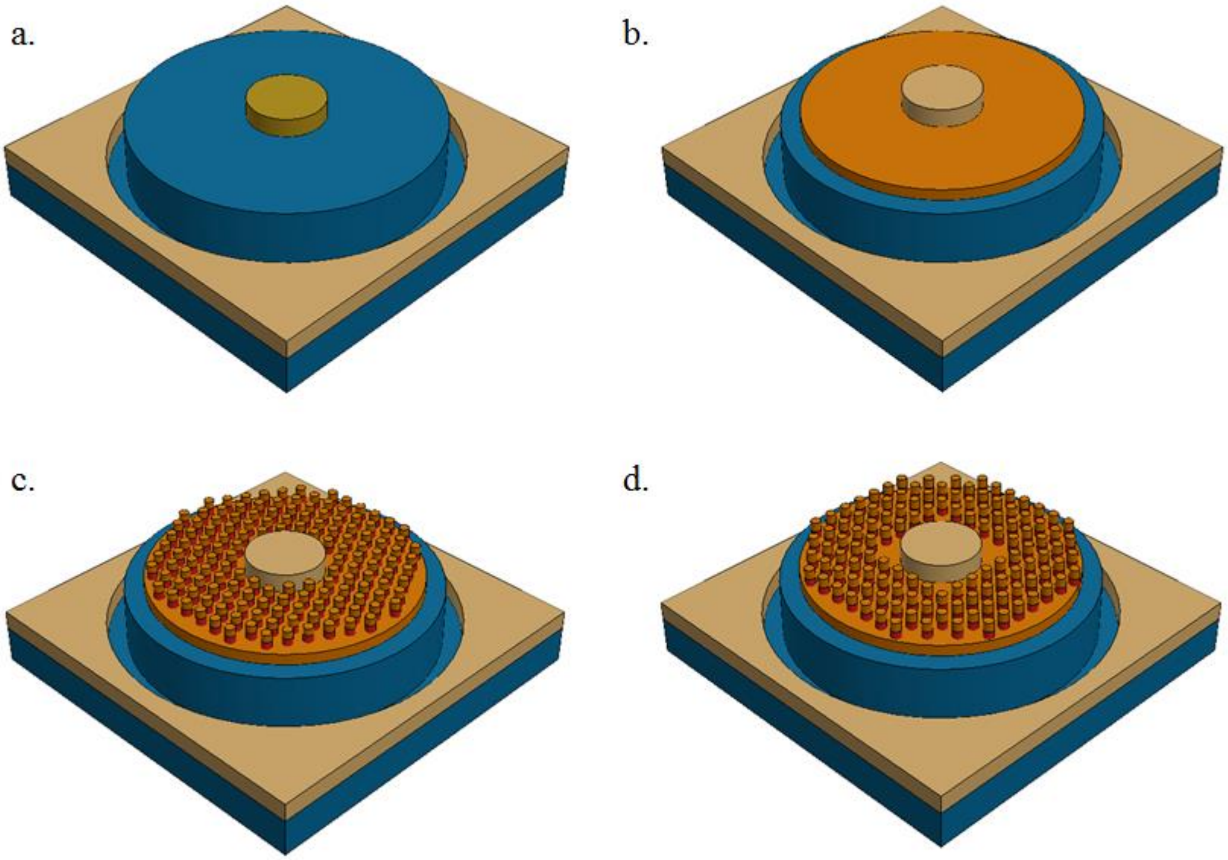

Figure 6.16 (a.) Planar, (b.) ITO, (c.) ITO Hybrid Triangular PhC, (d.) ITO Hybrid Square PhC

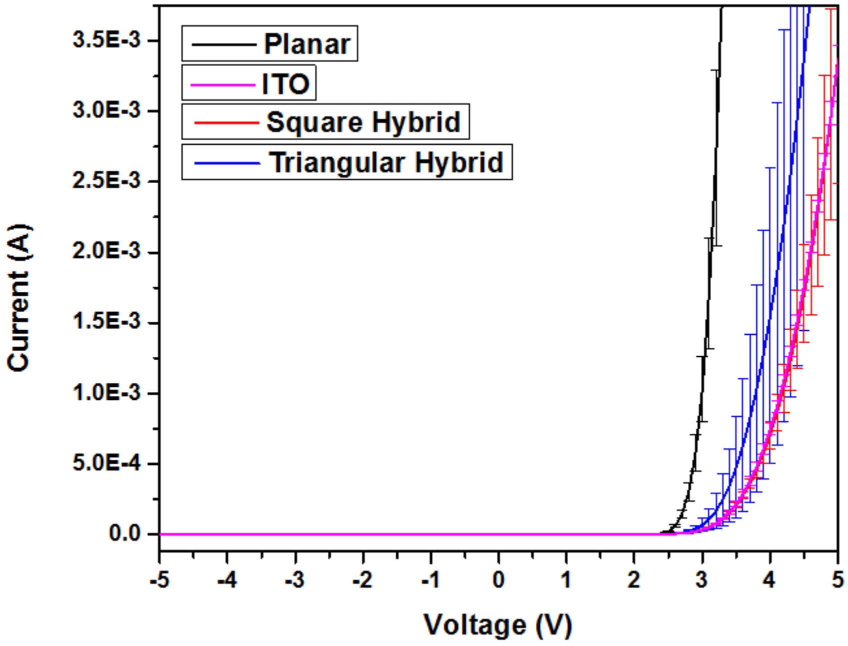

Figure 6.17 Current-Voltage Characteristics of 200µm Mesa Circular ITO LEDs and ITO LEDs with hybrid PhCs

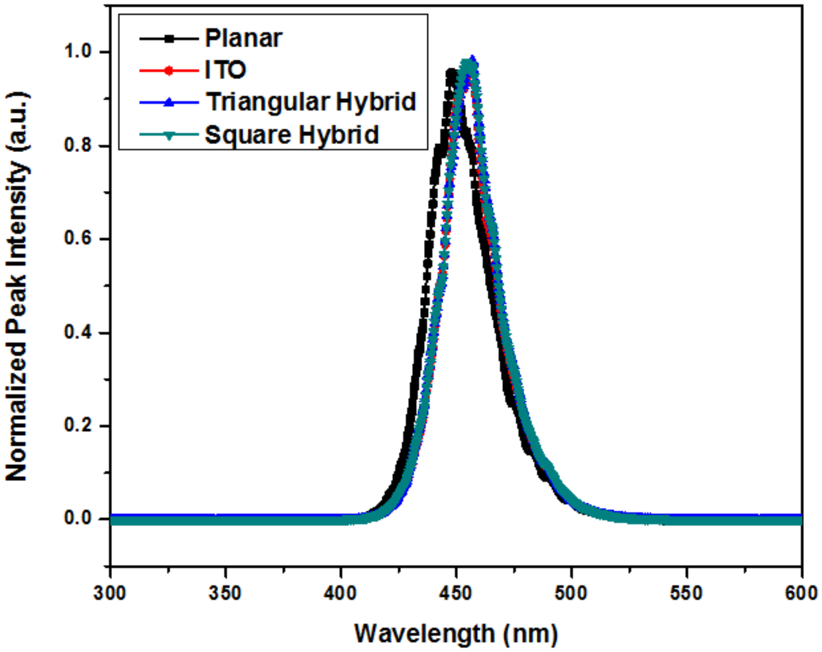

Figure 6.18 Normalized EL spectra for planar, ITO, triangular hybrid PhC and square hybrid PhC LEDs

Images were taken using the camera setup with a shutter speed of 1/8000 second and the Matlab image analysis program was used extract the blue intensities. Figure 6.19 shows the blue intensity profile of the planar, ITO, hybrid triangular PhC and hybrid square PhC LEDs. The image profiles along the horizontal axes of the images are extracted and the respective pixel intensities are compared, as shown in the Figure 6.20. These profiles are smoothed using the adjacent averaging method. The intensity profiles show an increase in the intensity in the patterned area while reducing the intensity around the edge of the contact. The averages of the pixel intensities over the area were also compared and the results are shown in Figure 6.21. The results obtained from the Matlab image processing technique indicate that the patterned ITO contact with hybrid PhC pillars improve the light extraction from the device.

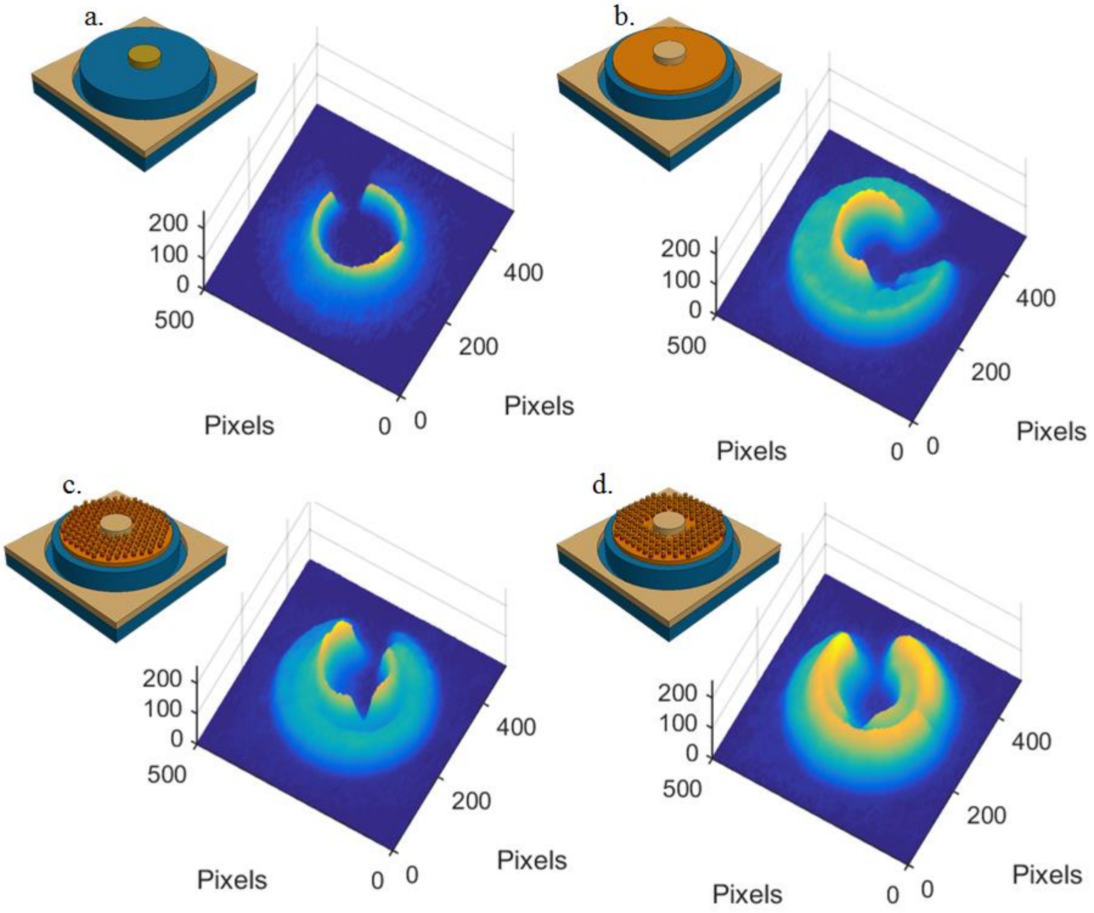

Figure 6.19 Extracted blue intensities of (a.) Planar, (b.) ITO, (c.) Hybrid Triangular PhC, and (d.) Hybrid Square PhC LEDs at 30 mA

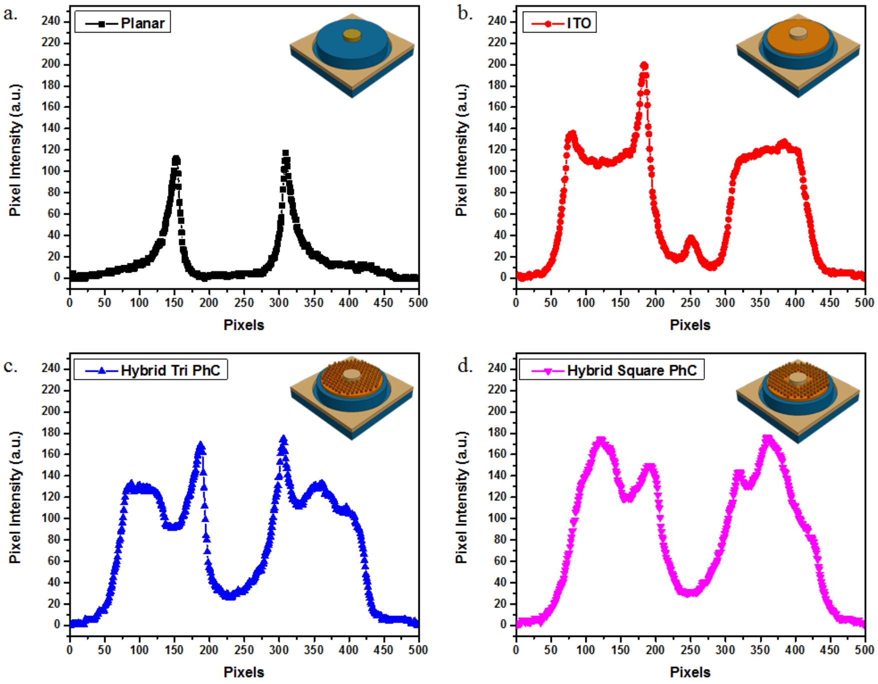

Figure 6.20 Row intensity profiles of (a.) Planar, (b.) ITO, (c.) Hybrid Triangular PhC and (d.) Hybrid Square PhC

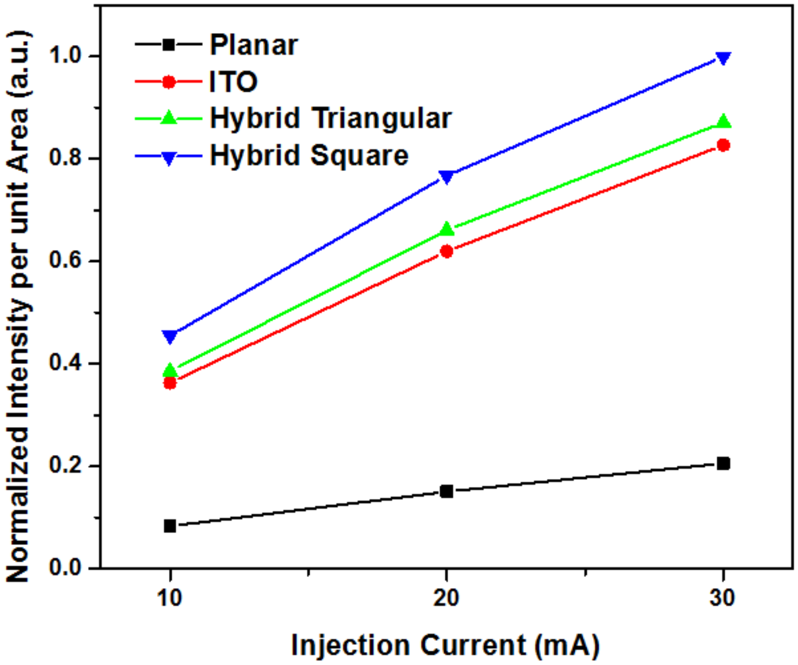

Figure 6.21 Normalized average intensities of the images of the planar, ITO, hybrid triangular PhC, and hybrid square PhC LEDs observed at injection currents 10mA, 20mA and 30mA

An improved extraction was observed from the patterned devices when compared with the unpatterned counterparts. Qualitatively, it is observed that the hybrid square PhC ITO LED, hybrid triangular PhC ITO LED, and ITO LED have 5.12x, 4.4x, and 4.15x times the average intensity when compared with the planar LED. Additionally, the radiation plots for each of these devices were extracted and compared in the Figure 6.22. From the radiation plots, it is clear that the field of view of all the devices lies in between ± 20^{o} and the hybrid square PhC LED has an improvement of 4.12x.

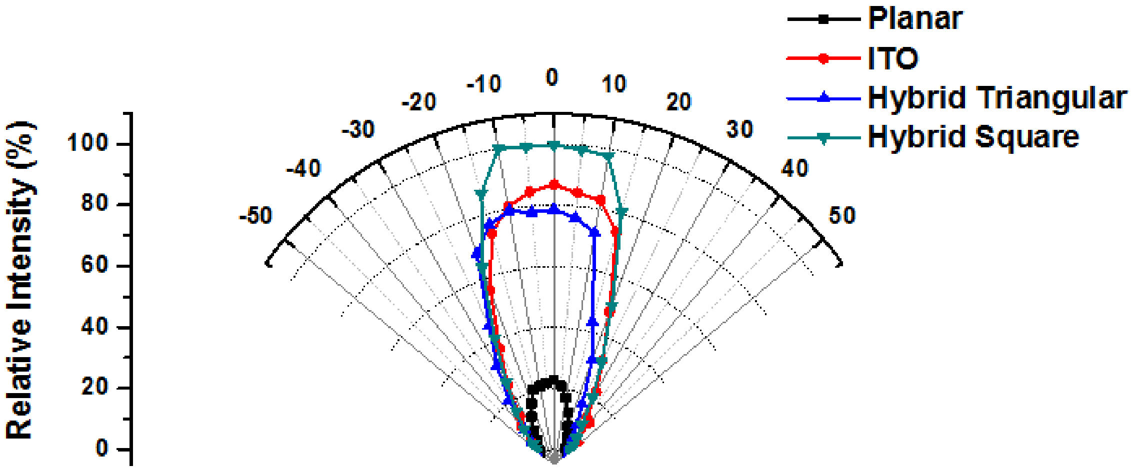

Figure 6.22 Radiation plots of the Planar, ITO, Hybrid Triangular and Hybrid Square LEDs

In summary, the square lattice of hybrid PhCs integrated in an LED showed a total improvement of 5.12x when compared to the planar device. This shows that the integration of the PhC structures, in this case, the hybrid PhCs have improved the light extraction from the LEDs.

7. Summary and Future Work

Solid-state lighting (SSL) is a lighting industry that use light-emitting diodes as the core elements to produce both commercial and household lighting. SSL industry has a lot of promise towards revolutionizing the lighting methods and contribute for energy efficient lighting. However, the core elements LEDs have device level issues that need to be addressed.

Group III-V nitride materials are the most popular materials that are being considered for these LED applications. The reason behind being the large and tunable band gap of the materials to produce a desired wavelength. Optimization of the materials and methods used in the fabrication of the core elements is important to produce an efficient light-emitting device. As mentioned earlier, the overall efficiency of these devices is classified into three major areas (injection, recombination and extraction). Of these, injection and recombination efficiencies can be optimized mostly by the material and fabrication optimization. Extraction on the other hand, requires additional methods to improve the efficiency. Several methods have been developed to improve the extraction efficiency, but require to change the structural properties of the device. By employing these methods, the extraction efficiency can be improved at the cost of the degrading other efficiencies (structural and electrical properties).

Photonic crystals (PhCs) are nanoscale periodic structures that have unique light modulating properties. With the ease of designing PhCs for specific wavelengths, several applications are emerging to use this technology. With the addition of PhCs into the device structure can help toward extraction of the light from LEDs by using their unique band gap or diffraction properties. MPB and Optiwave FDTD simulation software were used to find optimal PhC structures for maximum light extraction using either the band gap or diffraction properties. Tables 4.2 and 4.3 summarize the physical parameters of triangular and square lattice of air holes that possess a band gap for light extraction in LEDs.

One of the major hurdle is the integration of such structures into the LED structure. Development of fabrication and extraction methods that are less or non-invasive to the structural and electrical properties is the major concentration of this proposal. However, similar questions arise when traditional fabrication methods are used to integrate PhC structures with LEDs. Novel spin-on-dielectric (HSQ) was used to develop fabrication processes to help integrate hybrid and regular PhCs into the device structure without experiencing any performance degradation.

Electron beam lithography (EBL) is a lithography tool that uses an electron beam to convert the chemical state of a resist and generate a pattern. EBL in conjunction with HSQ type of resists can be a potential solution for transferring a pattern into the LED layers without major changes affecting the device structure. Results obtained by using HSQ cured into SiOx and used as a passive diffraction pattern in metal contacts show that the extraction can be improved by a significant amount. It is shown that a successful integration of hybrid PhC structures in metal and ITO contacts have improved the light extraction by 1.3x and 5.12x respectively.

However, EBL being an expensive technique for pattern transfer when large-scale production is considered, alternative techniques for pattern transfer like nanosphere lithography (NSL) were explored. Nanosphere that use nano-/micro- scale spheres to use as a mask for patterning. Two self-assembly methods, spin-coating and thermal evaporation were tested to uniformly coat a single layer of the spheres on a substrate. Of these two methods, thermal evaporation was found to be effective to coat a uniform layer of spheres on a 1.5 x 1.5 cm^2 substrate with 98.5% coverage.

In summary, the PhC integration processes into LEDs to improve the light extraction has been thoroughly studied, developed and optimized. In due course of this dissertation, design and optimization of the PhC structures for LED applications have been performed simultaneously. With the use of HSQ-EBL and NSL, the patterning of the LED structures non-invasively were done. A significant improvement in the light extraction was observed using the hybrid PhC structures and addition of other light extraction methods to the LED shown to further improve the extraction. Hence, the use of PhCs and novel hybrid PhCs show a promise in improving the light extraction from an LED and in turn the overall efficiency of the bulb. A fabrication process involving the use of self-assembly techniques was developed targeting large-scale fabrication of PhC structures for integration into commercial light bulbs.

Future work includes:

- More in-depth theoretical simulations using better simulation software and sources to find optimal PhC structures for improving the light extraction in the device.
- Hybrid PhC structures show a significant improvement in the light extraction, but do not adhere to the simulation results obtained. Further simulations need to be performed to understand the effect these hybrid PhC structures in improvement of light extraction.

- Implement and test the bilayer processing technique developed to pattern PhC lattices of air holes and quantitatively measure its effect.
- Nanosphere Lithography techniques developed in this research show a promising method to integrate PhCs into commercial devices. Future work should concentrate on developing and implementing of NSL techniques for large-scale patterning.

8. References

[1] U.S. Department of Energy, "SSL Basics," Office of Energy Efficiency & Renewable Energy, [Online]. Available: http://energy.gov/eere/ssl/ssl-basics. [Accessed 01 July 2014].

[2] N. Bardsley, S. Bland, L. Pattison, M. Pattison, K. Stober, F. Welsh and M. Yamada, "Solid-State Lighting Research and Development: Multi-Year Program Plan," U.S. Department of Energy, April 2014. [Online]. Available: http://apps1.eere.energy.gov/buildings/publications/pdfs/ssl/ssl_mypp2014_web.pdf. [Accessed 07 July 2014].

[3] General Electric Company, "60 Watt Light Bulb Comparison," General Electric Company, 2014. [Online]. Available: http://www.gelighting.com/LightingWeb/na/consumer/products/brightness/60-watt/. [Accessed 07 July 2014].

[4] S. Yi, W. J. Chung and J. Heo, "Stable and Color-Tailorable White Light from Blue LEDs Using Color-Converting Phosphor Glass Composites," *Journal of American Ceramic Society*, vol. 97, no. 2, pp. 342-345, 2014.

[5] S. Muthu, F. J. Schuurmans and M. D. Pashley, "Red, Green, and Blue LED based white light generation; Issues and control," *Industry Applications Conference*, vol. 1, pp. 327-333, 2002.

[6] E. F. Schubert, Light-Emitting Diodes, Cambridge: Cambridge University Press, 2003.

[7] P. Bhattacharya, "Light-Emitting Diodes," in *Semiconductor Optoelectronic Devices*, New Delhi, PHI Learning Private Limited, 2011, pp. 207-247.

[8] J. J. Wierer, A. David and M. M. Megens, "III-Nitride photonic-crystal light-emitting diodes with high extraction efficiency," *Nature Photonics*, vol. 3, pp. 163-169, 2009.

[9] G. Mueller, "Escape cone of light," in *Electroluminescence I*, San Diego, CA, Academic Press, 2000, pp. 67-69.

[10] S. E. Brinkley, C. L. Keraly, J. Sonoda, C. Weishbuch, J. S. Speck, S. Nakamura and S. P. DenBaars, "Chip Shaping for LIght Extraction Enhancement of Bulk c-plane Light Emitting Diodes," *Applied Physics Express* , vol. 5, pp. 032104-1 - 032104-3, 2012.

[11] W. Y. Fu, K. N. Hui, X. H. Wang, K. K. Y. Wong, P. T. Lai and H. W. Choi, "Geometrical Shaping of InGaN Light-Emitting Diodes by Laser Micromachining," *IEEE Photonics Techology Letters*, vol. 21, no. 15, pp. 1078-1080, 2009.

[12] P.-C. Wang, C.-L. Lin, Y.-K. Su, P.-C. Chien, G.-S. Huang, S.-C. Kuo and G.-C. Lyu, "Effects of TiO2-doped silicone encapsulation material on the light extraction efficiency of GaN-based blue light-emitting diodes," *Thin Solid Films*, 2014.

[13] F.-I. Lai, Y.-L. Hsieh and W.-T. Lin, "Enhancement in the extraction efficiency and resisting electrostatic discharge ability of GaN-based light emitting diode by naturally grown textured surface," *Diamond & Related Materials*, vol. 20, pp. 770-773, 2011.

[14] S.-J. Bae, J. Choi, D.-H. Kim, I.-C. Ju, C.-S. Shin, C.-G. Ko and J. S. Yu, "Characteristics and simulation analysis of GaN-based vertical light emitting diodes via wafer level surface roughening process," *Phys. Status Solidi (A)*, vol. 209, no. 6, pp. 1168-1173, 2012.

[15] T. Fujii, Y. Gao, E. Hu and S. Nakamura, "Highly efficient gallium nitride based light emitting diodes via surface roughening". Europe Patent EP 2 320 482 A2, 11 05 2011.

[16] N.-T. Yeh and C.-M. Lee, "Surface Roughening Method for Light Emitting Diode Substrate". US Patent US7901963B2, 08 03 2011.

[17] J.-H. Lee, J. Oh, Y. Kim and J.-H. Lee, "Stress Reduction and Enhanced Extraction Efficiency of GaN-Based LED Grown on Cone-Shape-Patterned-Sapphire," *IEEE Photonics Technology Letters*, vol. 20, no. 18, p. 1563, 2008.

[18] F. Bloch, "Über die Quantenmechanik der Elektronen in Kristallgittern," *Z. Physik,* vol. 52, p. 555, 1929.

[19] M. A. Mastro, B.-J. Kim, Y. Jung, J. K. Hite, C. R. Eddy Jr. and J. Kim, "Gallium nitride light emitter on a patterned sapphire substrate for improved deflectivity and light extraction efficiency," *Current Applied Physics,* vol. 11, pp. 682-686, 2011.

[20] J.-H. Lee, D.-Y. Lee, B.-W. Oh and J.-H. Lee, "Comparison of InGaN-Based LEDs Grown on Conventional Sapphire and Cone-Shape-Patterned Sapphire Substrate," *IEEE Transactions on Electron Devices,* vol. 57, no. 1, pp. 157-163, 2010.

[21] Q.-t. Xu, K. Li, F.-m. Kong and Q. Liu, "Enhancing extraction efficiency from GaN-based LED by using an omi-directional reflector and photonic crystal," *Optoelectronics Letters,* vol. 5, no. 6, pp. 405-408, 2009.

[22] K.-M. Huang, H.-J. Chang, C.-L. Ho and M.-C. Wu, "Enhanced light extraction efficiency of GaN-Based LEDs with 3D Colloidal-Photonic-Crystal Bottom Reflector," *IEEE Photonics Technology Letters,* vol. 24, no. 15, p. 1298, 2012.

[23] A. Zhmakin, "Enhancement of light extraction from light emitting diodes," *Physics Reports,* vol. 498, no. 4-5, pp. 189-241, 2011.

[24] X.-H. Li, P. Zhu, G. Liu, J. Zhang, R. Song, Y.-K. Ee, P. Kumnorkaew, J. F. Gilchrist and N. Tansu, "Light Extraction Efficiency Enhancement of III-Nitride Light-Emitting Diodes by using 2-D Close-Packed TiO2 Microsphere Arrays," *Journal of Display Technology,* vol. 9, no. 5, pp. 324-332, May 2013.

[25] L. E. Rodak and D. Korakakis, "Influence of the interface on growth in AlN/GaN short period superlattices via metal organic vapor phase epitaxy," *Applied Physics Letters,* vol. 99, no. 20, 2011.

[26] L. E. Rodak, C. M. Miller and D. Korakakis, "Surfactant effects of indium on cracking in AlN/GaN distributed bragg reflectors grown via metal organic vapor phase epitaxy," *Superlattices Microsturcutures,* vol. 49, pp. 52-59, 2011.

[27] L. E. Rodak and D. Korakakis, "Properties of aluminum gallium nitride digital alloy growth via metal organic vapor phasae epitaxy," *Journal of Electronic Materials,* vol. 40, pp. 388-393, 2011.

[28] J. Justice, A. Kadiyala, J. Dawson and D. Korakakis, "Group III-Nitride Based Electronic and Optoelectronic Integrated Circuits for Smart Lighting Applications," in *Material Research Society,* Boston, MA, 2013.

[29] K. Lee, L. E. Rodak, V. Kumbham, V. Narang, J. S. Dudding, R. Rahimi, S. Kuchibhatla, L. Hornak and D. Korakakis, "InGaN MQW LED structures using AlN/GaN DBR and Ag-based p-contact," in *Material Research Society Symposium Proceedings,* Boston, MA, 2010.

[30] S. G. Johnson and J. Joannopoulos, "Block-iterative frequency-domanin methods for Maxwell's equations in planewave basis," *Optics Express,* vol. 8, p. 173, 2001.

[31] E. Yablonovitch, "Inhibited spontaneous emission in solid-state physics and electronics," *Physical Review Letters,* vol. 58, p. 2059, 1987.

[32] X. Cao, S. J. Pearson, A. Zhang, G. T. Dang, F. Ren, R. Shul, L. Zhang, R. Hickman and J. V. Hove, "Electrical effects of plasma damage in p-GaN," *Applied Physics Letters,* vol. 75, no. 17, pp. 2569-2571, 1999.

[33] S. J. Pearton, F. Ren, A. Zhang and K. P. Lee, "Fabrication and performance of GaN electronic devices," *Materials Science and Engineering,* vol. R30, pp. 55-212, 2000.

[34] R. H. Horng, C. C. Yang, J. Y. Wu, S. H. Huang, C. E. Lee and D. S. Wuu, "GaN-based light-emitting diodes with indium tin oxide texturing window layers using natural lithography," *Applied Physics Letters,* vol. 86, p. 221101, 2005.

[35] Y. Yang and X. A. Cao, "Removing plasma-induced sidewall damage in GaN-based light-emitting diodes by annealing and wet chemical treatments," *Journal of Vacuum Science & Technology B,* vol. 27, no. 6, pp. 2337-2341, 2009.

[36] H.-Y. Lee, K.-H. Pan, C.-C. Lin, Y.-C. Chang, F.-J. Kao and C.-T. Lee, "Current spreading of III-nitride light emitting diodes using plasma treatment," *Journal of Vacuum Science & Technology B,* vol. 25, no. 4, pp. 1280-123, 2007.

[37] J.-M. Lee, C. Huh, D.-J. Kim and S.-J. Park, "Dry-etch damage and its recovery in InGaN/GaN multi quantum well light emitting diodes," *Semiconductor Science and Technology,* vol. 18, pp. 530-534, 2003.

[38] A. E. Grigorescu, M. v. Krogt, C. Hagen and P. Kruit, "10 nm lines and spaces written in HSQ, using electron beam lithography," *Microelectronic Engineering,* vol. 84, pp. 822-824, 2007.

[39] J. Vila-Comamla, S. Gorelick, V. A. Guzenko, E. Farm, M. Ritala and C. David, "Dense high aspect ratio hydrogen silsesquioxane nanostructures by 100 keV electron beam lithography," *Nanotechnology,* vol. 21, no. 28, p. 285305 (6pp), 2010.

[40] Y. Guerfi, F. Carcenac and G. Larrieu, "High resolution HSQ nanopillar arrays with low energy electron beam lithography," *Microelectronic Engineering,* vol. 110, pp. 173-176, 2013.

[41] Dow Corning, "FOX®-16 Flowable Oxide," [Online]. Available: http://www1.dowcorning.com/DataFiles/090007c880002427.pdf.

[42] B. Hamza, A. Kadiyala, L. A. Hornak, Y. Liu and J. M. Dawson, "Direct fabrication of two dimensional photonic crystal structures in silicon using positive and negative hydrogen silisesquioxane (HSQ) patterns," *Microelectronic Engineering,* Vols. 70-74, p. 91, 2012.

[43] Z. A. Lewicka, W. W. Yu and V. L. Colvin, "An alternate appraoch to fabricate metal nanoring structures based on nanosphere lithography," in *Proc. SPIE 8102, Nanoengineering: Fabrication, Properties, Optics, and Devices VIII,* 2011.

[44] M. Athanasiou, T. Kim, B. Liu, R. Smith and T. Wang, "Fabrication of two-dimensional InGaN/GaN photonic crystal structure using a modified nanosphere lithography," *Applied Physics Letters,* vol. 102, p. 191108 (6pp), 2013.

[45] J. D. Joannopoulos, R. D. Meade and J. N. Winn, Photonic Crystals: Molding the Flow of Light, New Jersey: Princeton University Press, 1995.

[46] J. Sancho, J. Bourderionnet, J. Lloret, S. Combrie and A. D. Rossi, "Integrable microwave filter based on a photonic crystal delay line," *Nature Communications,* vol. 3, 2012.

[47] X. Liu, W. Zhou, Z. Yin, X. Hao, Y. Wu and X. Xu, " Growth of single-crystalline rutile TiO2 nanorod arrays on GaN light-emitting diodes with enhanced light extraction," *Journal of Materials Chemistry,* vol. 22, pp. 3916-3921, 2012.

[48] B. M. P. F. A. Heiniger, "Limits of Diffusive Transport to an Optical Biosensor and the Impact of Optical Forces," *Frontiers in Optics*, 2012.

[49] S. A. Asher, "Adventures with Smart Chemical Sensing; Electrooptically Responsive Photonic Crystals," in *Nanoparticles: Building Blocks for Nanotechnology*, New York, 2004.

[50] J. S. Foresi, P. R. Villeneuve, J. Ferrer, E. R. Thoen, G. Steinmeyer, S. Fan, J. D. Joannopoulos, L. C. Kimerling, H. I. SMith and E. P. Ippen, "Photonic-bandgap microcavities in optical waveguides," *Letters to Nature,* vol. 390, pp. 143-145, 1997.

[51] A. Tandaechanurat, S. Ishida, D. Guimard, M. Nomura, S. Iwamoto and Y. Arakawa, "Lasing oscillation in a three-dimensional photonic crystal nanocavity with a complete bandgap," *Nature Photonics,* vol. 5, pp. 91-94, 2010.

[52] M. Boroditsky, T. F. Krauss, R. Coccioli, R. Vrijen, R. Bhat and E. Yablonovitch, "Light extraction from optically pumped light-emitting diode by thin-slab photonic crystals," *Applied Physics Letters,* vol. 75, no. 8, pp. 1036-1038, 1999.

[53] J. J. Wierer, A. David and M. M. Megens, "III-nitride photonic crystal light-emitting diodes with high extraction efficiency," *Nature Photonics,* vol. 3, pp. 163-169, 2009.

[54] H. Ouyang, L. A. DeLouise, B. L. Miller and P. M. Fauchet, "Label-Free quantitative detection of protein using macroporous silicon photonic bandgap sensors," *Analytical Chemistry,* vol. 79, pp. 1502-1506, 2007.

[55] M. Lee and P. M. Fauchet, "Two-dimensional silicon photonic crystal based biosensing platform for protein detection," *Optics Express,* vol. 15, no. 8, pp. 4530-4535, 2007.

[56] H. G. Park, S. H. Kim, S. H. Kwon, Y. G. Ju, J. K. Yang, J. H. Baek, S. B. Kim and Y. H. Lee, "Electrically driven single-cell photonic crystal laser," *Science,* vol. 305, pp. 1444-1447, 2004.

[57] S. H. Fan, P. R. Villeneuve, J. D. Joannopoulos and E. F. Schubert, "High extraction efficiency of spontaneous emission from slabs of photonic crystals," *Physics Review Letters,* vol. 78, pp. 3294-3297, 1997.

[58] M. Fujita, S. Takahashi, Y. Tanaka, T. Asano and S. Noda, "Simultaneous inhibition and redistribution of spontaneous light emission in photonic crystals," *Science,* vol. 308, pp. 1296-8, 2005.

[59] A. David, H. Benisty and C. Weisbuch, "Photonic Crystal Light-Emitting Sources," *Reports on Progress in Physics,* vol. 75, p. 126501 (38pp), 2012.

[60] O. B. Shchekin, J. E. Epler, T. A. Trottier, T. Margalith, D. A. Steigerwald, M. Holcomb, P. Martin and M. R. Krames, "High performance thin-film flip-chip InGaN-GaN light-emitting diodes," *Applied Physics Letters,* vol. 89, p. 071109, 2006.

[61] J. Wierer, A. David and M. Megens, "III-nitride photonic-crystal light-emitting diodes with high extraction efficiency," *Nature Photonics,* vol. 3, pp. 163-169, 2009.

[62] S. G. Johnson and J. D. Joannopoulos, "Block-iterative frequency-domain methods for Maxwell's equations in a planewave basis," *Optics Express,* vol. 8, no. 3, pp. 173-190, 2001.

[63] K. McGroddy, A. David, E. Matioli, M. Iza, S. Nakamura, S. DenBaars, J. S. Speck, C. Weisbuch and E. L. Hu, "Directional emission control and increased light extraction in GaN PhC light emitting diodes," *Applied Physics Letters,* vol. 93, pp. 103502-103506, 2008.

[64] A. David, T. Fujii, R. Sharma, K. McGroddy, S. Nakamura, S. P. DenBaars, E. L. Hu and C. Weisbuch, "Photonic-crystal GaN light-emitting diodes with tailored guided modes distribution," *Applied Physics Letters,* vol. 88, p. 061124, 2006.

[65] D.-H. Kim, C.-O. Cho, Y. S. Park, J. Cho, J. S. Im, Y. Park, W. J. Choi and Q.-H. Park, "Enhanced light extraction from GaN-based light-emitting diodes with holographically generated two-dimensional photonic crystal patterns," *Applied Physics Letters,* vol. 87, p. 203508, 2005.

[66] J. J. Wierer, A. David and M. M. Megens, "III-nitride photonic-crystal light-emitting didoes with high extraction efficiency," *Nature Photonics,* vol. 3, pp. 163-169, 2009.

[67] L. Rodak and D. Korakakis, "Aluminum Gallium Nitride Alloys grown via Metalorganic Vapor Phase Epitaxy using a digital growth technique," *Journal of Electronic Materials,* vol. 40, no. 4, pp. 388-393, April, 2011.

[68] L. E. Rodak, C. M. Miller and D. Korakakis, "Surfactant effects of Indium on cracking in AlN/GaN distributed bragg reflectors grown via metal organic vapour phase epitaxy," *Superlattices and Microstructures,* vol. 49, no. 1, pp. 52-59, January, 2011.

[69] S. Nakamura, T. Mukai, M. Senoh and N. Iwasa, "Thermal Annealing Effects on p-type Mg-Doped GaN Films," *Jpn. J. Applied Physics,* vol. 31, no. 2, pp. 139-142, February, 1992.

[70] L. Turlapati, Developing UV Photodetector and Ohmic Contact Techniques on GaN, Morgantown, WV, 2004.

[71] C. O'Dwyer, M. Szachowicz, G. Visimberga, V. Lavayen and C. Torres, "Bottom-up growth of fully transparent contact layers of indium tin oxide nanowiers for light-emitting diodes," *Nature Nanotechnology,* vol. 4, pp. 239-244, 2009.

[72] K. Sierros, D. Cairns, J. Abell and S. Kukureka, "Pulsed laser deposition of indium tin oxide films on flexible polyethylene naphthalate display substrates at room temperature," *Thin Solid Films,* vol. 518, no. 10, pp. 2623-2627, 2010.

[73] O. Tuna, Y. Selamet, G. Aygun and L. Ozyuzer, "High quality ITO thin films grown by dc and RF sputtering without oxygen," *J. Phys D: Appl. Phys.*, vol. 43, p. 055402 (7pp), 2010.

[74] S. Musunuru, Modeling and Analysis of GaN/InGaN Light Emitting Diodes, Morgantown, WV: West Virginia University, 2012.

[75] J. P. Ballantyne and G. R. Brewer, Electron-beam Technology in Microelectronic Fabrication, New York, NY: Academic Press, 2008.

[76] Z. Cui, Micro-nanofabrication: Technologies and Applications, New York, NY: Springer, 2005.

[77] S. Seal, Functional Nanostructures: Processing, Characterization, and Applications, New York, NY: Springer, 2008.

[78] G. Li, L. Wang, H. Ni and C. U. P. Jr., "Polyhedral Oligomeric Silsesquioxane (POSS) Polymers and Copolymers: A Review," *Journal of Inorganic and Organometallic Polymers,* vol. 11, no. 3, pp. 123-154, 2001.

[79] R. H. Baney, M. Itoh, A. Skakibara and T. Suzuki, "Silsesquioxanes," *Chemical Reviews,* vol. 95, no. 5, pp. 1409-1430, 1995.

[80] N. P. Hacker, "Semiconductor dielectric thin films". US Patent US6472076, 29 October 2002.

[81] H. G. Linde and R. A. Previti-Kelly, "Planarizing Silsesquioxane Copolymer Coating". US Patent US5043789 A, 27 August 1991.

[82] H.-J. Cho, D.-H. Hwang, J.-I. Lee, Y.-K. Jung, J.-H. Park, J. Lee, S.-K. Lee and H.-K. Shim, "Electroluminescent Polyhedral Oligomeric Silsesquioxane-Based Nanoparticle," *Chemistry of Materials,* vol. 18, no. 16, pp. 3780-3787, 2006.

[83] U. C. Pernisz, "Photoluminescent material from Hydrogen silsesquioxane resin". US Patent EP0934993B1, 4 Septemeber 2002.

[84] C.-C. Yang and W.-C. Chen, "The structures and properties of hydrogen silsesquioxane (HSQ) films produced by thermal curing," *Journal of Materials Chemistry,* vol. 12, pp. 1138-1141, 2002.

[85] R. C. Camilletti, I. Saadat and M. Thomas, "Curing Hydrogen Silsesquioxane Resin with an Electron Beam". US Patent 5609925, 11 March 1997.

[86] H. Namatsu, Y. Takahashi, K. Yamazaki, T. Yamaguchi, M. Nagase and K. Kurihara, "Three-dimensionsla siloxane resist for the formation of nanopatterns with minimum linewideth fluctuations," *Journal of Vacuum Science & Technology B,* vol. 16, no. 1, pp. 69-76, 1998.

[87] H. Namatsu, T. Yamaguchi, M. Nagase, K. Yamzaki and K. Kurihara, "Nano-patterning of a hydrogen silsesquioxane resist with reduced linewidth fluctuations," *Microelectronic Engineering,* Vols. 41-42, pp. 331-334, 1998.

[88] W. Henschel, Y. M. Georgiev and H. Kurz, "Study of high contrast process for hydrogen silsesquioxane as a negative tone e-beam resist," *Journal of Vacuum Science & Technology B,* vol. 21, pp. 2018-2025, 2003.

[89] Y. Chen, H. Yang and Z. Cui, "Effects of developing condtions on the contrast and sensitivity of hydrogen silsesquioxane," *Microelectronic Engineering,* vol. 83, no. 4-9, pp. 1119-1123, 2006.

[90] L. O'Faolain, M. V. Kotlyar, N. Tripathi, R. Wilson and T. F. Krauss, "Fabrication of photonic crystals using a spin-coated hydrogen silsesquioxane hard mask," *Journal of Vacuum Science & Technology B,* vol. 24, no. 1, pp. 336-339, 2006.

[91] J. Kretz, L. Dreeskornfeld, J. Hartwich and W. Rosner, "20 nm electron beam lithography and reactive ion etching for the fabrication of double gate FinFET devices," *Microelectronic Engineering,* Vols. 67-68, pp. 763-768, 2003.

[92] C. M. Falco, J. M. v. Delft, J. P. Weterings, A. K. v. Langen-Suurling and H. Romijn, "Hydrogren silsesquioxane/novolak bilayer resist for high aspect ratio nanoscale electron beam lithography," *Journal of Vacuum Science & Technology B,* vol. 18, no. 6, pp. 3419-3423, 2000.

[93] D. P. Mancini, K. A. Gehoski, E. Ainley, K. J. Nordquist, D. J. .. Resnick, T. C. Bailey, S. V. Sreenivasan, J. G. Ekerdt and C. G. Willson, "Hydrogen Silsesquioxane for direct electron-beam patterning of step and flash imprint lithography templates," *Journal of Vacuum Science & Technology B,* vol. 20, no. 6, pp. 2896-2901, 2002.

[94] C. L. Haynes and R. P. V. Duyne, "Nanosphere Lithography: A Versatile Nanofabrication Tool for Studies of Size-Dependent Nanoparticle Optics," *Journal of Physical Chemistry B,* vol. 105, no. 24, pp. 5599-5611, 2001.

[95] G. M. Whitesides and B. Grzybowski, "Self-Assembly at All Scales," *Science,* vol. 295, pp. 2418-2421, 2002.

[96] X. Zhang, C. R. Yonzon, M. A. Young, D. A. Stuart and R. P. V. Duyne, "Surface-enhanced Raman Spectroscopy Biosensors: Excitation Spectroscopy for Optimisation of Substrates Fabricated by Nanosphere Lithography," *IEE Proceedings - Nanobiotechnology* , vol. 152, no. 6, pp. 195-206, 2005.

[97] E. Wang and Y. Zhao, "Two-dimensional nanostructures on optical glass via nanosphere lithogrpahy and vapor HF etching," in *Nanostructured Thin Films VI,* 2013.

[98] M. Athanasiou, T. K. Kim, B. Liu, R. Smith and T. Wang, "Fabrication of two-dimensional InGaN/GaN photonic crystal structure using a modified nanosphere lithography technique," *Applied Physics Letters,* vol. 102, p. 191108, 2013.

[99] A. S. Hall, S. A. Friesen and T. E. Mallouk, "Wafer-Scale Fabrication of Plasmonic Crystals from Patterned Silicon Templates Prepared by Nanosphere Lithography," *Nano Letters,* vol. 13, no. 6, pp. 2623-2627, 2013.

[100] D. Chandler, "Interfaces and the driving force of hydrophobic assembly," *Nature,* vol. 437, pp. 640-647, 2005.

[101] K. Lee, H. Yalamanchili, L. E. Rodak, A. Kadiyala, J. Dawson and D. Korakakis, "Large-scale fabrication and observation of self-assembled silica nanospheres on GaN," *Microelectronic Engineering,* vol. 96, pp. 45-50, 2012.

[102] H. Li, J. Low, K. S. Brown and N. Wu, "Large-area well-ordered nanodot array pattern fabricated with self-assembled nanosphere template," *Sensors Journal, IEEE,* vol. 8, no. 6, pp. 880-884, 2008.

[103] B. T. Holland, C. F. Blanford and A. Stein, "Synthesis of macroporous minerals with highly ordered three-dimensional arrays of spheroidal voids," *Science,* vol. 281, pp. 538-540, 1998.

[104] P. Colson, R. Cloots and C. Henrist, "Experimental design applied to spin coating of 2D colloidal crystal masks: A relevant method?," *Langmuir,* vol. 27, no. 21, pp. 12800-12806, 2011.

[105] P. Jiang and M. J. McFarland, "Large-scale fabrication of wafer-size colloidal cyrstals, macroporous polymers, and nanocomposites by spin-coating," *Journal of American Chemical Society*, vol. 42, pp. 13778-13786, 2004.

[106] F. Iskandar, M. Abdullah, H. Yoden and K. Okuyama, "Silica films containing ordered pores prepared by dip coating of silica nanoparticles and polystyrene beads colloidal mixture," *Journal of Sol-Gel Sciene and Technology* , vol. 29, pp. 41-417, 2004.

[107] S. Rakers, L. F. Chi and H. Fuchs, "Influence of the evaporation rate on the packing order of polydisperse latex monofilms," *Langmuir,* vol. 13, pp. 7121-7124, 1997.

[108] B. G. Prevo, D. M. Kuncicky and O. D. Velev, "Engineered deposition of coatings from nano- and micro- particles: A brief review of convective assembly at high volume fraction," *Colloids and Surfaces A: Physicochemical and Engineering Aspects,* vol. 311, no. 1-3, pp. 2-10, 2007.

[109] R. Micheletto, H. Fukuda and M. Ohtsu, "A simple method for the production of a two-dimensional, ordered array of small latex particles," *Langmuir,* vol. 11, pp. 3333-3336, 1995.

[110] M.-Y. Hsieh, C.-Y. Wang, L.-Y. Chen, T.-P. Lin, M.-Y. Ke, Y.-W. Cheng, Y.-C. Yu, C. P. Chen, D.-M. Yeh, C.-F. Lu, C.-F. Lu, C.-F. Huang, C. C. Yang and J. J. Huang, "Improvement of external extraction efficiency in GaN-based LEDs by SiO2 Nanosphere lithography," *IEEE Electron Device Letters,* vol. 29, no. 7, pp. 658-660, 2008.

[111] F. C. M. J. M. v. Delft, F. J. H. v. d. Kruis, P. P. J. v. Eerd, H. A. v. Esch and H. W. J. J. v. d. Laar, "Reversing the hydrogen silsesquioxane image by silicon nitride and silicon oxide chemical mechanical polishing," *Journal of Vacuum Science & Technology B,* vol. 24, no. 6, pp. 3125-3127, 2006.

[112] W. Chen and H. Ahmed, "Fabrication of 5-7 nm wide etched lines in silicon using 100 keV electronbeam lithography and polymethylmethacrylate resist," *Applied Physics Letters,* vol. 62, pp. 1499-1501, 1993.

[113] A. Olkhovets and H. G. Craighead, "Low voltage electron beam lithography in PMMA," *Journal of Vacuum Science & Technology B,* vol. 17, pp. 1366-1370, 1999.

[114] F. C. v. Delft, J. P. Weterings, A. K. v. Langen-Suurling and H. Romijn, "Hydrogen silsesquioxane/novolak bilayer resist for high aspect ratio nanoscale electron-beam lithography," *Journal of Vacuum Science and Technology B,* vol. 18, p. 3419, 2000.

[115] W.-S. Chen, P.-S. Chen, H.-W. Wei, F. T. Chen, M.-J. Tsai and T.-K. ku, "Substrate and underlayer dependence of sub-32 nm e-beam HSQ pillar patterning process for RRAM application," in *Proceedings of SPIE* , 2012.

[116] H. Yang, A. Jin, Q. Luo, J. Li, C. Gu and Z. Cui, "Electron beam lithography of HSQ/PMMA bilayer resists for negative tone lift-off process," *Microelectronic Engineering,* vol. 85, no. 5-6, pp. 814-817, 2008.

[117] M. A. Mastro, B.-J. Kim, Y. Jung, J. K. Hite, C. R. Eddy Jr. and J. Kim, "Gallium nitride light emitter on a patterned sapphire substrate for improved deflectivity and light extraction efficiency," *Current Applied Physics*, vol. 11, no. 3, pp. 682-686, May, 2011.

[118] K.-M. Huang, H.-J. Chang, C.-L. Ho and M.-C. Wu, "Enhanced light extraction efficiency of GaN-Based LEDs with 3D Colloidal-Photonic-Crystal Bottom Reflector," *IEEE Photonics Technology Letters,* vol. 24, no. 15, pp. 1298-1300, August 1, 2012.

[119] J. Jewell, D. Simeonov, S.-C. Huang, Y.-L. Hu, S. Nakamura, J. Speck and C. Weisbuch, "Double embedded photonic crystals for extraction of guided light in light-emitting diodes," *Applied Physics Letters,* vol. 100, no. 17, p. 171105, April, 2012.

[120] X.-H. Li, R. Song, Y.-K. Ee, P. Kumnorkaew, J. Gilchrist and N. Tansu, "Light Extraction Efficiency and Radiation Patterns of III-Nitride Light Emitting Diodes with Colloidal Microlens Arrays With Various Aspect Ratios," *IEEE Photonics Journal,* vol. 3, no. 3, pp. 489-499, June, 2011.

[121] A. Khosroabadi, P. Gangopadhyay and R. Norwood, "Fabrication, electrical and optical properties of silver, indium tin oxide (ITO), and indium zinc oxide (IZO) nanostructure arrays," *Phys. Status Solidi A,* vol. 210, no. 5, pp. 831-838, 2013.

[122] M. M. El-Nahass and E. M. El-Menyawy, "Thickness dependence of structural and optical properties of indium tin oxide nanofiber thin films prepared by electron beam evaporation onto quartz substrates," *Materials Science and Engineering B,* vol. 177, pp. 145-150, 2012.

[123] M. M. Khan, "Development of a single-step fabrication process for nanoimprint stamps," Hamstad University, 2011.

[124] B. Hamza, A. Kadiyala, L. A. Hornak, Y. Liu and J. M. Dawson, "Direct fabrication of two-dimensional photonic crystal structures in silicon using positive and negative hydrogen silsesquioxane (HSQ) patterns," *Microelectronic Engineering,* vol. 91, no. --, pp. 70-74, March, 2012.

[125] Dow Corning, "FOX®-16 Flowable Oxide," [Online]. Available: http://www1.dowcorning.com/DataFiles/090007c880002427.pdf. [Accessed 20 January 2011].

[126] T. Peterson, "How to Choose the Right LED Lighting Product Color Temperature," 10 12 2010. [Online]. Available: http://www.seesmartled.com/kb/choosing_color_temperature/. [Accessed 15 07 2014].

9. Appendices

9.1. Appendix A – Band Gap Simulations

9.1.1. MPB Simulation Code

Control file required for simulating 2D PhC structures containing triangular lattice of holes.

Filename: control2d-tri.ctl

```
-----------------------------Start-of-File----------------------------
(define-param l 1) ;Define length
(define-param b 1) ;Define breadth
(define-param h 1) ;Define height
(define-param sch 12) ;Define supercell height
(define-param r 0.23) ;Define radius of the feature
(define-param nhigh 2.022) ;Dielectric constant for substrate material
(define-param nlow 1) ;Dielectric constant for hole material
(set! num-bands 8) ;Number of bands
(set! geometry-lattice (make lattice (size l b no-size)
                         (basis1 (/ (sqrt 3) 2) 0.5)
                         (basis2 (/ (sqrt 3) 2) -0.5))) ;Setting the
geometry of lattice
(set! geometry (list
(make block
                       (center 0 0 0) (size l b infinity)
                       (material (make dielectric (epsilon (* nhigh
nhigh))))) ;Defining substrate
(make cylinder
                       (center 0 0 0) (radius r) (height infinity)
                       (material (make dielectric (epsilon (* nlow
nlow))))) )) ;Defining feature
;Define k-points for simulation
(set! k-points (list (vector3 0 0 0)          ; Gamma
                     (vector3 0 0.5 0)        ; M
                     (vector3 (/ -3) (/ 3) 0) ; K
                     (vector3 0 0 0)))        ; Gamma
(set! k-points (interpolate 4 k-points)) ;Interpolation of k-points
(set! resolution 32) ;Resolution of the simulation space
(run-te) ;TE polarization
(run-tm) ;TM polarization
------------------------------End-of-File-----------------------------
```

Control file required for simulating 2D PhC structures containing square lattice of holes.

Filename: control2d-squ.ctl

```
-----------------------------Start-of-File----------------------------
(define-param l 1) ;Define length
(define-param b 1) ;Define breadth
(define-param h 1) ;Define height
```

```
(define-param sch 12) ;Define supercell height
(define-param r 0.23) ;Define radius of the feature
(define-param nhigh 2.022) ;Dielectric constant for substrate material
(define-param nlow 1) ;Dielectric constant for hole material
(set! num-bands 8) ;Number of bands
(set! geometry-lattice (make lattice (size l b no-size))) ;Setting the
geometry of lattice
(set! geometry (list
(make block
                       (center 0 0 0) (size l b infinity)
                       (material  (make  dielectric  (epsilon  (*  nhigh
nhigh))))) ;Defining substrate
(make cylinder
                       (center 0 0 0) (radius r) (height infinity)
                       (material  (make  dielectric  (epsilon  (*  nlow
nlow))))) )) ;Defining feature
(set! k-points (list (vector3 0 0 0)          ; Gamma
                     (vector3 0.5 0 0)        ; X
                     (vector3 0.5 0.5 0)      ; M
                     (vector3 0 0 0)))        ; Gamma
;Define k-points for simulation
(set! k-points (interpolate 4 k-points)) ;Interpolation of k-points
(set! resolution 32) ;Resolution of the simulation space
(run-te) ;TE polarization
(run-tm) ;TM polarization
------------------------------End-of-File-----------------------------
```

Scanning scripts were developed to pass command line parameters, simulate, extract and organize data using terminal based commands. The following file is a scanning script that simulates PhC structures in triangular lattice by changing the radius of the feature for each of the simulation.

Filename: 2dmpb-tri.sh

```
-----------------------------Start-of-File----------------------------

nhigh=(2.050 2.043 2.036 2.029 2.022) #Different Refractive Index
radius=(0.20 0.21 0.22 0.23 0.24 0.25 0.26 0.27 0.28 0.29 0.30 0.31
0.32 0.33 0.34 0.35 0.36 0.37 0.38 0.39 0.40) #Different Radii
nlow=(1) #Refractive Index of hole
for itemn in ${nhigh[*]}
do
    for itemnl in ${nlow[*]}
     do
     mkdir Info_"nh"$itemn"_nl"$itemnl
        mkdir Pictures
        mkdir TEData
        mkdir TMData
        mkdir Outfiles
        mkdir GapData
    for itemr in ${radius[*]}
     do
```

```
          #Run the simulation
          mpb l=1 b=1 r=$itemr nlow=$itemnl nhigh=$itemn control2d-
      tri.ctl > tri_nh$itemn"_nl"$itemnl"_r"$itemr.out
          #Rectangularizing the unit cell
          mpb-data -r -m 5 -n 64 epsilon.h5
          #Converting to .png
          h5topng -o tri_nh$itemn"_nl"$itemnl"_r"$itemr.png
epsilon.h5:data-new
          #Data Extraction
          grep tmfreqs tri_nh$itemn"_nl"$itemnl"_r"$itemr.out >&
tmfreqs_tri_nh$itemn"_nl"$itemnl"_r"$itemr.dat
          grep tefreqs tri_nh$itemn"_nl"$itemnl"_r"$itemr.out >&
tefreqs_tri_nh$itemn"_nl"$itemnl"_r"$itemr.dat
         grep Gap tri_nh$itemn"_nl"$itemnl"_r"$itemr.out >&
Gap_tri_nh$itemn"_nl"$itemnl"_r"$itemr.dat
         #Data Organization
          mv tri_nh$itemn"_nl"$itemnl"_r"$itemr.out Outfiles
          mv tmfreqs_tri_nh$itemn"_nl"$itemnl"_r"$itemr.dat TMData
          mv tefreqs_tri_nh$itemn"_nl"$itemnl"_r"$itemr.dat TEData
          mv Gap_tri_nh$itemn"_nl"$itemnl"_r"$itemr.dat GapData
          mv tri_nh$itemn"_nl"$itemnl"_r"$itemr.png Pictures

      done
      mv Pictures Info_"nh"$itemn"_nl"$itemnl
      mv TEData Info_"nh"$itemn"_nl"$itemnl
      mv TMData Info_"nh"$itemn"_nl"$itemnl
      mv Outfiles Info_"nh"$itemn"_nl"$itemnl
      mv GapData Info_"nh"$itemn"_nl"$itemnl

done

done
-----------------------------End-of-File------------------------------
```

The following file is a scanning script that simulates PhC structures in square lattice by changing the radius of the feature for each of the simulation.

Filename: 2dmpb-squ.sh

```
-----------------------------Start-of-File----------------------------

nhigh=(2.050 2.043 2.036 2.029 2.022) #Different Refractive Index
radius=(0.20 0.21 0.22 0.23 0.24 0.25 0.26 0.27 0.28 0.29 0.30 0.31
0.32 0.33 0.34 0.35 0.36 0.37 0.38 0.39 0.40) #Different Radii
nlow=(1) #Refractive Index of hole
for itemn in ${nhigh[*]}
do
    for itemnl in ${nlow[*]}
      do
      mkdir Info_"nh"$itemn"_nl"$itemnl
        mkdir Pictures
```

```
        mkdir TEData
        mkdir TMData
        mkdir Outfiles
        mkdir GapData
    for itemr in ${radius[*]}
     do
         #Run the simulation
         mpb l=1 b=1 r=$itemr nlow=$itemnl nhigh=$itemn control2d-
     squ.ctl > tri_nh$itemn"_nl"$itemnl"_r"$itemr.out
         #Rectangularizing the unit cell
         mpb-data -r -m 5 -n 64 epsilon.h5
         #Converting to .png
         h5topng -o tri_nh$itemn"_nl"$itemnl"_r"$itemr.png
epsilon.h5:data-new
         #Data Extraction
         grep tmfreqs tri_nh$itemn"_nl"$itemnl"_r"$itemr.out >&
tmfreqs_tri_nh$itemn"_nl"$itemnl"_r"$itemr.dat
         grep tefreqs tri_nh$itemn"_nl"$itemnl"_r"$itemr.out >&
tefreqs_tri_nh$itemn"_nl"$itemnl"_r"$itemr.dat
         grep Gap tri_nh$itemn"_nl"$itemnl"_r"$itemr.out >&
Gap_tri_nh$itemn"_nl"$itemnl"_r"$itemr.dat
         #Data Organization
         mv tri_nh$itemn"_nl"$itemnl"_r"$itemr.out Outfiles
         mv tmfreqs_tri_nh$itemn"_nl"$itemnl"_r"$itemr.dat TMData
         mv tefreqs_tri_nh$itemn"_nl"$itemnl"_r"$itemr.dat TEData
         mv Gap_tri_nh$itemn"_nl"$itemnl"_r"$itemr.dat GapData
         mv tri_nh$itemn"_nl"$itemnl"_r"$itemr.png Pictures

     done
     mv Pictures Info_"nh"$itemn"_nl"$itemnl
     mv TEData Info_"nh"$itemn"_nl"$itemnl
     mv TMData Info_"nh"$itemn"_nl"$itemnl
     mv Outfiles Info_"nh"$itemn"_nl"$itemnl
     mv GapData Info_"nh"$itemn"_nl"$itemnl

done

done
------------------------------End-of-File-----------------------------
```

To execute this file, go to the directory where the files are located and run the following command in a Linux terminal.

```
$ bash 2dmpb-tri.sh
Or
$ bash 2dmpb-squ.sh
```

Control file required for simulating finite thick PhC slab containing triangular lattice of holes.

Filename: control3d-tri.ctl

```
-----------------------------Start-of-File----------------------------

(define-param l 1) ;Define length
(define-param b 1) ;Define breadth
(define-param h 1) ;Define width
(define-param sch 12) ;Define supercell height
(define-param r 0.23) ;Define radius of hole
(define-param nhigh 2.1085) ;Refractive Index of substrate
(define-param nlow 1) ;Refractive Index of hole
(set! num-bands 8)
(set! geometry-lattice (make lattice (size l b sch)
                         (basis1 (/ (sqrt 3) 2) 0.5)
                         (basis2 (/ (sqrt 3) 2) -0.5)))
(set! geometry (list
(make block
                       (center 0 0 0) (size l b sch)
                       (material (make dielectric (epsilon (* nlow
nlow)))))
(make block
                       (center 0 0 0) (size l b h)
                       (material (make dielectric (epsilon (* nhigh
nhigh)))))
(make cylinder
                       (center 0 0 0) (radius r) (height h)
                       (material (make dielectric (epsilon (* nlow
nlow))))))
(set! k-points (list (vector3 0 0 0)          ; Gamma
                     (vector3 0 0.5 0)        ; M
                     (vector3 (/ -3) (/ 3) 0) ; K
                     (vector3 0 0 0)))        ; Gamma

(set! k-points (interpolate 4 k-points))
(set! resolution 32)
(run-zeven) ;TE polarization
(run-zodd) ;TM polarization
------------------------------End-of-File-----------------------------
```

Control file required for simulating finite thick PhC slab containing triangular lattice of holes.

Filename: control3d-squ.ctl

```
-----------------------------Start-of-File----------------------------

(define-param l 1) ;Define length
(define-param b 1) ;Define breadth
(define-param h 1) ;Define width
(define-param sch 12) ;Define supercell height
(define-param r 0.23) ;Define radius of hole
(define-param nhigh 2.1085) ;Refractive Index of substrate
(define-param nlow 1) ;Refractive Index of hole
(set! num-bands 8)
```

```
(set! geometry-lattice (make lattice (size l b sch)))
(set! geometry (list
(make block
                       (center 0 0 0) (size l b sch)
                       (material (make dielectric (epsilon (* nlow
nlow)))))
(make block
                       (center 0 0 0) (size l b h)
                       (material (make dielectric (epsilon (* nhigh
nhigh)))))
(make cylinder
                       (center 0 0 0) (radius r) (height h)
                       (material (make dielectric (epsilon (* nlow
nlow))))))
(set! k-points (list (vector3 0 0 0)          ; Gamma
                     (vector3 0 0.5 0)        ; M
                     (vector3 (/ -3) (/ 3) 0) ; K
                     (vector3 0 0 0)))        ; Gamma

(set! k-points (interpolate 4 k-points))
(set! resolution 32)
(run-zeven) ;TE polarization
(run-zodd) ;TM polarization
------------------------------End-of-File--------------------------------
```

The following file is a scanning script that simulates PhC structures in both triangular and square lattices by changing the radius and height of the feature for each of the simulation.

Filename: 3dmpb.sh

```
-----------------------------Start-of-File-------------------------------

nhigh=(2.036 2.029 2.022)
radius=(0.33 0.36 0.38)
height=(0.65 0.70 0.75 0.80 0.85 0.90 0.95 1.00 1.05 1.10 1.15 1.20)

mkdir Square3D
for itemn in ${nhigh1[*]}
do
     mkdir Info_$itemn
     mkdir Pictures
     mkdir TEData
     mkdir TMData
     mkdir Outfiles
     for itemh in ${height[*]}
     do
          for itemr in ${radius[*]}
          do
               mpirun -np 4 mpb-mpi l=1 b=1 h=$itemh r=$itemr
nhigh=$itemn tri_holes_ito.ctl >
tri_holes_ito_n$itemn"_h"$itemh"_r"$itemr.out
```

```
                mpb-data -r -m 5 -n 32 epsilon.h5
                h5topng -0z0 -o
tri_ito_holes_0z0_n$itemn"_h"$itemh"_r"$itemr.png epsilon.h5:data-new
                h5topng -0y0 -o
tri_ito_holes_0y0_n$itemn"_h"$itemh"_r"$itemr.png epsilon.h5:data-new
                h5topng -0x0 -o
tri_ito_holes_0x0_n$itemn"_h"$itemh"_r"$itemr.png epsilon.h5:data-new
                grep zoddfreqs
tri_holes_ito_n$itemn"_h"$itemh"_r"$itemr.out >&
zodd_tri_holes_ito_n$itemn"_h"$itemh"_r"$itemr.dat
                grep zevenfreqs
tri_holes_ito_n$itemn"_h"$itemh"_r"$itemr.out >&
zeven_tri_holes_ito_n$itemn"_h"$itemh"_r"$itemr.dat
                mv tri_holes_ito_n$itemn"_h"$itemh"_r"$itemr.out
Outfiles
                mv zodd_tri_holes_ito_n$itemn"_h"$itemh"_r"$itemr.dat
TMData
                mv zeven_tri_holes_ito_n$itemn"_h"$itemh"_r"$itemr.dat
TEData
                mv tri_ito_holes_0z0_n$itemn"_h"$itemh"_r"$itemr.png
tri_ito_holes_0y0_n$itemn"_h"$itemh"_r"$itemr.png
tri_ito_holes_0x0_n$itemn"_h"$itemh"_r"$itemr.png Pictures

           done

      done
      mv Pictures Info_$itemn
      mv TEData Info_$itemn
      mv TMData Info_$itemn
      mv Outfiles Info_$itemn
      mv Info_$itemn Triangle3D
done


nhigh=(2.050 2.043 2.036 2.029 2.022)
radius=(0.33 0.36 0.38)
height=(0.65 0.70 0.75 0.80 0.85 0.90 0.95 1.00 1.05 1.10 1.15 1.20)

for itemm in ${nhigh1[*]}
do
      mkdir Info_$itemm
      mkdir Pictures
      mkdir TEData
      mkdir TMData
      mkdir Outfiles
      for itemi in ${height[*]}
      do
           for itemu in ${radius[*]}
           do
                mpirun -np 4 mpb-mpi l=1 b=1 h=$itemi r=$itemu
nhigh=$itemm squ_holes_ito.ctl >
squ_holes_ito_n$itemm"_h"$itemi"_r"$itemu.out
```

```
                mpb-data -r -m 5 -n 32 epsilon.h5
                h5topng -0z0 -o
squ_ito_holes_0z0_n$itemm"_h"$itemi"_r"$itemu.png epsilon.h5:data-new
                h5topng -0y0 -o
squ_ito_holes_0y0_n$itemm"_h"$itemi"_r"$itemu.png epsilon.h5:data-new
                h5topng -0x0 -o
squ_ito_holes_0x0_n$itemm"_h"$itemi"_r"$itemu.png epsilon.h5:data-new
                grep zoddfreqs
squ_holes_ito_n$itemm"_h"$itemi"_r"$itemu.out >&
zodd_squ_holes_ito_n$itemm"_h"$itemi"_r"$itemu.dat
                grep zevenfreqs
squ_holes_ito_n$itemm"_h"$itemi"_r"$itemu.out >&
zeven_squ_holes_ito_n$itemm"_h"$itemi"_r"$itemu.dat
                mv squ_holes_ito_n$itemm"_h"$itemi"_r"$itemu.out
Outfiles
                mv zodd_squ_holes_ito_n$itemm"_h"$itemi"_r"$itemu.dat
TMData
                mv zeven_squ_holes_ito_n$itemm"_h"$itemi"_r"$itemu.dat
TEData
                mv squ_ito_holes_0z0_n$itemm"_h"$itemi"_r"$itemu.png
squ_ito_holes_0y0_n$itemm"_h"$itemi"_r"$itemu.png
squ_ito_holes_0x0_n$itemm"_h"$itemi"_r"$itemu.png Pictures

           done

     done
     mv Pictures Info_$itemm
     mv TEData Info_$itemm
     mv TMData Info_$itemm
     mv Outfiles Info_$itemm
     mv Info_$itemm Square3D
done
------------------------------End-of-File------------------------------
```

To execute this file, go to the directory where the files are located and run the following command in a Linux terminal.

```
$ bash 3dmpb.sh
```

9.1.2. Auto Plotting

The execution of the above MPB scanning scripts, generates data files containing the Eigen solutions of the Maxwell’s equations. The data file contains the solutions for 8 bands at each of the k-points simulated. A Matlab script was written to select multiple files and plot the individual data files. Alongside with data plotting, the band gaps between all or certain bands can be extracted and printed into a text file. The Matlab script has been updated with a graphical user interface (GUI) for ease of use.

Filename: plottingnew1.m

```
-------------------------------Start-of-File-------------------------------

function varargout = plottingnew1(varargin)
% PLOTTINGNEW1 MATLAB code for plottingnew1.fig
%      PLOTTINGNEW1, by itself, creates a new PLOTTINGNEW1 or raises the
existing
%      singleton*.
%
%      H = PLOTTINGNEW1 returns the handle to a new PLOTTINGNEW1 or the
handle to
%      the existing singleton*.
%
%      PLOTTINGNEW1('CALLBACK',hObject,eventData,handles,...) calls the local
%      function named CALLBACK in PLOTTINGNEW1.M with the given input
arguments.
%
%      PLOTTINGNEW1('Property','Value',...) creates a new PLOTTINGNEW1 or
raises the
%      existing singleton*.  Starting from the left, property value pairs are
%      applied to the GUI before plottingnew1_OpeningFcn gets called.  An
%      unrecognized property name or invalid value makes property application
%      stop.  All inputs are passed to plottingnew1_OpeningFcn via varargin.
%
%      *See GUI Options on GUIDE's Tools menu.  Choose "GUI allows only one
%      instance to run (singleton)".
%
% See also: GUIDE, GUIDATA, GUIHANDLES

% Edit the above text to modify the response to help plottingnew1

% Last Modified by GUIDE v2.5 05-Jun-2015 12:23:16

% Begin initialization code - DO NOT EDIT
gui_Singleton = 1;
gui_State = struct('gui_Name',       mfilename, ...
                   'gui_Singleton',  gui_Singleton, ...
                   'gui_OpeningFcn', @plottingnew1_OpeningFcn, ...
                   'gui_OutputFcn',  @plottingnew1_OutputFcn, ...
                   'gui_LayoutFcn',  [] , ...
                   'gui_Callback',   []);
if nargin && ischar(varargin{1})
    gui_State.gui_Callback = str2func(varargin{1});
end

if nargout
    [varargout{1:nargout}] = gui_mainfcn(gui_State, varargin{:});
else
    gui_mainfcn(gui_State, varargin{:});
end
% End initialization code - DO NOT EDIT


% --- Executes just before plottingnew1 is made visible.
```

```
function plottingnew1_OpeningFcn(hObject, eventdata, handles, varargin)
% This function has no output args, see OutputFcn.
% hObject    handle to figure
% eventdata  reserved - to be defined in a future version of MATLAB
% handles    structure with handles and user data (see GUIDATA)
% varargin   command line arguments to plottingnew1 (see VARARGIN)

% Choose default command line output for plottingnew1
handles.output = hObject;

% Update handles structure
guidata(hObject, handles);
clc
set(handles.panel_2D,'Visible','off')
set(handles.panel_3D,'Visible','off')
set(handles.btn_plot3D,'Visible','off')
set(handles.btn_plot2D,'Visible','off')
% UIWAIT makes plottingnew1 wait for user response (see UIRESUME)
% uiwait(handles.figure1);



% --- Outputs from this function are returned to the command line.
function varargout = plottingnew1_OutputFcn(hObject, eventdata, handles)
% varargout  cell array for returning output args (see VARARGOUT);
% hObject    handle to figure
% eventdata  reserved - to be defined in a future version of MATLAB
% handles    structure with handles and user data (see GUIDATA)

% Get default command line output from handles structure
varargout{1} = handles.output;



% --- Executes on button press in btn_2D.
function btn_2D_Callback(hObject, eventdata, handles)
% hObject    handle to btn_2D (see GCBO)
% eventdata  reserved - to be defined in a future version of MATLAB
% handles    structure with handles and user data (see GUIDATA)
set(handles.panel_3D,'Visible','off')
set(handles.btn_plot3D,'Visible','off')
visiblepanel=[1.8 11.231 92 7.231];
visiblebtn=[38 1.692 20.2 2.077];
set(handles.panel_2D,'Position',visiblepanel)
set(handles.btn_plot2D,'Position',visiblebtn);
set(handles.btn_plot2D,'Visible','on')
set(handles.panel_2D,'Visible','on')



% --- Executes on button press in btn_3D.
function btn_3D_Callback(hObject, eventdata, handles)
% hObject    handle to btn_3D (see GCBO)
% eventdata  reserved - to be defined in a future version of MATLAB
% handles    structure with handles and user data (see GUIDATA)
set(handles.btn_plot2D,'Visible','off')
set(handles.panel_2D,'Visible','off')
visiblepanel=[1.8 11.231 92 7.231];
```

```
visiblebtn=[38 1.692 20.2 2.077];
set(handles.panel_3D,'Position',visiblepanel)
set(handles.btn_plot3D,'Position',visiblebtn);
set(handles.btn_plot3D,'Visible','on')
set(handles.panel_3D,'Visible','on')


function material_Callback(hObject, eventdata, handles)
% hObject    handle to material (see GCBO)
% eventdata  reserved - to be defined in a future version of MATLAB
% handles    structure with handles and user data (see GUIDATA)

% Hints: get(hObject,'String') returns contents of material as text
%        str2double(get(hObject,'String')) returns contents of material as a
double


% --- Executes during object creation, after setting all properties.
function material_CreateFcn(hObject, eventdata, handles)
% hObject    handle to material (see GCBO)
% eventdata  reserved - to be defined in a future version of MATLAB
% handles    empty - handles not created until after all CreateFcns called

% Hint: edit controls usually have a white background on Windows.
%       See ISPC and COMPUTER.
if ispc && isequal(get(hObject,'BackgroundColor'),
get(0,'defaultUicontrolBackgroundColor'))
    set(hObject,'BackgroundColor','white');
end



function index_Callback(hObject, eventdata, handles)
% hObject    handle to index (see GCBO)
% eventdata  reserved - to be defined in a future version of MATLAB
% handles    structure with handles and user data (see GUIDATA)

% Hints: get(hObject,'String') returns contents of index as text
%        str2double(get(hObject,'String')) returns contents of index as a
double


% --- Executes during object creation, after setting all properties.
function index_CreateFcn(hObject, eventdata, handles)
% hObject    handle to index (see GCBO)
% eventdata  reserved - to be defined in a future version of MATLAB
% handles    empty - handles not created until after all CreateFcns called

% Hint: edit controls usually have a white background on Windows.
%       See ISPC and COMPUTER.
if ispc && isequal(get(hObject,'BackgroundColor'),
get(0,'defaultUicontrolBackgroundColor'))
    set(hObject,'BackgroundColor','white');
end
```

```
function wavelength_Callback(hObject, eventdata, handles)
% hObject    handle to wavelength (see GCBO)
% eventdata  reserved - to be defined in a future version of MATLAB
% handles    structure with handles and user data (see GUIDATA)

% Hints: get(hObject,'String') returns contents of wavelength as text
%        str2double(get(hObject,'String')) returns contents of wavelength as
a double


% --- Executes during object creation, after setting all properties.
function wavelength_CreateFcn(hObject, eventdata, handles)
% hObject    handle to wavelength (see GCBO)
% eventdata  reserved - to be defined in a future version of MATLAB
% handles    empty - handles not created until after all CreateFcns called

% Hint: edit controls usually have a white background on Windows.
%       See ISPC and COMPUTER.
if ispc && isequal(get(hObject,'BackgroundColor'),
get(0,'defaultUicontrolBackgroundColor'))
    set(hObject,'BackgroundColor','white');
end



% --- Executes on selection change in numbands.
function numbands_Callback(hObject, eventdata, handles)
% hObject    handle to numbands (see GCBO)
% eventdata  reserved - to be defined in a future version of MATLAB
% handles    structure with handles and user data (see GUIDATA)

% Hints: contents = cellstr(get(hObject,'String')) returns numbands contents
as cell array
%        contents{get(hObject,'Value')} returns selected item from numbands


% --- Executes during object creation, after setting all properties.
function numbands_CreateFcn(hObject, eventdata, handles)
% hObject    handle to numbands (see GCBO)
% eventdata  reserved - to be defined in a future version of MATLAB
% handles    empty - handles not created until after all CreateFcns called

% Hint: popupmenu controls usually have a white background on Windows.
%       See ISPC and COMPUTER.
if ispc && isequal(get(hObject,'BackgroundColor'),
get(0,'defaultUicontrolBackgroundColor'))
    set(hObject,'BackgroundColor','white');
end



function filepath_Callback(hObject, eventdata, handles)
```

```
% hObject    handle to filepath (see GCBO)
% eventdata  reserved - to be defined in a future version of MATLAB
% handles    structure with handles and user data (see GUIDATA)

% Hints: get(hObject,'String') returns contents of filepath as text
%        str2double(get(hObject,'String')) returns contents of filepath as a
double


% --- Executes during object creation, after setting all properties.
function filepath_CreateFcn(hObject, eventdata, handles)
% hObject    handle to filepath (see GCBO)
% eventdata  reserved - to be defined in a future version of MATLAB
% handles    empty - handles not created until after all CreateFcns called

% Hint: edit controls usually have a white background on Windows.
%       See ISPC and COMPUTER.
if ispc && isequal(get(hObject,'BackgroundColor'),
get(0,'defaultUicontrolBackgroundColor'))
    set(hObject,'BackgroundColor','white');
end

% --- Executes on button press in btn_plot2D.
function btn_plot2D_Callback(hObject, eventdata, handles)
% hObject    handle to btn_plot2D (see GCBO)
% eventdata  reserved - to be defined in a future version of MATLAB
% handles    structure with handles and user data (see GUIDATA)
rstart=str2double(get(handles.rstart,'String'));
rsteps=str2double(get(handles.rsteps,'String'));
rend=str2double(get(handles.rend,'String'));
radius= rstart:rsteps:rend;
rlength=length(radius);
TETM=upper(get(handles.TETM,'String'));
numbands=str2double(get(handles.numbands,'String'));
material=get(handles.material,'String');
index=get(handles.index,'String');
wavelength=get(handles.wavelength,'String');
phctype=get(handles.phctype,'Value');
[files,pathname]=uigetfile('*.dat','Select the file(s)','Multiselect','on');
filenames=sort(files);
set(handles.filepath,'String',pathname);
for i=1:rlength
    current=strcat(pathname,char(filenames(i)));
    data=dlmread(current,',',1,1);
    kindex=data(:,1);
    lightcone=data(:,5);
    bands=data(:,6:6+numbands-1);
    [row,col]=size(bands);
    bandb(i)=max(bands(:,1));
    bandt(i)=min(bands(:,2));
    if TETM == 'TE'
        plot(kindex,bands,'.-r','LineWidth',2);
        switch phctype
            case 2
```

```
        title(strcat('\bf{',TETM,'--Band diagram for -',material,'-
PhC of pillars with-(r=', num2str(radius(i)),',n=',index,', at
\lambda=',wavelength,'nm)}'));
      case 3
        title(strcat('\bf{',TETM,'--Band diagram for -',material,'-
PhC of holes with-(r=', num2str(radius(i)),',n=',index,', at
\lambda=',wavelength,'nm)}'));
      otherwise
        errordlg('Please select the PhC type');
    end
    xlabel('\bf{k-index}');
    ylabel('\bf{frequency (a/\lambda)}');
    axis tight;
    for j=1:col-2
      [band_bottom,k]=max(bands(:,j));
      [band_top,l]=min(bands(:,j+1));
      if band_top > band_bottom
        band_mid=(band_top + band_bottom)/2;
        band_gap=(band_top - band_bottom)*100/band_mid;
        text(6,0.1,strcat('\bf{Band
Bottom:',num2str(band_bottom),'}'));
        text(6,0.18,strcat('\bf{Band top:',num2str(band_top),'}'));
        text(6,band_mid,strcat('\bf{Gap}',num2str(j),'-
',num2str(j+1),' : ',num2str(band_gap),'%'));
      end
    end
else if TETM == 'TM'
    plot(kindex,bands,'.-b','LineWidth',2);
    switch phctype
      case 2
        title(strcat('\bf{',TETM,'--Band diagram for -',material,'-
PhC of pillars with-(r=', num2str(radius(i)),',n=',index,', at
\lambda=',wavelength,'nm)}'));
      case 3
        title(strcat('\bf{',TETM,'--Band diagram for -',material,'-
PhC of holes with-(r=', num2str(radius(i)),',n=',index,', at
\lambda=',wavelength,'nm)}'));
      otherwise
        errordlg('Please select the PhC type');
    end
    xlabel('\bf{k-index}');
    ylabel('\bf{frequency (a/\lambda)}');
    axis tight;
    for j=1:col-2
      [band_bottom,k]=max(bands(:,j));
      [band_top,l]=min(bands(:,j+1));
      if band_top > band_bottom
        band_mid=(band_top + band_bottom)/2;
        band_gap=(band_top - band_bottom)*100/band_mid;
        text(6,0.1,strcat('\bf{Band
Bottom:',num2str(band_bottom),'}'));
        text(6,0.18,strcat('\bf{Band top:',num2str(band_top),'}'));
        text(6,band_mid,strcat('\bf{Gap}',num2str(j),'-
',num2str(j+1),' : ',num2str(band_gap),'%'));
      end
    end
    end
```

```
    end
    pause(0.5);
    switch phctype
            case 2

fname=strcat(pathname,TETM,'_holes_n',num2str(index),'_r',num2str(radius(i)),
'.jpg');
            case 3

fname=strcat(pathname,TETM,'_pillars_n',num2str(index),'_r',num2str(radius(i)
),'.jpg');
        otherwise
                errordlg('Please select the PhC type');
    end
    export_fig(handles.axes,fname);
    im=imread(fname);
    im2=imcrop(im,[500 80 475 375]);
    imwrite(im2,fname,'jpeg');
end

% --- Executes on button press in btn_plot3D.
function btn_plot3D_Callback(hObject, eventdata, handles)
% hObject    handle to btn_plot3D (see GCBO)
% eventdata  reserved - to be defined in a future version of MATLAB
% handles    structure with handles and user data (see GUIDATA)
hstart=str2double(get(handles.hstart,'String'));
hsteps=str2double(get(handles.hsteps,'String'));
hend=str2double(get(handles.hend,'String'));
height= hstart:hsteps:hend;
fradius=str2double(get(handles.fradius,'String'));
radius=get(handles.fradius,'String');
selectband=str2double(get(handles.selectband,'String'));
hlength=length(height);
bandtop=zeros(1,hlength);
bandbottom=zeros(1,hlength);
Zevenodd=upper(get(handles.Zevenodd,'String'));
numbands=str2double(get(handles.numbands,'String'));
material=get(handles.material,'String');
index=get(handles.index,'String');
wavelength=get(handles.wavelength,'String');
phctype=get(handles.phctype,'Value');
[files,pathname]=uigetfile('*.dat','Select the file(s)','Multiselect','on');
filenames=sort(files);
set(handles.filepath,'String',pathname);
for i=1:hlength
    current=strcat(pathname,char(filenames(i)));
    data=dlmread(current, ',',1,1);
    kindex=data(:,1);
    lightcone=data(:,5);
    bands=data(:,6:6+numbands-1);
    [row col]=size(bands);
    j=selectband;
    [x,y]=curveintersect(kindex,lightcone,kindex,bands(:,j+1));
    band_bottom=max(bands(:,j));
    band_top=min(bands(:,j+1));
    if strcmp(Zevenodd,'ZEVEN')
        plot(kindex,bands,'.-r','LineWidth',2);
```

```
        hold on;
        plot(x,y,'b*','LineWidth',2,'MarkerSize',10);
        if band_top > band_bottom
            band_mid=(band_top + band_bottom)/2;
            band_gap=(band_top - band_bottom)*100/band_mid;
            dlmwrite(strcat(pathname,'Zeven_bandgaps_',radius,'.txt'),
[height(i) band_gap],'-append','delimiter',' ','newline','pc',
'precision',3);
            text(6,0.1,strcat('\bf{Band Bottom:',num2str(band_bottom),'}'));
            text(6,0.18,strcat('\bf{Band top:',num2str(band_top),'}'));
            text(6,band_mid,strcat('\bf{Gap}',num2str(j),'-',num2str(j+1),' :
',num2str(band_gap),'%'));
        end
        plot(kindex,lightcone,'.-k','LineWidth',3);
        hold off;
        switch phctype
            case 2
                title(strcat('\bf{',Zevenodd,'--Band diagram for -
',material,'-PhC of pillars with-(r=',
num2str(fradius),',h=',num2str(height(i)),'n=',index,', at
\lambda=',wavelength,'nm)}'));
            case 3
                title(strcat('\bf{',Zevenodd,'--Band diagram for -
',material,'-PhC of holes with-(r=',
num2str(fradius),',h=',num2str(height(i)),',n=',index,', at
\lambda=',wavelength,'nm)}'));
            otherwise
                errordlg('Please select the PhC type');
        end
        xlabel('\bf{k-index}');
        ylabel('\bf{frequency (a/\lambda)}');
    elseif strcmp(Zevenodd,'ZODD')
        plot(kindex,bands,'.-b','LineWidth',2);
        hold on;
        plot(x,y,'r*','LineWidth',2,'MarkerSize',10);
        if band_top > band_bottom
            band_mid=(band_top + band_bottom)/2;
            band_gap=(band_top - band_bottom)*100/band_mid;
            dlmwrite(strcat(pathname,'Zodd_bandgaps_',radius,'.txt'),
[height(i) band_gap],'-append','delimiter',' ','newline','pc',
'precision',3);
            text(6,0.1,strcat('\bf{Band Bottom:',num2str(band_bottom),'}'));
            text(6,0.18,strcat('\bf{Band top:',num2str(band_top),'}'));
            text(6,band_mid,strcat('\bf{Gap}',num2str(j),'-',num2str(j+1),' :
',num2str(band_gap),'%'));
        end
        plot(kindex,lightcone,'.-k','LineWidth',3);
        hold off;
        switch phctype
            case 2
                title(strcat('\bf{',Zevenodd,'--Band diagram for -
',material,'-PhC of pillars with-(r=',
num2str(fradius),',h=',num2str(height(i)),'n=',index,', at
\lambda=',wavelength,'nm)}'));
            case 3
                title(strcat('\bf{',Zevenodd,'--Band diagram for -
',material,'-PhC of holes with-(r=',
```

```
num2str(fradius),',h=',num2str(height(i)),',n=',index,', at
\lambda=',wavelength,'nm)}'));
            otherwise
                errordlg('Please select the PhC type');
        end
        xlabel('\bf{k-index}');
        ylabel('\bf{frequency (a/\lambda)}');
    end
    pause(0.5);
    switch phctype
            case 2

fname=strcat(pathname,Zevenodd,'_holes_n',num2str(index),'_r',num2str(fradius
),'_h',num2str(height(i)),'.jpg');
            case 3

fname=strcat(pathname,Zevenodd,'_pillars_n',num2str(index),'_r',num2str(fradi
us),'_h',num2str(height(i)),'.jpg');
        otherwise
                errordlg('Please select the PhC type');
    end
    export_fig(handles.axes,fname);
    im=imread(fname);
    im2=imcrop(im,[500 80 475 375]);
    imwrite(im2,fname,'jpeg');
end

function hstart_Callback(hObject, eventdata, handles)
% hObject    handle to hstart (see GCBO)
% eventdata  reserved - to be defined in a future version of MATLAB
% handles    structure with handles and user data (see GUIDATA)

% Hints: get(hObject,'String') returns contents of hstart as text
%        str2double(get(hObject,'String')) returns contents of hstart as a
double


% --- Executes during object creation, after setting all properties.
function hstart_CreateFcn(hObject, eventdata, handles)
% hObject    handle to hstart (see GCBO)
% eventdata  reserved - to be defined in a future version of MATLAB
% handles    empty - handles not created until after all CreateFcns called

% Hint: edit controls usually have a white background on Windows.
%       See ISPC and COMPUTER.
if ispc && isequal(get(hObject,'BackgroundColor'),
get(0,'defaultUicontrolBackgroundColor'))
    set(hObject,'BackgroundColor','white');
end



function hsteps_Callback(hObject, eventdata, handles)
% hObject    handle to hsteps (see GCBO)
% eventdata  reserved - to be defined in a future version of MATLAB
```

```
% handles    structure with handles and user data (see GUIDATA)

% Hints: get(hObject,'String') returns contents of hsteps as text
%        str2double(get(hObject,'String')) returns contents of hsteps as a
double


% --- Executes during object creation, after setting all properties.
function hsteps_CreateFcn(hObject, eventdata, handles)
% hObject    handle to hsteps (see GCBO)
% eventdata  reserved - to be defined in a future version of MATLAB
% handles    empty - handles not created until after all CreateFcns called

% Hint: edit controls usually have a white background on Windows.
%       See ISPC and COMPUTER.
if ispc && isequal(get(hObject,'BackgroundColor'),
get(0,'defaultUicontrolBackgroundColor'))
    set(hObject,'BackgroundColor','white');
end




function hend_Callback(hObject, eventdata, handles)
% hObject    handle to hend (see GCBO)
% eventdata  reserved - to be defined in a future version of MATLAB
% handles    structure with handles and user data (see GUIDATA)

% Hints: get(hObject,'String') returns contents of hend as text
%        str2double(get(hObject,'String')) returns contents of hend as a
double


% --- Executes during object creation, after setting all properties.
function hend_CreateFcn(hObject, eventdata, handles)
% hObject    handle to hend (see GCBO)
% eventdata  reserved - to be defined in a future version of MATLAB
% handles    empty - handles not created until after all CreateFcns called

% Hint: edit controls usually have a white background on Windows.
%       See ISPC and COMPUTER.
if ispc && isequal(get(hObject,'BackgroundColor'),
get(0,'defaultUicontrolBackgroundColor'))
    set(hObject,'BackgroundColor','white');
end


% --- Executes on selection change in Zevenodd.
function Zevenodd_Callback(hObject, eventdata, handles)
% hObject    handle to Zevenodd (see GCBO)
% eventdata  reserved - to be defined in a future version of MATLAB
% handles    structure with handles and user data (see GUIDATA)

% Hints: contents = cellstr(get(hObject,'String')) returns Zevenodd contents
as cell array
```

```
%        contents{get(hObject,'Value')} returns selected item from Zevenodd


% --- Executes during object creation, after setting all properties.
function Zevenodd_CreateFcn(hObject, eventdata, handles)
% hObject    handle to Zevenodd (see GCBO)
% eventdata  reserved - to be defined in a future version of MATLAB
% handles    empty - handles not created until after all CreateFcns called

% Hint: popupmenu controls usually have a white background on Windows.
%       See ISPC and COMPUTER.
if ispc && isequal(get(hObject,'BackgroundColor'),
get(0,'defaultUicontrolBackgroundColor'))
    set(hObject,'BackgroundColor','white');
end



function fradius_Callback(hObject, eventdata, handles)
% hObject    handle to fradius (see GCBO)
% eventdata  reserved - to be defined in a future version of MATLAB
% handles    structure with handles and user data (see GUIDATA)

% Hints: get(hObject,'String') returns contents of fradius as text
%        str2double(get(hObject,'String')) returns contents of fradius as a
double


% --- Executes during object creation, after setting all properties.
function fradius_CreateFcn(hObject, eventdata, handles)
% hObject    handle to fradius (see GCBO)
% eventdata  reserved - to be defined in a future version of MATLAB
% handles    empty - handles not created until after all CreateFcns called

% Hint: edit controls usually have a white background on Windows.
%       See ISPC and COMPUTER.
if ispc && isequal(get(hObject,'BackgroundColor'),
get(0,'defaultUicontrolBackgroundColor'))
    set(hObject,'BackgroundColor','white');
end



function rstart_Callback(hObject, eventdata, handles)
% hObject    handle to rstart (see GCBO)
% eventdata  reserved - to be defined in a future version of MATLAB
% handles    structure with handles and user data (see GUIDATA)

% Hints: get(hObject,'String') returns contents of rstart as text
%        str2double(get(hObject,'String')) returns contents of rstart as a
double


% --- Executes during object creation, after setting all properties.
```

```
function rstart_CreateFcn(hObject, eventdata, handles)
% hObject    handle to rstart (see GCBO)
% eventdata  reserved - to be defined in a future version of MATLAB
% handles    empty - handles not created until after all CreateFcns called

% Hint: edit controls usually have a white background on Windows.
%       See ISPC and COMPUTER.
if ispc && isequal(get(hObject,'BackgroundColor'),
get(0,'defaultUicontrolBackgroundColor'))
    set(hObject,'BackgroundColor','white');
end



function rsteps_Callback(hObject, eventdata, handles)
% hObject    handle to rsteps (see GCBO)
% eventdata  reserved - to be defined in a future version of MATLAB
% handles    structure with handles and user data (see GUIDATA)

% Hints: get(hObject,'String') returns contents of rsteps as text
%        str2double(get(hObject,'String')) returns contents of rsteps as a
double


% --- Executes during object creation, after setting all properties.
function rsteps_CreateFcn(hObject, eventdata, handles)
% hObject    handle to rsteps (see GCBO)
% eventdata  reserved - to be defined in a future version of MATLAB
% handles    empty - handles not created until after all CreateFcns called

% Hint: edit controls usually have a white background on Windows.
%       See ISPC and COMPUTER.
if ispc && isequal(get(hObject,'BackgroundColor'),
get(0,'defaultUicontrolBackgroundColor'))
    set(hObject,'BackgroundColor','white');
end



function rend_Callback(hObject, eventdata, handles)
% hObject    handle to rend (see GCBO)
% eventdata  reserved - to be defined in a future version of MATLAB
% handles    structure with handles and user data (see GUIDATA)

% Hints: get(hObject,'String') returns contents of rend as text
%        str2double(get(hObject,'String')) returns contents of rend as a
double


% --- Executes during object creation, after setting all properties.
function rend_CreateFcn(hObject, eventdata, handles)
% hObject    handle to rend (see GCBO)
% eventdata  reserved - to be defined in a future version of MATLAB
% handles    empty - handles not created until after all CreateFcns called
```

```
% Hint: edit controls usually have a white background on Windows.
%       See ISPC and COMPUTER.
if ispc && isequal(get(hObject,'BackgroundColor'),
get(0,'defaultUicontrolBackgroundColor'))
    set(hObject,'BackgroundColor','white');
end


% --- Executes on selection change in TETM.
function TETM_Callback(hObject, eventdata, handles)
% hObject    handle to TETM (see GCBO)
% eventdata  reserved - to be defined in a future version of MATLAB
% handles    structure with handles and user data (see GUIDATA)

% Hints: contents = cellstr(get(hObject,'String')) returns TETM contents as
cell array
%        contents{get(hObject,'Value')} returns selected item from TETM


% --- Executes during object creation, after setting all properties.
function TETM_CreateFcn(hObject, eventdata, handles)
% hObject    handle to TETM (see GCBO)
% eventdata  reserved - to be defined in a future version of MATLAB
% handles    empty - handles not created until after all CreateFcns called

% Hint: popupmenu controls usually have a white background on Windows.
%       See ISPC and COMPUTER.
if ispc && isequal(get(hObject,'BackgroundColor'),
get(0,'defaultUicontrolBackgroundColor'))
    set(hObject,'BackgroundColor','white');
end


% --- Executes on selection change in phctype.
function phctype_Callback(hObject, eventdata, handles)
% hObject    handle to phctype (see GCBO)
% eventdata  reserved - to be defined in a future version of MATLAB
% handles    structure with handles and user data (see GUIDATA)

% Hints: contents = cellstr(get(hObject,'String')) returns phctype contents
as cell array
%        contents{get(hObject,'Value')} returns selected item from phctype


% --- Executes during object creation, after setting all properties.
function phctype_CreateFcn(hObject, eventdata, handles)
% hObject    handle to phctype (see GCBO)
% eventdata  reserved - to be defined in a future version of MATLAB
% handles    empty - handles not created until after all CreateFcns called

% Hint: popupmenu controls usually have a white background on Windows.
%       See ISPC and COMPUTER.
```

```
if ispc && isequal(get(hObject,'BackgroundColor'),
get(0,'defaultUicontrolBackgroundColor'))
    set(hObject,'BackgroundColor','white');
end



function selectband_Callback(hObject, eventdata, handles)
% hObject    handle to selectband (see GCBO)
% eventdata  reserved - to be defined in a future version of MATLAB
% handles    structure with handles and user data (see GUIDATA)

% Hints: get(hObject,'String') returns contents of selectband as text
%        str2double(get(hObject,'String')) returns contents of selectband as
a double


% --- Executes during object creation, after setting all properties.
function selectband_CreateFcn(hObject, eventdata, handles)
% hObject    handle to selectband (see GCBO)
% eventdata  reserved - to be defined in a future version of MATLAB
% handles    empty - handles not created until after all CreateFcns called

% Hint: edit controls usually have a white background on Windows.
%       See ISPC and COMPUTER.
if ispc && isequal(get(hObject,'BackgroundColor'),
get(0,'defaultUicontrolBackgroundColor'))
    set(hObject,'BackgroundColor','white');
end

function [x,y]=curveintersect(varargin)
% Curve Intersections.
% [X,Y]=CURVEINTERSECT(H1,H2) or [X,Y]=CURVEINTERSECT([H1 H2]) finds the
% intersection points of the two curves on the X-Y plane identified
% by the line or lineseries object handles H1 and H2.
%
% [X,Y]=CURVEINTERSECT(X1,Y1,X2,Y2) finds the intersection points of the
% two curves described by the vector data pairs (X1,Y1) and (X2,Y2).
%
% X and Y are empty if no intersection exists.
%
% Example
% -------
% x1=rand(10,1); y1=rand(10,1); x2=rand(10,1); y2=rand(10,1);
% [x,y]=curveintersect(x1,y1,x2,y2);
% plot(x1,y1,'k',x2,y2,'b',x,y,'ro')
%
% Original Version (-> curveintersect_local)
% ---------------------------------------
% D.C. Hanselman, University of Maine, Orono, ME 04469
% Mastering MATLAB 7
% 2005-01-06
%
% Improved Version (-> this function)
% -----------------------------------
```

```
% S. Hölz, TU Berlin, Germany
% v 1.0: October 2005
% v 1.1: April   2006     Fixed some minor bugs in function 'mminvinterp'

x=[]; y=[];
[x1,y1,x2,y2]=local_parseinputs(varargin{:});
ind_x1=sign(diff(x1)); ind_x2=sign(diff(x2));

ind1=1;
while ind1<length(x1)
    ind_max = ind1+min(find(ind_x1(ind1:end)~=ind_x1(ind1)))-1;
    if isempty(ind_max) | ind_max==ind1; ind_max=length(x1); end
    ind1=ind1:ind_max;

    ind2=1;
    while ind2<length(x2)
        ind_max = ind2+min(find(ind_x2(ind2:end)~=ind_x2(ind2)))-1;
        if isempty(ind_max) | ind_max==ind2; ind_max=length(x2); end
        ind2=ind2:ind_max;

        % Fallunterscheidung
        if ind_x1(ind1(1))==0 & ind_x2(ind2(1))~=0
            x_loc=x1(ind1(1));
            y_loc=interp1(x2(ind2),y2(ind2),x_loc);
            if ~(y_loc>=min(y1(ind1)) && y_loc<=max(y1(ind1))); y_loc=[];
x_loc=[]; end

        elseif ind_x2(ind2(1))==0 & ind_x1(ind1(1))~=0
            x_loc=x2(ind2(1));
            y_loc=interp1(x1(ind1),y1(ind1),x_loc);
            if ~(y_loc>=min(y2(ind2)) && y_loc<=max(y2(ind2))); y_loc=[];
x_loc=[]; end

        elseif ind_x2(ind2(1))~=0 & ind_x1(ind1(1))~=0

[x_loc,y_loc]=curveintersect_local(x1(ind1),y1(ind1),x2(ind2),y2(ind2));

        elseif ind_x2(ind2(1))==0 & ind_x1(ind1(1))==0
            [x_loc,y_loc]=deal([]);

        end
        x=[x; x_loc(:)];
        y=[y; y_loc(:)];
        ind2=ind2(end);
    end
    ind1=ind1(end);
end

% -----------------------------------------------
function [x,y]=curveintersect_local(x1,y1,x2,y2)

if ~isequal(x1,x2)
   xx=unique([x1 x2]); % get unique data points
   xx=xx(xx>=max(min(x1),min(x2)) & xx<=min(max(x1),max(x2)));
   if numel(xx)<2
```

```
      x=[];
      y=[];
      return
   end
   yy=interp1(x1,y1,xx)-interp1(x2,y2,xx);
else
   xx=x1;
   yy=y1-y2;
end
x=mminvinterp(xx,yy,0); % find zero crossings of difference
if ~isempty(x)
   y=interp1(x1,y1,x);
else
   x=[];
   y=[];
end

%--------------------------------------------------------------------------
%--------------------------------------------------------------------------
function [xo,yo]=mminvinterp(x,y,yo)
%MMINVINTERP 1-D Inverse Interpolation. From the text "Mastering MATLAB 7"
% [Xo, Yo]=MMINVINTERP(X,Y,Yo) linearly interpolates the vector Y to find
% the scalar value Yo and returns all corresponding values Xo interpolated
% from the X vector. Xo is empty if no crossings are found. For
% convenience, the output Yo is simply the scalar input Yo replicated so
% that size(Xo)=size(Yo).
% If Y maps uniquely into X, use INTERP1(Y,X,Yo) instead.
%
% See also INTERP1.

if nargin~=3
   error('Three Input Arguments Required.')
end
n = numel(y);
if ~isequal(n,numel(x))
   error('X and Y Must have the Same Number of Elements.')
end
if ~isscalar(yo)
   error('Yo Must be a Scalar.')
end

x=x(:); % stretch input vectors into column vectors
y=y(:);

if yo<min(y) || yo>max(y) % quick exit if no values exist
   xo = [];
   yo = [];
else                       % find the desired points

   below = y<yo;           % True where below yo
   above = y>yo;           % True where above yo
   on    = y==yo;          % True where on yo

   kth = (below(1:n-1)&above(2:n)) | (above(1:n-1)&below(2:n));     % point k
   kp1 = [false; kth];                                               % point
k+1
```

```
   xo = [];                                                        %
distance between x(k+1) and x(k)
   if any(kth);
       alpha = (yo - y(kth))./(y(kp1)-y(kth));
       xo = alpha.*(x(kp1)-x(kth)) + x(kth);
   end
   xo = sort([xo; x(on)]);                                         % add
points, which are directly on line

   yo = repmat(yo,size(xo));                                       %
duplicate yo to match xo points found
end
%--------------------------------------------------------------------------
function [x1,y1,x2,y2]=local_parseinputs(varargin)

if nargin==1 % [X,Y]=CURVEINTERSECT([H1 H2])
   arg=varargin{1};
   if numel(arg)==2 && ...
      all(ishandle(arg)) && all(strcmp(get(arg,'type'),'line'))
      data=get(arg,{'XData','YData'});
      [x1,x2,y1,y2]=deal(data{:});
   else
      error('Input Must Contain Two Handles to Line Objects.')
   end
elseif nargin==2 % [X,Y]=CURVEINTERSECT(H1,H2)
   arg1=varargin{1};
   arg2=varargin{2};
   if numel(arg1)==1 && ishandle(arg1) && strcmp(get(arg1,'type'),'line')...
   && numel(arg2)==1 && ishandle(arg2) && strcmp(get(arg2,'type'),'line')

      data=get([arg1;arg2],{'XData','YData'});
      [x1,x2,y1,y2]=deal(data{:});
   else
      error('Input Must Contain Two Handles to Line Objects.')
   end
elseif nargin==4
   [x1,y1,x2,y2]=deal(varargin{:});
   if ~isequal(numel(x1),numel(y1))
      error('X1 and Y1 Must Contain the Same Number of Elements.')
   elseif ~isequal(numel(x2),numel(y2))
      error('X2 and Y2 Must Contain the Same Number of Elements.')
   end
   x1=reshape(x1,1,[]); % make data into rows
   x2=reshape(x2,1,[]);
   y1=reshape(y1,1,[]);
   y2=reshape(y2,1,[]);

else
   error('Incorrect Number of Input Arguments.')
end
if min(x1)>max(x2) | min(x2)>max(x1) | min(y2)>max(y1) | min(y1)>max(y2) %
Polygons can not have intersections
    x1=[]; y1=[]; x2=[]; y2=[]; return
end
if numel(x1)<2 || numel(x2)<2 || numel(y1)<2 || numel(y2)<2
```

```
   error('At Least Two Data Points are Required for Each Curve.')
end
------------------------------End-of-File------------------------------
```

The .fig file associated with this file is shown in the Figure 9.1.

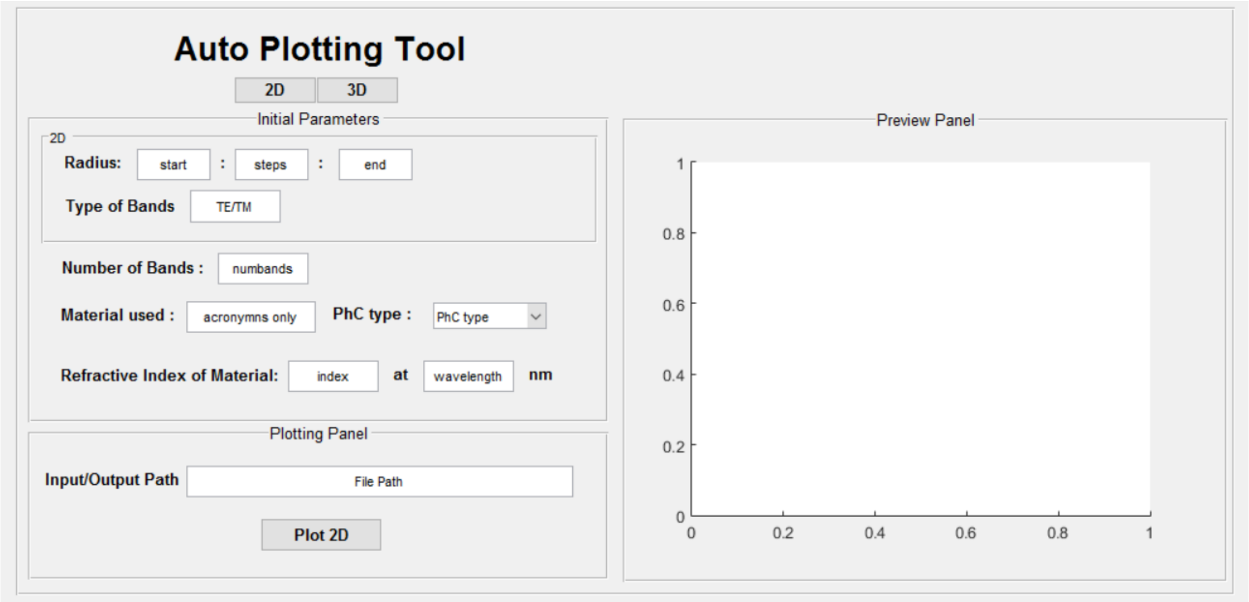

Figure 9.1 GUI layout for plotting 2D & 3D simulation data

The following Figures show the step by step process of plotting the data either for 2D or 3D simulations. For 2D data plotting, click on the 2D button and a form appears with text fields for parameters like the radius, bands type, number of bands, material used, PhC type, refractive index and the wavelength. After filling this information, click on the Plot 2D button and this prompts for selecting the data files as shown in the Figure 9.2. Navigate to the file location and select all the files to be plotted. The software then sorts and starts to plot the data in the preview pane as shown in the Figure 9.3.

For 3D data plotting, click on the 3D button and a form appears with text fields for parameters like the radius, height, bands type, number of bands, material used, PhC type, refractive index and the wavelength. After filling this information, click on the Plot 3D button and this prompts for selecting the data files as shown in the Figure 9.4. Navigate to the file location and select all the files to be plotted. The software then sorts and starts to plot the data in the preview pane as shown in the Figure 9.5.

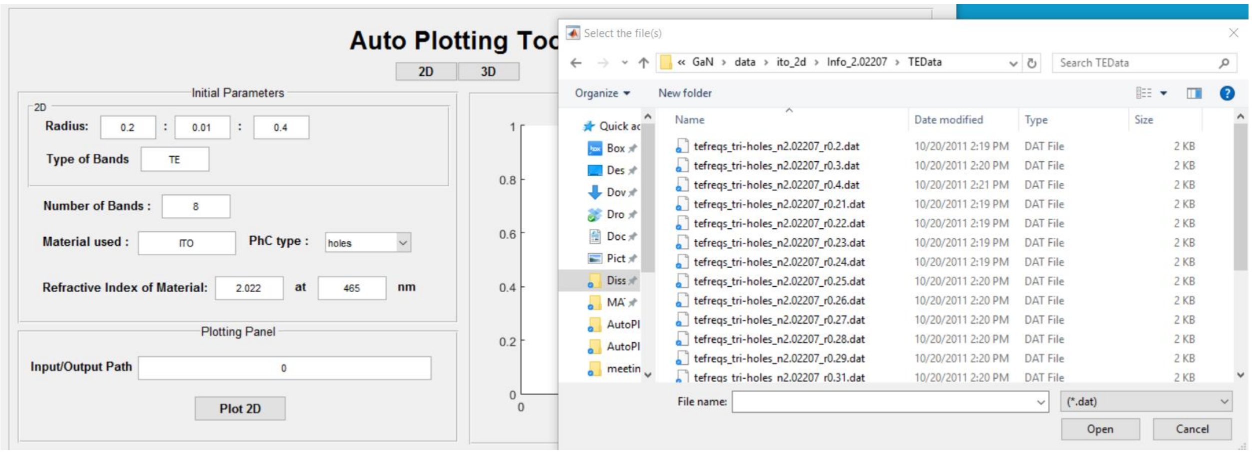

2D

Radius: 0.2 : 0.01 : 0.4

Type of Bands: TE

Number of Bands : 8

Material used : ITO

PhC type : holes

Refractive Index of Material: 2.022 at 465 nm

Input/Output Path: 0

« GaN › data › ito_2d › Info_2.02207 › TEData

Search TEData

Name	Date modified	Type	Size
tefreqs_tri-holes_n2.02207_r0.2.dat	10/20/2011 2:19 PM	DAT File	2 KB
tefreqs_tri-holes_n2.02207_r0.3.dat	10/20/2011 2:20 PM	DAT File	2 KB
tefreqs_tri-holes_n2.02207_r0.4.dat	10/20/2011 2:21 PM	DAT File	2 KB
tefreqs_tri-holes_n2.02207_r0.21.dat	10/20/2011 2:19 PM	DAT File	2 KB
tefreqs_tri-holes_n2.02207_r0.22.dat	10/20/2011 2:19 PM	DAT File	2 KB
tefreqs_tri-holes_n2.02207_r0.23.dat	10/20/2011 2:19 PM	DAT File	2 KB
tefreqs_tri-holes_n2.02207_r0.24.dat	10/20/2011 2:19 PM	DAT File	2 KB
tefreqs_tri-holes_n2.02207_r0.25.dat	10/20/2011 2:20 PM	DAT File	2 KB
tefreqs_tri-holes_n2.02207_r0.26.dat	10/20/2011 2:20 PM	DAT File	2 KB
tefreqs_tri-holes_n2.02207_r0.27.dat	10/20/2011 2:20 PM	DAT File	2 KB
tefreqs_tri-holes_n2.02207_r0.28.dat	10/20/2011 2:20 PM	DAT File	2 KB
tefreqs_tri-holes_n2.02207_r0.29.dat	10/20/2011 2:20 PM	DAT File	2 KB
tefreqs_tri-holes_n2.02207_r0.31.dat	10/20/2011 2:20 PM	DAT File	2 KB

File name:

(*.dat)

Figure 9.2 2D Data files selection window

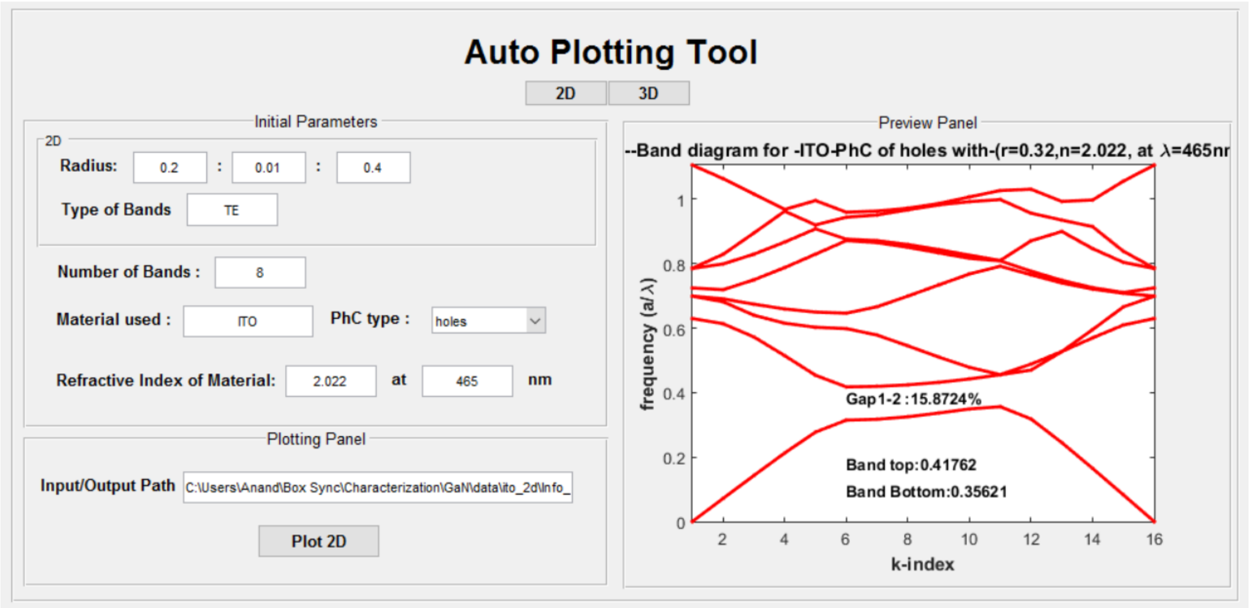

2D

Radius: 0.2 : 0.01 : 0.4

Type of Bands: TE

Number of Bands : 8

Material used : ITO

PhC type : holes

Refractive Index of Material: 2.022 at 465 nm

Input/Output Path: C:\Users\Anand\Box Sync\Characterization\GaN\data\ito_2d\Info_

Figure 9.3 Screenshot of the Auto Plotting Tool with the 2D band diagram preview

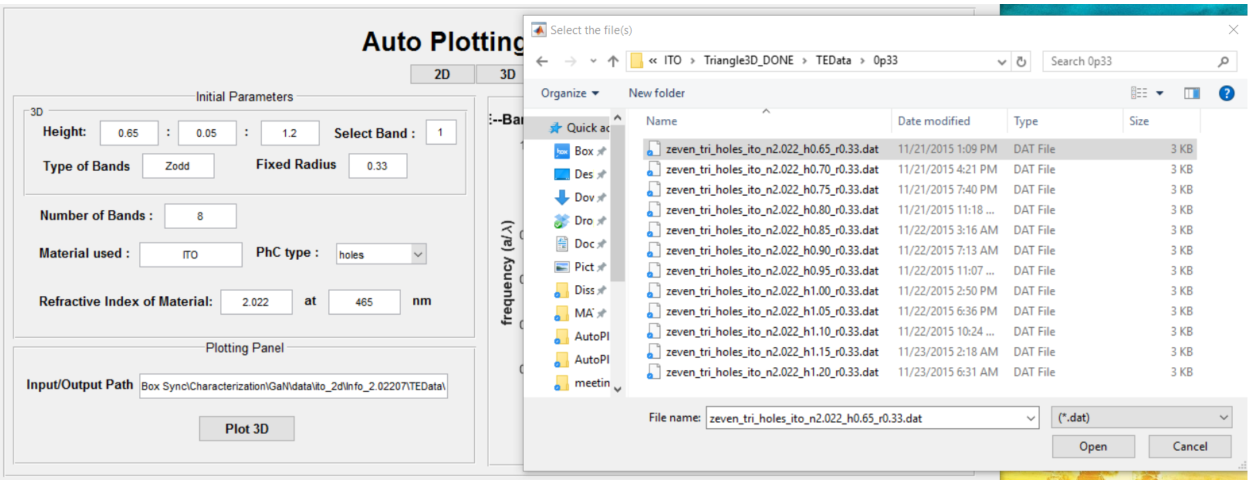

3D
Height: 0.65 : 0.05 : 1.2
Select Band : 1
Type of Bands: Zodd
Fixed Radius: 0.33
Number of Bands : 8
Material used : ITO
PhC type : holes
Refractive Index of Material: 2.022 at 465 nm
Input/Output Path: Box Sync\Characterization\GaN\data\ito_2d\Info_2.02207\TEData\

« ITO › Triangle3D_DONE › TEData › 0p33
Search 0p33

Name	Date modified	Type	Size
zeven_tri_holes_ito_n2.022_h0.65_r0.33.dat	11/21/2015 1:09 PM	DAT File	3 KB
zeven_tri_holes_ito_n2.022_h0.70_r0.33.dat	11/21/2015 4:21 PM	DAT File	3 KB
zeven_tri_holes_ito_n2.022_h0.75_r0.33.dat	11/21/2015 7:40 PM	DAT File	3 KB
zeven_tri_holes_ito_n2.022_h0.80_r0.33.dat	11/21/2015 11:18 ...	DAT File	3 KB
zeven_tri_holes_ito_n2.022_h0.85_r0.33.dat	11/22/2015 3:16 AM	DAT File	3 KB
zeven_tri_holes_ito_n2.022_h0.90_r0.33.dat	11/22/2015 7:13 AM	DAT File	3 KB
zeven_tri_holes_ito_n2.022_h0.95_r0.33.dat	11/22/2015 11:07 ...	DAT File	3 KB
zeven_tri_holes_ito_n2.022_h1.00_r0.33.dat	11/22/2015 2:50 PM	DAT File	3 KB
zeven_tri_holes_ito_n2.022_h1.05_r0.33.dat	11/22/2015 6:36 PM	DAT File	3 KB
zeven_tri_holes_ito_n2.022_h1.10_r0.33.dat	11/22/2015 10:24 ...	DAT File	3 KB
zeven_tri_holes_ito_n2.022_h1.15_r0.33.dat	11/23/2015 2:18 AM	DAT File	3 KB
zeven_tri_holes_ito_n2.022_h1.20_r0.33.dat	11/23/2015 6:31 AM	DAT File	3 KB

File name: zeven_tri_holes_ito_n2.022_h0.65_r0.33.dat
(*.dat)

Figure 9.4 3D Data files selection window

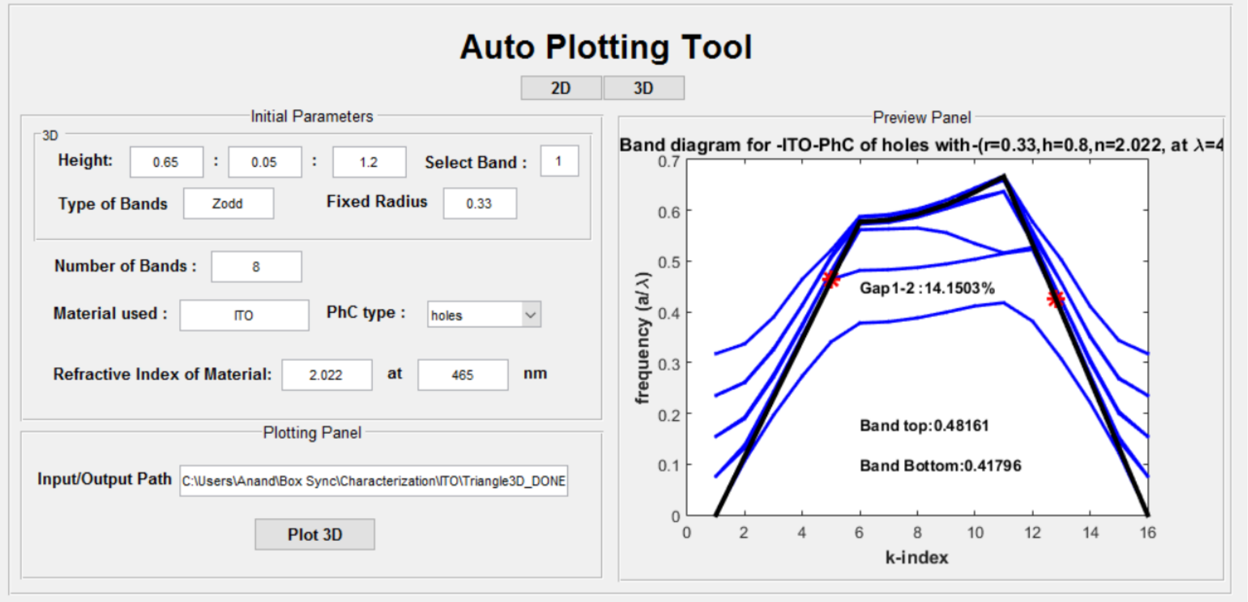

3D
Height: 0.65 : 0.05 : 1.2
Select Band : 1
Type of Bands: Zodd
Fixed Radius: 0.33
Number of Bands : 8
Material used : ITO
PhC type : holes
Refractive Index of Material: 2.022 at 465 nm
Input/Output Path: C:\Users\Anand\Box Sync\Characterization\ITO\Triangle3D_DONE

Figure 9.5 Screenshot of the Auto Plotting Tool with the 3D band diagram preview

The Matlab script is compiled to be a standalone software and is available at this link.

9.2. Appendix B – Time Domain Simulations

9.2.1. OptiFDTD Simulation Code

Optiwave FDTD software uses visual basic scripting language to define and simulate optical elements. Using scanning scripts, the feature sizes can be varied and simulate that set of parameters. The following codes are used for simulation of PhC lattices of holes and hybrid pillars that are set in triangular and square lattices. Before executing the scripts, the materials of interest (gallium nitride, indium tin oxide and hydrogen silsesquioxane) need to be defined using the profile manager of the software. Once the materials are defined, the simulations can be ran using the simulation manager and checking the simulate using script option. Upon execution, the simulation outputs 21 analyzer files for further analysis.

Filename: Triangular Holes

```
-------------------------------Start-of-File--------------------------------
WGMgr.DeleteAll
ObservePtMgr.DeleteAll
PointSourceMgr.DeleteAll
InputPlaneMgr.DeleteAll

Dim Linear2
Set Linear2 = WGMgr.CreateObj ( "WGLinear", "Linear2" )
Linear2.SetPositionEx    0,    0,    6,    0, "", "0", "", ""
Linear2.SetAttr "WidthExpr", "6"
Linear2.SetAttr "Depth", "-1"
Linear2.SetAttr "StartThickness", "1.14"
Linear2.SetAttr "EndThickness", "1.14"
Linear2.SetProfileName "GaN_Channel"
Linear2.SetDefaultThicknessTaperMode False
' Set thickness taper type to 1 (Linear)
Linear2.SetThicknessTaperType 1

Dim Linear1
Set Linear1 = WGMgr.CreateObj ( "WGLinear", "Linear1" )
Linear1.SetPosition 0,    0, 6,    0
Linear1.SetAttr "WidthExpr", "6"
Linear1.SetAttr "Depth", "0.14"
Linear1.SetAttr "StartThickness", "0.165"
Linear1.SetAttr "EndThickness", "0.165"
Linear1.SetProfileName "ITO_Channel"
Linear1.SetDefaultThicknessTaperMode False
' Set thickness taper type to 1 (Linear)
Linear1.SetThicknessTaperType 1

TimeOff = 40e-15
Dim PointSource1
Set PointSource1 = PointSourceMgr.CreatePointSource ( PointSourceMgr.FindID(
"PointSource" ) )
PointSource1.SetPositionExt "",    3,"", 0'0.25+znx, "",    zny
PointSource1.SetDepthExpr "-1"
PointSource1.Enable  True
PointSource1.SetAsKeyPointSource
PointSource1.SetWavelengthExpr ".465"
PointSource1.SetAmplitude 1.000000
'The selection of field components for 3D simulation: 0 - Ex, 1 - Ey, 2 - Ez.
PointSource1.SetField3D 1
'Time domain waveform selection: 0 - CW, 1 - GMCW.
PointSource1.SetWaveformType 1
PointSource1.SetHalfWidthExpr "1.5e-14"
```

```
PointSource1.SetTimeOffsetExpr TimeOff

Dim ObservationArea1
Set ObservationArea1 = ObservePtMgr.CreateObservationArea (
"ObservationArea1", False, True, False )
ObservationArea1.SetCenter CDbl( 3 ), CDbl( 0 )
ObservationArea1.SetDepthExpr "1"
ObservationArea1.SetEnabled  True
ObservationArea1.Collect2DTE  True, True
ObservationArea1.Collect2DTM  True, True
ObservationArea1.Collect3D  True, True, True, True, True, True
'For XZ-Areas: Width - size in Z direction, Height - size in X direction.
ObservationArea1.SetWidthOffset  6.000000
ObservationArea1.SetWidthExpr  ""
ObservationArea1.SetHeightOffset  6.000000
ObservationArea1.SetHeightExpr  ""

Dim PBG1
Set PBG1 = WGMgr.CreateObj ( "WGPBGCrystalStruct", "PBG1" )
PBG1.SetStart 0.25, -2.5
PBG1.SetAttr "Depth", "0.14"
PBG1.SetRotateAngleYExpr "0.0"
PBG1.SetLatticeType "2D HEXAGONAL"
PBG1.SetLatticeFill "BLOCK"
PBG1.SetLatticeScaleExpr "1.0"
PBG1.SetCountA 7
PBG1.SetCountB 1
PBG1.SetCountC 6
PBG1.SetCurrentEditLayer 0
Dim r
r=0

'Unit Cell
Dim CellAtomHSQ_PBG1
Set CellAtomHSQ_PBG1 = PBG1.AddAtomToUnitCell ("WGELLIPTIC")
CellAtomHSQ_PBG1.SetStart    0,    0

Const NumIterations = 21
For x = 1 to NumIterations

CellAtomHSQ_PBG1.SetAttr "MajorOffset", CDbl( r )
CellAtomHSQ_PBG1.SetAttr "MinorOffset", CDbl( r )
CellAtomHSQ_PBG1.SetAttr "AngleOffset", CDbl( 0 )
CellAtomHSQ_PBG1.SetAttr "Depth", "0"
CellAtomHSQ_PBG1.SetAttr "StartThickness", "0.500000"
CellAtomHSQ_PBG1.SetAttr "EndThickness", "0.500000"
CellAtomHSQ_PBG1.SetProfileName "Air_Channel"
CellAtomHSQ_PBG1.SetDefaultThicknessTaperMode True

PBG1.ResetAllToUnitCell
PBG1.ResetUnmodifiedCellsToUnitCell
ParamMgr.Simulate
WGMgr.Sleep( 50 )
r=r+0.025
Next
-------------------------------End-of-File-------------------------------
```

Filename: Square Holes

```
-------------------------------Start-of-File--------------------------------

WGMgr.DeleteAll
ObservePtMgr.DeleteAll
PointSourceMgr.DeleteAll
InputPlaneMgr.DeleteAll

Dim Linear2
Set Linear2 = WGMgr.CreateObj ( "WGLinear", "Linear2" )
Linear2.SetPositionEx    0,    0,    6,    0, "", "0", "", ""
Linear2.SetAttr "WidthExpr", "6"
Linear2.SetAttr "Depth", "-1"
Linear2.SetAttr "StartThickness", "1.14"
Linear2.SetAttr "EndThickness", "1.14"
Linear2.SetProfileName "GaN_Channel"
Linear2.SetDefaultThicknessTaperMode False
' Set thickness taper type to 1 (Linear)
Linear2.SetThicknessTaperType 1

Dim Linear1
Set Linear1 = WGMgr.CreateObj ( "WGLinear", "Linear1" )
Linear1.SetPosition 0,    0, 6,    0
Linear1.SetAttr "WidthExpr", "6"
Linear1.SetAttr "Depth", "0.14"
Linear1.SetAttr "StartThickness", "0.165"
Linear1.SetAttr "EndThickness", "0.165"
Linear1.SetProfileName "ITO_Channel"
Linear1.SetDefaultThicknessTaperMode False
' Set thickness taper type to 1 (Linear)
Linear1.SetThicknessTaperType 1

TimeOff = 40e-15
Dim PointSource1
Set PointSource1 = PointSourceMgr.CreatePointSource ( PointSourceMgr.FindID(
"PointSource" ) )
PointSource1.SetPositionExt "",    3,"", 0'0.25+znx, "",    zny
PointSource1.SetDepthExpr "-1"
PointSource1.Enable  True
PointSource1.SetAsKeyPointSource
PointSource1.SetWavelengthExpr ".465"
PointSource1.SetAmplitude 1.000000
'The selection of field components for 3D simulation: 0 - Ex, 1 - Ey, 2 - Ez.
PointSource1.SetField3D 1
'Time domain waveform selection: 0 - CW, 1 - GMCW.
PointSource1.SetWaveformType 1
PointSource1.SetHalfWidthExpr "1.5e-14"
PointSource1.SetTimeOffsetExpr TimeOff

Dim ObservationArea1
Set ObservationArea1 = ObservePtMgr.CreateObservationArea (
"ObservationArea1", False, True, False )
ObservationArea1.SetCenter CDbl( 3 ), CDbl( 0 )
ObservationArea1.SetDepthExpr "1"
ObservationArea1.SetEnabled  True
```

```
ObservationArea1.Collect2DTE  True, True
ObservationArea1.Collect2DTM  True, True
ObservationArea1.Collect3D  True, True, True, True, True, True
'For XZ-Areas: Width - size in Z direction, Height - size in X direction.
ObservationArea1.SetWidthOffset  6.000000
ObservationArea1.SetWidthExpr  ""
ObservationArea1.SetHeightOffset  6.000000
ObservationArea1.SetHeightExpr  ""

Dim PBG1
Set PBG1 = WGMgr.CreateObj ( "WGPBGCrystalStruct", "PBG1" )
PBG1.SetStart 0.5, -2.5
PBG1.SetAttr "Depth", "0.14"
PBG1.SetRotateAngleYExpr "0.0"
PBG1.SetLatticeType "2D RECTANGULAR"
PBG1.SetLatticeFill "BLOCK"
PBG1.SetLatticeScaleExpr "1.0"
PBG1.SetCountA 6
PBG1.SetCountB 1
PBG1.SetCountC 6
PBG1.SetCurrentEditLayer 0
Dim r
r=0

'Unit Cell
Dim CellAtomHSQ_PBG1
Set CellAtomHSQ_PBG1 = PBG1.AddAtomToUnitCell ("WGELLIPTIC")
CellAtomHSQ_PBG1.SetStart    0,    0


Const NumIterations = 21
For x = 1 to NumIterations

CellAtomHSQ_PBG1.SetAttr "MajorOffset", CDbl( r )
CellAtomHSQ_PBG1.SetAttr "MinorOffset", CDbl( r )
CellAtomHSQ_PBG1.SetAttr "AngleOffset", CDbl( 0 )
CellAtomHSQ_PBG1.SetAttr "Depth", "0"
CellAtomHSQ_PBG1.SetAttr "StartThickness", "0.500000"
CellAtomHSQ_PBG1.SetAttr "EndThickness", "0.500000"
CellAtomHSQ_PBG1.SetProfileName "Air_Channel"
CellAtomHSQ_PBG1.SetDefaultThicknessTaperMode True

PBG1.ResetAllToUnitCell

PBG1.ResetUnmodifiedCellsToUnitCell

ParamMgr.Simulate
WGMgr.Sleep( 50 )
r=r+0.025
Next
-------------------------------End-of-File--------------------------------
```

Filename: Triangular Hybrid Pillars

```
------------------------------Start-of-File-------------------------------

WGMgr.DeleteAll
```

```
ObservePtMgr.DeleteAll
PointSourceMgr.DeleteAll
InputPlaneMgr.DeleteAll

Dim Linear2
Set Linear2 = WGMgr.CreateObj ( "WGLinear", "Linear2" )
Linear2.SetPositionEx    0,    0,    6,    0, "", "0", "", ""
Linear2.SetAttr "WidthExpr", "6"
Linear2.SetAttr "Depth", "-1"
Linear2.SetAttr "StartThickness", "1.14"
Linear2.SetAttr "EndThickness", "1.14"
Linear2.SetProfileName "GaN_Channel"
Linear2.SetDefaultThicknessTaperMode False
' Set thickness taper type to 1 (Linear)
Linear2.SetThicknessTaperType 1

Dim Linear1
Set Linear1 = WGMgr.CreateObj ( "WGLinear", "Linear1" )
Linear1.SetPosition 0,    0, 6,    0
Linear1.SetAttr "WidthExpr", "6"
Linear1.SetAttr "Depth", "0.14"
Linear1.SetAttr "StartThickness", "0.165"
Linear1.SetAttr "EndThickness", "0.165"
Linear1.SetProfileName "ITO_Channel"
Linear1.SetDefaultThicknessTaperMode False
' Set thickness taper type to 1 (Linear)
Linear1.SetThicknessTaperType 1

TimeOff = 40e-15
Dim PointSource1
Set PointSource1 = PointSourceMgr.CreatePointSource ( PointSourceMgr.FindID(
"PointSource" ) )
PointSource1.SetPositionExt "",    3,"", 0'0.25+znx, "",    zny
PointSource1.SetDepthExpr "-1"
PointSource1.Enable  True
PointSource1.SetAsKeyPointSource
PointSource1.SetWavelengthExpr ".465"
PointSource1.SetAmplitude 1.000000
'The selection of field components for 3D simulation: 0 - Ex, 1 - Ey, 2 - Ez.
PointSource1.SetField3D 1
'Time domain waveform selection: 0 - CW, 1 - GMCW.
PointSource1.SetWaveformType 1
PointSource1.SetHalfWidthExpr "1.5e-14"
PointSource1.SetTimeOffsetExpr TimeOff

Dim ObservationArea1
Set ObservationArea1 = ObservePtMgr.CreateObservationArea (
"ObservationArea1", False, True, False )
ObservationArea1.SetCenter CDbl( 3 ), CDbl( 0 )
ObservationArea1.SetDepthExpr "1"
ObservationArea1.SetEnabled  True
ObservationArea1.Collect2DTE  True, True
ObservationArea1.Collect2DTM  True, True
ObservationArea1.Collect3D  True, True, True, True, True, True
'For XZ-Areas: Width - size in Z direction, Height - size in X direction.
ObservationArea1.SetWidthOffset  6.000000
ObservationArea1.SetWidthExpr  ""
```

```
ObservationArea1.SetHeightOffset  6.000000
ObservationArea1.SetHeightExpr  ""

Dim PBG1
Set PBG1 = WGMgr.CreateObj ( "WGPBGCrystalStruct", "PBG1" )
PBG1.SetStart 0.25, -2.5
PBG1.SetAttr "Depth", "0.14"
PBG1.SetRotateAngleYExpr "0.0"
PBG1.SetLatticeType "2D HEXAGONAL"
PBG1.SetLatticeFill "BLOCK"
PBG1.SetLatticeScaleExpr "1.0"
PBG1.SetCountA 7
PBG1.SetCountB 1
PBG1.SetCountC 6
PBG1.SetCurrentEditLayer 0
Dim r
r=0

'Unit Cell
Dim CellAtomHSQ_PBG1
Set CellAtomHSQ_PBG1 = PBG1.AddAtomToUnitCell ("WGELLIPTIC")
CellAtomHSQ_PBG1.SetStart    0,    0

Dim CellAtomITO_PBG1
Set CellAtomITO_PBG1 = PBG1.AddAtomToUnitCell ("WGELLIPTIC")
CellAtomITO_PBG1.SetStart    0,    0

Const NumIterations = 21
For x = 1 to NumIterations

CellAtomHSQ_PBG1.SetAttr "MajorOffset", CDbl( r )
CellAtomHSQ_PBG1.SetAttr "MinorOffset", CDbl( r )
CellAtomHSQ_PBG1.SetAttr "AngleOffset", CDbl( 0 )
CellAtomHSQ_PBG1.SetAttr "Depth", "0"
CellAtomHSQ_PBG1.SetAttr "StartThickness", "0.500000"
CellAtomHSQ_PBG1.SetAttr "EndThickness", "0.500000"
CellAtomHSQ_PBG1.SetProfileName "HSQ_Channel"
CellAtomHSQ_PBG1.SetDefaultThicknessTaperMode True

CellAtomITO_PBG1.SetAttr "MajorOffset", CDbl( r )
CellAtomITO_PBG1.SetAttr "MinorOffset", CDbl( r )
CellAtomITO_PBG1.SetAttr "AngleOffset", CDbl( 0 )
CellAtomITO_PBG1.SetAttr "Depth", ".5"
CellAtomITO_PBG1.SetAttr "StartThickness", "0.165000"
CellAtomITO_PBG1.SetAttr "EndThickness", "0.165000"
CellAtomITO_PBG1.SetProfileName "ITO_Channel"
CellAtomITO_PBG1.SetDefaultThicknessTaperMode True

PBG1.ResetAllToUnitCell

PBG1.ResetUnmodifiedCellsToUnitCell

ParamMgr.Simulate
WGMgr.Sleep( 50 )
r=r+0.025
Next
--------------------------------End-of-File--------------------------------
```

Filename: Square Hybrid Pillars

```
-------------------------------Start-of-File--------------------------------
WGMgr.DeleteAll
ObservePtMgr.DeleteAll
PointSourceMgr.DeleteAll
InputPlaneMgr.DeleteAll

Dim Linear2
Set Linear2 = WGMgr.CreateObj ( "WGLinear", "Linear2" )
Linear2.SetPositionEx    0,    0,    6,    0, "", "0", "", ""
Linear2.SetAttr "WidthExpr", "6"
Linear2.SetAttr "Depth", "-1"
Linear2.SetAttr "StartThickness", "1.14"
Linear2.SetAttr "EndThickness", "1.14"
Linear2.SetProfileName "GaN_Channel"
Linear2.SetDefaultThicknessTaperMode False
' Set thickness taper type to 1 (Linear)
Linear2.SetThicknessTaperType 1

Dim Linear1
Set Linear1 = WGMgr.CreateObj ( "WGLinear", "Linear1" )
Linear1.SetPosition 0,    0, 6,    0
Linear1.SetAttr "WidthExpr", "6"
Linear1.SetAttr "Depth", "0.14"
Linear1.SetAttr "StartThickness", "0.165"
Linear1.SetAttr "EndThickness", "0.165"
Linear1.SetProfileName "ITO_Channel"
Linear1.SetDefaultThicknessTaperMode False
' Set thickness taper type to 1 (Linear)
Linear1.SetThicknessTaperType 1

TimeOff = 40e-15
Dim PointSource1
Set PointSource1 = PointSourceMgr.CreatePointSource ( PointSourceMgr.FindID(
"PointSource" ) )
PointSource1.SetPositionExt "",    3,"", 0'0.25+znx, "",    zny
PointSource1.SetDepthExpr "-1"
PointSource1.Enable  True
PointSource1.SetAsKeyPointSource
PointSource1.SetWavelengthExpr ".465"
PointSource1.SetAmplitude 1.000000
'The selection of field components for 3D simulation: 0 - Ex, 1 - Ey, 2 - Ez.
PointSource1.SetField3D 1
'Time domain waveform selection: 0 - CW, 1 - GMCW.
PointSource1.SetWaveformType 1
PointSource1.SetHalfWidthExpr "1.5e-14"
PointSource1.SetTimeOffsetExpr TimeOff

Dim ObservationArea1
Set ObservationArea1 = ObservePtMgr.CreateObservationArea (
"ObservationArea1", False, True, False )
ObservationArea1.SetCenter CDbl( 3 ), CDbl( 0 )
ObservationArea1.SetDepthExpr "1"
ObservationArea1.SetEnabled  True
```

```
ObservationArea1.Collect2DTE  True, True
ObservationArea1.Collect2DTM  True, True
ObservationArea1.Collect3D  True, True, True, True, True, True
'For XZ-Areas: Width - size in Z direction, Height - size in X direction.
ObservationArea1.SetWidthOffset  6.000000
ObservationArea1.SetWidthExpr  ""
ObservationArea1.SetHeightOffset  6.000000
ObservationArea1.SetHeightExpr  ""

Dim PBG1
Set PBG1 = WGMgr.CreateObj ( "WGPBGCrystalStruct", "PBG1" )
PBG1.SetStart 0.5, -2.5
PBG1.SetAttr "Depth", "0.14"
PBG1.SetRotateAngleYExpr "0.0"
PBG1.SetLatticeType "2D RECTANGULAR"
PBG1.SetLatticeFill "BLOCK"
PBG1.SetLatticeScaleExpr "1.0"
PBG1.SetCountA 6
PBG1.SetCountB 1
PBG1.SetCountC 6
PBG1.SetCurrentEditLayer 0
Dim r
r=0

'Unit Cell
Dim CellAtomHSQ_PBG1
Set CellAtomHSQ_PBG1 = PBG1.AddAtomToUnitCell ("WGELLIPTIC")
CellAtomHSQ_PBG1.SetStart    0,    0

Dim CellAtomITO_PBG1
Set CellAtomITO_PBG1 = PBG1.AddAtomToUnitCell ("WGELLIPTIC")
CellAtomITO_PBG1.SetStart    0,    0

Const NumIterations = 21
For x = 1 to NumIterations

CellAtomHSQ_PBG1.SetAttr "MajorOffset", CDbl( r )
CellAtomHSQ_PBG1.SetAttr "MinorOffset", CDbl( r )
CellAtomHSQ_PBG1.SetAttr "AngleOffset", CDbl( 0 )
CellAtomHSQ_PBG1.SetAttr "Depth", "0"
CellAtomHSQ_PBG1.SetAttr "StartThickness", "0.500000"
CellAtomHSQ_PBG1.SetAttr "EndThickness", "0.500000"
CellAtomHSQ_PBG1.SetProfileName "HSQ_Channel"
CellAtomHSQ_PBG1.SetDefaultThicknessTaperMode True

CellAtomITO_PBG1.SetAttr "MajorOffset", CDbl( r )
CellAtomITO_PBG1.SetAttr "MinorOffset", CDbl( r )
CellAtomITO_PBG1.SetAttr "AngleOffset", CDbl( 0 )
CellAtomITO_PBG1.SetAttr "Depth", ".5"
CellAtomITO_PBG1.SetAttr "StartThickness", "0.165000"
CellAtomITO_PBG1.SetAttr "EndThickness", "0.165000"
CellAtomITO_PBG1.SetProfileName "ITO_Channel"
CellAtomITO_PBG1.SetDefaultThicknessTaperMode True

PBG1.ResetAllToUnitCell

PBG1.ResetUnmodifiedCellsToUnitCell
```

```
ParamMgr.Simulate
WGMgr.Sleep( 50 )
r=r+0.025
Next
-------------------------------End-of-File---------------------------------
```

9.2.2. Near and Far Field Plotting

The field patterns are then exported manually from each of the analyzer documents in the form of .f3d files. A Matlab script was written to plot the near-field pattern and compute the far-field pattern using free space transfer function and convolution of the near-field patterns. The following script plots, computes and exports text files containing overall intensities for each radii of the feature in the pattern.

Filename: f3dplotmulti.m

```
------------------------------Start-of-File--------------------------------

close all;
clear all;
clc;

dstart=0; % diameter start
dstep=50; % step
dend=1000; % diameter end
diameter = dstart:dstep:dend;
dlength=length(diameter);
[files,pathname]=uigetfile('*.f3d','Select the file(s)','Multiselect','on');
filenames=sort(files);
% Far-field Calculation
d=2.5E-2; % Far-field distance in meters
lambda=465e-9; % wavelength of interest in meters
k=2*pi/lambda; % k-space
h0=(j/(lambda*d))*exp(-j*k*d); %  Free space transfer function
for kl=1:dlength
    current=strcat(pathname,char(filenames(kl)));
    data = dlmread(current,',',3,0);
    [l,w]=size(data);
    row=sqrt(l);
    col=row;
    rdata=zeros(row,col);
    idata=zeros(row,col);
    sz=6;
    x=0:sz/(row-1):sz;
    y=-sz/2:sz/(col-1):sz/2;
    % separating real and imaginary data
    realdata=data(:,1);
    imagdata=data(:,2);
    % rearranging the data into rxc format
    i=1;
    while i <= l
        for r=1:row
```

```
            for c=1:col
                rdata(r,c)=realdata(i);
                idata(r,c)=imagdata(i);
                i=i+1;
            end
        end
    end
    fulldata=rdata + j*idata;
    amp=sqrt(rdata.^2 + idata.^2);
    mr=max(amp);
    mnearfield(kl)=max(mr);

    % Far-field Calculation
    for a=1:length(x)
        for b=1:length(y)
            h(a,b)=h0* exp(-j*k*(x(a)^2 + y(b)^2)/2*d);
        end
    end

    g=conv2(fulldata,h,'same'); % Far-field data using convolution of data
    gsr=sum(abs(g));
    mfr=max(abs(g));
    mfarfield(kl)=max(mfr);
   end
mnear=max(mnearfield);
mfar=max(mfarfield);
for kl=1:dlength
    current=strcat(pathname,char(filenames(kl)));
    data = dlmread(current,',',3,0);
    [l,w]=size(data);
    row=sqrt(l);
    col=row;
    rdata=zeros(row,col);
    idata=zeros(row,col);
    sz=6;
    x=0:sz/(row-1):sz;
    y=-sz/2:sz/(col-1):sz/2;
    % separating real and imaginary data
    realdata=data(:,1);
    imagdata=data(:,2);
    % rearranging the data into rxc format
    i=1;
    while i <= l
        for r=1:row
            for c=1:col
                rdata(r,c)=realdata(i);
                idata(r,c)=imagdata(i);
                i=i+1;
            end
        end
    end
    fulldata=rdata + j*idata;
    amp=sqrt(rdata.^2 + idata.^2);
    % plotting the original data
    mesh(x,y,amp);
    xlabel('Z (\mum)');
```

```
    ylabel('X (\mum)');
    colormap hot;
    axis([0 sz -sz/2 sz/2 0 mnear]);
    title('Ey DFT at 1 \mum')
    colorbar;
    caxis([0 mnear]);
    view(0,90);
    outputfname=filenames(kl);
    outputfname1=char(outputfname);
    ol=length(outputfname1);
    onl=ol-4;
    saveas(gcf,strcat(pathname,'\',outputfname1(1:onl)),'tif');


    % Far-field Calculation
    for a=1:length(x)
        for b=1:length(y)
            h(a,b)=h0* exp(-j*k*(x(a)^2 + y(b)^2)/2*d);
        end
    end

    g=conv2(fulldata,h,'same'); % Far-field data using convolution of data
    gsr=sum(abs(g));
    figure(); % New Figure
    mesh(x,y,abs(g));
    xlabel('Z (\mum)');
    ylabel('X (\mum)');
    colormap hot;
    colorbar;
    axis([0 sz -sz/2 sz/2 0 mfar]);
    title(strcat('Ey DFT at ', num2str(d*100),' cm'));
    view(0,90);
    caxis([0 mfar]);
    outputfname2=strcat('Far-field_',outputfname1(1:onl));
    saveas(gcf,strcat(pathname,'\',upper(outputfname2)),'tif');
    sr=sum(amp);
    NearField(kl)=sum(sr);
    FarField(kl)=sum(gsr);
   end
dlmwrite(strcat(pathname,'NearField.txt'),[diameter' NearField']);
dlmwrite(strcat(pathname,'FarField.txt'),[diameter' FarField']);
plot(diameter,NearField,'-ro');
xlabel('Diameter (nm)');
ylabel('Intensity (a.u.)');
title('Near Field Intensity vs Diameter');
saveas(gcf,strcat(pathname,'\NearField'),'tif');
plot(diameter,FarField,'-b*');
xlabel('Diameter (nm)');
ylabel('Intensity (a.u.)');
title('Far Field Intensity vs Diameter');
saveas(gcf,strcat(pathname,'\FarField'),'tif');
close all;

-------------------------------End-of-File--------------------------------
```

9.3. Appendix C – Fabrication Processes

9.3.1. Cadence Mask Layout

A 6 layer set of photolithography masks were designed using Cadence's Virtuoso tool for fabrication of LEDs. Following Figure 9.6 shows the layout that spans over 1.5 x 1.5 cm^2 containing a total of 640 devices and TLM patterns. Figure 9.7 shows the different types of devices in the masks and Figure 9.8 shows the naming convention used with this mask set. Table 9.1 shows the different contact sizes for different types of mesa sizes.

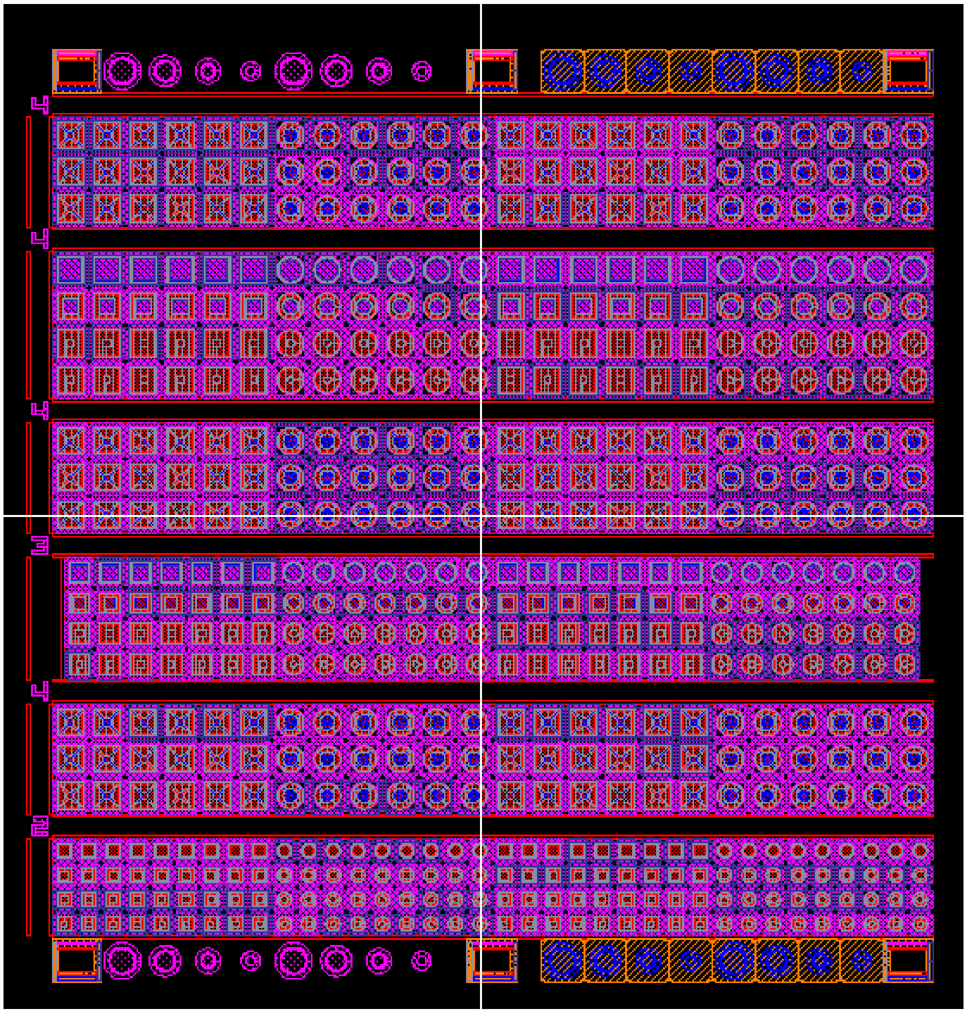

Figure 9.6 Overview of the mask layout

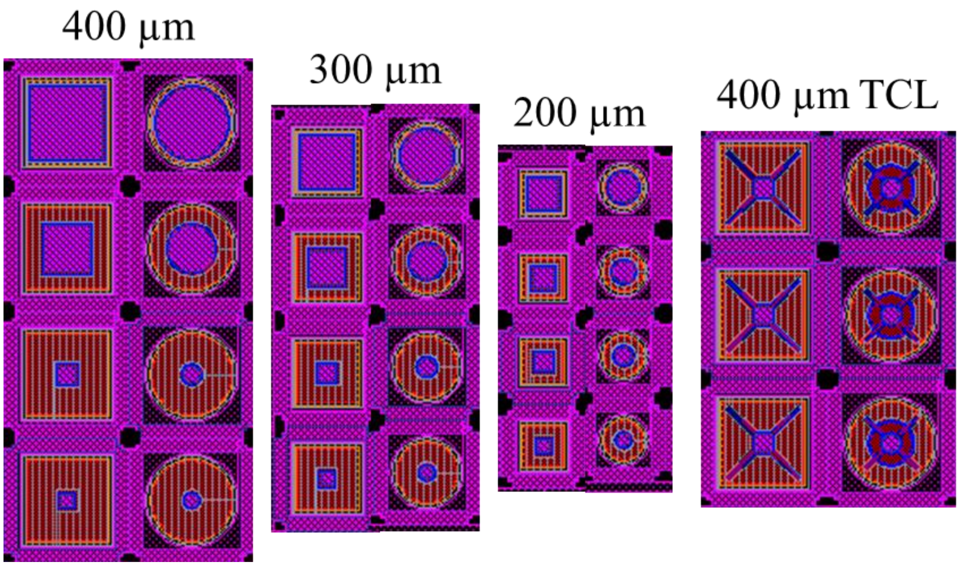

Figure 9.7 Types of devices on the mask

Table 9.1 Contact sizes on the masks

Contact/Mesa	**400µm LEDs**	**300µm LEDs**	**200µm LEDs**	**TCL LEDs**
P1 (TCL)	**360µm (380µm)**	**260µm (280µm)**	**160µm (180µm)**	**100µm (380µm)**
P2 (TCL)	**240µm (380µm)**	**180µm (280µm)**	**120µm (180µm)**	**100µm (380µm)**
P3 (TCL)	**100µm (380µm)**	**100µm (280µm)**	**100µm (180µm)**	**100µm (380µm)**
P4 (TCL)	**80µm (380µm)**	**80µm (280µm)**	**80µm (180µm)**	**100µm (380µm)**

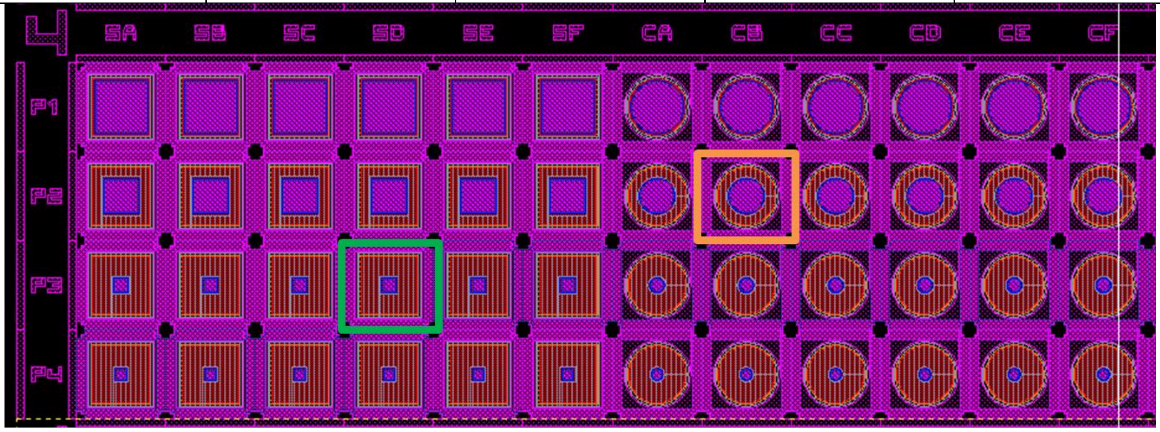

4SDP3 : 400µm Mesa, Square, 4th Column, 100µm p-contact

4CBP2 : 400µm Mesa, Circular, 2nd Column, 240µm p-contact

Figure 9.8 Naming convention for individual devices on the mask

9.3.2. Electron Beam Lithography – NPGS CAD File Generator

PhC fabrication requires a CAD file with exact dimensions and lattice configurations. In order to create specific CAD files, DesignCAD express software is utilized. A Matlab script was written to generate the CAD files which has options to select the type of lattice, size of the contact and size of the features and the lattice constant. Using the selected options, a CAD file with an extension .dc2 is created. This resultant CAD file is loaded using the NPGS software and the pattern is centered and the magnification is set for writing the pattern.

Filename: NPGS_Export.m

```
-------------------------------Start-of-File--------------------------------

clear all;
clc;
n=-400:400;
r1=0.075;%input('Enter the radius of the hole (r) in microns = ');
r=r1*8;
a1=0.5;%input('Enter the lattice constant (a) in microns = ');
a=a1*8;
LR1=75;%input('Enter the ITO contact size = ');
LR=LR1*8;
LR2=55;%input('Enter the metal contact size = ');
LRR=LR2*8;
latticetype='Triangular'; % Triangular or Square
contacttype='Circular'; % Square or Circular
fname=strcat(contacttype,'cont','_',latticetype,'_r',num2str(r1*1000),'nm_a',
num2str(a1*1000),'nm_R1_',num2str(LR1),'um_R2_',num2str(LR2),'um.dc2');
fid = fopen(fname, 'w');

%%-----------------Necessary Lines for the NPGS CAD files----------------%%
l1='-42.6739 -39.5408 80.3972 79.9594 0 -0.0000 0.0000';
l2='42 20 0 0 0 0';
l3='8.000000';
l4='8.000000, 0.800000';
l5='8.000000';
l5='3';
l6='16.000000';
l7='0.000000';
l8='0.000000';
l9='1.000000';
l10='1';
l11='0';
l12='1';
l13='SIMPLEX2.VFN';
l14='0.00000000 0.00000000 0.00000000 0.00000000';
l15='0.00000000 0.00000000 0.00000000 0.00000000';
l16='0.00000000 0.00000000 0.00000000 0.00000000';
l17='0.00000000 0.00000000 0.00000000 0.00000000';
l18='1 0 0 0 0 0 0 0';
l19='0.00000000 0.00000000 0.00000000 0.00000000';
l20='0.00000000 0.00000000 0.00000000 0.00000000';
```

```
l21='; DesignCAD Drawing Comments /w ';' as 1st char.';
l22='23 1 0 0 0 0';
l23='Do Not Use';
l24='21 1 0 0 0 0';

entity='16 4 1.6000 0 1 13 0 1 0 255 236 60 0 1';

fwrite(fid,(l1));
fprintf(fid,'\r\n');
fwrite(fid,(l2));
fprintf(fid,'\r\n');
fwrite(fid,(l3));
fprintf(fid,'\r\n');
fwrite(fid,l4);
fprintf(fid,'\r\n');
fwrite(fid,(l5));
fprintf(fid,'\r\n');
fwrite(fid,(l6));
fprintf(fid,'\r\n');
fwrite(fid,(l7));
fprintf(fid,'\r\n');
fwrite(fid,(l8));
fprintf(fid,'\r\n');
fwrite(fid,(l9));
fprintf(fid,'\r\n');
fwrite(fid,(l10));
fprintf(fid,'\r\n');
fwrite(fid,(l11));
fprintf(fid,'\r\n');
fwrite(fid,(l12));
fprintf(fid,'\r\n');
fwrite(fid,l13);
fprintf(fid,'\r\n');
fwrite(fid,(l14));
fprintf(fid,'\r\n');
fwrite(fid,(l15));
fprintf(fid,'\r\n');
fwrite(fid,(l16));
fprintf(fid,'\r\n');
fwrite(fid,(l17));
fprintf(fid,'\r\n');
fwrite(fid,(l18));
fprintf(fid,'\r\n');
fwrite(fid,(l19));
fprintf(fid,'\r\n');
fwrite(fid,(l20));
fprintf(fid,'\r\n');
fwrite(fid,l21);
fprintf(fid,'\r\n');
fwrite(fid,(l22));
fprintf(fid,'\r\n');
fwrite(fid,l23);
fprintf(fid,'\r\n');
fwrite(fid,(l24));
fprintf(fid,'\r\n\r\n');
switch contacttype
```

```
    case 'Square'
        if strcmp(latticetype,'Triangular')
 %----------------------------Triangular Lattice-------------------------%%
            for i=1:length(n)
                for j=1:length(n)
                    znx(i,j)=a*n(i) + a*0.5* abs(cos((n(j)+1)*pi/2));
                    zny(i,j)=a*n(j)*0.866;

                    sx(i,j)=znx(i,j)+r;
                    sy(i,j)=zny(i,j);
                    center=[znx(i,j), zny(i,j)];
                    start=[sx(i,j),sy(i,j)];
                    ending=[sx(i,j),sy(i,j)];
                    t1x=znx(i,j);
                    t1y=zny(i,j);
                    R = sqrt( znx(i,j)^2 + zny(i,j)^2 );
                    if (-LR <= t1x  && t1x <= -LRR && -LR <= t1y && t1y <=
LR) || ((-LRR < t1x && t1x < LRR) && (LRR <= t1y && t1y <= LR)) || ((-LRR <
t1x && t1x < LRR) && (-LR <= t1y && t1y <= -LRR)) || ((LRR <= t1x && t1x <=
LR) && (-LR <= t1y && t1y <= LR))
                        tx(i,j)=znx(i,j);
                        ty(i,j)=zny(i,j);
                        fwrite(fid, (entity));
                        fprintf(fid,'\r\n');
                        fwrite(fid,num2str(center));
                        fprintf(fid,'\r\n');
                        fwrite(fid, num2str(start) );
                        fprintf(fid,'\r\n');
                        fwrite(fid, num2str(ending));
                        fprintf(fid,'\r\n');
                        fwrite(fid,num2str(center));
                        fprintf(fid,'\r\n\r\n');
                    end
                end
            end

        elseif strcmp(latticetype,'Square')
%----------------------------Square Lattice------------------------------%%
            for i=1:length(n)
                for j=1:length(n)
                    znx(i,j)=a*n(i);
                    zny(i,j)=a*n(j);

                    sx(i,j)=znx(i,j)+r;
                    sy(i,j)=zny(i,j);
                    center=[znx(i,j), zny(i,j)];
                    start=[sx(i,j),sy(i,j)];
                    ending=[sx(i,j),sy(i,j)];

                    R = sqrt( znx(i,j)^2 + zny(i,j)^2 );
                    t1x=znx(i,j);
                    t1y=zny(i,j);

                    if (-LR <= t1x  && t1x <= -LRR && -LR <= t1y && t1y <=
LR) || ((-LRR < t1x && t1x < LRR) && (LRR <= t1y && t1y <= LR)) || ((-LRR <
```

```
t1x && t1x < LRR) && (-LR <= t1y && t1y <= -LRR)) || ((LRR <= t1x && t1x <=
LR) && (-LR <= t1y && t1y <= LR))
                        tx(i,j)=znx(i,j);
                        ty(i,j)=zny(i,j);
                        fwrite(fid, (entity));
                        fprintf(fid,'\r\n');
                        fwrite(fid,num2str(center));
                        fprintf(fid,'\r\n');
                        fwrite(fid, num2str(start) );
                        fprintf(fid,'\r\n');
                        fwrite(fid, num2str(ending));
                        fprintf(fid,'\r\n');
                        fwrite(fid,num2str(center));
                        fprintf(fid,'\r\n\r\n');
                    end
                end
            end

        end
    case 'Circular'
        if strcmp(latticetype,'Triangular')
%----------------------------Triangular Lattice-------------------------%%
            for i=1:length(n)
                for j=1:length(n)
                    znx(i,j)=a*n(i) + a*0.5* abs(cos((n(j)+1)*pi/2));
                    zny(i,j)=a*n(j)*0.866;

                    sx(i,j)=znx(i,j)+r;
                    sy(i,j)=zny(i,j);
                    center=[znx(i,j), zny(i,j)];
                    start=[sx(i,j),sy(i,j)];
                    ending=[sx(i,j),sy(i,j)];
                    t1x=znx(i,j);
                    t1y=zny(i,j);
                    R = sqrt( znx(i,j)^2 + zny(i,j)^2 );
                    if (R <= LR) && (R >= LRR)% for circular pattern
                        tx(i,j)=znx(i,j);
                        ty(i,j)=zny(i,j);
                        fwrite(fid, (entity));
                        fprintf(fid,'\r\n');
                        fwrite(fid,num2str(center));
                        fprintf(fid,'\r\n');
                        fwrite(fid, num2str(start) );
                        fprintf(fid,'\r\n');
                        fwrite(fid, num2str(ending));
                        fprintf(fid,'\r\n');
                        fwrite(fid,num2str(center));
                        fprintf(fid,'\r\n\r\n');
                    end
                end
            end

        elseif strcmp(latticetype,'Square')
%----------------------------Square Lattice------------------------------%%
            for i=1:length(n)
                for j=1:length(n)
```

```
                    znx(i,j)=a*n(i);
                    zny(i,j)=a*n(j);

                    sx(i,j)=znx(i,j)+r;
                    sy(i,j)=zny(i,j);
                    center=[znx(i,j), zny(i,j)];
                    start=[sx(i,j),sy(i,j)];
                    ending=[sx(i,j),sy(i,j)];

                    R = sqrt( znx(i,j)^2 + zny(i,j)^2 );
                    t1x=znx(i,j);
                    t1y=zny(i,j);

                    if (R <= LR) && (R >= LRR) % for circular contact
patterns
                        tx(i,j)=znx(i,j);
                        ty(i,j)=zny(i,j);
                        fwrite(fid, (entity));
                        fprintf(fid,'\r\n');
                        fwrite(fid,num2str(center));
                        fprintf(fid,'\r\n');
                        fwrite(fid, num2str(start) );
                        fprintf(fid,'\r\n');
                        fwrite(fid, num2str(ending));
                        fprintf(fid,'\r\n');
                        fwrite(fid,num2str(center));
                        fprintf(fid,'\r\n\r\n');
                    end
                end
            end

        end
end

%%---------------------------Fibonacci Spiral----------------------------%%
% for k=1:length(n)
% zn(k)=sqrt(n(k)) * exp(j * 2 * pi * n(k) * 0.61803);
% end
% for k=1:length(n)
%     znx(k)=a*sqrt(n(k)) * cos( 2 * pi * n(k) * 0.61803);
%     zny(k)=%a*sqrt(n(k)) * sin( 2 * pi * n(k) * 0.61803);
%
%     sx(k)=znx(k)+r;
%     sy(k)=zny(k);
%     center=[znx(k), zny(k)];
%     start=[sx(k),sy(k)];
%     ending=[sx(k),sy(k)];
%
%     R = sqrt( znx(k)^2 + zny(k)^2 );
%     if (R <= LR)%(znx(k) <= LR) && (zny(k)<= LR) && (znx(k) >= -LR) &&
(zny(k)>= -LR)
%     fwrite(fid, (entity));
%     fprintf(fid,'\r\n');
%     fwrite(fid,num2str(center));
%     fprintf(fid,'\r\n');
%     fwrite(fid, num2str(start) );
```

```
%     fprintf(fid,'\r\n');
%     fwrite(fid, num2str(ending));
%     fprintf(fid,'\r\n');
%     fwrite(fid,num2str(center));
%     fprintf(fid,'\r\n\r\n');
%
% %     hold on;
%
%     end
%
% end
fclose(fid);
plot(tx,ty,'bo');
-------------------------------End-of-File------------------------------
```

The Figure 9.9 shows a preview of the type of CAD files generated using the above program.

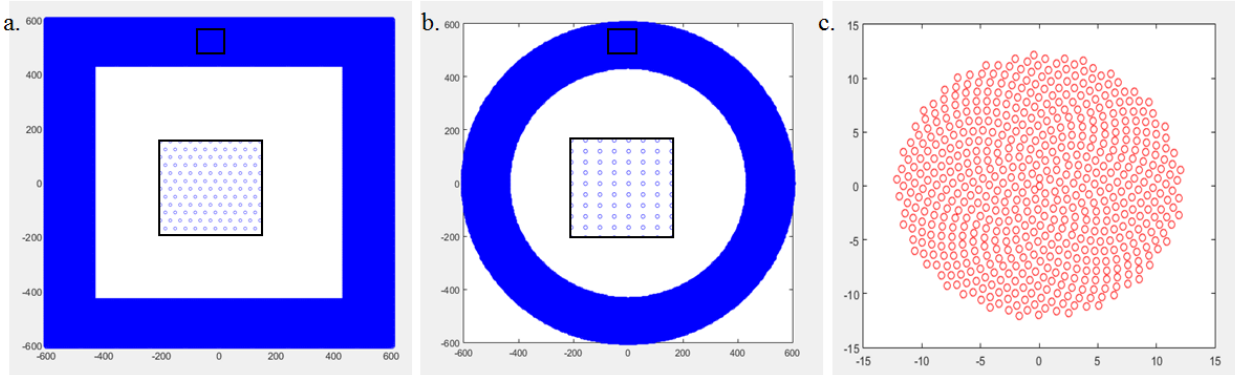

Figure 9.9 CAD files generated using the NPGS_Export program (a.)Square contact with a triangular lattice, (b.) Circular contact with a square lattice, (c.) Fibonacci lattice representing sunflower seeds

9.3.3. Electrical Beam Lithography – Optimization

The ebeam resists used for fabrication of PhC structures in this research are 950 PMMA A3, maN-2403, and FOx-16. Typically for any resist, the optimization procedures follow a similar procedure that follows exposure of the resist with a range of dosages, development and characterization. A generic pattern with triangular lattice of pillars/holes was used for characterizing the resist exposure parameters. The target size of the feature was 300 nm separated by a pitch of 500 nm.

950 PMMA A3

The typical exposure dosages for PMMA resist lie in the range of 160 µC/cm^2 to 375 µC/cm^2 and the following Figures 9.10 show the resulting patterns observed at 160, 333 and 375 µC/cm^2. Samples were developed using MIBK:IPA (1:3) developer for about 70 seconds. A Matlab script was written to extract the features based on the contrast between the features and background. Figure 9.11 shows the extracted features and mean diameter of the features at respective dosages.

From the analysis, dosage 333 μC/cm^2 reproduces features with a mean diameter of 302 nm which is close to the target feature size.

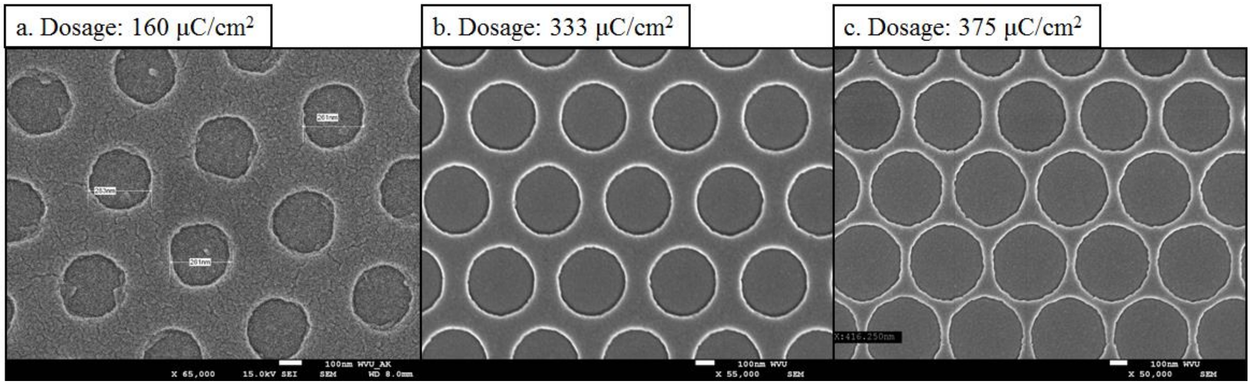
a. Dosage: 160 μC/cm^2 b. Dosage: 333 μC/cm^2 c. Dosage: 375 μC/cm^2

Figure 9.10 SEM images of triangular lattice of holes in PMMA exposed at dosages (a.) 160 μC/cm^2, (b.) 333 μC/cm^2, (c.) 375 μC/cm^2

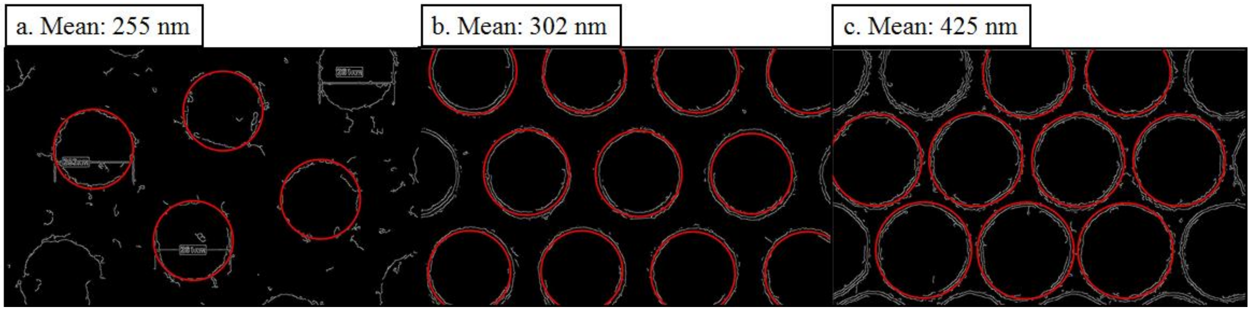
a. Mean: 255 nm b. Mean: 302 nm c. Mean: 425 nm

Figure 9.11 Matlab extracted images showing mean diameter from the respective SEM images at dosages (a.) 160 μC/cm^2, (b.) 333 μC/cm^2, (c.) 375 μC/cm^2

Table 9.2 Optimal processing parameters for 950 PMMA A3

EBL processing parameters for 950 PMMA A3	
Spin Recipe	5000 rpm for 50 seconds
Exposure Dosage	310-340 μC/cm^2
Developer	MIBK:IPA (1:3)
Development Time	70-75 seconds

maN-2403

The typical exposure dosages for maN-2403 resist lie in the range of 45 μC/cm^2 to 75 μC/cm^2 and the following Figures 9.12 show the resulting patterns observed at 45, 63 and 75 μC/cm^2. Samples were developed in maD-525 developer for about 70 seconds. The Matlab script was used to extract the features based on the contrast between the features and background. Figure 9.13 shows the extracted features and mean diameter of the features at respective dosages. From the analysis, dosage 63 μC/cm^2 reproduces features with a mean diameter of 296 nm which is close to the target feature size.

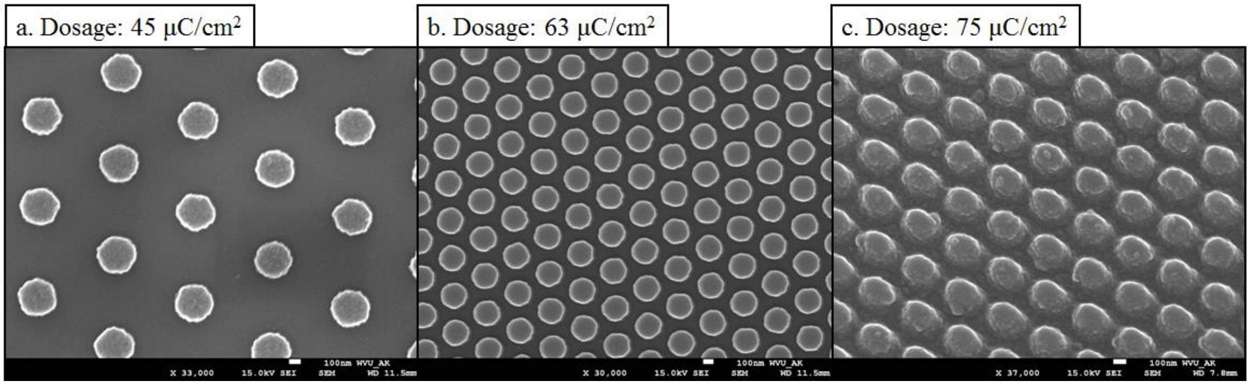
a. Dosage: 45 μC/cm^2

b. Dosage: 63 μC/cm^2

c. Dosage: 75 μC/cm^2

Figure 9.12 SEM images of triangular lattice of pillars in maN-2403 exposed at dosages (a.) 45 μC/cm^2, (b.) 63 μC/cm^2, (c.) 75 μC/cm^2

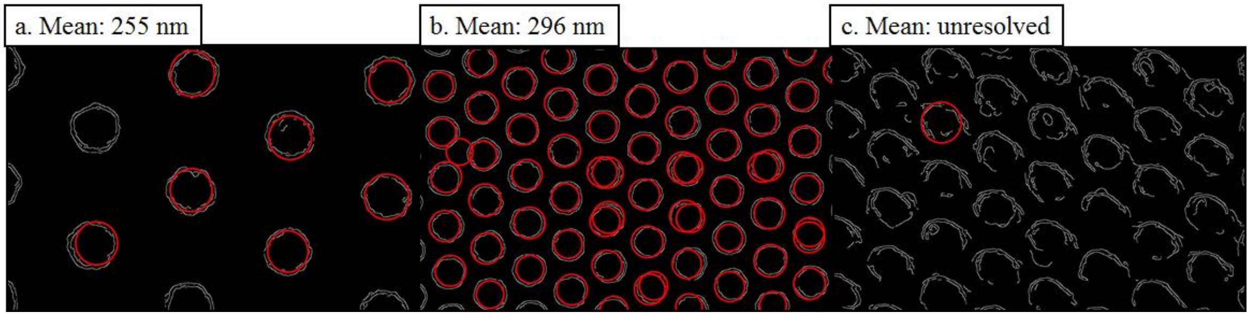
a. Mean: 255 nm

b. Mean: 296 nm

c. Mean: unresolved

Figure 9.13 Matlab extracted images showing mean diameter from the respective SEM images at dosages(a.) 45 μC/cm^2, (b.) 63 μC/cm^2, (c.) 75 μC/cm^2

Table 9.3 Optimal processing parameters for maD-525

EBL processing parameters for maN-2403	
Spin Recipe	5000 rpm for 50 seconds
Exposure Dosage	55-65 μC/cm^2
Developer	maD-525
Development Time	70-75 seconds

FOx-16

The typical exposure dosages for FOx-16 resist lie in the range of 200 μC/cm^2 to 600 μC/cm^2. Samples were then developed in MF-CD 26A developer set on a hot plate at 80^{o}C for about 12 minutes. Figure 9.14 show the resulting patterns observed at 200, and 600 μC/cm^2. The Matlab script was used to extract the features based on the contrast between the features and background. Figure 9.15 shows the extracted features and mean diameter of the features at respective dosages. From the analysis, it is observed that all the dosages have a mean diameter of 440-445 nm which is close to the target feature size of 440 nm. However, it is observed that the pillars developed at higher dosages seem to have a bell shape than a cylinder as shown in the Figure 9.16.

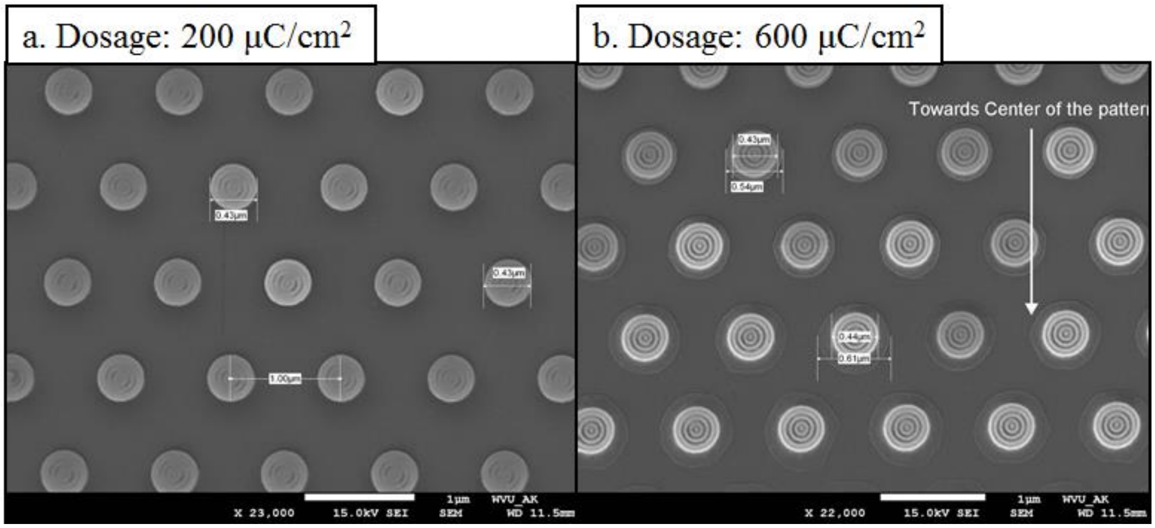

Figure 9.14 SEM images of triangular lattice of holes in FOx-16 exposed at dosages (a.) 200 μC/cm^2, (b.) 600 μC/cm^2

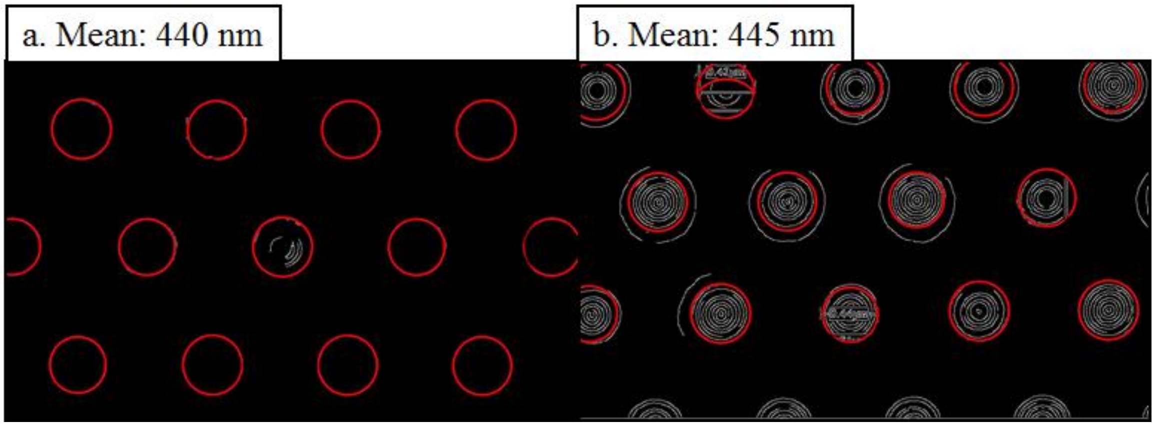

Figure 9.15 Matlab extracted images showing mean diameter from the respective SEM images at dosages (a.) 200 μC/cm^2, (b.) 600 μC/cm^2

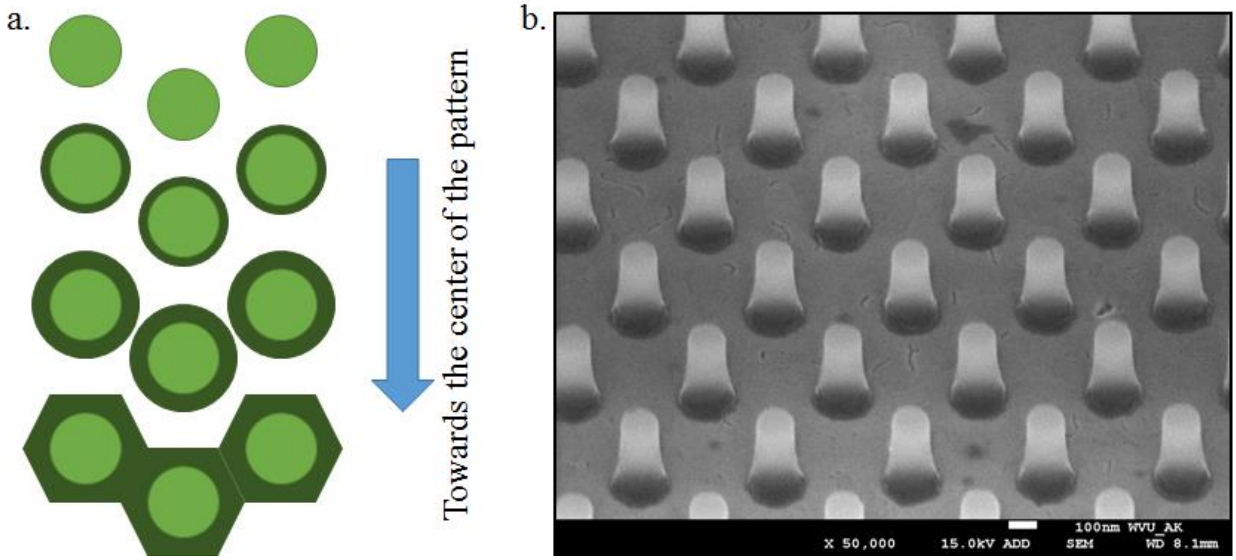

Figure 9.16 (a.) Illustration of the development regime at higher dosages, (b.) SEM image of the bell shaped pillars observed at 400µC/cm^2

The sidewall quality can be improved further by increasing the exposure dosages and using a potassium hydroxide based developer. The exposure dosages are now increased to 1000 µC/cm^2 to 10000 µC/cm^2. For this study, a gradient pattern was designed in the CAD software to understand the effect of the dosage on the feature size. Figure 9.17 shows the gradient pattern illustration that contains features ranging from 150 nm to 500 nm in diameter.

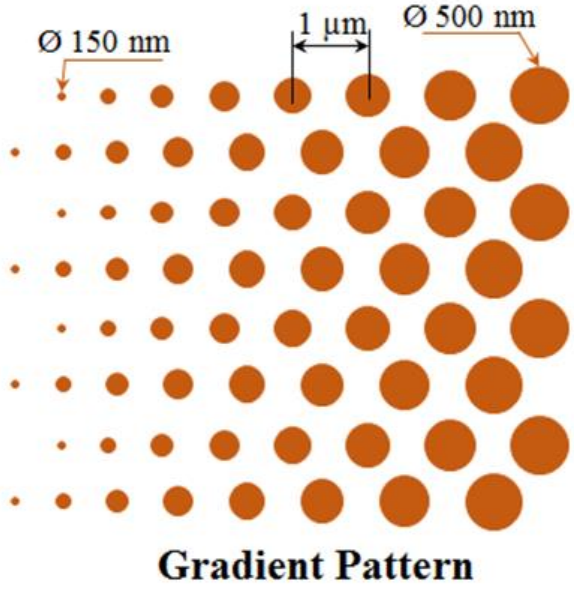

Figure 9.17 Illustration of the gradient pattern

Samples were exposed with dosages from 1000 μC/cm^2 to 7500 μC/cm^2 and developed in an AZ 400 K developer diluted in DI water (1:1) for about 150 seconds. Figure 9.18 shows the resultant patterns observed at 1000 μC/cm^2 and 6000 μC/cm^2. It is observed that the smaller features are developed at higher dosages and larger features are exposed at almost every exposure dosages.

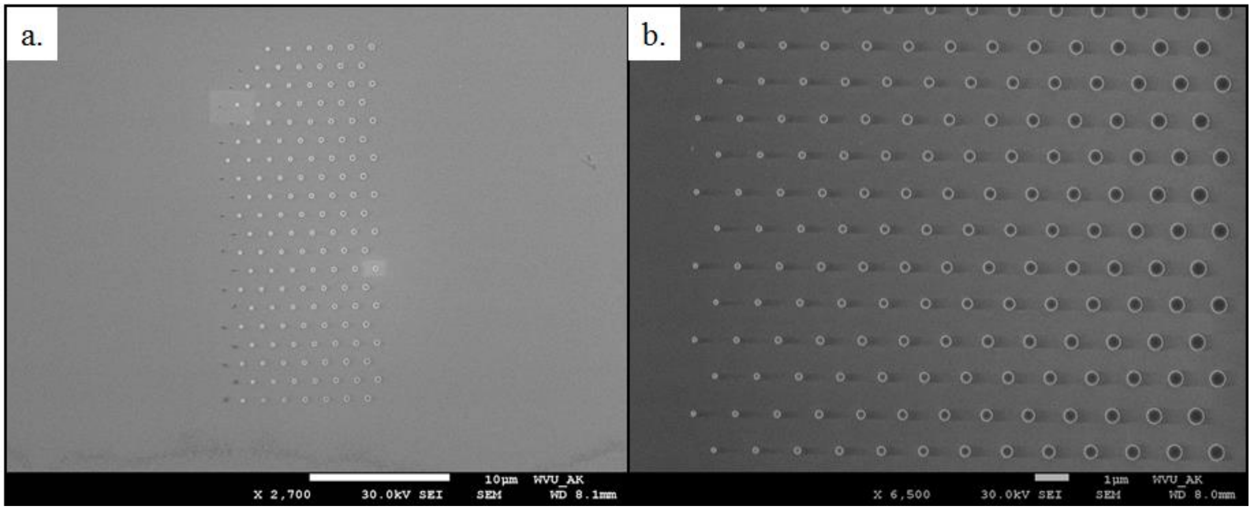

Figure 9.18 SEM image of developed patterns at (a.) 1000 μC/cm^2, (b.) 6000 μC/cm^2

Using the above determined dosage and development process, FOx-16 patterns were developed with highly anisotropic sidewalls as shown in the Figure 9.19.

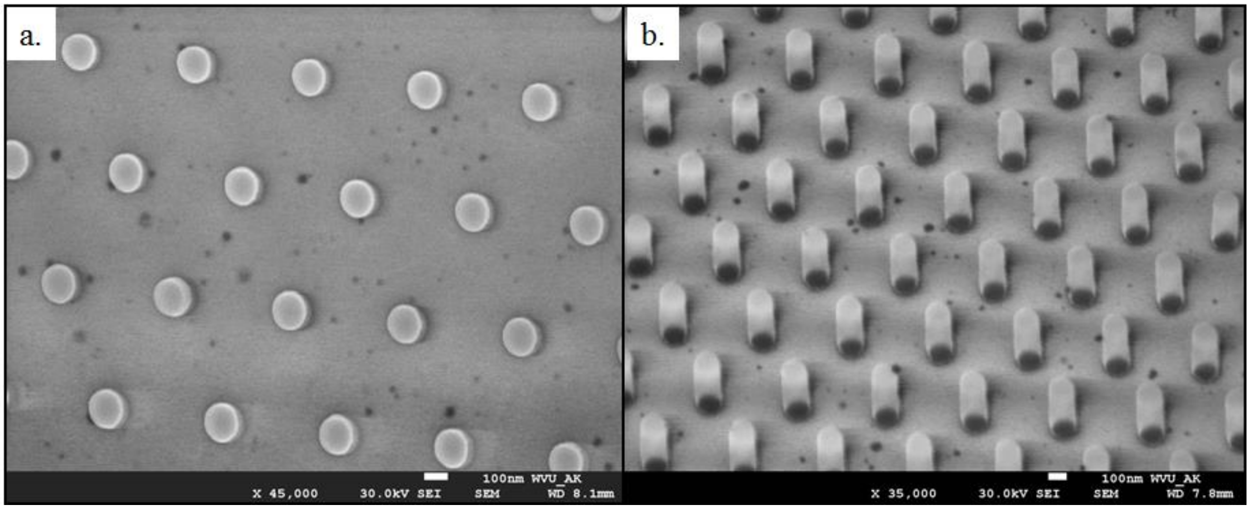

Figure 9.19 SEM images of PhC patterns developed using higher exposure energy and KOH based developer (a.) top view, (b.) Tilted view showing the sidewall

Table 9.4 Optimal processing parameters for FOx-16 and MF CD-26A

EBL processing parameters for FOx-16 using MF CD-26A	
Spin Recipe	3000 rpm for 60 seconds
Exposure Dosage	200-300 μC/cm^2
Developer	MF CD-26A (80^{o}C)
Development Time	12 minutes

Table 9.5 Optimal processing parameters for FOx-16 and AZ 400K

EBL processing parameters for FOx-16 using AZ 400K	
Spin Recipe	3000 rpm for 60 seconds
Exposure Dosage	4500-6000 μC/cm^2
Developer	AZ 400K : DI Water (1:1)
Development Time	150 seconds

9.3.4. SEM Characterization – Matlab Script

The Matlab script for characterizing the SEM images requires both the image and the text file associated with it. The script checks the text file for the number of pixels representing the scale on the image and uses that information to calculate the radii of the features from pixels to actual scale. The parameters that are critical to improve the image analysis are the edge detection sensitivity, minimum and maximum radius, and circle detection sensitivity. For better results using this code, the SEM images are to be captured at same magnification and have proper contrast.

Filename: SEM_Characterization.m

```
-----------------------------Start-of-File------------------------------

clear all
close all
clc

[filename, filepath] = uigetfile('*.tif','Select the image file');
flength=length(filename);
fname=filename(1:flength-4);
I = imread(strcat(filepath,filename));
I2=imcrop(I,[124.5 151.5 1044 650]);
ac=edge(I2,'canny',0.15); % Edge detection (source, 'Method', Sensitivity)
%%Vary the sensitivity to improve the edge detection%%
figure();
```

```
imshow(ac);
%%Find the circular features
min_r=50;
max_r=100;
[centers, radii] = imfindcircles(ac,[min_r max_r],'ObjectPolarity','bright',
...
    'Sensitivity',0.95,'Method','twostage');
% (source, [min_r max_r], 'Sensitivity')
% Vary the sensitivity to improve finding the circles
h = viscircles(centers,radii);
saveas(h,strcat(filepath,fname,'_analysis'),'jpg');
% To extract the pixel and micronbar information from the text file.
fileid = strcat(filepath,fname,'.txt');
delimiter = ' ';
startRow = 55; %55 or 65
endRow = 56; %56 or 66
formatSpec = '%s%f%*s%*s%*s%*s%*s%*s%*s%*s%*s%*s%*s%*s%[^\n\r]';
fid = fopen(fileid,'r');
dataArray = textscan(fid, formatSpec, endRow-startRow+1, 'Delimiter',
delimiter, 'MultipleDelimsAsOne', true, 'HeaderLines', startRow-1,
'ReturnOnError', false);
fclose(fid);
% Actual extracted information
info=dataArray{:,2};
% Pixel and Micronbar information
pixels=info(1,1);
micronbar=info(2,1);
% nm/pixel
mpixel=micronbar/pixels;
actual_diameters=2*radii.*mpixel;
mean_diameter_in_nm= mean(actual_diameters)
---------------------------------End-of-File--------------------------------
```

9.3.5. Etching

Throughout this dissertation, materials like gallium nitride, silicon dioxide, silicon, indium tin oxide were etched using the inductively coupled plasma reactive ion etching (ICP/RIE). These dry etching processes were carried out on a Trion Minilock Phantom III ICP/RIE. Typical process parameters to generate a plasma include, the chemical gas composition, gas flow, chamber pressure, ICP power, RIE power, and DC bias.

Gallium Nitride

A BCl_3/Cl_2 plasma is used to etch gallium nitride (GaN) and the initial processing parameters are listed in the Table 9.6. Listed parameters produce an etch depth of 560 nm over a time of 300 seconds resulting in a 1.8 nm/s etch rate. Figure 9.20 shows the etch profile achieved using the listed initial parameters. As observed, it produced a very rough sidewall profile.

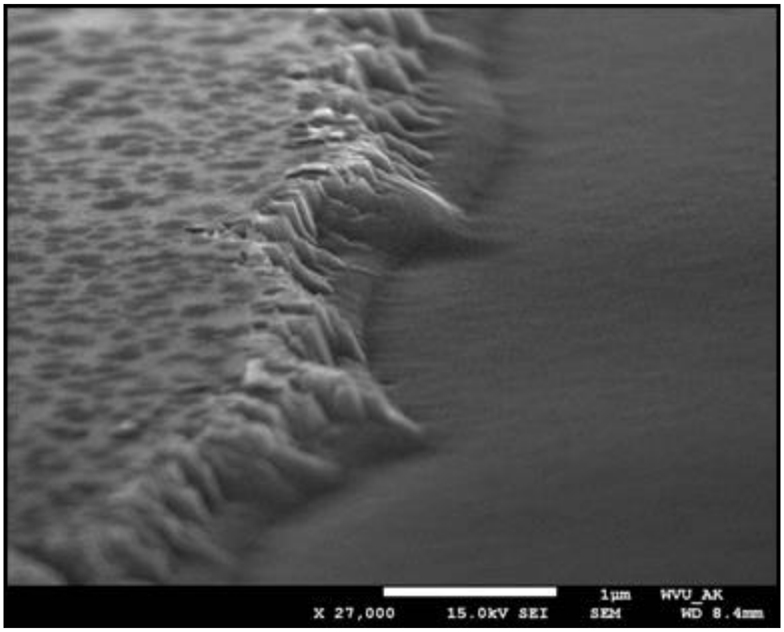

Figure 9.20 Rough sidewall produced using initial parameters

Table 9.6 Initial etch parameters for etching gallium nitride

Pressure	10 mT
Gas 1 – Boron Trichloride (BCl_3)	10 sccm
Gas 2 – Chlorine (Cl_2)	20 sccm
ICP Power	400 W
RIE Power	100 W
Time	300 seconds

Using these initial set of parameters, the etch rates and depths were inconsistent and further investigation was done to improve the etch profile. A 60 second etch was done on samples at regular intervals using the same set of parameters and the data was used to analyze and control the process for consistent etch rates. A summary of the data acquired over a span of 10 weeks is shown in the Figure 9.21. It was also observed that the back side cooling of the wafer done by helium gas played a key role in achieving a consistent etch rate. Figure 9.22 shows the etch rate plotted against the helium flow rate of the electrostatic chuck. The etch rate is found to be consistent when the helium flow is below 1.0 sccm as seen in the Figure. When the helium flow is above 1.0 sccm, the helium gas is believed to dilute the etch gases and reduce the etch rates. This way, the helium flow rate is also added as a factor to control the etch rate to produce consistent results.

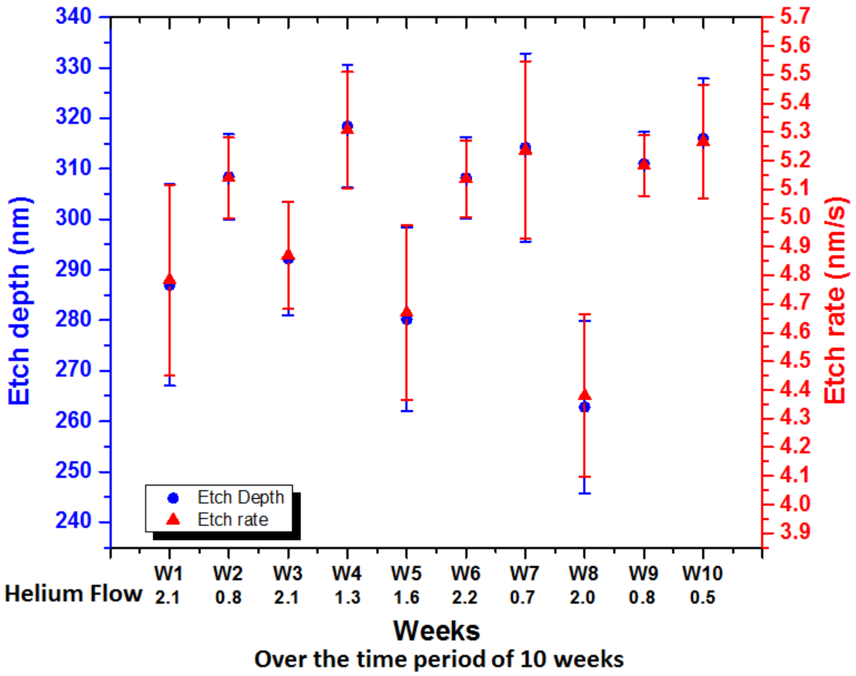

Figure 9.21 Summary of the etch rates and etch depths achieved over a span of 10 weeks

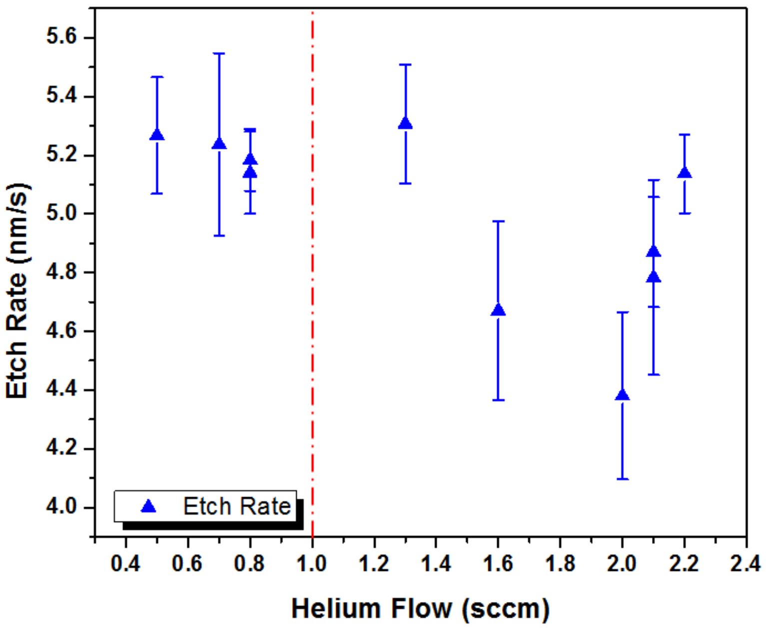

Figure 9.22 Etch rate versus helium flow rate

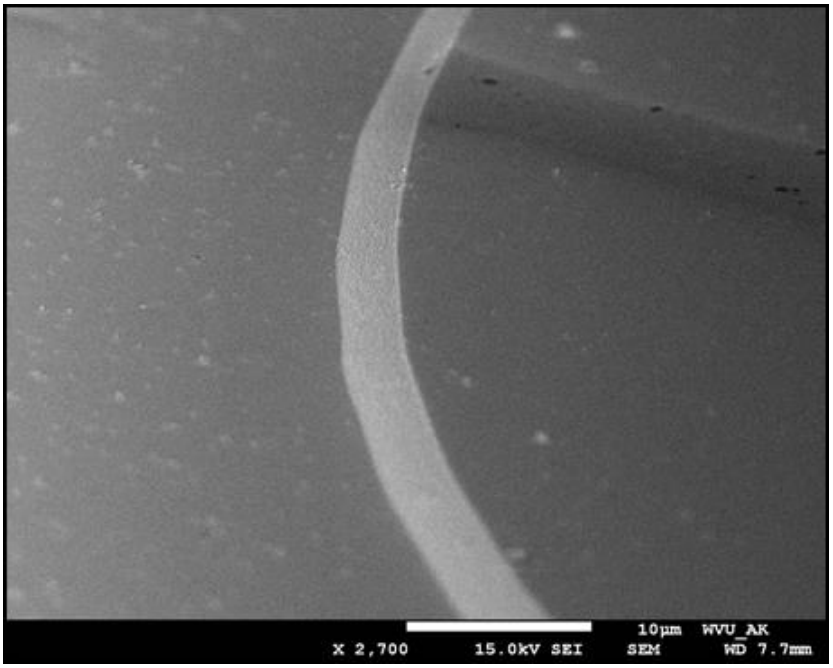

Figure 9.23 Smooth sidewall achieved after resolving the helium flow issue

Figure 9.23 shows the etch profile achieved with the electrostatic chuck replaced to have helium consistent flow rate below 1.0 sccm. The final etch parameters to etch gallium nitride is listed in the Table 9.4. With the new etch rates, an etch depth of 500 nm could be achieved with less than 120 seconds of etch process time.

Table 9.7 Optimized etch parameters for etching gallium nitride (GaN)

Pressure	10 mT
Gas 1 – Boron Trichloride (BCl_3)	10 sccm
Gas 2 – Chlorine (Cl_2)	20 sccm
ICP Power	375 W
RIE Power	100 W
Helium Flow	≤ 1.0 sccm
Time	120 seconds
DC Bias	-150 V
Etch Depth	~ 500 nm

Similarly, the etch parameters for ITO, and silicon dioxide are listed in the following Tables 9.8, and 9.9.

Indium Tin Oxide

Table 9.8 Optimized etch parameters for etching indium tin oxide (ITO)

Pressure	10 mT
Gas 1 – Boron Trichloride (BCl_3)	12 sccm
Gas 2 – Chlorine (Cl_2)	12 sccm
Gas 3 – Tetrafluoromethane (CF_4)	6 sccm
ICP Power	400 W
RIE Power	100 W
Helium Flow	≤ 1.0 sccm
Time	120 seconds
Etch Depth	~ 250 nm

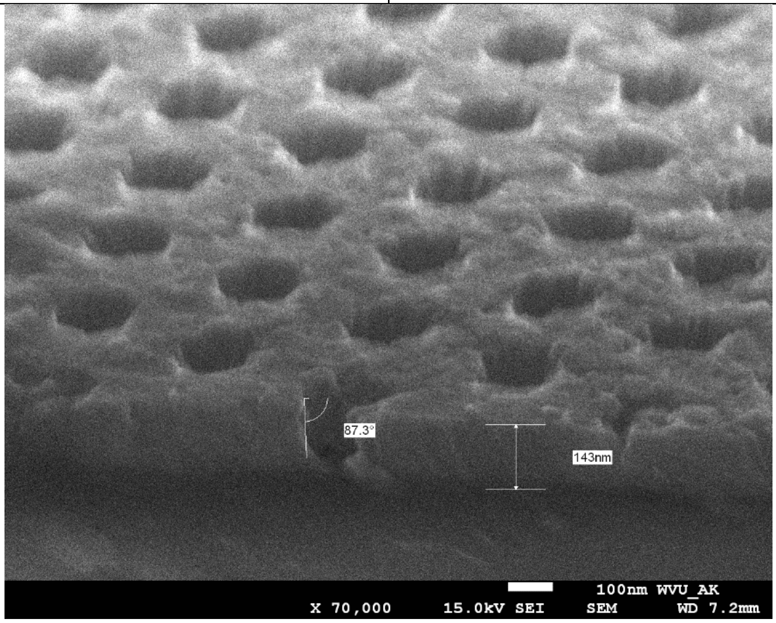

Figure 9.24 ITO holes etched using the above process parameters

Silicon Dioxide

Table 9.9 Optimized etch parameters for etching silicon dioxide (SiO_2)

Pressure	10 mT
Gas 1 – Tetrafluoromethane (CF_4)	18 sccm
Gas 2 – Oxygen (O_2)	6 sccm
ICP Power	375 W

RIE Power	100 W
Helium Flow	≤ 1.0 sccm
Time	60-90 seconds
Etch Depth	~ 400 nm

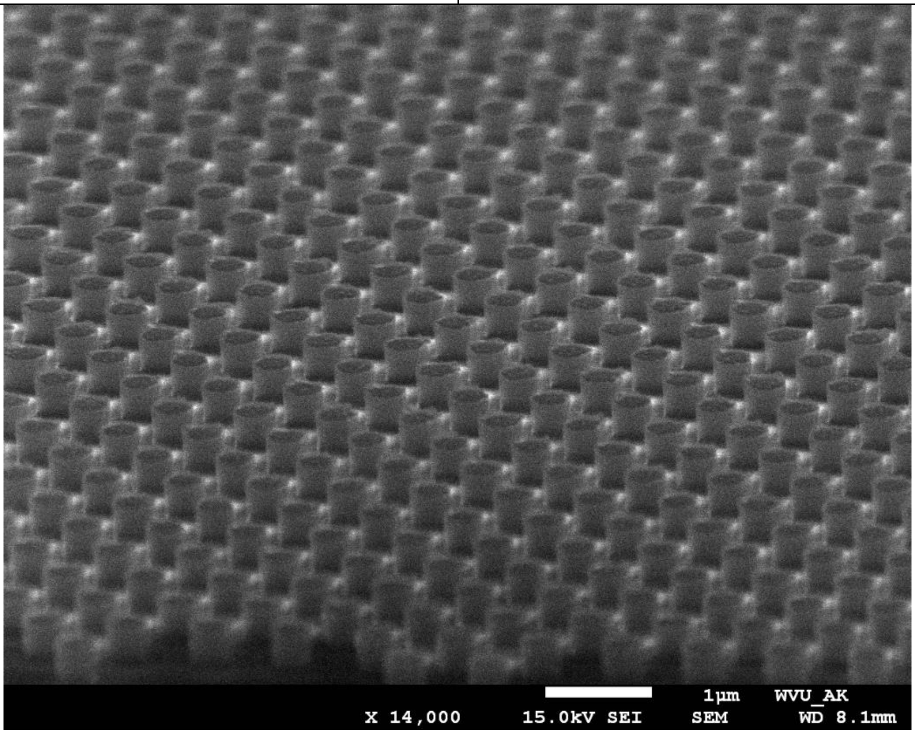

Figure 9.25 SiO_2 pillars etched using the above recipe

PMMA Etch

Etching 950 PMMA A7 was necessary to enable the bilayer processing and easy lift-off using HSQ for patterning holes in a material. A simple oxygen plasma was used to etch the sacrificial layer in a March PX-250 Oxygen Plasma Asher. The respective processing parameters are listed in the Table 9.10 to achieve the 500 nm etch of the PMMA layer with undercut.

Table 9.10 Optimized etch parameters for etching 950 PMMA A7 (Bilayer processing)

Pressure	300 mT
Gas 1 – Oxygen (O_2)	Depends on the tank pressure
RF Power	300 W
Time	180-240 seconds
Etch Depth	~ 500 nm with undercut

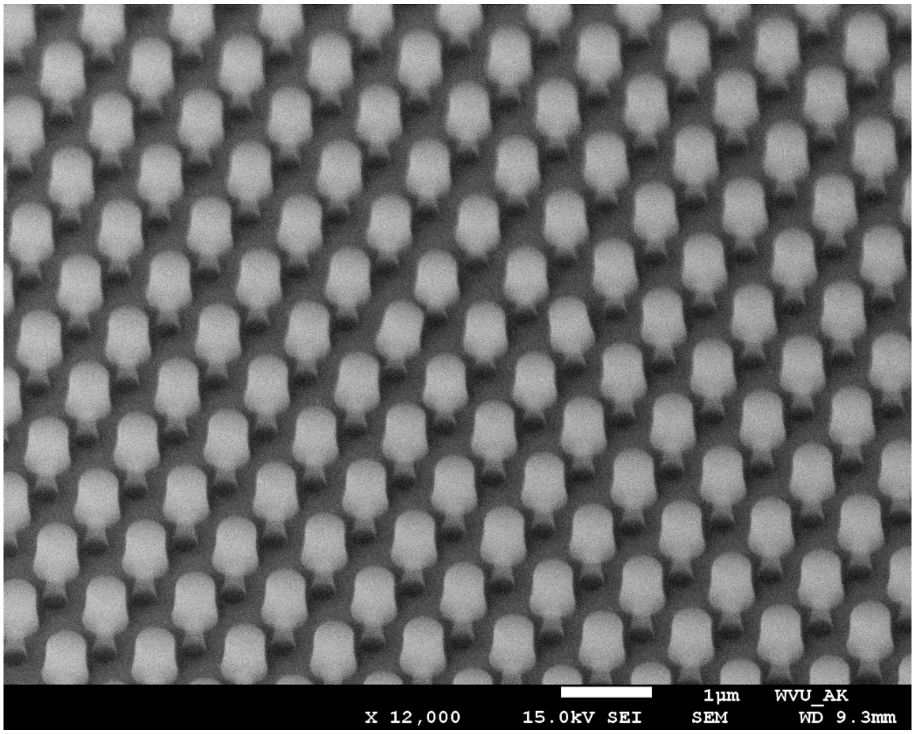

Figure 9.26 Sacrificial PMMA layer etched using the oxygen plasma recipe

9.3.6. Sample Mounting Method – ICP/RIE

The samples prepared for etching using ICP/RIE need to be mounted on a 4 inch silicon wafer. For some etch recipes, by products produced by the exposure of silicon may cause issues to the etch rates. To counter this, a sample mounting method was developed using AZ 4400 photoresist. The 4 inch silicon wafer is spin coated with AZ 4400 at a spin speed of 4000 rpm for 30 seconds. This should produce a 4.4 µm thick layer of photoresist.

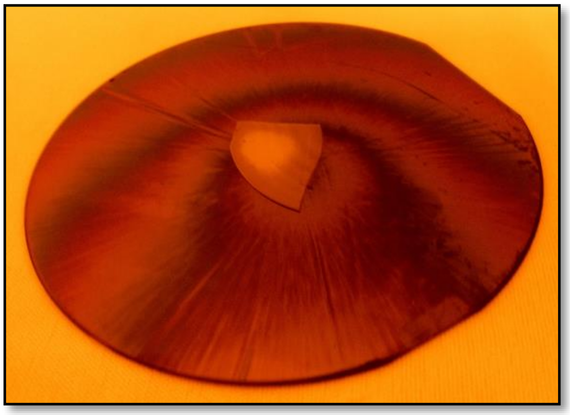

Figure 9.27 Sample attached to the carrier wafer using photoresist

Due to the solvents present in the photoresist, the surface is sticky and can adhere to any sample placed on it. Gently place the sample on the resist layer and press all four corners to ensure sample is secured to the carrier wafer. Hard bake the sample along with the carrier wafer at 120°C for 20 minutes. The carrier wafer is shown in the Figure 9.27. After the etching is done, the sample and the carrier wafer are cleaned in heated bath of AZ 300T stripper for 1 hour. This length of time should strip off the photoresist on both the sample and the wafer.

9.4. Appendix D – Characterization

9.4.1. Optimal Thickness for Maximum Transmittance

Optimal thickness of ITO for maximum transmittance has been discussed in the fabrication chapter. The following Matlab script is used to simulate various thicknesses of ITO layer to find the thickness with maximum transmittance.

Filename: ito_optimal_thickness.m

```
--------------------------------Start-of-File-------------------------------

clear all;
close all;
clc;

n1 = 1;  %layer 1 Air
n2 = 2.0227; %layer 2 ITO
n3 = 2.4736; %layer 3 GaN

lambda=440e-9; %wavelength
layername='ITO';

r12=(n1-n2)/(n1+n2);
r23=(n2-n3)/(n2+n3);
hh=[];
rr_tot=[];

for h=0:1e-9:350e-9;
    hh=[hh h];
    beta=(2*pi*n2*h/lambda);

r_tot=((r12^2)+(r23^2)+(2*r12*r23*cos(2*beta)))/(1+((r12^2)*(r23^2))+(2*r12*r
23*cos(2*beta)));
    rr_tot=[rr_tot r_tot];
end

HH=hh.*10^9;
plot(HH, 1-rr_tot,'b.-','LineWidth',1.25);
hold on;
[x,i]=max(1-rr_tot);
[r c] = find( (1-rr_tot) > x-0.0001)
```

```
plot(HH(c),1-rr_tot(c),'r*');
hold on;
text(HH(10),0.985,strcat('\bf{Max:',num2str(x*100),'%
at:',num2str(HH(i)),'nm}'),'FontSize',12);
hold on;
text(HH(10),0.97,strcat('\bf{- 0.001% at thickness of--
',mat2str(HH(c)),'nm}'),'FontSize',10);
hold off;
title(strcat('\bf{Optimal Thickness of--', layername,'--in GaN/ITO/Air stack
at \lambda=',num2str(lambda*10^9),'nm}'));
xlabel('\bf{Thickness (nm)}');
ylabel('\bf{Transmittance}');
axis([0 300 0.8 1]);
filename1=strcat('Opt_thick_',layername,'_',num2str(lambda*10^9));
saveas(gcf,strcat(filename1,'.tiff'));
---------------------------------End-of-File--------------------------------
```

9.4.2. Setup for Transmittance Measurement

For measuring the transmittance of a thin film, an optical setup was constructed to gather spectra from the substrate and thin film that is deposited on the substrate. Dividing the two spectra obtained from plain substrate and the combo thin film/substrate results in the transmittance characteristics of the thin film. Figure 9.27 shows the setup of the transmittance measurement. A white light source is used as the input and a visible spectrometer (BWTek Quest-U CCD Array Spectrometer) is used for collecting the transmitted photons. Two optical fibers are used in this setup, one for the source light and the other for transmitted light. The two fibers are aligned using x-y manipulators for maximum transmission before the measurement.

The sample is placed on the flat edge flush to the optical fiber as shown in the Figure 9.28 inset. BWTek software is used to collect the intensities of the photons w.r.t. the wavelength that are transmitted through the sample/substrate. Two individual spectra are collected and divided to get the transmittance of the thin film as shown in the Equation (9.1).

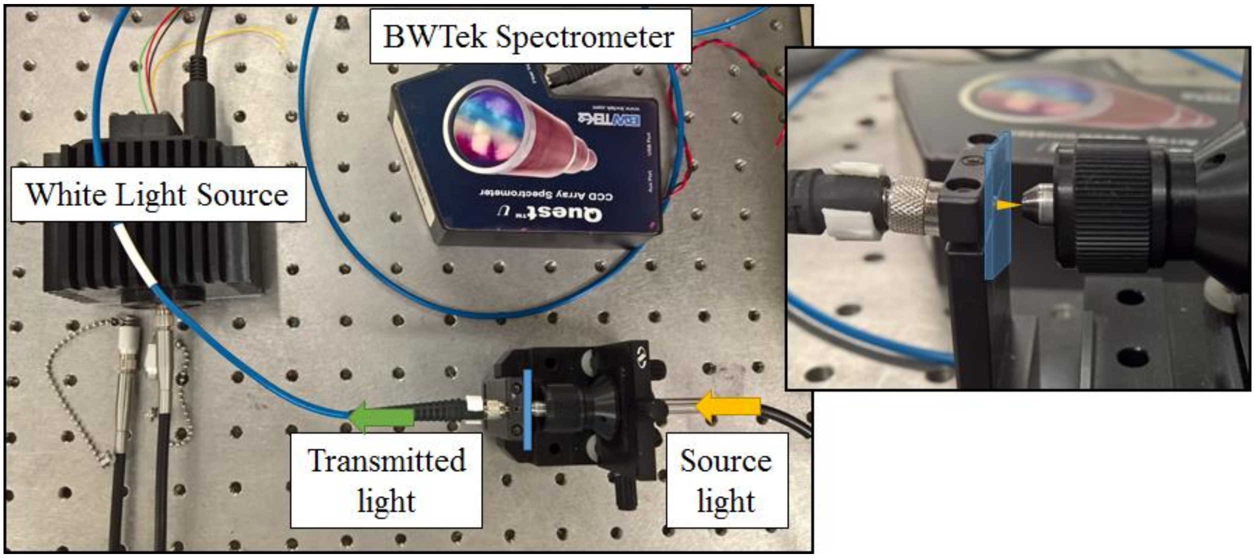

Figure 9.28 Optical Transmittance Measurement Setup

$$T\ (\%) = \frac{Spectrum\ of\ Thin\ Film\ on\ the\ Substrate}{Spectrum\ of\ the\ Substrate} \times 100 \tag{9.1}$$

9.4.3. LED Characterization Setup

Characterization of LEDs include gathering important data like current-voltage (IV) characteristics, electroluminescence spectra (EL), and radiation spectra. Several characterization equipment like parameter analyzer for IV measurement, constant current source and CCD array spectrometer for electroluminescence data are required. A WILD microscope with a 50x objective is used in conjunction with a Canon 5D Mark III camera to facilitate live view and probing the contacts as shown in the Figure 9.29. All the equipment required is setup on a cart for ease of use as shown in the Figure 9.29 (inset). The parameter analyzer is used to gather IV characteristics of the device that is probed using the probe micromanipulators. Initially, the IV-EL switch is set to IV and the parameter analyzer is used to gather the IV data. Usual data range for an IV measurement is -5V to 5V with a step of 0.1V. Once the IV data is saved, the IV-EL switch is flipped to the EL position. At this point the optical fiber is placed above the LED as shown in the Figure 9.30 and a dark spectrum is taken by the BWTek spectrometer and the software. After that, a constant current is injected into the device and the respective EL data is taken. Different EL spectra is taken at different injection currents to observe the shift in the emission wavelength as the current increases.

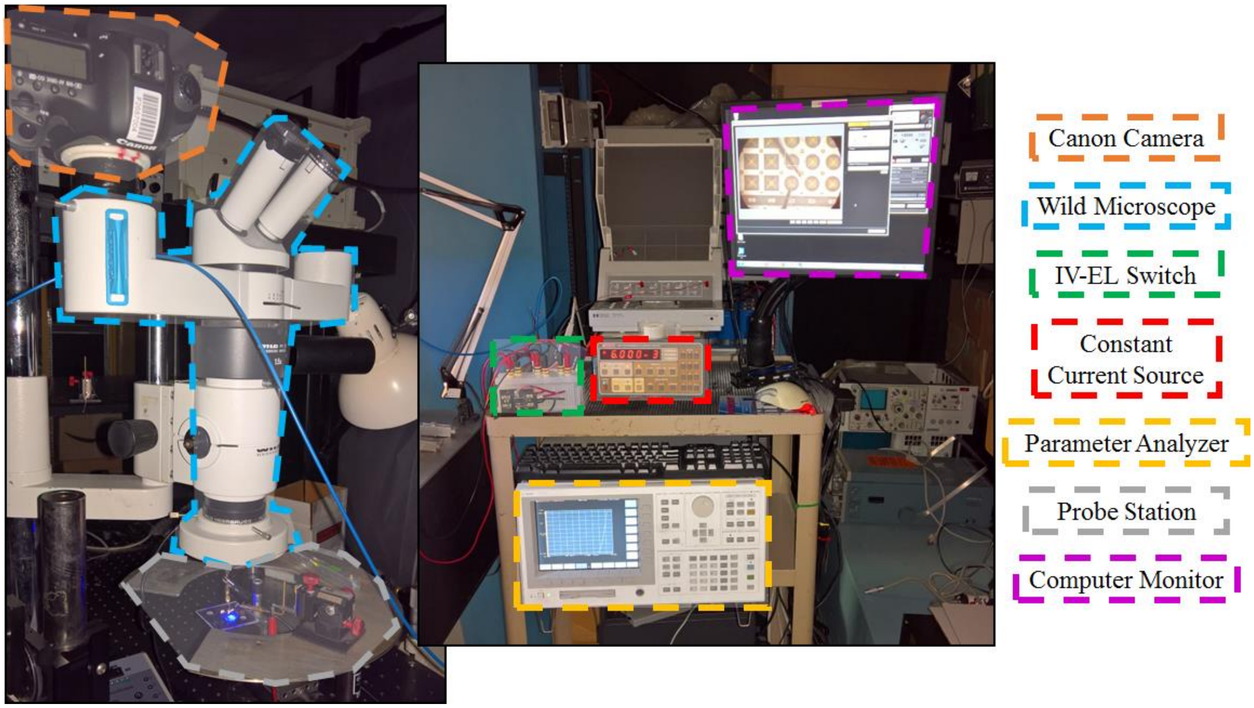

Figure 9.29 Characterization setup with different equipment

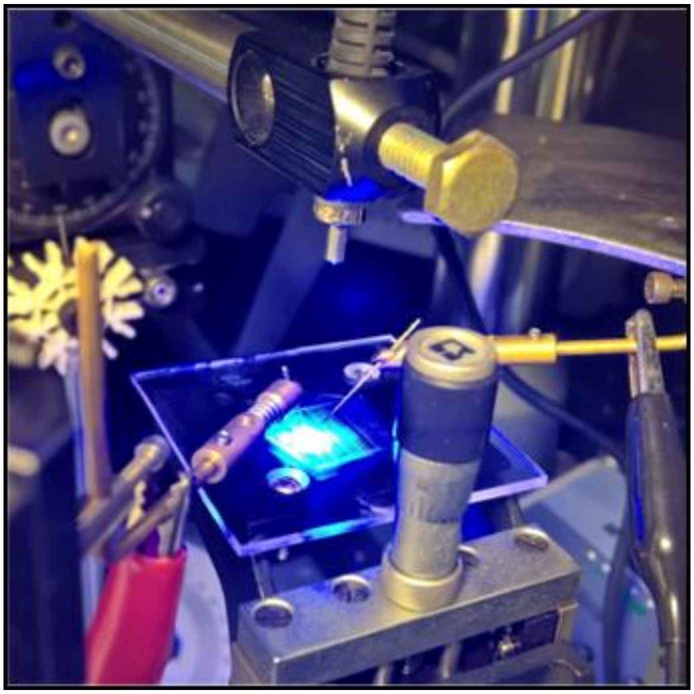

Figure 9.30 Setup for gathering EL spectra for an LED

9.4.4. Image Analysis Setup

Analyzing the overall performance of the LED in this research is done by a Matlab based image analysis program. After the critical data (IV-EL) is saved, the same setup is used for capturing images for further analysis. Canon’s camera software is used to take pictures of the LED at 50x magnification at different injection currents. These images are taken with identical imaging settings like the ISO, shutter speed and color balance. ISO represents the sensitivity of the imaging sensor in the camera. A number is usually associated with the ISO of the sensor, for example, ISO 100 or ISO 3200. As the ISO number increases, the sensitivity increases which also increases noise in the images taken. Finding an appropriate ISO value is critical in taking images for image analysis.

Shutter speed is the time for which the camera sensor is exposed the light coming through the microscope. Figure 9.31 shows the images of the same LED captured at different shutter speeds. As seen, the amount of light can be regulated using the shutter speed as well. The goal here is to find the appropriate shutter speed for image analysis that enables capturing of images without any saturation. If multiple types of LEDs are being compared, always chose the shutter speed that is best suited for the brightest LED and use the same conditions for the others.

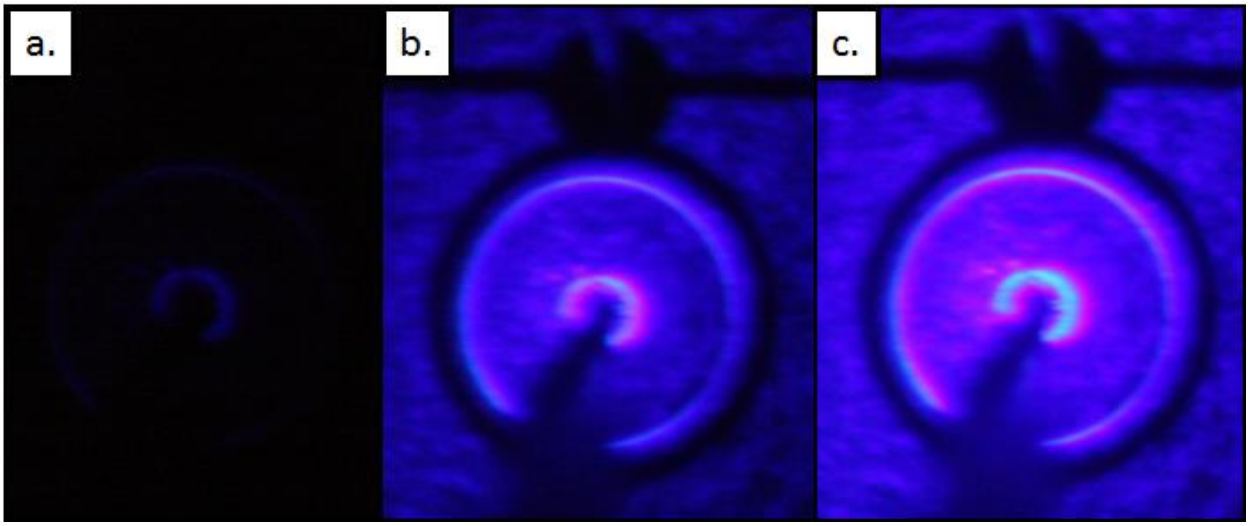

Figure 9.31 Variation of shutter speed (a.) 1/160 s, (b.) 1/4 s, and (c.)1/2 s

Finally, the other parameter is the color balance that is required for imaging purposes. This parameter is a preset condition in the camera that ensures proper representation of the colors in the image. As the images captured are of blue LEDs, the color balance for the images is set to the color temperature option with a temperature set to 10000K. This temperature has the highest sensitivity to the photons with wavelength in the blue region.

After setting the initial parameters, a background image is taken with the LED turned OFF. This is used for the residual noise reduction in the analysis step. The LED is turned ON by the injecting a constant current using the current source. Images are captured at set parameters using the Canon's EOS software. The resulting images are shown in the Figure 9.32. These images are cropped around the LED and then plugged into the image analysis program for further analysis.

Figure 9.32 Raw image data captured using the setup. Cropped area shown using red line

The image analysis code, takes in the cropped images (LED and background) and subtracts them to remove any residual noise. After de-noising, the resultant image is split into red, green and blue components. This data is an integral part of a jpeg image from a camera. Of the three components, only the blue component is used for further analysis. At this point, if multiple images are compared, then the overall intensity profiles, histograms, row-col profiles are extracted for individual images and multiple graphs are exported. The following section shows the Matlab script written to extract the above mentioned profiles from the data. At the end of the execution of the script, it opens a comparison window with the intensity profiles of the two images as shown in the Figure 9.33. Additional text files with the extracted data are also exported for further analysis if needed.

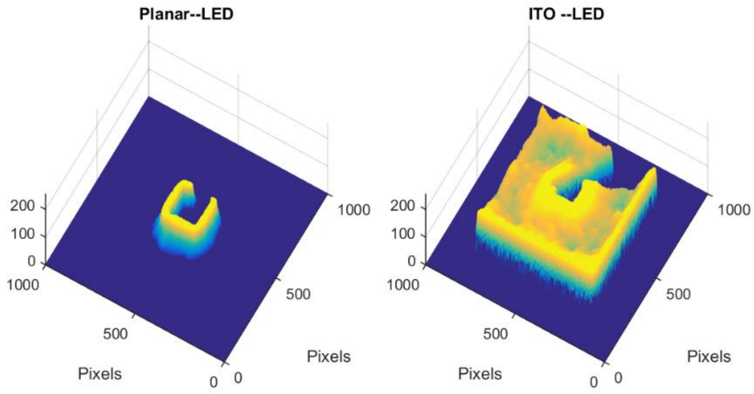

Figure 9.33 Intensity profiles of the two LEDs compared using the image analysis script

9.4.5. Image Analysis Code

The following code is written to compare four different types of LEDs.

Filename: image_analysis_4files.m

```
-------------------------------Start-of-File--------------------------------

clear all
clc

% File Namings
strpic1=input('Enter Picture 1 Type : ', 's');
strpic2=input('Enter Picture 2 Type : ', 's');
strpic3=input('Enter Pictrue 3 Type : ', 's');
strpic4=input('Enter Pictrue 4 Type : ', 's');

% IO Path Definition
iopath=uigetdir('C:\','Select the Input Output Directory');

% Background Image
[bgfile,bgpath]=uigetfile('*.jpg','Select the Background Image',iopath);
BG=imread(strcat(bgpath,bgfile),'jpg');

% File1 Image
[file1name,file1path]=uigetfile('*.jpg',strcat('Select the--', strpic1,'--
Image'),iopath);
File1=imread(strcat(file1path,file1name),'jpg');

% File2 Image
[file2name,file2path]=uigetfile('*.jpg',strcat('Select the--', strpic2,'--
Image'),iopath);
File2=imread(strcat(file2path,file2name),'jpg');
```

```
% File3 Image
[file3name,file3path]=uigetfile('*.jpg',strcat('Select the--', strpic3,'--
Image'),iopath);
File3=imread(strcat(file3path,file3name),'jpg');

% File4 Image
[file4name,file4path]=uigetfile('*.jpg',strcat('Select the--', strpic4,'--
Image'),iopath);
File4=imread(strcat(file4path,file4name),'jpg');

% Output Path
outputpath=strcat(iopath,'\');

% Background Subtraction
File1BG = File1-BG;
File2BG = File2-BG;
File3BG = File3-BG;
File4BG = File4-BG;

% Blue Intensity Extraction
File1blue = File1BG(:,:,3);
File2blue = File2BG(:,:,3);
File3blue = File3BG(:,:,3);
File4blue = File4BG(:,:,3);

% Size of the Images
[r,c]=size(File1blue);
M=1:r;
N=1:c;
index=M';

% File1 Row and Colum Slices
File1Row = File1blue(r/2,:);
File1Col = File1blue(:,c/2);
dlmwrite(strcat(outputpath,'Row_',strpic1,'.txt'),[index File1Row']);
dlmwrite(strcat(outputpath,'Col_',strpic1,'.txt'),[index File1Col]);

% File2 Row and Colum Slices
File2Row = File2blue(r/2,:);
File2Col = File2blue(:,c/2);
dlmwrite(strcat(outputpath,'Row_',strpic2,'.txt'),[index File2Row']);
dlmwrite(strcat(outputpath,'Col_',strpic2,'.txt'),[index File2Col]);

% File3 Row and Colum Slices
File3Row = File3blue(r/2,:);
File3Col = File3blue(:,c/2);
dlmwrite(strcat(outputpath,'Row_',strpic3,'.txt'),[index File3Row']);
dlmwrite(strcat(outputpath,'Col_',strpic3,'.txt'),[index File3Col]);

% File4 Row and Colum Slices
File4Row = File4blue(r/2,:);
File4Col = File4blue(:,c/2);
dlmwrite(strcat(outputpath,'Row_',strpic4,'.txt'),[index File4Row']);
dlmwrite(strcat(outputpath,'Col_',strpic4,'.txt'),[index File4Col]);
```

```
% File 1 Bar Row Plot
figure()
bar(N,File1Row);
title(strcat('Row Intensity Profile for--',strpic1,'--LED'));
xlabel('Pixels');
ylabel('Blue Intensity');
saveas(gcf,strcat(outputpath,'Intensity_Profile_Row_',strpic1),'tif');

% File 1 Bar Col Plot
figure()
barh(M,File1Col);
title(strcat('Column Intensity Profile for--',strpic1,'--LED'));
xlabel('Pixels');
ylabel('Blue Intensity');
saveas(gcf,strcat(outputpath,'Intensity_Profile_Col_',strpic1),'tif');

% File 1 Histogram Plot
figure()
hist(double(File1Row));
title(strcat('Histogram of--',strpic1,'--LED'));
xlabel('Pixel Intensity');
ylabel('No of Pixels');
saveas(gcf,strcat(outputpath,'Histogram_Row_',strpic1),'tif');

% File 2 Histogram Plot
figure()
hist(double(File2Row));
title(strcat('Histogram of--',strpic2,'--LED'));
xlabel('Pixel Intensity');
ylabel('No of Pixels');
saveas(gcf,strcat(outputpath,'Histogram_Row_',strpic2),'tif');

% File 3 Histogram Plot
figure()
hist(double(File3Row));
title(strcat('Histogram of--',strpic3,'--LED'));
xlabel('Pixel Intensity');
ylabel('No of Pixels');
saveas(gcf,strcat(outputpath,'Histogram_Row_',strpic3),'tif');

% File 4 Histogram Plot
figure()
hist(double(File4Row));
title(strcat('Histogram of--',strpic4,'--LED'));
xlabel('Pixel Intensity');
ylabel('No of Pixels');
saveas(gcf,strcat(outputpath,'Histogram_Row_',strpic4),'tif');

% File 2 Bar Row Plot
figure()
bar(N,File2Row);
title(strcat('Row Intensity Profile for--',strpic2,'--LED'));
xlabel('Pixels');
ylabel('Blue Intensity');
```

```
saveas(gcf,strcat(outputpath,'Intensity_Profile_Row_',strpic2),'tif');

% File 2 Bar Col Plot
figure()
barh(M,File2Col);
title(strcat('Column Intensity Profile for--',strpic2,'--LED'));
xlabel('Pixels');
ylabel('Blue Intensity');
saveas(gcf,strcat(outputpath,'Intensity_Profile_Col_',strpic2),'tif');

% File 3 Bar Row Plot
figure()
bar(N,File3Row);
title(strcat('Row Intensity Profile for--',strpic3,'--LED'));
xlabel('Pixels');
ylabel('Blue Intensity');
saveas(gcf,strcat(outputpath,'Intensity_Profile_Row_',strpic3),'tif');

% File 3 Bar Col Plot
figure()
barh(M,File3Col);
title(strcat('Column Intensity Profile for--',strpic3,'--LED'));
xlabel('Pixels');
ylabel('Blue Intensity');
saveas(gcf,strcat(outputpath,'Intensity_Profile_Col_',strpic3),'tif');

% File 4 Bar Row Plot
figure()
bar(N,File4Row);
title(strcat('Row Intensity Profile for--',strpic4,'--LED'));
xlabel('Pixels');
ylabel('Blue Intensity');
saveas(gcf,strcat(outputpath,'Intensity_Profile_Row_',strpic4),'tif');

% File 3 Bar Col Plot
figure()
barh(M,File4Col);
title(strcat('Column Intensity Profile for--',strpic4,'--LED'));
xlabel('Pixels');
ylabel('Blue Intensity');
saveas(gcf,strcat(outputpath,'Intensity_Profile_Col_',strpic4),'tif');

% Row Comparison
figure()
plot(M,File1Row,'k');
hold on;
plot(M,File2Row,'b');
hold on;
plot(M,File3Row,'r');
hold on;
plot(M,File4Row,'g');
hold off;
title(strcat('Row Intensity Profile Comparison'));
xlabel('Pixels');
ylabel('Blue Intensity');
axis tight;
```

```
saveas(gcf,strcat(outputpath,'Intensity_Profile_Row_All'),'tif');

% Column Comparison
figure()
plot(File1Col,M,'k');
hold on;
plot(File2Col,M,'b');
hold on;
plot(File3Col,M,'r');
hold on;
plot(File4Col,M,'g');
hold off;
title(strcat('Column Intensity Profile Comparison'));
xlabel('Pixels');
ylabel('Blue Intensity');
axis tight;
saveas(gcf,strcat(outputpath,'Intensity_Profile_Col_All'),'tif');

% File 1 Blue Intensity
figure()
image(File1blue);
colormap([zeros(256,1), zeros(256,1),[0:1/255:1]']);
colorbar;
title(strcat(strpic1,' --LED Blue Intensity '));
saveas(gcf,strcat(outputpath,strpic1,'_LED_Blue_Intensity'),'tif');

% File 2 Blue Intensity
figure();
image(File2blue);
colormap([zeros(256,1), zeros(256,1),[0:1/255:1]']);
colorbar;
title(strcat(strpic2,' --LED Blue Intensity '));
saveas(gcf,strcat(outputpath,strpic2,'_LED_Blue_Intensity'),'tif');

% File 3 Blue Intensity
figure();
image(File3blue);
colormap([zeros(256,1), zeros(256,1),[0:1/255:1]']);
colorbar;
title(strcat(strpic3,' --LED Blue Intensity '));
saveas(gcf,strcat(outputpath,strpic3,'_LED_Blue_Intensity'),'tif');

% File 4 Blue Intensity
figure();
image(File4blue);
colormap([zeros(256,1), zeros(256,1),[0:1/255:1]']);
colorbar;
title(strcat(strpic4,' --LED Blue Intensity '));
saveas(gcf,strcat(outputpath,strpic4,'_LED_Blue_Intensity'),'tif');

% Intensities
File1intensity= sum(sum(File1blue));
File2intensity= sum(sum(File2blue));
File3intensity= sum(sum(File3blue));
File4intensity= sum(sum(File4blue));
intensities = [File1intensity File2intensity File3intensity File4intensity];
```

```
disp(strcat(strpic1,' Intensity : ',num2str(sum(sum(File1blue))) ));
disp(strcat(strpic2,' Intensity : ',num2str(sum(sum(File2blue))) ));
disp(strcat(strpic3,' Intensity : ',num2str(sum(sum(File3blue))) ));
disp(strcat(strpic4,' Intensity : ',num2str(sum(sum(File4blue))) ));

% Intensity Comparison
figure()
bar(intensities);
title(strcat('Overall LED Blue Intensities'));
axis tight
saveas(gcf,strcat(outputpath,'LED_Blue_Intensities'),'tif');
dlmwrite(strcat(outputpath,'Intensities.txt'),intensities);

% LED Intensity Profile Comparison
figure()
ax(1)=subplot(2,2,1);
mesh(double(File1blue));
title(strcat(strpic1,'--LED'));
xlabel('Pixels');
ylabel('Pixels');
axis([0 500 0 500 0 255]);
ax(2)=subplot(2,2,2);
mesh(double(File2blue));
axis([0 500 0 500 0 255]);
title(strcat(strpic2,' --LED'));
xlabel('Pixels');
ylabel('Pixels');
ax(3)=subplot(2,2,3);
mesh(double(File3blue));
axis([0 500 0 500 0 255]);
title(strcat(strpic3,' --LED'));
xlabel('Pixels');
ylabel('Pixels');
ax(4)=subplot(2,2,4);
mesh(double(File4blue));
axis([0 500 0 500 0 255]);
title(strcat(strpic4,' --LED'));
xlabel('Pixels');
ylabel('Pixels');
rotate3d on
linkprop(ax,...
    {'cameraviewangle',...
     'cameraposition',...
     'cameraupvector',...
     'cameratarget',...
     'cameraviewangle'});
view(-60,70);
saveas(gcf,strcat(outputpath,'LED_Blue_Intensity_Profile'),'tif');
close all;

% Preview LED Intensity Profile Comparison
figure()
ax(1)=subplot(2,2,1);
mesh(double(File1blue));
title(strcat(strpic1,'--LED'));
```

```
xlabel('Pixels');
ylabel('Pixels');
axis([0 500 0 0500 0 255]);
ax(2)=subplot(2,2,2);
mesh(double(File2blue));
axis([0 500 0 500 0 255]);
title(strcat(strpic2,' --LED'));
xlabel('Pixels');
ylabel('Pixels');
ax(3)=subplot(2,2,3);
mesh(double(File3blue));
axis([0 500 0 500 0 255]);
title(strcat(strpic3,' --LED'));
xlabel('Pixels');
ylabel('Pixels');
ax(4)=subplot(2,2,4);
mesh(double(File4blue));
axis([0 500 0 500 0 255]);
title(strcat(strpic4,' --LED'));
xlabel('Pixels');
ylabel('Pixels');
rotate3d on
linkprop(ax,...
    {'cameraviewangle',...
     'cameraposition',...
     'cameraupvector',...
     'cameratarget',...
     'cameraviewangle'});
-----------------------------End-of-File------------------------------
```

9.4.6. Radiation Pattern Generation Setup

An additional performance metric used to evaluate light extraction in LEDs is the radiation spectra. The radiation spectra usually is used for determining the field of view of a device. A rotary setup was constructed to perform this task and is swiveled into place right after the device is probed using the micro manipulators as shown in the Figure 9.34. An optical fiber and the spectrometer is used to gather EL spectra at each angle. As shown in the Figure 9.35, the rotary setup is manually moved to different angles to gather EL data. From the EL data taken at normal, the peak emission wavelength is extracted and the intensity at that peak wavelength for each angle is used for generating the radiation spectrum of a device. A Matlab script is written to search the spectrometer data for the given peak wavelength and its respective intensity. This search is done on each EL spectrum taken at different angles and the respective intensities are plotted against the angles. This method was first tested on a commercial LED for which the radiation spectra was known. The results from this setup show a close resemblance to the data from the data sheet as seen in Figure 9.36.

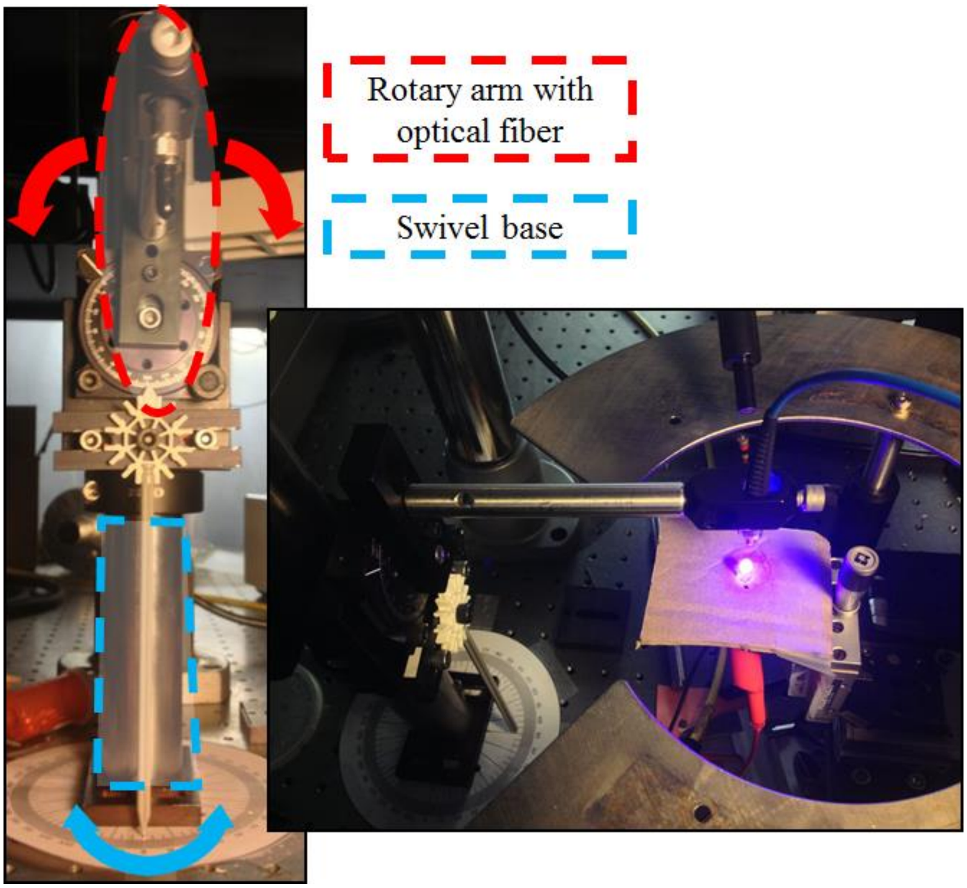

Figure 9.34 Rotary arm setup for radiation pattern generation (inset: top view of the rotary arm)

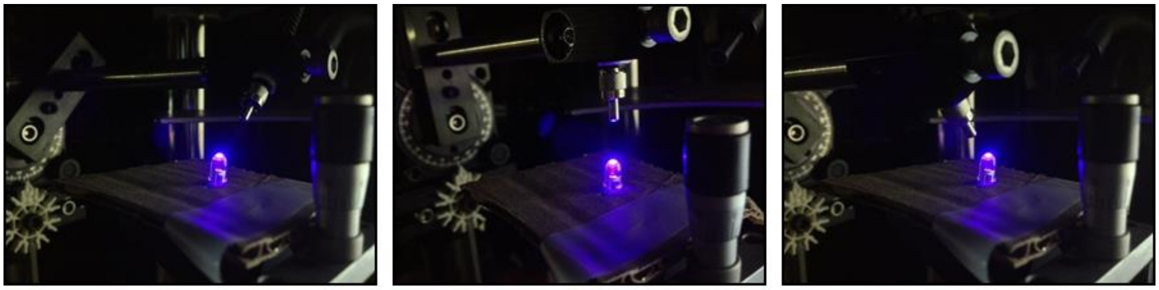

-40° 0° 40°

Figure 9.35 EL spectrum taken at angles -40^{o}, 0^{o}, and 40^{o} using the rotary arm setup

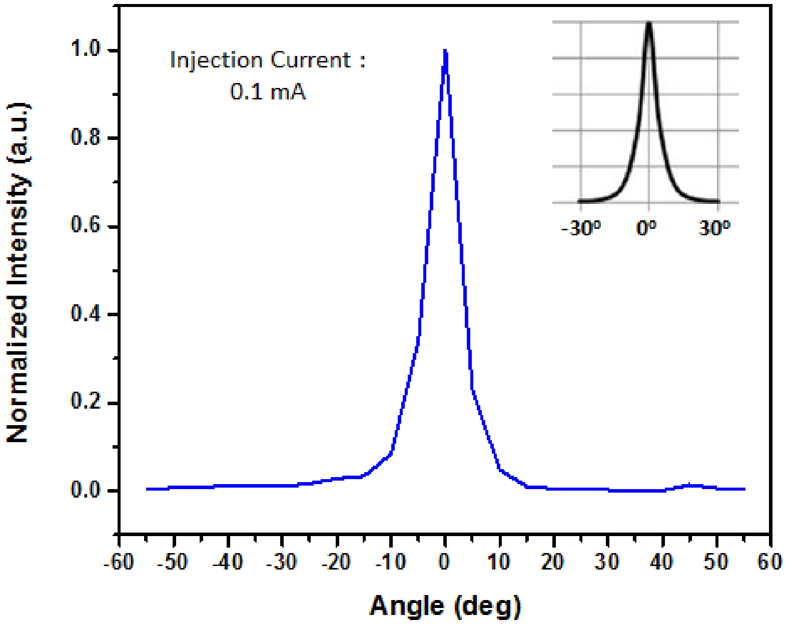

Figure 9.36 Radiation spectra of the commercial blue LED generated using the rotary arm setup (inset: Actual data from datasheet)

9.4.7. Radiation Plot Generator

The Matlab script for searching all the EL data and generating the radiation plot is shown here.

Filename: radiation_plot_generator.m

```
------------------------------Start-of-File-------------------------------

clear all;
clc;
sangle=-55;%input('Enter start angle:');
step=5;%input('Enter the step:');
eangle=55;%input('Enter end angle:');
range=sangle:step:eangle;
wl=input('Enter the target wavelength:');
LED=input('Enter the LED name:');% Should be in the form of
2CAP3_60mA_250ms_20reps_0deg
filepath=uigetdir();

for i=1:length(range)

filenames=strcat(filepath,'\',LED,'_10mA_100ms_20reps_',num2str(range(i)),'_d
eg.txt');
    temp=dlmread(filenames,';',403,1);
    index=find(temp(:,1) == wl);
    intensity(i)=temp(index,7);
end
```

```
nintensity=intensity./max(intensity);
angles=range.*(pi/180);
polar((pi/2)+angles,nintensity);
axis([-pi/2 pi/2 0 1]);
xlabel('Angles');
ylabel('Normalized Intensity');
saveas(gcf,strcat(filepath,'\',LED,'_',num2str(wl)),'tif');
dlmwrite(strcat(filepath,'\',LED,'_',num2str(wl*100),'.txt'),[range',intensity']);

--------------------------------End-of-File---------------------------------
```